InSb AND InAsSb INFRARED PHOTODIODES ON ALTERNATIVE SUBSTRATES AND InP/InGaAs QUANTUM WELL INFRARED PHOTODETECTORS: PIXEL AND FOCAL PLANE ARRAY PERFORMANCE

A THESIS SUBMITTED TO
THE GRADUATE SCHOOL OF NATURAL AND APPLIED SCIENCES
OF
MIDDLE EAST TECHNICAL UNIVERSITY

BY

SELÇUK ÖZER

IN PARTIAL FULFILLMENT OF THE REQUIREMENTS
FOR
THE DEGREE OF DOCTOR OF PHILOSOPHY
IN
ELECTRICAL AND ELECTRONICS ENGINEERING

MAY 2005

Approval of Graduate School of Natural and Applied Sciences.

Prof. Dr. Canan ÖZGEN
Director

I certify that this thesis satisfies all the requirements as a thesis for the degree of Doctor of Philosophy.

Prof. Dr. İsmet ERKMEN
Head of Department

We certify that we have read this thesis and that in our opinion it is fully adequate, in scope and quality, as a thesis for the degree of Doctor of Philosophy.

Prof. Dr. Cengiz BEŞİKCİ
Supervisor

Examining Committee Members:

Prof. Dr. Tayfun AKIN (METU, EE) ____________________

Prof. Dr. Cengiz BEŞİKCİ (METU, EE) ____________________

Prof. Dr. Ekmel ÖZBAY (Bilkent University) ____________________

Prof. Dr. Murat EYÜBOĞLU (METU, EE) ____________________

Dr. Haluk KÜLAH (METU, EE) ____________________

I hereby declare that all information in this document has been obtained and presented in accordance with academic rules and ethical conduct. I also declare that, as required by these rules and conduct, I have fully cited and referenced all material and results that are not original to this work.

Name, Last name :

Signature :

ABSTRACT

InSb AND InAsSb INFRARED PHOTODIODES ON ALTERNATIVE SUBSTRATES AND InP/InGaAs QUANTUM WELL INFRARED PHOTODETECTORS: PIXEL AND FOCAL PLANE ARRAY PERFORMANCE

ÖZER, Selçuk
Ph.D., Department of Electrical and Electronics Engineering
Supervisor: Prof. Dr. Cengiz BEŞİKCİ

May 2005, 213 pages

$InAs_xSb_{1-x}$ (Indium Arsenide Antimonide) is an important low bandgap semiconductor whose high quality growth on GaAs or Si substrates is indispensible for low cost, large format infrared focal plane arrays (FPAs). Quantum well infrared photodetector (QWIP) technology, relying on mature semiconductors, is also promising for the above purpose. While AlGaAs/GaAs has been the standard material system for QWIPs, the search for alternative materials is needed for better performance. This thesis reports a detailed investigation of molecular beam epitaxy grown mid-wavelength infrared $InAs_xSb_{1-x}$ photodiodes on alternative substrates, and long wavelength infrared InP/InGaAs QWIPs.

In the first part of the study, InSb and $InAs_{0.8}Sb_{0.2}$ photodiodes grown on Si and GaAs substrates are investigated to reveal the performance degrading mechanisms due to large lattice mismatch. $InAs_{0.8}Sb_{0.2}$/GaAs photodiodes yield peak detectivities of 1.4×10^{10} and 7.5×10^{8} $cmHz^{1/2}/W$ at 77 K and 240 K, respectively, showing that the alloy is promising for both cooled and near room temperature detectors. Under moderate reverse bias, 80 K R_oA product limiting mechanism is trap assisted tunneling, which introduces considerable $1/f$ noise. InSb/Si photodiodes display peak 77 K detectivity as high as $\sim1\times10^{10}$ $cmHz^{1/2}/W$ and reasonably high peak quantum efficiency in spite of large lattice mismatch. R_oA product of detectors at 80 K is limited by Ohmic leakage with small activation energy (25 meV). Bias and temperature dependence of $1/f$ noise is in reasonable agreement with Kleinpenning's mobility fluctuation model, confirming the validity of this approach.

The second part of the study concentrates on $InP/In_{0.53}Ga_{0.47}As$ QWIPs, and 640×512 FPA, which to our knowledge, is the largest format InP/InGaAs QWIP FPA reported. InP/InGaAs QWIPs yield quantum efficiency-gain product as high as 0.46 under moderate bias. At 70 K, detector performance is background limited with f/2 aperture up to ~3 V bias where peak responsivity (2.9 A/W) is thirty times higher than that of the $Al_{0.275}Ga_{0.725}As/GaAs$ QWIP with similar spectral response. Impact ionization in InP/InGaAs QWIPs does not start until the average electric-field reaches 25 kV/cm, maintaining high detectivity under moderate bias.

The 640×512 InP/InGaAs QWIP FPA yields noise equivalent temperature difference of ~40 mK at an FPA temperature as high as 77 K and reasonably low NETD even with short integration times (τ). 70 K NETD values of the FPA with f/1.5 optics are 36 and 64 mK under –0.5 V (τ=11 ms) and –2 V (τ=650 μs) bias, respectively. The results clearly show the potential of InP/InGaAs QWIPs for thermal imaging applications requiring short integration times.

Keywords: Cooled infrared detectors, InAsSb, QWIP, focal plane array.

ÖZ

ALTERNATİF TABANLAR ÜZERİNDE InSb VE InAsSb KIZILÖTESİ FOTODİYOTLAR VE InP/InGaAs KUANTUM KUYULU KIZILÖTESİ FOTODEDEKTÖRLER: PİKSEL VE ODAK DÜZLEM MATRİSİ PERFORMANSI

ÖZER, Selçuk
Doktora, Elektrik ve Elektronik Mühendisliği Bölümü
Tez Yöneticisi: Prof. Dr. Cengiz BEŞİKCİ

Mayıs 2005, 213 sayfa

$InAs_xSb_{1-x}$ (İndiyum Arsenik Antimon) düşük maliyetli, geniş formatlı odak düzlem matrisleri (ODM) için GaAs veya Si tabanlar üzerinde yüksek kalitede büyütülmesi mühim olan önemli bir düşük bant aralıklı yarı-iletkendir. Olgun yarıiletkenler üzerine kurulu kuvantum kuyulu kızılötesi fotodedektör (KKKF) teknolojisi de bu konuda ümit vericidir. AlGaAs/GaAs malzemesi KKKF'ler için standart bir malzemedir fakat daha iyi performans gösterecek alternatif malzemelerin araştırılması gerekmektedir. Bu tez, alternatif tabanlar üzerine moleküler ışın epitaksisi ile büyütülmüş orta dalgaboylu kızılötesi $InAs_xSb_{1-x}$ fotodiyotlar ile uzun dalga boylu InP/InGaAs KKKF'ler üzerindeki detaylı çalışmaları içermektedir.

Çalışmanın ilk kısmında, Si ve GaAs tabanlar üzerine büyütülmüş InSb ve $InAs_{0.8}Sb_{0.2}$ fotodiyotlar, büyük miktardaki örgü uyumsuzuluğundan kaynaklanan performans sınırlayıcı mekanizmaların tesbiti amacıyla incelenmiştir. $InAs_{0.8}Sb_{0.2}$/GaAs fotodiyotların 77 K ve 240 K sıcaklıklarda sahip olduğu dedektivite değerleri sırasıyla 1.4×10^{10} ve 7.5×10^{8} $cmHz^{½}/W$ olarak ölçülmüştür ve bu sonuç alaşımın soğutmalı ve yaklaşık oda sıcaklığında çalışan dedektörler için ümit verici olduğunu göstermektedir. Orta derecelerdeki ters eğilimleme durumunda, 80 K sıcaklıkta R_oA çarpımını etkileyen mekanizmanın tuzak yardımlı tünelleme mekanizması olduğu tesbit edilmiştir ve bu mekanizma aynı zamanda 1/f gürültüsünü de önemli bir miktarda arttırmaktadır. InSb/Si fotodiyotlar, büyük miktarlardaki örgü uyumsuzluğuna rağmen 77 K sıcaklıkta $\sim1\times10^{10}$ $cmHz^{1/2}/W$ gibi yüksek bir tepe dedektivite değeri ve kabul edilebilir kuvantum verimliliği vermektedir. Dedektörlerin 80 K sıcaklıktaki R_oA çarpımı, düşük aktivasyon enerjili (25 meV) ohmik kaçak mekanizması tarafından sınırlanmaktadır. 1/f gürültüsünün gözlenen eğilim ve sıcaklık bağımlılığı, Kleinpenning'in taşınırlık dalgalanma modelini doğrulamaktadır.

Çalışmanın ikinci kısmında InP/$In_{0.53}Ga_{0.47}As$ KKKF'ler ve bildiğimiz kadarıyla şimdiye kadar rapor edilen en büyük InP/InGaAs KKKF ODM formatı olan 640×512 formatında ODM'ler incelenmektedir. InP/InGaAs KKKF'ler -3 V eğilimleme altında 0.46 kadar yüksek kuvantum verimliliği-kazanç çarpımı vermektedir. Bu dedektörler, 70 K sıcaklıkta ve f/2 açıklık ile ~3 V eğilimlemeye kadar arkaplan sınırlı performans göstermektedir ve bu eğilimlemedeki tepe tepkisellik (2.9 A/W), benzer izgesel cevaba sahip $Al_{0.275}Ga_{0.725}As$/GaAs KKKF'lerinkinden 10 kat daha fazladır. Sonuçlar InP/InGaAs KKKF'lerdeki çarpışma iyonizasyonunun, ortalama elektrik alan 25 kV/cm değere ulaşıncaya kadar başlamadığını ve dedektivitenin orta dereceli eğilimlemede yüksek kaldığını göstermektedir.

640×512 InP/InGaAs KKKF ODM 77 K sıcaklıkta ~40 mK değerinde gürültü eşdeğer sıcaklık farkı (GESF) vermektedir. ODM kısa entegrasyon sürelerinde (τ) bile düşük GESF sunabilmektedir. f/1.5 optik ile ODM'nin 70 K sıcaklığındaki GESF değerleri, –0.5 V (τ=11 ms) ve –2 V (τ=650 μs) eğilimleme durumlarında sırasıyla 36 ve 64 mK'dir. Sonuçlar InP/InGaAs KKKF'lerin kısa entegrasyon süreleri gerektiren termal görüntüleme uygulamaları için yeterliliğini göstermektedir.

Anahtar Kelimeler: Soğutmalı kızılötesi dedektörler, InAsSb, QWIP, odak düzlem matrisi.

To My Family

ACKNOWLEDGMENTS

I would like to thank my supervisor, Professor Cengiz Beşikci, for his enlightened guidance, constant encouragement, and generous support, which have led me to successfully complete this thesis. It has been a fortune for me to have the privilege of working with him.

I would like to thank Professor Tayfun Akın and Professor Ekmel Özbay for serving on my progress committees, providing indispensable advice, and their invaluable collaboration by opening the doors of their laboratories to me. I would also like to thank my thesis defense committee members Professor Murat Eyüboğlu and Dr. Haluk Külah for taking time to read my thesis.

I am pleased to thank Oray Orkun Cellek for his continuous assistance and cooperation in many stages of the experimental work, and for his helpful discussions throughout my Ph.D study. I also thank him for sharing some of his Monte Carlo simulation results with me.

I must thank Ümid Tümkaya for his collaboration during the early stages of my Ph.D. study and preparing the photolithography masks. Many thanks extend to our research group members Burak Aşıcı, Sema Memiş, Umut Bostancı, Hasan Koçer, and Özlem Ersagun for creating a friendly working environment.

I also like to express my great appreciation to Orhan Akar for his patience during the dicing of the detector samples and read out ICs many times. I would like to thank Selim Eminoğlu for sharing his noise measurement setup and guidance during the noise measurements of the photodiodes. I must also mention the assistance of Murat Güre, Necmi Bıyıklı, and İbrahim Kimukin during the dry etching of the detectors at Bilkent University. I also have to express my thanks to Prof. Tayfun Akin's group members for their friendship.

I would like to thank Dr. Chris Van Hoof for giving access to his laboratories, and Dr. Joachim John, Lars Zimmerman, and Patrick Merken for their welcoming cooperation during my studies at Interuniversity Microelectronics Center (IMEC), Belgium. I would also like to express my thanks to Stefan Nemeth form XenICs, Belgium, for the growth of $InAs_{1-x}Sb_x$ photodiodes. Moreover, I must express my gratitude to Professor Manijeh Razeghi from Northwestern University, U.S.A., for providing the InSb/Si and AlInSb/InSb/Si wafers. I must thank Professor John David from the Sheffield University, U.K., for supplying the MOCVD grown AlGaAs/GaAs QWIP wafer.

I would like to acknowledge the bottomless support of my family, especially my sister İlknur, and their encouraging and motivating attitude towards me during my Ph.D. study. I am also grateful to the friends outside the department for their support.

Finally, I would like to thank ASELSAN Inc., the Research and Development Department of the Ministry of Defense and Scientific and Technical Research Council of Turkey (TUBITAK) for funding this research study.

TABLE OF CONTENTS

CHAPTER

APPENDIX

CHAPTER I

INTRODUCTION

Infrared (IR) radiation is a form of electromagnetic radiation. Therefore, IR radiation obeys the same laws as the other forms of electromagnetic radiation like visible light, radio waves, and x-rays. The wavelength of IR radiation extends from 0.7 to 1000 µm in the electromagnetic spectrum.

The IR radiation was first discovered by Sir William Herschel in 1800 while investigating the energy distribution of the solar spectrum by using a simple mercury-in-glass thermometer. In 1830, the discovery of the thermoelectric effect by Seeback [1] allowed the study of the emission and transmission spectrum of various materials. The photoconductive effect was discovered by Smith in 1873 [1], and the first infrared photoconductor of high responsivity was developed by Case in 1917 [1].

Recent success in remote sensing applications has been made possible by the rapid development of the infrared detector technology over the last five decades. Earlier developments in the narrow bandgap semiconductors, such as InSb and HgCdTe, have lead to high performance IR photon detectors. Recent advances in the epitaxial semiconductor growth technology have facilitated the fabrication of quantum well and superlattice heterostructures with the mature GaAs and InP technologies. Following these advances, IR detectors utilizing such semiconductor structures have emerged as an alternative to the conventional low bandgap semiconductor IR photon detectors. As the result of this development, quantum well infrared photodetector (QWIP) focal plane arrays (FPAs) have already been commercialized by several manufacturers. Superlattice infrared photodetectors can be expected to share the IR detector market in the near future.

Today, there is a serious competition between the HgCdTe and QWIP technologies both in the long-wavelength infrared (LWIR, 8-12 µm) and mid-wavelength infrared (MWIR, 3-5 µm) bands for thermal imaging applications. AlGaAs/GaAs has been the most widely employed semiconductor system for QWIPs both at research and production stages. Relying on the mature GaAs technology, QWIPs offer much better uniformity, especially for LWIR FPAs, as well as much lower fabrication cost. Nevertheless, the low quantum efficiency of the standard AlGaAs/GaAs QWIPs has been a bottleneck for widespread utilization of this detector in high performance thermal imaging systems. However, the QWIP technology is relatively new, and the QWIP performance has improved rapidly through studies on new quantum well structures, as well as on new material systems for QWIPs.

Development of the infrared detector technology calls for long, comprehensive and systematic studies covering material growth, material characterization, detector modeling/design, fabrication process optimization, test detector fabrication/characterization, FPA level process optimization, and FPA fabrication/testing. Understanding and correctly interpreting the detector characteristics are especially important for the optimization of the IR detectors based on new structures and/or materials. Process optimization studies are also very important in order to achieve the best possible performance with a reasonably high fabrication yield. With the primary objective of contributing to the advancement of LWIR and MWIR detector technology, a considerable portion of this study deals with the above issues.

The main objectives of this thesis work are as follows:

(i) In the first part of the study, we carried out detailed investigation of the characteristics of middle wavelength infrared (3-5 μm) InSb and $InAs_{0.8}Sb_{0.2}$ photovoltaic detectors on alternative substrates such as Si and GaAs, which offer considerably higher quality and size when compared with the conventional InSb substrates. In the scope of this part of the study, detailed characterization and dark current modeling were performed on InSb and $InAs_{1-x}Sb_x$ test detectors to reveal the performance limiting mechanisms. This work was followed by the fabrication of 128×128 FPAs to assess the FPA performance. The results of these studies yielded invaluable information on the feasibility of large format, low cost InSb and $InAs_{1-x}Sb_x$ IR FPAs on Si and GaAs substrates, as well as considerable contribution to the literature on the dark current and 1/f noise mechanisms in IR detectors fabricated on lattice mismatched substrates.

(ii) The second part of the study focused on the QWIPs. The objectives of this part were the development of the fabrication and hybridization technologies for very large format LWIR QWIP FPAs, the investigation of the performance of the InP/InGaAs semiconductor system as an alternative to AlGaAs/GaAs for QWIP applications, and the achievement of a better understanding of QWIP operation and the underlying physics. As to our knowledge, the largest format (640×512) InP/InGaAs QWIP FPA, ever reported, has been fabricated through this study. This FPA is also the first molecular beam epitaxy grown LWIR InP/InGaAs QWIP FPA. We investigated the characteristics of AlGaAs/GaAs and InP/InGaAs QWIPs both at pixel and FPA levels in a very detailed manner. Achieved pixel performance, uniformity levels and the noise equivalent temperature differences (NETDs) show that the InP/InGaAs material system is a very good alternative to the most widely used AlGaAs/GaAs system, especially for applications requiring short integration times and high responsivities.

Detailed discussions on the above issues, as well as the results and the conclusions will be presented in the following chapters. Chapter I serves as an introduction to the IR detector technology by presenting the IR imaging applications, the general theory of IR radiation, basic building blocks of an infrared imager, and infrared detector types and figures of merit.

1.1 Infrared Imaging Applications

Infrared imaging finds numerous application areas both in civil and military fields, and some of them are given in Table 1.1. This section briefly discusses some of the infrared imaging applications.

Table 1.1: Civil and military applications of infrared imagers.

Civil Applications	**Military Applications**
• Drivers Vision Enhancement • Security Systems • Industrial Process Control • Fire Alarms • Medical Imaging • Satellite Instruments	• Night Vision Systems • Thermal Vision Systems • Mine Detection • Search and Track • Reconnaissance • Fire Control Systems

Fire fighting: Infrared imagers can be utilized for fighting against the forest fires. Normally it is not possible to see hot spots or flames from the air due to the dense smoke above the region. However smoke is transparent to the infrared light, and firefighters can see and concentrate on the critical points in the region [2].

Medicine: Infrared imaging is a promising technique for screening and diagnosing purposes in medicine. Clinical trials using an infrared imager have been discussed by Fauci *et. al.* [3]. Medical applications require high LWIR sensitivity, small number of dead pixels, high thermal and spatial resolution, short acquisition time, compatibility with large focal depth optics, and low cost FPAs, all of which are fulfilled with the state of the art IR technology [4].

Defense: In military applications, temperature of the target and background may change dramatically. When warm targets with high background irradiance are observed, discrimination of the target from the background is necessary which requires highly sensitive FPAs. The demand for very high performance, multispectral, uniform and high yield FPAs becomes more severe when strategic applications are considered. Degraded or dead pixels may cause a target to be missed completely. Missile seeker systems require higher operating temperatures, and lower cooldown times. On the other hand, reconnaissance systems require medium to large format FPAs, and use closed-cycle cooling to reach operating temperatures of 77 K.

Additionally, it has been shown that multispectral IR sensors can be used to detect buried land mines [5]. When the soil is disturbed to bury a mine, emission spectrum of the quartz in the soil changes, and returns to its steady state emission after several weeks. Most significant change in the emissivity occurs in a narrow band between 8-9 μm requiring two-color narrow-band detection.

1.2 General Theory of Infrared Radiation

All objects emit electromagnetic radiation with the properties depending on the temperature of the object. For objects near room temperature, the wavelength of the emitted radiation falls in the infrared range of the electromagnetic spectrum, which is invisible to human eye. The function of a thermal imager is the conversion of the infrared image of an object to visible one. Thermal imagers consist of several elements like optics assembly, infrared photodetector, signal processing and video electronics, and a monitor.

One of the key parameters determining the quality of the image obtained from a distant target is the amount of radiation the thermal imager can receive from that target. The intensity of IR light emitted from an object depends on several parameters like temperature of the object, distance from the object and its emissivity, which is simply defined as “how easily it can emit radiation”.

Furthermore, due to its absorption, the medium between the target and the imager also has an effect on the amount of light the imager can receive. All the issues counted above are in the scope of infrared thermography whose basic principles will be presented in this chapter.

1.2.1 Emission of IR light by matter

According to the Maxwell's laws, when an electric charge is accelerated it emits radiation. When a substance is heated, vibrational energy of its molecules is increased resulting in the acceleration of particular charge carriers and, hence, the generation of radiation. The following equation gives us the relationship between the wavelength of emitted radiation and the amount of energy that the radiation carries:

$$W = \frac{hc}{\lambda} \tag{1.1}$$

where λ is the wavelength, c is the speed of light and h is Plank's constant.

1.2.2 Black-body radiation

Power distribution spectrum of the radiation emitted by an object follows the Max Planck's radiation law. Actually, not all objects emit radiation according to Planck's law, it only states the limiting case. On the other hand, ideal emitters called blackbodies match the limiting curve of Planck's radiation law, so called the "blackbody radiation curve". According to Planck's law, spectral distribution of radiant photon emittance of a blackbody is given by

$$M_q(\lambda, T) = \frac{2\pi c}{\lambda^4 \left(e^{hc/\lambda kT} - 1\right)} \tag{1.2}$$

where c is speed of light in vacuum, h is Planck's constant, and k is Boltzmann's constant [6]. Figure 1.1 shows the plot of spectral radiant photon emittance with respect to wavelength for the blackbodies at various temperatures. As can be seen from the figure, when the source is warmer, total radiant energy emitted by this object is higher, and the peak emittance wavelength decreases with increasing temperature.

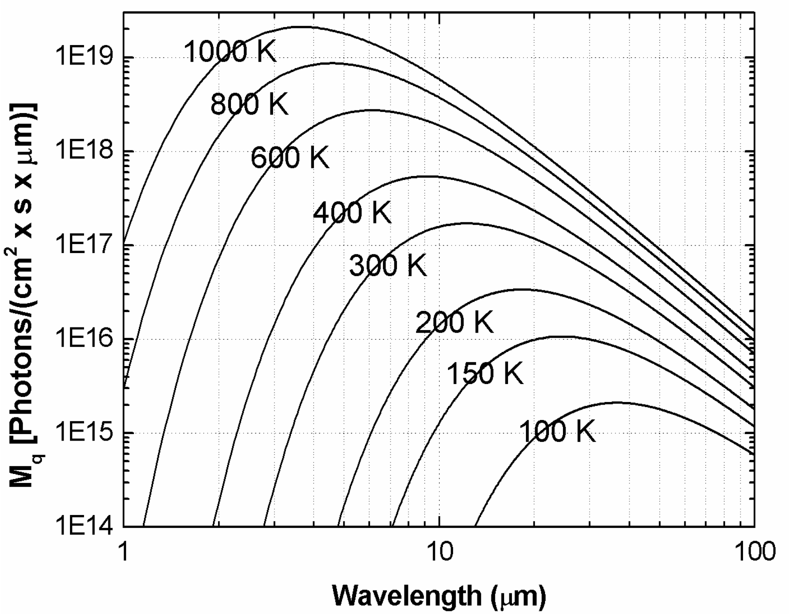

Figure 1.1: Blackbody radiation curve for various object temperatures.

1.2.3 Atmospheric transmission

For ground based applications, atmosphere plays an important role in the detection of infrared light from distant objects in two ways. Firstly, atmosphere, by itself, is also a source of radiation constituting a background to the target. Secondly, it attenuates the radiation coming from the object in two different ways: absorption by the atmospheric gas molecules and scattering of light by particles. Either absorption or scattering results in removal of energy from the incident radiation. Absorption by molecules is either due to electronic transitions in constituent atoms or vibrational states of atoms in the gas molecules. Major IR absorbing molecules in the atmosphere are H_2O, O_3, N_2O, CO, CH_4 and N_2. Figure 1.2 shows the atmospheric transmission spectrum and the molecules responsible for the absorption lines or bands. As can be seen from the figure, atmosphere is relatively transparent at certain wavelength ranges that are called "atmospheric transmission windows". In the literature, these windows are classified as follows:

- Near Infrared (NIR): 0.7 to 1.5 µm.
- Short Wavelength Infrared (SWIR): 1.5 to 3 µm.
- Mid Wavelength Infrared (MWIR): 3 to 5 µm.
- Long Wavelength Infrared (LWIR): 8 to 12 µm.
- Very Long Wavelength Infrared (VLWIR): 12 to 25 µm.
- Far Infrared (FIR): longer than 25 µm.

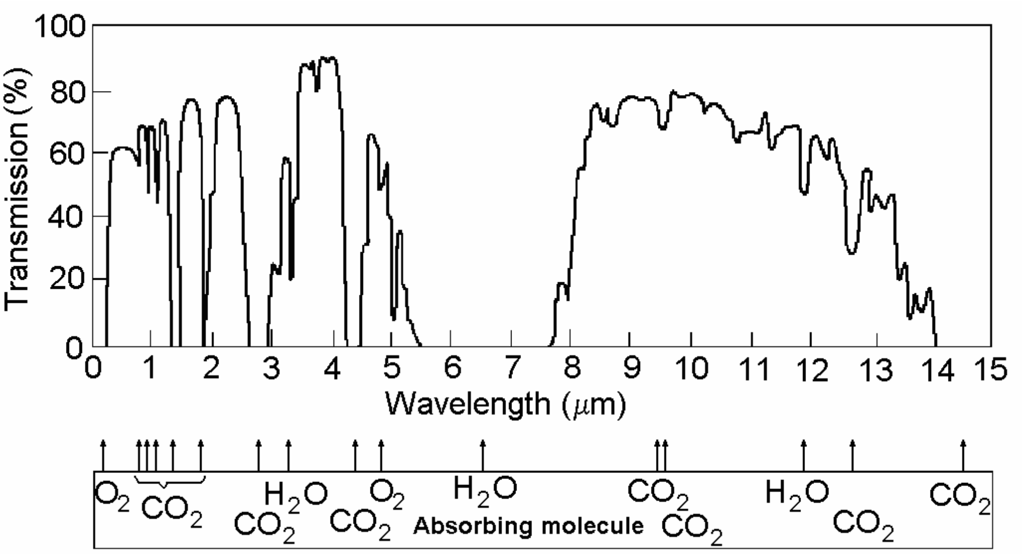

Figure 1.2: Atmospheric transmission spectrum and absorbing molecules. Spectrum was measured at sea level and through 6000 ft horizontal path [7].

The atmospheric transmission spectrum given in Figure 1.2 is not constant for all conditions. It depends on the atmospheric circumstances like altitude, relative humidity, climate, and gas content. Besides, the atmosphere is not a homogeneous medium, and its refractive index is a complex function of position and time, depending on winds, thermal convection currents, the gravitational field, and humidity. Additionally, man-made atmospheric conditions like battlefield circumstances can significantly affect the transmission [8], since battlefield obscurants like artillery round dust, fog oil, and white phosphorus scatter the light and reduce transmission.

MWIR and LWIR bands are usually employed in the ground based tactical applications, because the peak radiant power emitted by objects of interest occurs in these bands. In the MWIR band, thermal contrast, which is defined as the percent change in the emitted flux for one Kelvin change in target temperature, is two times larger than that in LWIR band. Temperature variation on a surface is more observable when the thermal contrast is high.

Spectral band choice depends on the target signature (target versus background), atmospheric transmission, and sensor response (optics and detector). For example, for naval applications, where the humidity is relatively high, MWIR is suitable. LWIR is more appropriate in low humidity and cold environments. Under battlefield conditions LWIR is more appropriate because longer wavelength radiation penetrates the obscurants more effectively [8]. Additionally, there are several high intensity sources like muzzle flash on a battle ground scene resulting in partially saturated images. MWIR imagers are more severely affected by such sources because of the very large difference in the emittance of the hot and room temperature objects in this band. For particular scenes, both MWIR and LWIR imagers may miss some details. Figure 1.3 shows two images of the same sight taken with MWIR and LWIR FPAs, which signifies the importance of the use of both MWIR and LWIR bands simultaneously [9].

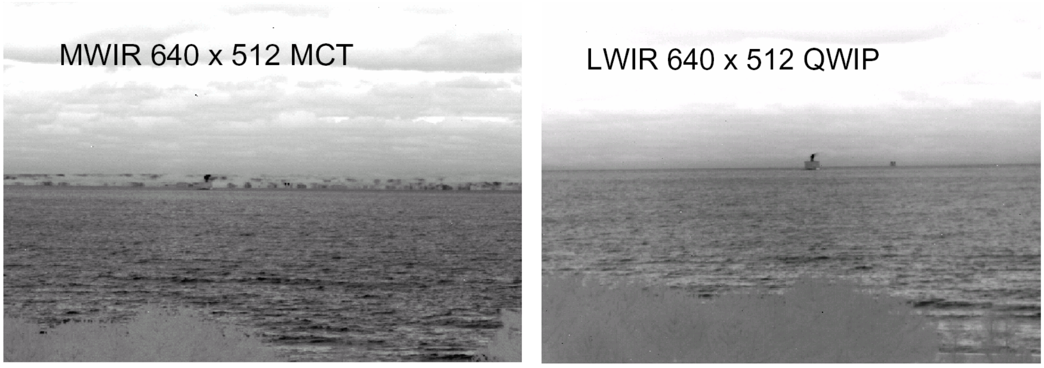

(a) (b)

Figure 1.3: Images taken with (a) MWIR 640×512 MCT and (b) LWIR 640×512 QWIP FPAs [9].

1.3 Basic Blocks of an Infrared Imager

The quality of infrared imaging depends on target signature, environmental conditions, and building components of the imager. Basic building blocks of an infrared imager are illustrated in Figure 1.4 and discussed in the following subsections.

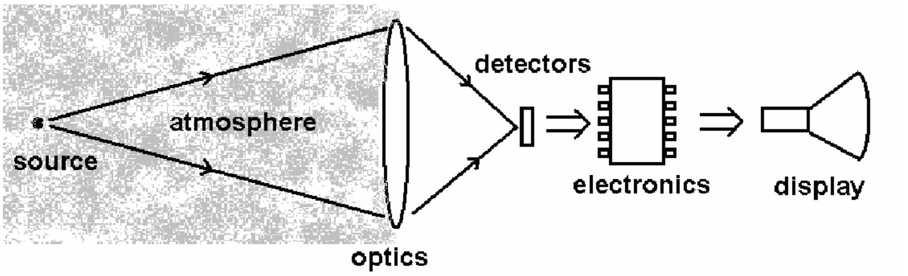

Figure 1.4: Basic building blocks of an infrared imager.

1.3.1 Optics for infrared systems

Either transparent lenses or reflective mirrors can be used to form the image of a target on detectors. Transparency of the lens must be as high as possible, and dependency of its refractive index on wavelength and temperature must be minimized. Transmission spectrum of the lens material and anti-reflection coatings determine the wavelength band whom the lens is transparent. Ge, ZnS and ZnSe are the most widely used lens materials for detection in the MWIR and LWIR bands.

Another way to form an image on focal plane is the usage of mirrors. Unlike lenses, mirrors are achromatic allowing the operation of all wavelengths in the infrared range. Reflection of mirrors, which can be improved by surface coating, must be very high.

1.3.2 Scanning and Staring Systems

A thermal imager can have either a scanning or staring optics depending on the number of pixels on detector array. An IR detection system can be a single pixel detector, a line array, or a two-dimensional staring array. Figure 1.5 illustrates the scanning and staring systems. In scanning systems, spinning mirrors or refracting prisms are driven mechanically to project the segments of the target scene onto detector elements sequentially. When a single pixel sensor is used in a system, image is scanned in both horizontal and vertical directions. On the other hand, scanning is performed in only one direction when the detector consists of linear array of elements.

A staring array is made up of 2-D array of detector pixels and does not require mechanical scanning. Linear arrays require bulky mechanical scanning systems and are usually used when it is not easy to produce large format, uniform 2-D detector arrays. Besides, integration times of linear arrays are usually very short when compared with that of 2-D staring arrays. Longer integration time results in high FPA sensitivity even the single pixel performance of the detector is not good.

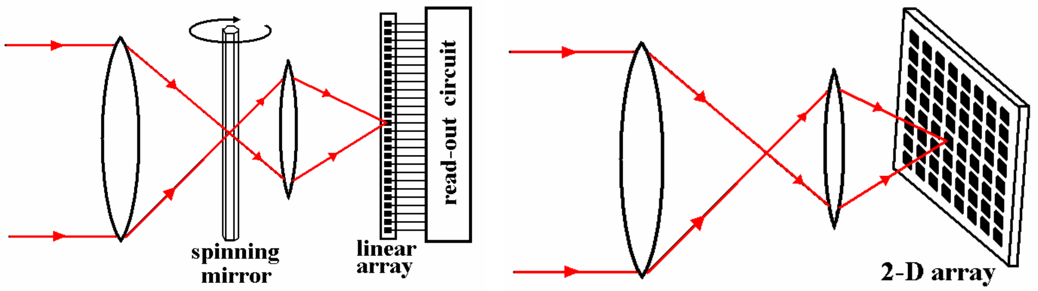

(a) (b)

Figure 1.5: Illustration of a (a) scanning and (b) staring system.

Uniformity of the 2-D arrays must be very high, which is not easy to achieve with some material systems. On the other hand, line arrays are implemented on a small wafer area, therefore the uniformity problem is not stringent. Some scanning systems provide additional signal processing methods to enhance the signal-to-noise ratio like time-delay integration (TDI) and signal processing in the element (SPRITE) techniques [10]. In linear arrays, it is also possible to update the correction table of nonuniformity in pixel responses between each scanned frame. This process is carried out in real-time allowing the adaptation of the imager to changing environmental conditions, and the residual fixed pattern noise does not evolve with time unlike 2-D arrays. Finally, staggered pixel distribution of some TDI arrays results in reduced optical crosstalk levels when compared with staring FPAs [11].

1.4 Types of Infrared Detectors

There are several material systems, and structures used for the fabrication of infrared detectors. IR detectors can be classified into two groups based on the physical principles of operation: photon detectors and thermal detectors. In photon detectors, radiation is absorbed by interaction of incident photons with electrons in the detector material. This leads to a change in the electronic charge distribution which can be sensed with the help of an external electric circuitry. Since photons carry relatively low energy packets in the IR region, detector temperature must be kept low to reduce the thermally generated noise below the useful electrical signal produced in the device. Cooling requirements make the imagers based on photon detectors expensive and bulky. On the other hand, this type of detectors give very high signal-to-noise ratios and short response times. Besides, photon detectors are quite wavelength selective when compared with thermal detectors, which becomes an advantage for the construction of multiband sensors.

In thermal detectors, electromagnetic radiation alters the temperature of an absorbing layer, and hence changes some physical properties of the material. This change is translated into electrical signals and measured by a circuitry. Although cryogenic cooling is not a requirement, isolation of the thermal detectors from the ambient temperature fluctuations is usually required. They are quite slow in response time when compared with photon detectors. Additionally, unlike photon detectors, thermal detectors are not spectrally selective. On the other hand, they are reliable, light, and low cost detectors, which make them proper for most of the civil applications. Some examples of widely used thermal detectors are explained briefly below:

Bolometers: Conductivity of the active material is changed as the result of absorption of the incident radiation. When bias is applied between the terminals, current flowing through the bolometer increases or decreases depending on the temperature change. Usually a thin metal or semiconductor film is deposited as the absorber layer on the bolometer structure which is isolated from the substrate to minimize the heat flow. The state of the art microbolometer FPAs with 640×480 array size yield 50 mK NETD using f/1 lens [12].

Pyroelectric detectors: Pyroelectric detectors consist of crystal wafers that produce surface charge due to internal polarization when heated. When the incident infrared radiation is modulated using a chopper, an alternating current flows in an external circuit connected to the opposite faces of the pyroelectric material. Amount of the alternating current is proportional to the intensity of the absorbed light. There are pyroelectric FPAs in the commercial market with 320×240 array size with NETD values smaller than 100 mK [13].

Thermocouples and thermopiles: Thermocouples generate thermo-electric emf when heated. Thermopiles consist of a large number of thermocouples connected in series to increase thermally generated emf. One junction of the thermocouples is in connection to a substrate whose temperature is constant. Infrared radiation heats the other junctions and generates a voltage signal in each thermocouple whose amplitude depends on the amount of infrared radiation. It is not practical to implement large format FPAs with thermocouples. The maximum reported array size is 128×128 with NETD of 500 mK with an f/1 lens [14].

Pneumatic detectors: Infrared radiation heats a gas container having a thin membrane of pneumatic detector. Expansion of heated gas deforms the membrane, and the amount of deformation is measured by electromechanical or optical methods.

1.5 Infrared photon sensors

Photon detectors can be divided into several subgroups depending on the nature of electron-photon interaction. Most important ones and their operational principles are given below:

Intrinsic detectors: Electron transition occurs from valance to conduction energy band in the semiconductor crystal. Bandgap of the semiconductor alloy determines the cut-off wavelength of the absorption spectrum. InSb, HgCdTe, InAs, PbTe, PbSe, PbS, and PbSnTe are the most widely used intrinsic detector materials. Detectivity spectra of various infrared detectors are given in Figure 1.6. Spectra of some thermal detectors are also given in the same figure for comparison.

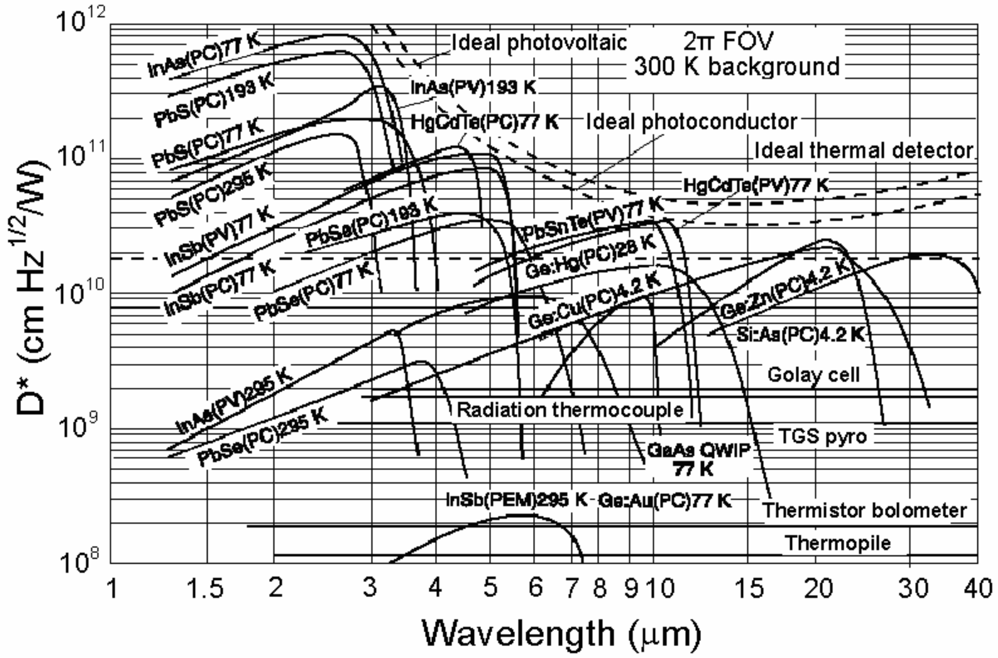

Figure 1.6: Ideal detectivity (D*) spectra of several IR detectors looking at 300 K background through 180˚ FOV. Operating temperature and structure of the detectors are indicated in the figure [7].

Extrinsic detectors: In this type of detectors, a large bandgap semiconductor is doped with impurities which introduce energy levels close to the conduction band. Activation energy of the impurities determines the cut-off wavelength of the detector. Si/In, Si/Ga, Ge/Cu, and Ge/Hg are the most widely used semiconductor/impurity systems in this type of detectors. Cooling requirements of the extrinsic detectors are more severe than that of the intrinsic detectors when both types have the same cut-off wavelength. On the other hand, very long wave detection up to 300 µm is possible with extrinsic detectors, and their fabrication technology is relatively simple. Actually, extrinsic detector technology is the foremost technology used for detection beyond 20 µm.

Schottky diodes: In schottky barrier photoemissive detectors, radiation is not absorbed in the semiconductor but in the metal constituting the schottky contact. The most common schottky-barrier detector is the PtSi detector, which operates in the MWIR band. LWIR detection is possible using IrSi, but this requires cooling below 77 K. In PtSi detectors, radiation passes through transparent p-type silicon and absorbed in PtSi layer. This way hot electrons are created, which are subsequently emitted over the potential barrier, leaving the silicide charged. Then, this charge can be transferred to CCD by direct injection methods.

Although quantum efficiency of the schottky-barrier detectors is very low when compared with that of other photon detectors (of the order of 1%), this technology has several advantages like monolithic integration of the detector FPAs with standard silicon very large scale integration (VLSI) process. Besides, schottky photoemission is independent of the parameters like semiconductor doping, minority carrier lifetime and alloy composition. Therefore, spatial uniformity is only limited by the geometry of the detectors, which makes the schottky-barrier detector FPAs very uniform and reproducible.

Quantum wells and superlattice detectors: QWIP technology is the freshest one amongst the technologies mentioned previously. In QWIPs, photon absorption takes place in quantum wells sandwiched between barriers. Generally QWIPs consist of quantum well – barrier stacks, and generally 30-50 wells are used in QWIP structures. Large bandgap material systems are used to implement QWIPs, which are enduring and resistant to process conditions. High uniformity over the growth area makes the production of large format FPAs possible. Furthermore, detection wavelength tuning by bandgap engineering, and possibility of LWIR and VLWIR detection make the QWIP technology an alternative to HgCdTe (MCT) technology. While QWIPs cannot compete with MCT detectors when single pixel performances are compared, FPA performances of these technologies are comparable. More detail on this issue will be given in Chapter II.

In addition to MCT and QWIP technologies, strained layer superlattice (SLS) technology also offers multi-color detection and wavelength tuning. Type II InAs/InGaSb alloy system has been the most commonly investigated SLS material system. As illustrated in Figure 1.7, in this type-II system, InAs conduction band energy level is lower than InGaSb valance band energy level leading to energy states accommodating hole and electron minibands. The gap between the hole and electron minibands is lower than the bandgaps of both InAs and InGaSb. This results in a virtually narrow bandgap semiconductor. Advantages of this technology over QWIP technology are higher quantum efficiency, broader absorption spectrum, lower operation bias, and more flexibility in bandgap engineering. SLS detectors have also some advantages over HgCdTe detectors. Electron effective mass in HgCdTe LWIR detectors is considerably less than that in InAs/InGaSb SLS detectors, which leads to enhanced tunnelling currents, and hence higher leakage currents and noise levels in HgCdTe detectors.

Photon detectors can be classified into two groups; photoconductive and photovoltaic detectors, which will be described in the following subsections. Following this description, we will extend the discussion on QWIPs, which can be either a photoconductive or a photovoltaic detector.

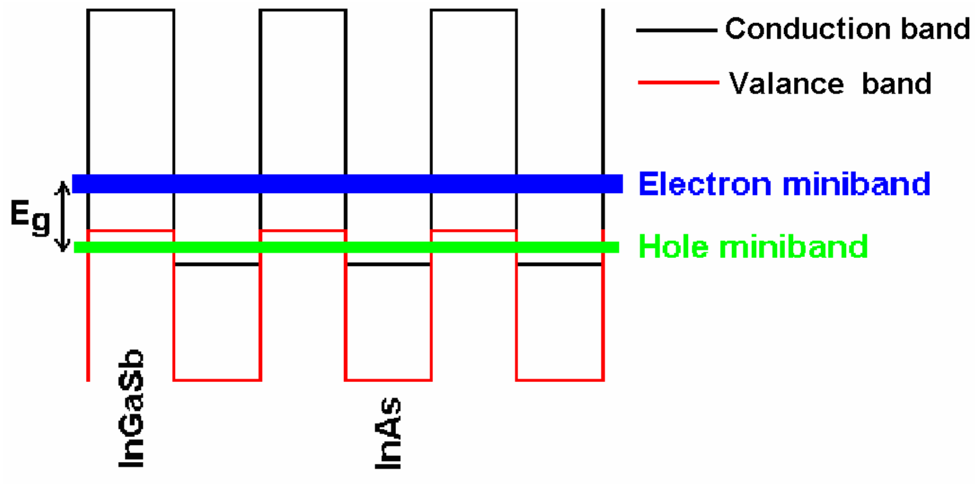

Figure 1.7: Illustration of the band profile of a type II InAs/InGaSb superlattice detector. Electron and hole minibands formed in the device are also illustrated.

1.5.1 Photoconductive Detectors

Photoconductive IR detectors can be based on either intrinsic or extrinsic semiconductor materials. Basic operation of a photoconductor is illustrated in Figure 1.8. Semiconductor absorbs the incident photons having energies larger than the bandgap energy (or impurity activation energy for extrinsic detectors). Absorption increases the number of free carriers by exciting electrons from valance band to conduction band (from impurity level to conduction band for extrinsic detectors), hence the conductivity of the detector changes. Amount of conductivity change, which is a measure of incident radiation intensity, is sensed by an external circuitry. This type of detector was used during the early stages of the thermal imager history. Low bandgap photoconductive detectors are low impedance devices; therefore, implementation of large format photoconductive detector FPAs is not practical due to intolerable I^2R power dissipation. On the other hand, photovoltaic detectors have high impedance and dissipate very little power. Besides, photovoltaic detectors show faster response due to the physical nature of the excited carrier transport as explained in the next section.

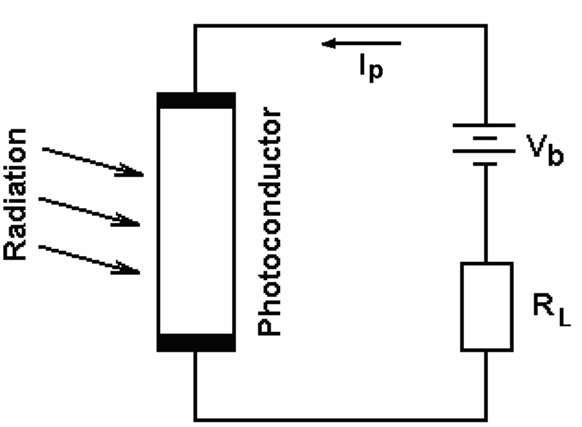

Figure 1.8: A photoconductor and read-out circuitry.

1.5.2 Photovoltaic Detectors

Photovoltaic effect can simply be defined as the separation of the excited positive and negative carriers with the help of a potential barrier. Principal photovoltaic detectors can be counted as p-n or p-i-n diodes, heterostructure diodes, Schottky barrier diodes, and metal-insulator-semiconductor (MIS) photo-capacitor devices. Figure 1.9 illustrates the structure and operation of a simple photodiode. Incident radiation excites electrons and creates electron-hole pairs in p- and n-type regions. Created electrons or holes diffuses towards the junction and are swept to the opposite side by the strong electric field in the depletion region. By this way, photocurrent is generated in the device, and the amount of photocurrent is

$$I_{ph} = \eta q A \Phi \tag{1.3}$$

where η is the quantum efficiency, q is the charge of electron, A is the area of the photodiode, and Φ is the incident photon flux density.

Photodiodes are generally operated around zero-bias voltage. “Zero-bias differential resistance area product” (R_0A) of the photodiode is one of the most important figure of merit for photodiodes. R_0A product for a photodiode can be given as

$$R_0 A = \left(\frac{\partial J}{\partial V} \right)^{-1}_{|V_b=0} \tag{1.4}$$

where J is the current density.

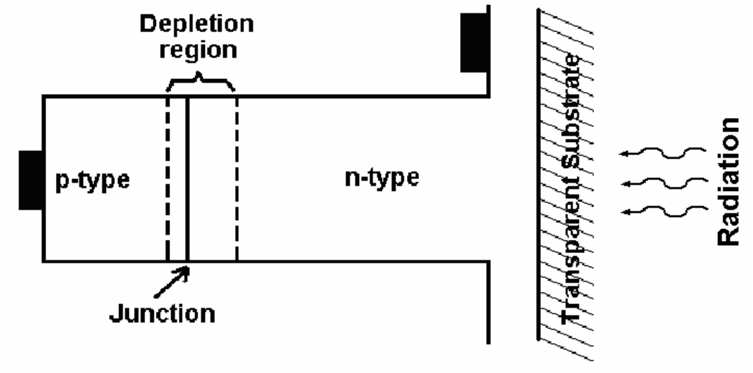

(a)

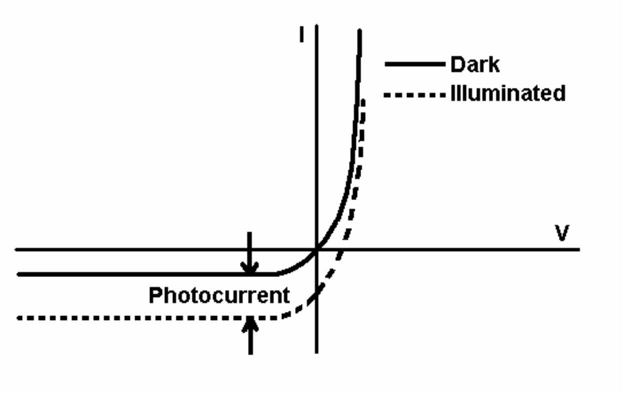

(b)

Figure 1.9: Structure (a), and I-V curve (b) of a photovoltaic p-n diode.

Quantum efficiency of a photodiode depends on the absorption coefficient of the constituent material, and the thickness of the base region (lightly doped region for p-n diodes and intrinsic region for p-i-n diodes). Direct bandgap materials are commonly used due to their higher absorption coefficients.

In an optimized photodiode, thickness of the base region is generally tuned for highest quantum efficiency, and a low dark current. Doping of this layer must be low to achieve high quantum efficiency. Generally, the diffusion length of the carriers is larger than the base region length. Therefore, almost all of the optically generated minority carriers reach the junction before recombining. Sometimes reflectors are used to increase the quantum efficiency by providing double pass of the radiation in the base region. Electronic contacts to the p- and n-type regions, which transfer photogenerated carriers to external read-out circuits, should not contribute to dark current and noise of the photodiode. Surfaces of the narrow bandgap regions must be passivated to provide isolation from the ambient. This way, photogenerated carriers in the absorption layer are kept away from the surface where strong recombination takes place due to localized surface states.

1.6 Quantum Well Infrared Photodetectors (QWIPs)

In conventional intrinsic infrared photodetectors, interband absorption takes place in narrow bandgap semiconductors. On the other hand, growth and processing of low-bandgap materials are rather difficult when compared with those of large bandgap materials like GaAs. It was understood that infrared detection is possible by using larger bandgap materials after Esaki and Sakaki proposed AlGaAs/GaAs quantum well structures for IR detection in 1977 [15]. Levine *et. al.* [16] demonstrated the first QWIPs in 1987. Since then, this technology has been investigated so extensively that large format (1024×1024) MWIR and LWIR QWIP FPAs, which show comparable performance to state-of-the-art HgCdTe detectors, are available today [17].

As illustrated in Figure 1.10, in a typical QWIP, a slightly lower bandgap semiconductor (quantum well material) is sandwiched between two semiconductor layers (barrier materials) having larger bandgaps. States in the potential well are quantized, and the energy difference between the first two quantized state energy levels controls the peak absorption wavelength of the structure. Fortunately, the difference between quantized energy levels (subbands) can be varied by adjusting the compositional and dimensional parameters of the quantum well and barrier. This provides a great flexibility to designer, and it becomes possible to detect infrared light even in the VLWIR (>12 µm) range. Hitherto, AlGaAs/GaAs has been the most commonly employed material system. Some advantages of AlGaAs/GaAs QWIPs over narrow bandgap intrinsic photodetectors are higher yield, radiation hardness, and lack of 1/f noise till very low frequencies. In addition to AlGaAs/GaAs material system, there are other material systems that can be used to implement QWIP structures like InGaAs/InAlAs, InGaAs/InP, GaAs/GaInP, GaAs/AlInP, and InGaAs/GaAs.

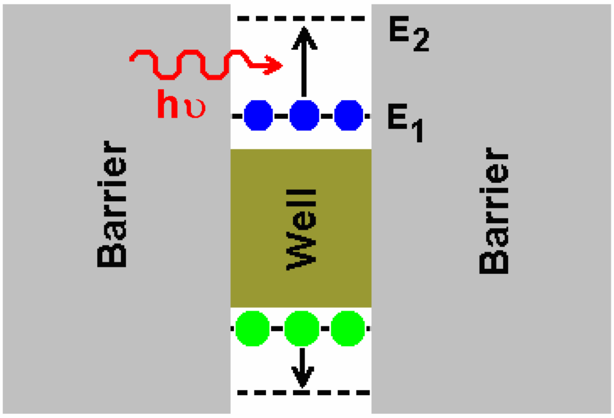

Figure 1.10: Illustration of quantum well energy band diagram. Quantum well is formed by sandwiching a well material (dark green) between larger bandgap barrier materials (gray). Electrons (blue) or holes (light green) are excited to second subband under illumination.

In contrast to intrinsic photodetectors, quantum wells must be doped, because the ground state subband (E_1 in Figure 1.10) must accommodate electrons for absorption to take place. Quantum wells can be either n-type or p-type doped depending on the material systems and structures used. Generally, n-type doping is employed. In n-type QWIPs, absorption of radiation propagating normal to the quantum wells is not possible due to some quantum mechanical selection rules. Electromagnetic radiation must have polarization component that is not normal to the quantum wells. Therefore, grating structures are used to diffract and reflect the radiation back to the quantum wells to provide absorption [18]. Figure 1.11 illustrates a simple QWIP pixel having a grating structure. As shown in the figure, incident radiation comes from the backside of the substrate and reflected from the reflector metallization just above the grating structures. Diffracted and reflected light propagate in altered directions, and have polarization components that are not normal to the quantum wells (QWs).

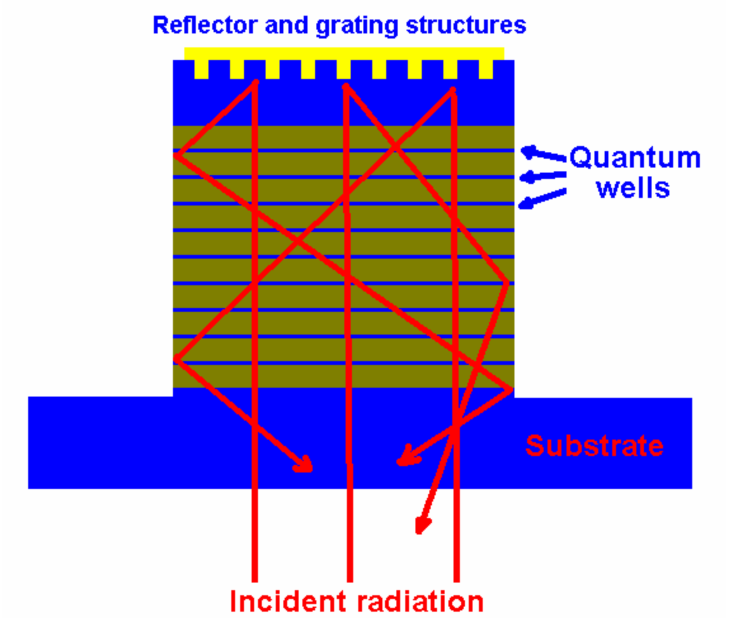

Figure 1.11: Diffraction and reflection of impinging light from reflector and grating structures in a QWIP.

In Figure 1.12 conduction band diagrams of a QWIP are depicted before and after application of the bias voltage. Electrons are injected from the emitter contact and collected at the collector contact. When the detector is under dark conditions (no incident light), a leakage current, due to thermally generated carriers, flows through the device. As the photons having energies larger than the subband energy difference are absorbed, photogenerated electrons transit to the second subband or continuum states (states covering the energies just above the conduction band energy level of the barrier) generating photocurrent.

QWIPs are classified into three groups according to the position of their second subband: bound-to-bound, bound-to-quasibound and bound-to-continuum QWIPs, where the second subband energy level is slightly lower than, nearly equal to, and larger than the barrier energy level, respectively. In bound-to-bound and bound-to-quasi bound QWIPs, high electric field is required for the excited electrons in the second subband to tunnel through the tip of the barrier and to contribute to the photocurrent in continuum. This is not the case for bound-to-continuum QWIPs, as illustrated in Figure 1.13, since the second subband is already located in continuum.

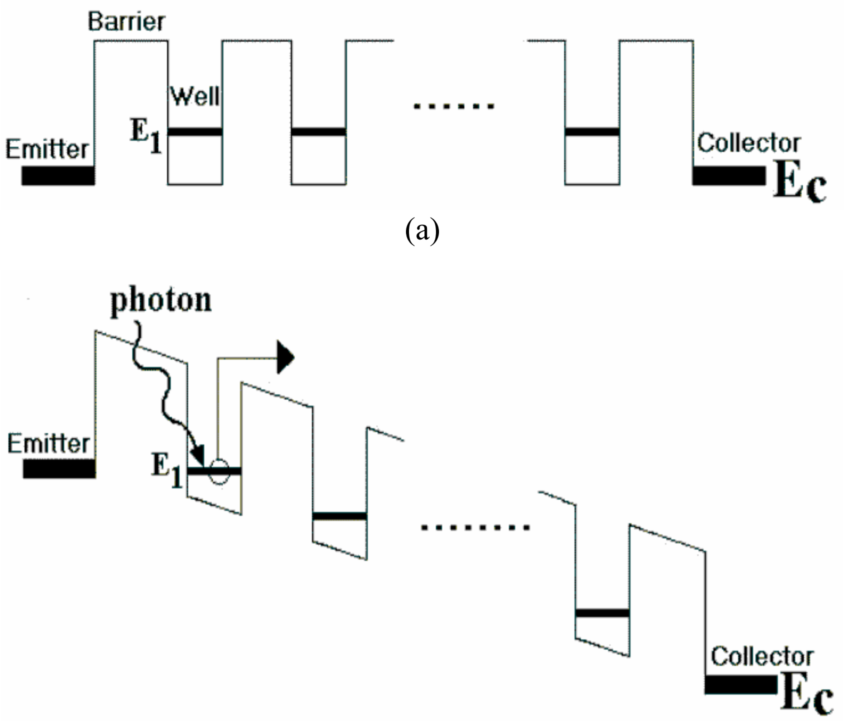

(a)

(b)

Figure 1.12: Band diagram of a QWIP before (a) and after (b) application of bias.

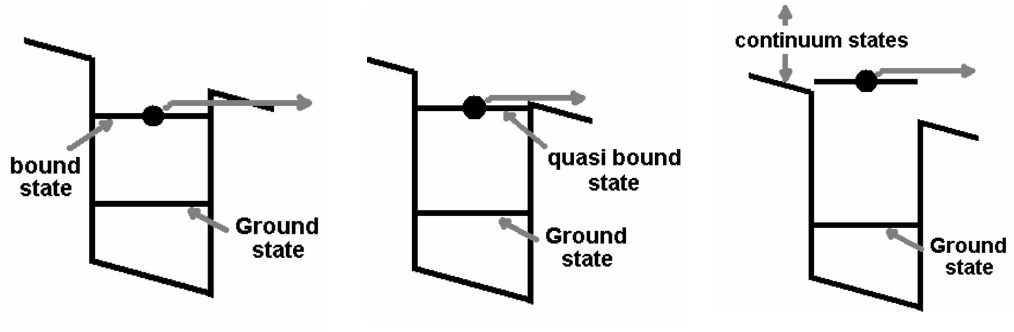

(a) (b) (c)

Figure 1.13: Band diagram of a quantum well with bound-to-bound (a), bound-to-quasi bound (b), and bound-to-continuum (c) transitions.

In bound-to-bound QWIPs strong electric fields, which are required to push the excited electron to the continuum, enhance the ground state sequential tunneling through the barriers. However, this tunneling-induced dark current can be reduced by using thicker barriers [2]. In bound-to-continuum QWIPs, tunneling through the tip of the barrier is not required for transition of the photoexcited electron to the continuum. Therefore, bias required to collect photoexcited electrons is reduced dramatically when compared with bound-to-bound QWIPs. Furthermore, since tunneling is not a requisite, the barrier can be extended indefinitely to reduce the ground state tunneling without reducing the photocurrent significantly.

When compared with the intrinsic photodetectors, QWIPs exhibit narrower absorption spectrum width, because the states in the second subband are localized in energy. On the other hand, spectral width can be broadened by utilizing separate quantum wells tuned to different peak absorption wavelengths in the same detector. Implementation of multicolor and multiband QWIPs are also possible by following the same approach.

1.7 Figures of Merit and Detector Parameters

Photon detectors and FPAs are compared according to certain figure of merits in the literature. These criterions are briefly discussed below. More measures for QWIPs will be defined in Chapter IV.

Responsivity: Responsivity can be defined as the ratio of the output signal to the input signal. The output can be the amount of photovoltage or photocurrent, and the input signal is the radiant input in Watts. Responsivity is not sufficient to indicate the performance of the detector, because it does not specify the signal to noise ratio of the detector.

Signal to Noise Ratio (SNR): Noise can be defined as the undesired signals observed at the output. It cannot be surmounted completely, but may be kept at a minimum level. SNR, by itself, is not the measure of the detector performance, since by increasing the radiant input power SNR can be increased. On the other hand, noise equivalent power (NEP) is a measure of the detector sensitivity. NEP can be defined as the amount of radiant power that detector receives to produce an SNR of unity, and is given by

$$NEP = \frac{noise}{responsivity} \tag{1.5}$$

There are several noise sources, some of which are fundamental and cannot be avoided. On the other hand, those arise externally can be eliminated to some degree. Fundamental noise sources generally stem from the fluctuations in photon arrival rate, lattice vibrations in semiconductor, and random movement of electrons in the detector.

In general, fundamental noise sources show white noise behaviour. However in some cases, noise spectrum carries more power at some frequencies. For example, 1/f noise possesses more power at low frequencies than that at high frequencies.

Detectivity: NEP depends on the detector area, and detectors of different sizes will have different NEPs. On the other hand, detectivity is scaled to the detector area and is sufficient to specify the detector performance. Detectivity is given by

$$D^* = \frac{responsivity \times \sqrt{area \times \Delta f}}{noise} = \frac{R\sqrt{A_d \times \Delta f}}{N} \tag{1.6}$$

Responsivity and detectivity are the commonly used indicators to show single pixel detector performances. Spatial issues require some other measures for indication of FPA performance. The most widely used definitions that specify the FPA performance are spatial uniformity and NETD.

NETD is defined as the minimum temperature difference to which the camera gives SNR of 1. General NETD relation which includes spatial noise is given by [18]

$$NETD = \frac{N_n}{dN_B / dT_B} \tag{1.7}$$

where T_B is the background temperature, and N_n is the total number of noise electrons per pixel, which is given by

$$N_n^2 = N_t^2 + N_B + u^2 N_B^2 \tag{1.8}$$

where N_t is the temporal noise, N_B is the shot noise originating from background radiation, and u is residual nonuniformity after calibration. Although, FPA nonuniformity can be corrected to some degree with signal processing algorithms, it is the typical performance limiting factor in large format FPAs. When the system NETD is limited by nonuniformity, Equation 1.7 becomes

$$NETD = \frac{u\bar{\lambda} T_B^2}{1.44} \tag{1.9}$$

where $\bar{\lambda} = (\lambda_1 + \lambda_2)/2$ is the average wavelength in the spectral band from λ_1 to λ_2. On the other hand, when NETD is limited by detectivity of the detectors, it is given by [19]

$$NETD = \frac{\sqrt{A\Delta f}}{D_B^*(dP_B / dT)\sin^2(\theta / 2)} \tag{1.10}$$

where A is single pixel detector area, Δf is bandwidth, D_B^* is the blackbody detectivity, and dP_B/dT is the change in the integrated blackbody power with respect to temperature. The integrated blackbody power, in the spectral range between λ_1 and λ_2, is given by

$$P_B = A\sin^2(\theta/2)\cos\phi\int_{\lambda_1}^{\lambda_2} W(\lambda)d\lambda \tag{1.11}$$

where $W(\lambda)$ is the blackbody spectral density expressed as

$$W(\lambda) = (2\pi c^2 h/\lambda^5)(e^{hc/\lambda kT_B} - 1)^{-1} \tag{1.12}$$

Theoretical NETD versus D^* characteristics for two different nonuniformity values are given in Figure 1.14. For D^* larger than 10^{10} cmHz$^{1/2}$/W, NETD is limited by nonuniformity (u).

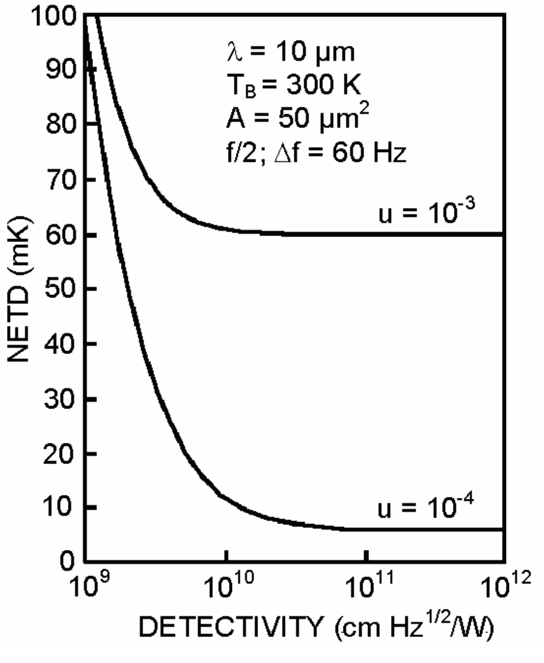

Figure 1.14: Dependence of NETD on detectivity for two different nonuniformity values u=10^{-3} and u=10^{-4} [18].

1.8 Multicolor/multiband FPAs

Offering several advantages over single color FPAs, multicolor and multiband detectors are essential in advanced infrared systems. Absolute temperature of a target can be determined by using the information from distinct infrared bands. Furthermore, the fusion of images from different bands can reveal some signatures that are not observable by employing only one band [20]. Dual-band cameras can also effectively overcome IR countermeasures like smoke, camouflage, and flares.

At present, multispectral systems generally use separate one color FPAs, and the images obtained from both FPAs are combined to achieve multicolor or multiband images. However, this technology requires complex systems, and accurate pixel-to-pixel alignment of the images from both FPAs, which make these systems massive and expensive. Fortunately, QWIP technology, in addition to SLS and HgCdTe technologies, allows fabrication of monolithic, multicolor and multiband FPAs. Multicolor QWIPs have been investigated extensively by several groups, and high performance multicolor QWIPs have been demonstrated both in single pixel and FPA formats [20-25]. The state of the art multiband and multicolor detectors will be discussed in Chapter II.

There are several techniques to realize multicolor QWIP FPAs depending on the read-out schemes employed. One of the most developed structures is the voltage-tunable two-stack QWIP [26-32]. In this type of QWIP, two stacks are tuned to different bands, and the response from each stack is selected by forming electric field domains. One drawback of this method is the necessity of different bias voltages to switch from one band to the other, and the stack that senses the long-wavelength band requires very high bias voltages (> 8V) [2]. This method requires complicated read-out circuit designs. Additionally, switching from one band to the other occurs sequentially, and it is not possible to obtain simultaneous data from both bands. Another method is to use a two-stack structure, which provides electrical contacts from both stacks [2]. In contrast to voltage-tunable scheme, this technique offers simultaneous real-time imaging.

1.9 Thesis Organization

The organization of this thesis and the contents of the following chapters can be summarized as follows:

Chapter II presents a more comprehensive discussion on the InSb, HgCdTe and QWIP photodetectors including the state-of-the art LWIR, MWIR and multiband FPA technologies.

Chapter III reports the fabrication of $InAs_{1-x}Sb_x$ p-i-n photodetectors and 128×128 FPAs on silicon and GaAs substrates, and the results of detailed electrical and optical characterization performed on these detectors. Electrical and noise characterization results are compared with dark current and noise models to reveal the performance-limiting mechanisms of photodiodes.

Chapter IV explains the design considerations for QWIP FPAs. Factors affecting the QWIP FPA performance and dependence of these factors on design parameters are discussed. Additionally, commonly employed read-out approaches are presented in this chapter.

Chapter V discusses the 640×512 QWIP FPA fabrication process developed in this study and the FPA characterization setup and test procedure. The characterization results of a 640×512 AlGaAs/GaAs QWIP FPA are also presented.

Chapter VI presents the results of electrical and optical characterization on AlGaAs/GaAs and InP/InGaAs test QWIPs, as well as a comparison of the performances of these QWIPs which display similar peak responsivity wavelengths. The experimental comparison is supported by theoretical Monte Carlo simulations.

Chapter VII presents the characterization results of 640×512 InP/InGaAs QWIP FPA. Finally, Chapter VIII summarizes this study and lists the important conclusions that can be withdrawn from this work.

CHAPTER II

InSb, HgCdTe and QUANTUM WELL PHOTODETECTOR TECHNOLOGIES

This chapter serves as a comprehensive introduction to the InSb, HgCdTe, and QWIP technologies, which are the most prominent infrared photon detector technologies at present. InSb and HgCdTe materials were discovered in 1955 and 1960, respectively. Until recently, these materials have been the principal semiconductor alloys for infrared detection in the MWIR and LWIR bands. QWIP technology was introduced in 1987 as a potential alternative to replace problematic narrow bandgap InSb and HgCdTe technologies. The QWIP technology has been evolved so rapidly that present QWIP imagers offer comparable performance to the state of the art InSb and HgCdTe based thermal imaging systems for many applications.

The first three sections of this chapter discuss $InAs_{1-x}Sb_x$, HgCdTe, and QWIP technologies separately. $InAs_{1-x}Sb_x$ and HgCdTe technologies for MWIR detection are compared in Section 4. Assessment of QWIP and HgCdTe technologies for LWIR detection is also given in Section 4. Finally, Section 5 discusses the state of the art IR FPAs based on these technologies developed by several research institutes over the world.

2.1 $InAs_{1-x}Sb_x$ Technology

The importance of InSb on infrared detection was noticed in 1950s, and at that time, InSb was the smallest bandgap semiconductor ever known. Since then, InSb detectors have been extensively studied and used in infrared detection systems. The InSb detector technology has developed to such an extent that high quality and dense hybrid arrays are commercially available. The bandgap of InSb semiconductor alloy is suitable for detection in the MWIR band at 77 K. On the other hand, the bandgap of $InAs_{1-x}Sb_x$, which is another III-V compound semiconductor used for infrared detection, can be adjusted by changing antimony (Sb) mole fraction (x). Dependence of $InAs_{1-x}Sb_x$ bandgap on Sb mole fraction (x) is given in Figure 2.1. Cut-off wavelength adjustment option is an advantage of $InAs_{1-x}Sb_x$ technology over InSb technology. Detector dark current depends on the cut-off wavelength exponentially. Thus, reducing the cut-off wavelength slightly can decrease the dark current significantly. Theoretically, the detection wavelength of $InAs_{1-x}Sb_x$ detectors can be extended up to 10 µm. However, device quality growth of $InAs_{1-x}Sb_x$ has been limited due to crystal synthesis problems. Over the last two decades, these problems have been studied extensively, and high-quality $InAs_{1-x}Sb_x$ photodiodes for MWIR detection have been developed [33, 34]. $InAs_{1-x}Sb_x$ is a much more stable material with stronger bonding, and a weaker dependence of the bandgap on composition when compared with $Hg_{1-x}Cd_xTe$.

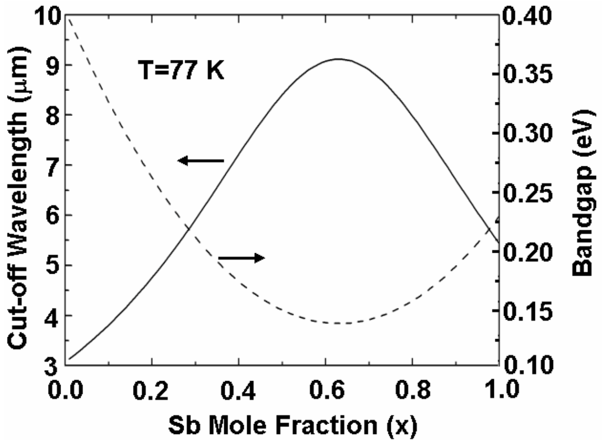

Figure 2.1: Dependence of $InAs_{1-x}Sb_x$ bandgap on Sb mole fraction (x).

2.2 QWIP Technology and Material Systems of Interest

The QWIP technology is relatively new, but rapidly developing when compared with other photon detector technologies. One of the reasons for this rapid advancement is the design flexibility that the QWIP technology offers. Possibility of bandgap engineering and availability of various material systems give more freedom to QWIP designers. As mentioned before, AlGaAs/GaAs has been the most commonly used material system in the QWIP technology. Mature GaAs technology offers high-yield, and reproducible, uniform LWIR QWIP FPAs.

For MWIR detection, AlGaAs/GaAs QWIPs are not feasible, because when the Al mole fraction is increased to reduce the peak absorption wavelength, conduction band of the $Al_xGa_{1-x}As$ barrier becomes indirect beyond x = 0.4 (which corresponds to $\lambda_c = 5.6$ μm). This degrades the barrier transport of the electrons that contributes to the photocurrent [2]. $In_{0.53}Ga_{0.47}As$/ $In_{0.52}Al_{0.48}As$ is the first material system used for the realization of a MWIR QWIP [35]. This lattice-matched structure was grown on InP substrate using the molecular beam epitaxy (MBE) technique. Bound-to-bound $In_{0.53}Ga_{0.47}As$/ $In_{0.52}Al_{0.48}As$ QWIP with 50 Å well and 150 Å barrier widths yielded an absorption peak at $\lambda = 4.4$ μm. Afterward, Hasnain *et. al.* [36] demonstrated a 50-period bound-to-continuum multi quantum well (MQW) structure using the same material system, which gave the same peak absorption wavelength (4.4 μm), while the well and barrier widths were 30 Å and 300 Å.

In addition to $In_{0.53}Ga_{0.47}As/In_{0.52}Al_{0.48}As$ QWIPs, $GaAs/Al_{0.5}In_{0.5}P$ QWIPs can be used for detection in the MWIR region. Although $Al_{0.5}In_{0.5}P$ is an indirect bandgap semiconductor, large Γ-valley conduction band discontinuity ($\Delta E_C \sim 0.5$ eV) at the heterointerface makes this material system suitable for the implementation of MWIR QWIPs [37]. A 20-period MQW structure grown on GaAs substrate, which had 30 Å GaAs quantum wells and 500 Å $Al_{0.5}In_{0.5}P$ barriers, yielded a peak absorption wavelength of 3.25 μm [37]. Since this structure is lattice matched to GaAs, it is possible to fabricate monolithic multicolor infrared detectors growing GaAs/$Al_{0.5}In_{0.5}P$ and AlGaAs/GaAs structures on the same GaAs substrate.

While the AlGaAs/GaAs material system has been used for LWIR QWIPs with success, there has also been interest in the alternative material systems for better QWIP performance. Lattice matched InP/$In_{0.53}Ga_{0.47}As$ material system is an alternative to AlGaAs/GaAs system for LWIR detection. This system has been used extensively for optical communication devices, therefore, this technology has been matured to a good level.

Lattice matched, aluminium-free $Ga_{0.5}In_{0.5}P$/GaAs material system is another alternative to AlGaAs/GaAs system for LWIR detection. Gunapala *et. al.* investigated a 10-period $Ga_{0.5}In_{0.5}P$/GaAs QWIP grown on GaAs substrate [38]. The structure, which gave spectrum peak at 8 μm, had 40 Å GaAs quantum wells doped with $N_D=2\times10^{18}$ cm^{-3}, and 300 Å undoped $Ga_{0.5}In_{0.5}P$ barriers. Jelen *et. al.* demonstrated a QWIP utilizing the same material system, which yielded 13 μm spectral peak [2].

$In_{0.15}Ga_{0.85}As$/GaAs has also been considered as an alternative to AlGaAs/GaAs for QWIP applications. This material system is especially suitable for very long wavelength (λ > 14 μm) QWIPs, because the growth of strain layer heterostructures is possible for low indium (In) concentrations ($x < 0.2$), which results in lower conduction band discontinuity. Investigation of $In_{0.15}Ga_{0.85}As$/GaAs system by several groups [2] revealed that binary GaAs barrier yields outstanding transport properties leading to high photoconductive gains, and small carrier capture probabilities.

2.3 HgCdTe Technology

$Hg_xCd_{1-x}Te$ is a direct bandgap material, and the bandgap of this alloy can be adjusted by changing the molecular fractions of HgTe and CdTe. Bandgap of

HgCdTe can be varied to tune detection cut-off wavelength from 0.7 μm to 25 μm. Additionally, its direct bandgap brings in very high absorption strength allowing the production of high quantum efficiency detectors based on this material. Lattice constant of $Hg_xCd_{1-x}Te$ depends on x so slightly that the variation in lattice constant is lower than 0.3% from x=0 to x=1. This facilitates the implementation of multiband or multicolor detectors based on lattice matched heterostructures.

The relationship between $Hg_xCd_{1-x}Te$ bandgap (E_g), x, and temperature (T) can be expressed by the empirical equation, which is given by [39]

$$E_g(x,T) = -0.302 + 1.93x - 0.81x^2 + 0.832x^3 + 5.35(1-2x)10^{-4}\left(\frac{-1822+T^3}{255.2+T^2}\right) \quad (2.1)$$

where E_g is in eV, and T is in K. Cut-off wavelength (λ_c), which is calculated by $\lambda_c=1.24/E_g$, is plotted against x for several temperatures in Figure 2.2. As seen in the figure, cutoff wavelength strongly depends on composition especially in the LWIR and VLWIR regions. Therefore, small compositional variations over two-dimensional arrays result in large nonuniformities, which make large format LWIR and VLWIR HgCdTe FPAs challenging. The problem is less severe for MWIR region, and as will be discussed in one of the following sections, MWIR HgCdTe FPAs up to formats of 1024×1024 have already been developed.

Main HgCdTe crystal growth methods are bulk crystal growth, liquid phase epitaxy (LPE), molecular beam epitaxy (MBE), and vapor phase epitaxy (VPE). There are two methods for VPE: chemical vapor deposition (CVD), such as metal-organic chemical vapor deposition (MOCVD), and physical vapor deposition (PVD). The combinations of growth methods are also possible like metalorganic molecular beam epitaxy (MOMBE), which is a combination of MBE and MOCVD [39]. Lower growth temperatures are used in the epitaxial growth methods when compared with the bulk growth methods. For the fabrication of high performance large format detector FPAs, high quality and large area substrates, which are lattice matched to HgCdTe, should be used. Lattice matched CdZnTe substrate, which includes 4% ZnTe, is widely used for epitaxial growth. CdZnTe substrates are transparent to infrared radiation in the MWIR and LWIR spectral bands. However, large area CdZnTe substrates with acceptable quality are not available. Today, the area of high quality CdZnTe substrates is limited to 30 cm^2. Additionally, these substrates exhibit low mechanical strength, and their thermal expansion is not matched with silicon read-out circuits. Hetero-epitaxial growth of HgCdTe on alternative substrates like sapphire, GaAs, InSb, Si, and Ge is also possible [39]. In the hetero-epitaxial growth of HgCdTe, buffer layers are used to compensate the mismatch between the lattice constants of substrate material and HgCdTe.

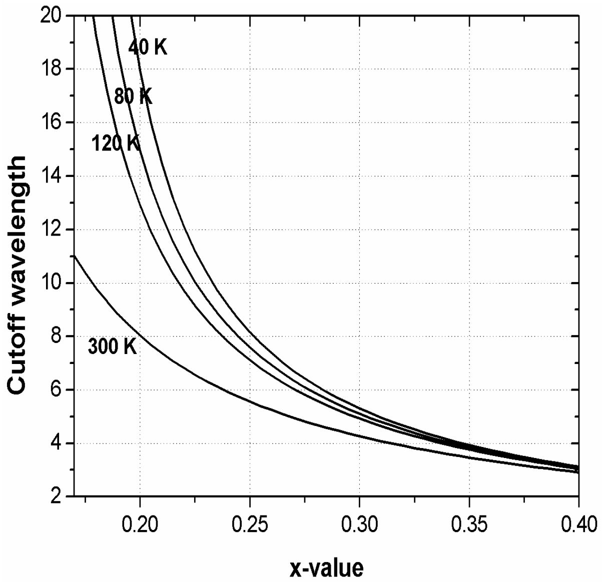

Figure 2.2: $Hg_xCd_{1-x}Te$ cutoff wavelength versus x at several temperatures.

Silicon substrates, which are low cost and available in large sizes up to 182 cm^2, have better mechanical properties when compared with CdZnTe substrates. Additionally, the thermal expansion mismatch problem between detector FPA and Si ROIC is prevented when the detector structures are grown on Si substrates. On the other hand, growth on silicon substrates yields large defect densities (in the $10^6/cm^2$ range), and suitable buffer layers are not well developed [39].

Bulk photoconductive or photovoltaic diode configurations for HgCdTe detectors are possible. The p-n junctions are formed by Hg diffusion, impurity diffusion, ion implantation, electron bombardment, and doping during growth. Passivation of surfaces is very important and affects the performance of photodiodes significantly by reducing surface leakage current. There are several techniques for HgCdTe passivation like native films, deposited dielectrics, and in-situ grown heterostructures [33]. Generally, Ti, Al, In, and Cr are the metals used for ohmic contact formation. Ohmic contact to p-type HgCdTe is more difficult to achieve than to n-type material.

2.4 Comparison of InSb, HgCdTe, and QWIP Technologies

The detectors operating in different spectral windows yield different characteristics and performance. Therefore, we will compare the above IR detector technologies separately in the MWIR and LWIR bands in the following subsections.

2.4.1 InSb versus HgCdTe for MWIR Band

InSb and HgCdTe technologies have long been in competition in the MWIR band detection. Up to now, megapixel FPAs from both technologies have been demonstrated. The formats of the largest InSb and MWIR HgCdTe FPAs are 2048×2048 [40] and 1024×1024 [41], respectively. InSb is a binary compound while $Hg_xCd_{1-x}Te$ is ternary. Bandgap and cut-off wavelength of the $Hg_xCd_{1-x}Te$ detectors depend on HgTe mole fraction (x). Therefore, compositional nonuniformity must be as low as possible. On the other hand, cut-off wavelength of the InSb detectors is fixed at λ_c=5.5 μm yielding perfect spectral uniformity. Although fixed cut-off wavelength of InSb provides high uniformities, it cannot be tuned to operate in desired absorption cut-off as offered by HgCdTe.

Growth and processing of the III-V materials are considered to be easier than that of II-VI materials [39], and HgCdTe detectors are more prone to damage during fabrication processes. Additionally, higher mobility of InSb results in small series resistance in large arrays. On the other hand, performance of InSb detectors is poor above 80 K when compared with HgCdTe detectors because of higher trap densities in InSb (10 times higher than HgCdTe) [39].

2.4.2 QWIP versus HgCdTe Photodetectors for LWIR Band

Due to the well known problems of HgCdTe for LWIR FPAs, some III-V compounds like InAsSb [42-49], InSbBi [50, 51], InAsBi [52], InAsSbBi [52, 53], GaInSbBi [54], InTlSb [55-59], and InTlAs [60] have been investigated as an alternative to HgCdTe. However, probably the most successful alternative appeared with the development of the QWIP technology. The advantages of QWIP technology, compared with MCT technology, include the mature GaAs growth and processing technologies, which lead to high uniformity, excellent reproducibility, and large area, low cost staring arrays. In addition, the ability to control the spectral response by bandgap engineering allows monolithically integrated multispectral infrared detectors. Finally, the possibility of growth on GaAs wafers makes monolithic integration of QWIPs with high-speed GaAs multiplexers and other electronics feasible. However, the relatively low quantum efficiency of the standard QWIP remains as a bottleneck.

Although the production yield of HgCdTe detectors has been advanced to good levels, it is still lower than that of AlGaAs/GaAs QWIPs. HgCdTe detectors have higher price/performance ratios. Comparison of the production costs of two technologies is given in Table 2.1 [61].

When two technologies are compared in single pixel level, HgCdTe detectors may show better performance under low background radiation due to higher quantum efficiency. It has been proposed that HgCdTe detectors and QWIPs show similar dark current and detectivity characteristics when HgCdTe operates at temperatures 25 K higher than QWIP operating temperature [62]. As a result, HgCdTe based IR imagers necessitate less stringent cooling requirements and can work at elevated temperatures. On the other hand, optimization of growth parameters, structural design, and quantum well doping level significantly improves the performance of QWIPs. For example, by the utilization of corrugated QWIP structure, which will be discussed in Chapter IV, dark current can be reduced while increasing the quantum efficiency.

Table 2.1: Comparison of the production costs of HgCdTe and QWIP FPA technologies [61].

	HgCdTe FPA	QWIP FPA
Material Cost	\$3000/inch^2	\$300/inch^2
Size of Wafer	7 inch^2	7 inch^2
Lot Cost (10 wafers, 2 inch dia)	\$210,000	\$21,000
Processing Cost (for 70 inch^2)	\$140,000	\$20,000
Total Cost	\$350,000	\$41,000
Chip Yield (FPA)	25%	50%
Relative Cost	17	1

Detectivity of a QWIP is a strong function of temperature, which increases an order of magnitude for every 10 K drop in operating temperature below 70 K. Theoretical estimations show that HgCdTe detectivity is superior to QWIP detectivity, when LWIR detection is considered. However, when MWIR performance is concerned or LWIR operating temperature is below 50 K, QWIPs show better detectivities [62]. Below 50 K, some inherent problems of HgCdTe material like p-type doping, Shockley-Read recombination, trap-assisted tunneling, and surface and interface instabilities limit the detector performance [63]. Additionally, detectivity of the HgCdTe detectors is limited by the quality of the material, and so far, minimum achievable defect density is around 10^5 cm^{-2} [64]. The QWIP technology is a relatively new and rapidly developing technology. Although it is argued that development of the QWIP technology will slow down due to some physical limits [62], new QWIP designs, and material systems are believed to surpass these restrictions.

As discussed in the previous paragraphs, HgCdTe technology may be superior to QWIP technology when only single pixel performances are compared. On the other hand, the FPA performance is not determined only by the pixel performance and depends on the uniformity of the material strongly. Growth of highly uniform HgCdTe material is rather difficult, especially for detection in the LWIR band, because of the strong dependence of the bandgap on composition, as discussed previously (Figure 2.2). In contrast, owing to mature GaAs technology, growth of very uniform and large area QWIP wafers is possible. Indeed, based on this technology, QWIP FPA nonuniformity values as low as 0.01% are achievable after two-point correction [62]. Noise equivalent temperature difference (NETD) of an infrared detector, which is an FPA performance indicator, is improved with increasing homogeneity and detectivity. It is claimed that when the detectivity of a photodetector is above $\sim 10^{10}$ $cm \times Hz^{1/2}/W$, NETD depends only on the uniformity of the FPA [18]. As the result, FPAs fabricated from uniform materials should give better NETD performances. Therefore, it is not surprizing that AIM has already reported an NETD value lower than 10 mK for a 640×512 QWIP FPA [65].

Integration time is another factor to be considered when preferring a technology for a specific application. When a rapidly changing scene is imaged, fast frame rate operations are desirable. Integration times of LWIR HgCdTe FPAs are as short as 100 μs allowing very fast frame rates. On the other hand, since quantum efficiency of AlGaAs/GaAs QWIPs is significantly lower than that of HgCdTe detectors, integration time of AlGaAs/GaAs QWIPs is generally set to values as high as 5-20 ms to increase the signal-to-noise ratios.

For applications requiring multispectral detection, QWIP technology has several advantages over HgCdTe technology. Complicated layer structures are easier to realize with the GaAs technology, and this material is more stable against the more involved fabrication processes of multiband or multicolor FPAs. Additionally, QWIPs have relatively narrow-band spectral shape ($\Delta\lambda/\lambda$=10-

20%) resulting in good separation between different bands, which prevents spectral crosstalk. As will be discussed in the following section, most of the state of the art multispectral FPAs demonstrated up to now are based on QWIP technology, which is an indication of feasibility of QWIP technology for multispectral detection.

2.5 State of the Art InSb, HgCdTe, and QWIP FPAs

First generation thermal imaging systems were widely employed between 1960 and 1980. These imagers use linear single color scanned arrays with less than several hundred pixels. Second generation FPAs are single band, linear or staring arrays fabricated with larger formats such as 288×4 or 320×240. In the third generation systems, multiband and very large format FPAs will be used. Therefore, the main motivation in the high performance infrared imaging field is to achieve very large format multiband FPAs.

There are several factors determining the maximum number of pixels realizable on an FPA. Lack of high quality large area substrates for HgCdTe detectors limits the format of LWIR FPAs based on this technology. HgCdTe can also be grown on high quality, and very large diameter silicon substrates, but excessive leakage currents in hetero-epitaxially grown HgCdTe photodetectors make the growth of HgCdTe on Si substrates impractical. Fabrication of very large format homo-epitaxially grown InSb FPAs needs state of the art InSb substrates (up to a diameter of 100 mm). QWIP technology offers important advantages in terms of the availability of large area wafers and uniformity over a large area.

Read-out electronics starts to play an important role, as the FPA sizes are scaled up, and multispectral detection becomes a necessity. The demand for large formats requires reduction on pixel pitch, which also reduces the integration capacitor area. As the die size is increased, production of ROIC becomes more expensive. However, new approaches for very large format FPAs, like two or three side butted configurations, multiplicate the number of pixels by utilization of several detector FPAs and ROICs side by side. Some multicolor FPA pixel structures require multiple contacts per pixel, which complicates the ROIC design. Therefore, ROIC technology must be developed in parallel to detector technology for the implementation of the third generation high-performance infrared imaging systems.

In summary, very large format and multispectral FPAs are to be used in the third generation infrared imagers. The following subsections briefly discuss the recent achievements toward these systems. The discussion on the state of the art detectors is organized according to the band of operation.

2.5.1 State of the Art MWIR FPAs

Although there is a competition between staring and scanning FPAs in the LWIR band, staring arrays are usually preferred for the MWIR band. High resolution MWIR staring FPAs find applications especially in astronomy, and a number of them have been installed in several observatories. Large format InSb, HgCdTe, and quantum well photodetector FPAs are already available in megapixel formats.

Raytheon has long been developing megapixel detector FPAs and ROICs. Their 1K×1K InSb FPAs (Aladdin) has been in production since 1994 [66]. They also demonstrated a 2-side buttable 2048×2048 InSb FPA, which allows construction of mosaic FPAs having a format as large as 4096×4096. Their antireflection-coated FPA gives a quantum efficiency of 80-95% from visible to 5 μm radiation. The average dark current of the detector pixels was measured to be 0.01 electrons/second at 30 K.

CMC Electronics Cincinnati is another company producing 1K×1K InSb FPAs. The average NETD of their 1K×1K FPAs is 13mK for 25 ˚C background [40]. They also have 2K×2K InSb FPAs in low volume production. The dark current in their 25 µm square pixels is around 1 pA at 77 K. IR images from their 2K×2K FPA are given in Figure 2.3.

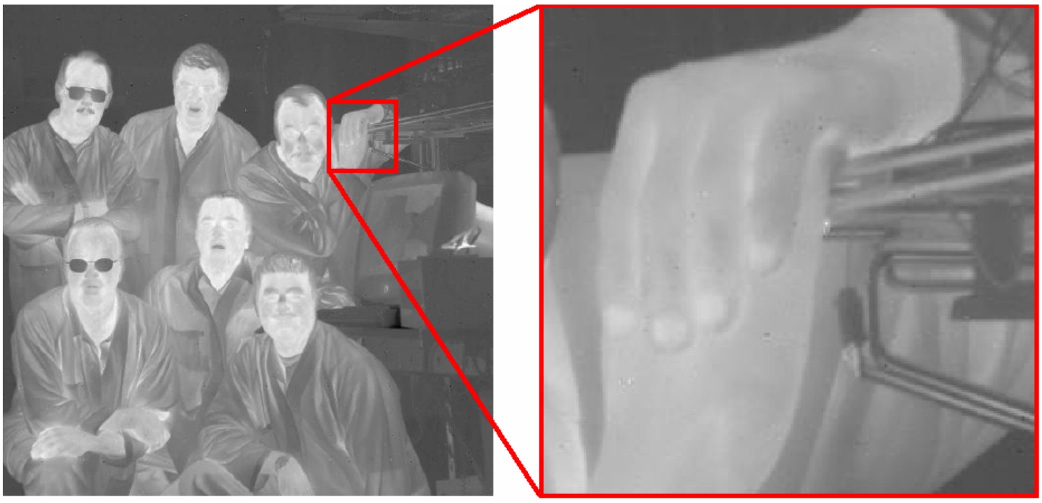

Figure 2.3: Images from 2K×2K InSb FPA produced by CMC Electronics Cincinnati. The magnified portion of the image shows the resolution of the FPA [40].

BAE Systems in collaboration with Defence and Technology Laboratory, UK, and Qinetiq Ltd. have developed 1024×768 InSb FPAs with 26 micron pitch [67]. The average NETD of this FPA is 11mK, with f/2.3 optics, and at an operating temperature of 77 K. An image taken with this FPA is given in Figure 2.4.

LETI has reported 1024×1024 MWIR HgCdTe FPA in 2004 [41]. The mean NETD of this megapixel FPA is 20 mK with 55° field of view, 77 K operating temperature and under mid dynamic range conditions (charge handling capacity of the ROIC is 9 Me). An image obtained with this FPA is given in Figure 2.5. LETI also produced a 640×512 MWIR HgCdTe FPA having mean NETD of 15 mK with f/2 optics, and 4 ms integration time. The NETD of the FPA remains constant up to 120 K operation temperature [68].

Figure 2.4: Image taken with 1024×768 InSb FPA produced by BAE Systems in collaboration with Defence and Technology Laboratory and Qinetiq Ltd. The field of view of camera and integration time is f/4.5 and 3ms, respectively. Operating temperature of the FPA is 77 K [67].

Figure 2.5: Image obtained from megapixel MWIR HgCdTe FPA of LETI [41].

Jet Propulsion Laboratory (JPL), in collaboration with U.S. Missile Defense Agency, and U.S. Air Force Research Laboratory demonstrated a 1024×1024 MWIR QWIP FPA based on AlGaAs/GaAs/InGaAs material system [69]. They achieved an NETD of 19 mK at 95 K operating temperature with f/2.5 optics looking at 300 K background. Figure 2.6 shows a real-time image obtained with this camera.

Figure 2.6: An example image taken with 1024×1024 MWIR QWIP camera developed by JPL in collaboration with U.S. Missile Defense Agency and U.S. Air Force Research Laboratory [69].

2.5.2 State of the Art LWIR FPAs

The QWIP and HgCdTe technologies are in competition in the LWIR band. Since QWIPs are based on large bandgap and mature material systems, it is relatively easy to produce very large format FPAs. However, uniformity problems of HgCdTe alloy makes the implementation of large format FPAs based on this material difficult. Therefore, linear arrays are usually employed to increase the resolution of the LWIR HgCdTe FPAs.

Sofradir, a French company, repoted that they have delivered more than 10,000 LWIR TDI arrays up to date [70]. They started to produce 320×256 staring LWIR FPAs in 2001, and demonstrated several LWIR staring HgCdTe FPAs with different cut-off wavelengths. Properties of these FPAs are summarized in Table 2.2 [70].

Table 2.2: Properties of Several LWIR HgCdTe FPAs produced by Sofradir [70].

Format	Operating Temperature	Spectral Range (μm)	NETD
320×256	80K	7.8-9.6	15.4mK (f/2, 300K blackbody, 200μs integration time)
320×256	77K	7.8-11.2	13.8mK (f/2.1, 300K blackbody, 50μs integration time)
384×288	85K	7.8-8.7	13.8mK (f/2, 300K blackbody, 400μs integration time)

Rockwell Scientific Company developed a 512×512 LWIR HgCdTe FPA with 9.6 μm cut-off wavelength [71]. The preliminary characterizations show that dark current of the 99.23% of detectors is less than 30 electron/second at operating temperature of 30 K.

Sofradir, in collaboration with Thales Research Technology has developed a 640×512 LWIR QWIP FPA with 9 μm cut-off (50%) [11]. The NETD of their FPA was measured to be 28 mK with f/2 field of view, 70 K operating temperature, 4 ms integration time and 20 ˚C background.

Very recently, Jet Propulsion Laboratory, in collaboration with NASA Goddard Space Flight Center, and Army Research Laboratory developed a 1024×1024 8.4-9 μm QWIP FPA, which shows BLIP performance at an operating temperature of 76 K with f/2 optics [72]. The average NETD of the system is 16 mK at an operating temperature of 72 K, with 29 msec integration time, and f/2.5 optics. An image taken with this system is given in Figure 2.7.

1024×1024 LWIR QWIP FPAs are already in the product list of QWIPTECH. [73]. The measured temporal NETD is lower than 35 mK at 65 K operation temperature, with f/2 field of view and 15 ms integration time. Their FPAs give corrected nonuniformity better than 0.05%.

Figure 2.7: Image taken with the 1K×1K LWIR QWIP camera developed at JPL [72].

2.5.3 State of the Art Dualband and Multiband FPAs

In 1999, NASA JPL laboratory reported a 640×512 LWIR-VLWIR QWIP camera [74]. The FPA, used in this camera, shows response between 8 μm – 9.0 μm for LWIR band and 14 μm – 15 μm for VLWIR band. The NETD values were measured as 36 mK (MWIR) and 44 mK (VLWIR) at 40 K operation temperature and with f/2 lens. An image taken with with this two-color camera is shown in Figure 2.8.

Recently, NASA JPL laboratory, in collaboration with U.S. Army Research Laboratory, demonstrated a 640×512 QWIP imager which performs detection in four different spectral bands [23]. The experimentally measured NETDs of 4–5.5, 8.5–10, 10–12, and 13.5–15 μm detectors at 40 K are 21.4, 45.2, 13.5, and 44.6 mK, respectively. A picture taken with this 4-band camera is given in Figure 2.8. JPL also developed a 320×256 simultaneously readable dualband (MWIR/LWIR) focal plane array. The peaks of MWIR and LWIR responses occur at 4.6 μm and 8.5 μm, respectively.

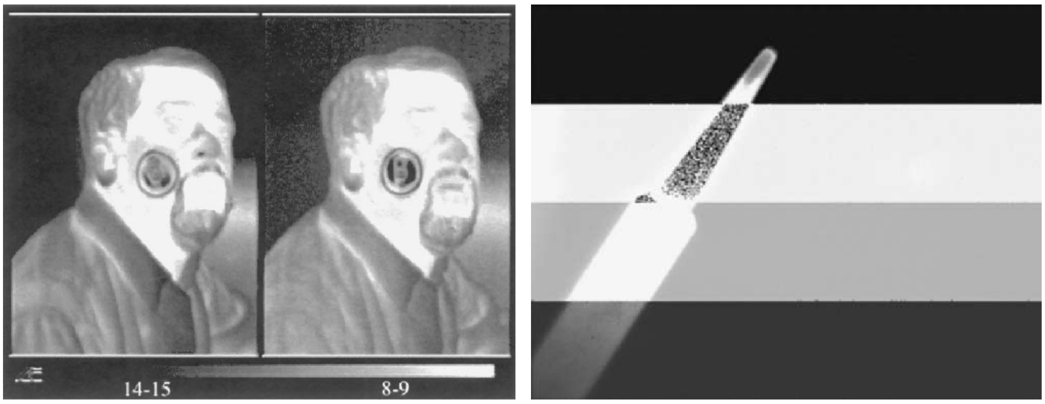

(a) (b)

Figure 2.8: (a) Image taken with 640×512 LWIR-VLWIR dualband camera [74]. (b) Video image of a soldering iron taken with 640×512 four-band camera developed at JPL [23].

Lockheed-Martin reported a 256×256 MWIR-MWIR, LWIR-MWIR, and LWIR-LWIR QWIP imagers in 2001 [25]. Performances of these imagers are summarized in Table 2.3, and the real-time images obtained with these cameras are shown in Figure 2.9.

Table 2.3: Results from 256×256 MWIR-MWIR, LWIR-MWIR, and LWIR-LWIR QWIP imagers developed at Lockheed-Martin [25].

MWIR-MWIR	NETD	41mK and 32mK
	Peak absorption wavelength	4.0 μm and 4.7 μm
	Operating temperature	90 K
	Lens	f/3
MWIR-LWIR	NETD	<35 mK (for both bands)
	Peak absorption wavelength	8.5 μm and 5.1 μm
	Operating temperature	65 K
	Lens	f/2
LWIR-LWIR	NETD	43 mK and 23 mK
	Peak absorption wavelength	8.3 μm and 11.2 μm
	Operating temperature	40 K
	Lens	f/3

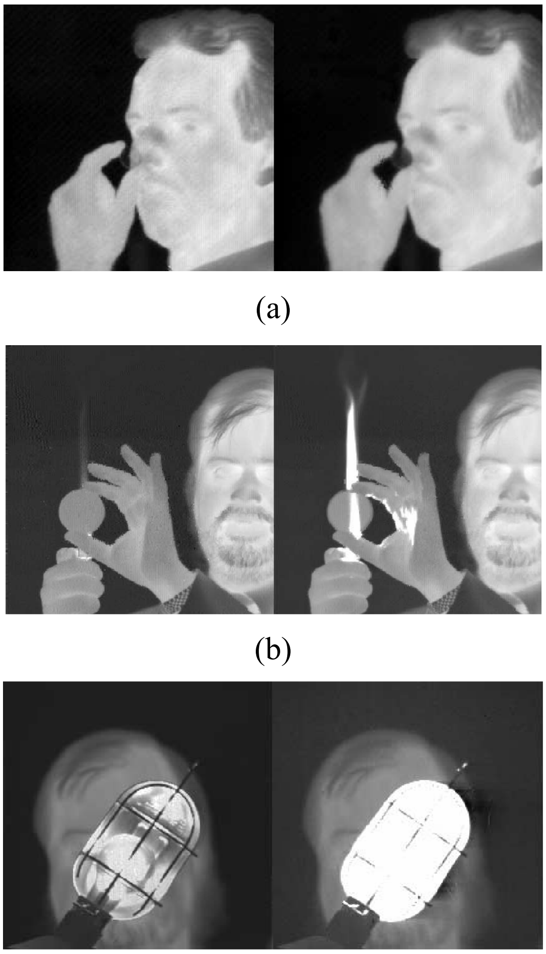

(a)

(b)

(c)

Figure 2.9: Images from 256×256 (a) LWIR/LWIR, (b) LWIR/MWIR, and (c) MWIR/MWIR QWIP FPAs developed at Lockheed-Martin [25].

LETI infrared laboratory, in collaboration with French Ministry of Defense and SOFRADIR, has developed two-color (MWIR-MWIR) HgCdTe FPAs [75]. The reported results obtained from these FPAs are given in Table 2.4.

Table 2.4: Performance of two-color (MWIR-MWIR) HgCdTe FPAs developed at LETI infrared laboratory [75].

R_0A	10^7 Ω×cm^2 (Band 1) and 4×10^5 Ω×cm^2 (Band 2)	
Absorption band	Band 1	2.3 μm – 3.1 μm
	Band 2	3.2 μm – 5.0 μm
Quantum efficiency	Band 1	50 % (without antireflection coating)
	Band 2	75 % (without antireflection coating)

U.S. Army Research Laboratory has reported a 256×256 MWIR-LWIR dualband QWIP imager with properties given in Table 2.5 [20, 76]. The images taken with this camera are given in Figure 2.10. Additionally, Army Research Laboratory, in collaboration with DRS Infrared Technology and BAE Systems developed 320×240×2 format QWIP and 640×512 format HgCdTe MWIR-LWIR FPAs. They followed "multicontact per pixel" approach for QWIP FPA while HgCdTe FPA is in interlaced configuration. Measured NETD values of the QWIP FPA are 34 mK (LWIR) and 30 mK (MWIR) at 60 K operation temperature, with 8 ms integration time, and f/2.5 field of view. For the HgCdTe array, NETD values are measured as 26 mK (LWIR) and 21 mK (MWIR) at 77 K operation temperature, with f/3 field of view, and integration time of 104 µs for LWIR and 755 µs for MWIR band.

Table 2.5: Properties of 256×256 MWIR-LWIR QWIP imager developed at U.S. Army Research Laboratory [20, 76].

NETD	30 mK (MWIR) and 34 mK (LWIR)
Spectral response	8.2 µm – 9.0 µm for LWIR 4.7 µm – 5.2 µm for MWIR
Operation temperature	60K
Field of view	5.86° with f/3 lens

AIM-AEG Infrarot-Module GmbH has developed a 384×288×2 format MWIR/LWIR dualband QWIP FPA [77, 78]. Peak detection wavelengths for MWIR and LWIR bands of this FPA are 4.8 µm and 8.0 µm, respectively. They obtained average NETD values of 17.1 mK (MWIR) and 43 mK (LWIR) with f/2 field of view, and 7.6 ms integration time.

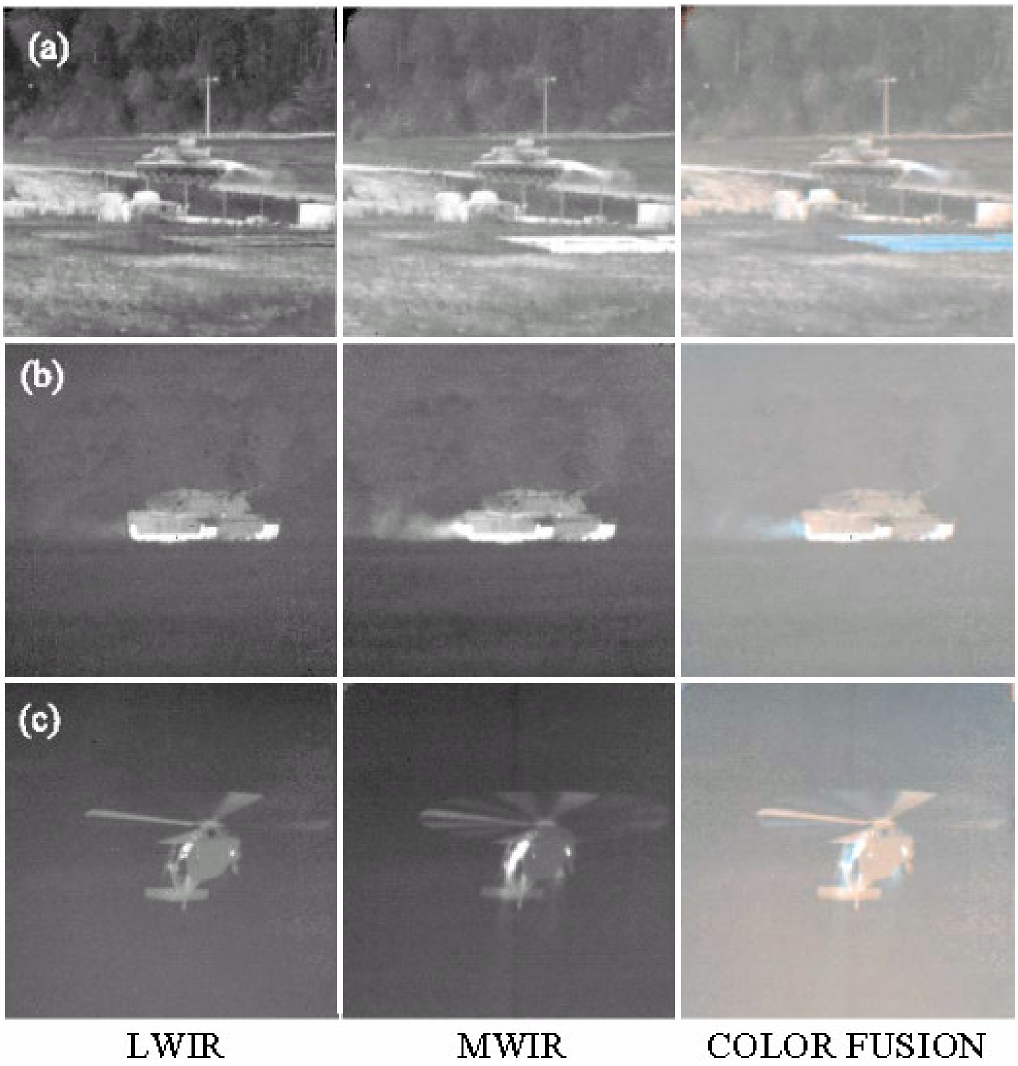

Figure 2.10: Images taken with 256×256 dual band QWIP FPA developed at U.S. Army Research Laboratory: (a) M60 tank, (b) M1-A1 tank, and (c) Blackhawk helicopter [20].

2.6 Conclusions and Summary

This chapter has discussed the most important infrared photon detector technologies. InSb and HgCdTe technologies were introduced about 45-50 years ago, therefore, these “validated” sensors have been installed to many infrared imaging systems. On the other hand, QWIP technology is relatively young, and this technology has to prove itself. The design flexibility it offers, possibility of the multispectral detection, and maturity of the employed material systems make the development speed of QWIP technology high. With this speed, QWIP technology is believed to take its place in the third generation high-performance infrared imaging systems.

Future’s infrared imagers will use very large format, and multispectral FPAs. Many research institutes are concentrated on the development of these high-performance sensors. They have already reported megapixel FPAs based on InSb, HgCdTe, and QWIP technologies, as well as large format multiband FPAs.

One of the approaches adopted toward lowering the fabrication cost of very large format IR FPAs is the growth of the detector material on large area GaAs and Si substrates under lattice mismatched conditions. This approach may be successful only if detector quality material can be grown on such substrates. Determination of the degrading affects of lattice-mismatched epitaxy, and detector performance limiting mechanisms is invaluable for the optimization of the detector structure and the growth conditions. The work, which will be presented in the following chapter, is concentrated on this issue. We report the fabrication of $InAs_{1-x}Sb_x$ p-i-n photodetectors and 128×128 FPAs on silicon and GaAs substrates, and the results of detailed electrical and optical characterization performed on these detectors. Electrical and noise characterization results, which are compared with dark current and noise models to reveal the performance-limiting mechanisms of photodiodes, will also be discussed in detail.

CHAPTER III

$InAs_{1-x}Sb_x$ P-I-N PHOTODETECTORS AND FOCAL PLANE ARRAYS ON ALTERNATIVE SUBSTRATES

There has been a considerable amount of work on InSb detectors and detector arrays fabricated on InSb substrates [79-82]. In addition to the homo-epitaxially grown InSb detectors and arrays [81], high quality $InAs_{1-x}Sb_x$ photodiodes (mostly for 3-5 µm region) have been fabricated on InAs, InSb, and GaSb substrates [83-86]. Device quality hetero-epitaxial growth of these materials on Si or GaAs substrates is necessary for the development of large area FPAs and the monolithic integration of the detector array with the read-out circuit. Growth on Si and GaAs substrates also eliminates the need for the substrate thinning process in hybrid-integration of the detector array with the read-out circuit. Additionally, growth of the detector material on Si substrate reduces the problems regarding the thermal expansion coefficient mismatch between the detector array and Si read-out circuit. Therefore, high quality growth of III-V infrared detector materials especially on Si is very important in order to increase the reliability and decrease the cost of the infrared detector systems [34].

The lattice mismatch between InSb and GaAs (14.5%) is lower than that between InSb and Si (19%). Most of the previous studies on the growth of InSb on GaAs showed that although the density of dislocations at the InSb/GaAs interface is high, the crystal quality and Hall mobility improve with increasing layer thickness [87-91]. It was also reported that Hall mobility monotonically decreased with decreasing temperature below room temperature. Similar behaviour was observed in $InAs_{1-x}Sb_x$ grown on GaAs substrates [87, 92, 93]. Several techniques, like utilization of AlSb buffer layers [94] or atomic layer epitaxy InSb layers at the interface [95], were suggested to reduce the interfacial dislocations and improve the material quality. Michel *et. al.* [96] achieved high quality InSb grown on GaAs by molecular beam epitaxy (MBE).

In spite of very large lattice mismatch, there has also been some effort on the growth of InSb on Si [97-104]. Chyi *et. al.* [98] reported room temperature mobilities of 48 000 and 39 000 $cm^2V^{-1}s^{-1}$ for 3.2 μm thick MBE grown InSb with and without a thin GaAs buffer layer, respectively. Mori *et. al.* [102] used Ge buffer layers, and Liu *et. al.* [103] achieved 65 000 $cm^2V^{-1}s^{-1}$ mobility at room temperature using fluoride buffer layers. Michel *et. al.* [97] obtained an x-ray full width at half maximum of 109 arcsec in MBE grown InSb on GaAs coated Si substrate. Recently, Rao *et. al.* [104] reported an improvement in the InSb/Si(111) epilayer quality when a two-step growth procedure is used.

Few studies have been reported on the fabrication of $InAs_{1-x}Sb_x$ detectors on GaAs substrate [97, 105, 106]. Dobbelaere *et. al.* [46] used the MBE technique to fabricate $InAs_{0.85}Sb_{0.15}$ photodiodes on GaAs substrates. Before growing the p-n junction, a 4.5 μm thick GaAs buffer layer, a 30 nm thick InAs layer and a 1 μm thick linearly graded $InAs_{1-x}Sb_x$ ($0.01 < x < 0.15$) epilayer were grown. It was observed that only a limited number of dislocations reached the p-n junction. Kim *et. al.* [42] fabricated $InSb/InAs_{0.15}Sb_{0.85}/InSb$ p-i-n detectors on GaAs substrates by using low-pressure metallorganic chemical vapor deposition. While the responsivity of the diodes was low, they observed photovoltaic response up to 13 μm at 300 K.

Characteristics of HgCdTe detectors on Si substrates [107-109], and the effects of dislocations on HgCdTe detector performance [110-112] have also been investigated extensively. However, when compared with the material and device-related work on HgCdTe, there has been very limited amount of study reported on the characteristics of InSb and $InAs_{1-x}Sb_x$ detectors on Si and GaAs substrates [97, 105, 106]. In particular, performance limiting mechanisms and noise characteristics of hetero-epitaxially grown InSb photodiodes are not known as extensively as those of HgCdTe diodes.

The main objective of the study presented in this chapter is to assess the performance of InSb and $InAs_{0.8}Sb_{0.2}$ photodetectors grown on Si and GaAs substrates, respectively. In order to reveal the performance limiting mechanisms in these detectors, detailed electrical and optical characterization was performed on InSb/Si and $InAs_{1-x}Sb_x$ /GaAs test detectors. Additionally, 128×128 FPAs based on some of these photodiodes were fabricated, and real-time images from these FPAs were obtained using a prototype thermal imager.

The epilayer structures of the detector materials employed in this study are described in the first section of this chapter. Following the description of the test detector characterization set up in Section 2, characterization work, results, and discussions are presented in Section 3 supplemented with a theoretical study. Section 4 describes the 128×128 FPA fabrication process, and thermal imaging with the FPAs. Finally, the conclusions of this study are given in Section 5.

3.1 Epilayer Structures

Figure 3.1 illustrates the epilayer structures of the $InAs_{0.8}Sb_{0.2}$ and InSb detectors grown on GaAs and Si substrates, respectively. Structure 1 is a homojunction $InAs_{0.8}Sb_{0.2}$ photodetector grown on GaAs substrate by MBE technique at Interuniversity Micro-Electronics Center (IMEC), Belgium. The doping levels of the p^+- and n^+-layers are 3×10^{18} and 2×10^{18} cm^{-3}, respectively. The thicknesses of the p^+, n^+, and intrinsic layers are 300 nm, 4 μm, and 1.5 µm, respectively. The Sb mole fraction of $InAs_{0.8}Sb_{0.2}$/GaAs detector corresponds to a cut-off wavelength of 4.8 µm at 77K.

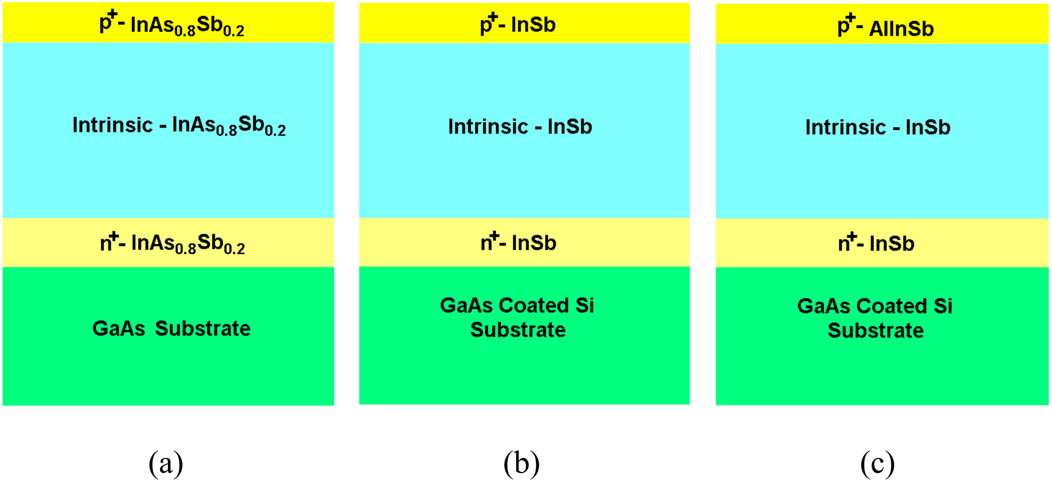

Figure 3.1: Epilayer structures of detectors investigated in this study: (a) structure 1, (b) structure 2, and (c) structure 3.

Structure 2 is a homojunction InSb p-i-n photodetector grown on GaAs coated Si substrate. Growth of this structure was carried out with the MBE technique at Northwestern University, USA. The lattice-mismatch between InSb and GaAs (14.5%) is lower than that between InSb and Si (19%), therefore, a 2 µm thick GaAs was grown on Si substrate to reduce the stress between the substrate and epilayers. Epilayer structure of the detector consists of a 1.5 µm thick n^+-layer, ~5 µm thick unintentionally doped (n-type) layer and a 1 µm thick p^+-layer. n^+- and p^+-layers serve as bottom and top electrical contact layers, respectively, and the undoped layer is the active layer absorbing the infrared radiation. Beryllium (Be) and Tellurium (Te) were used as p- and n-type dopants, respectively. The epilayers exhibited mirror-like surface morphology.

Structure 3, which includes a larger bandgap material ($Al_{0.1}In_{0.9}Sb$) as the p^+ layer, was also grown at Northwestern University with MBE technique. Utilization of larger bandgap contact layer is believed to reduce the dark current by lowering the thermal generation rate in this layer [113]. Large bandgap material could also be used for the bottom contact layer. However, AlInSb is not lattice-matched to InSb, and a wider bandgap material lattice-matched to InSb is not available. Strain between AlInSb and InSb may result in dislocation generation. Additionally, dislocations generated at the heterointerface at the bottom contact can propagate towards the intrinsic region and p^+-i junction, which may significantly degrade the detector performance. Epilayer thicknesses used in this structure are 1 µm p^+ - AlInSb, 6 µm intrinsic – InSb, and 1 µm n^+ InSb.

3.2 Characterization Set up

Detailed electrical and optical characterizations were performed on the test detectors to measure their performances, and to reveal the mechanisms limiting the detector performance. Following subsections present the characterization set ups used in this study.

3.2.1 Dark Current Measurement Set Up

Illustration of the I-V characterization set up is given in Figure 3.2. In order to study the detector dark current, I-V characteristics were measured using a Keithley 238 source-measure unit under computer control. An HP-VEE program controls the source-measure unit, and the system generates the I-V plot by sweeping the bias voltage, and measuring the detector current step by step.

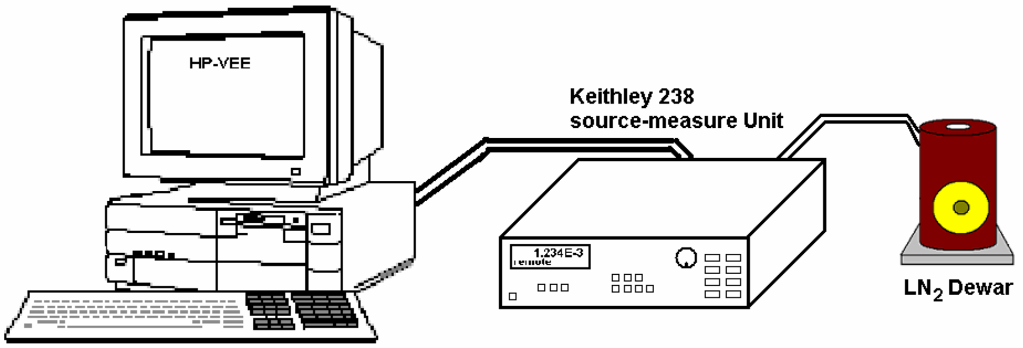

Figure 3.2: Illustration of the dark current measurement set up.

3.2.2 Noise Measurement Set up

The block diagram of the noise measurement set up is given in Figure 3.3. Detectors were mounted into a shielded liquid nitrogen (LN_2) dewar, and biased through a low noise amplifier, which amplifies the noise signals to the measurable levels. The biasing circuit is a simple voltage divider with filter capacitors. In order to prevent noise interference from the mains, batteries are used in power supply and biasing circuit blocks. The noise spectrum at the output of the amplifier is measured with an Agilent 4395A spectrum analyzer. Measured noise is the superposition of the detector noise and the amplifier noise. Therefore, at every measurement, noise spectrum of the amplifier is measured, and the detector noise is extracted from the total noise spectrum.

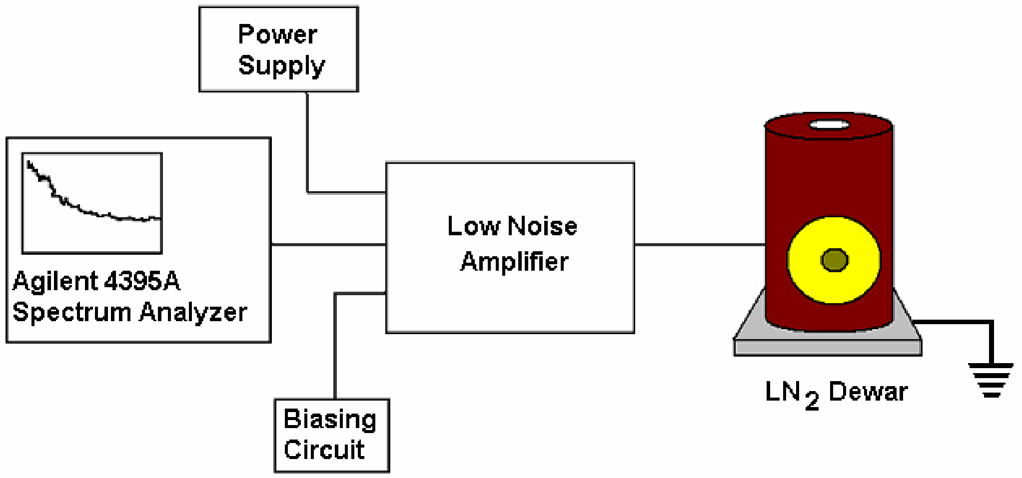

Figure 3.3: Block diagram of set up used for noise measurements.

3.2.3 Optical Measurement Set up

The optical measurements were performed using a computer controlled characterization system. Block diagram and a picture of the set up utilized for responsivity and detectivity measurements are given in Figure 3.4. The chopper modulates the blackbody radiation, and the detector signal is amplified with a lock-in amplifier, which is locked to chopper frequency. Detector is aligned with the blackbody aperture with the help of an XYZ stage. A low-noise transimpedance preamplifier is utilized for amplification.

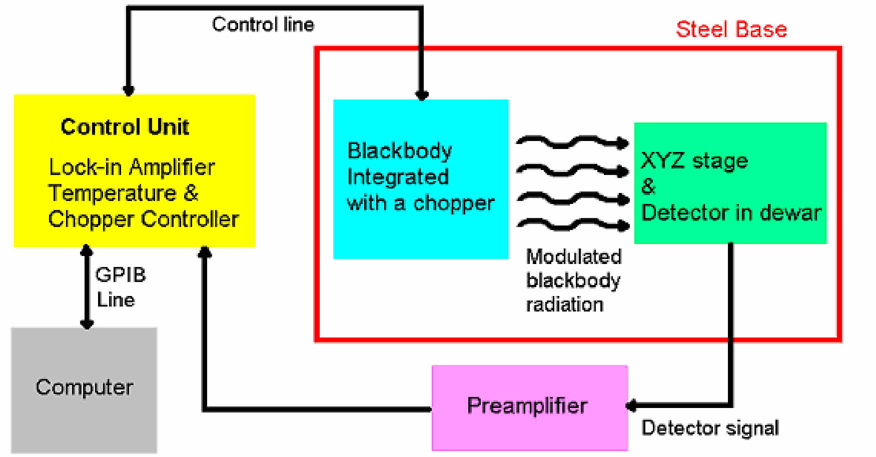

(a)

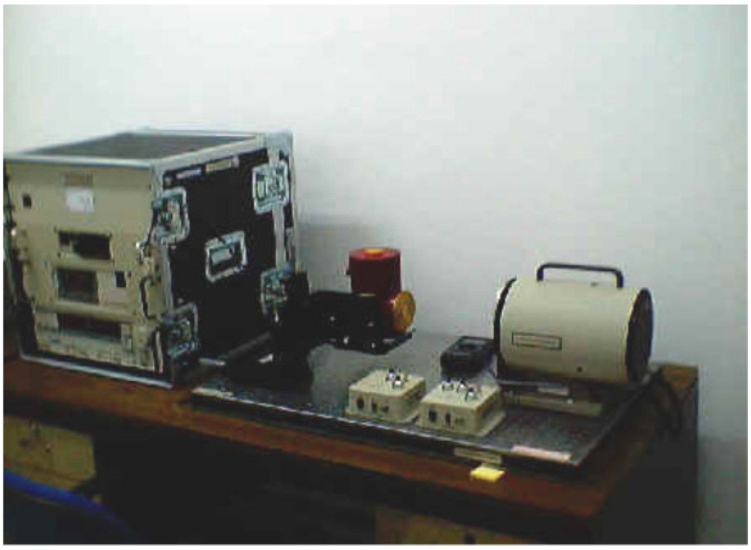

(b)

Figure 3.4: (a) Block diagram and (b) picture of the responsivity and detectivity measurement set up.

Spectral response of the detectors were measured with an Oriel MIR-8000 FTIR system whose block diagram and picture are shown in Figure 3.5. The Fourier transform interferometer (FTIR) is a Michelson interferometer type instrument. A pyroelectric detector having wide-band spectral response is used to obtain a reference spectral response. The system extracts the detector spectral response, and minimizes the effects of the dependency of the blackbody radiation on wavelength, as well as the characteristics of the measurement medium using this reference.

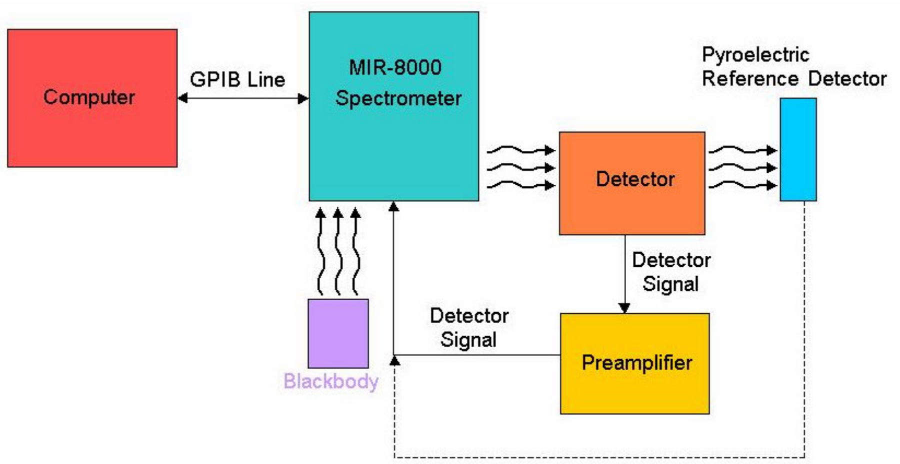

(a)

(b)

Figure 3.5: (a) Block diagram and (b) picture of the set up used for spectral responsivity measurements.

3.3 Test Detector Fabrication, Characterization, Results and Discussion

Fabrication of the test detectors using the epilayer structures shown in Figure 3.1, the results of the electrical and optical characterization, dark current modeling, and interpretation will be presented in this section.

3.3.1 InAs$_{0.8}$Sb$_{0.2}$/GaAs Photodetector (Structure 1)

The characteristics of the photodetectors fabricated with structure 1 were evaluated by fabricating variable area test detectors illuminated from front-side through a window [47]. Characterizations of the detectors with different periphery/area ratios allow the isolation of the surface and bulk dark current mechanisms affecting the detector performance. Fabrication process of this type of test samples includes the following steps:

- Alignment mark deposition
- Mesa etch
- Passivation
- Contact and fan-out metallization
- Gold plating for bonding pads

Mesas were etched down to bottom n^+ contact layer to isolate the detectors electrically and to define their area. Subsequently, the photodiodes were passivated with polyimide to decrease the surface leakage and to protect them from the ambient. Next, the contacts were formed by metal deposition and lift-off. Finally, gold (Au) was coated on the bonding pad regions by electro-plating technique. Wire bonding completed the fabrication process. Picture and cross sectional illustration of a fabricated test detector are given in Figure 3.6.

Each test sample contains 32 detectors with various dimensions: 200×500 μm^2, 200×200 μm^2, 100×500 μm^2, 100×100 μm^2, 50×500 μm^2, 50×100 μm^2, 50×200 μm^2, and 25×100 μm^2. Figure 3.7 shows the picture of a test sample and SEM picture of an individual detector.

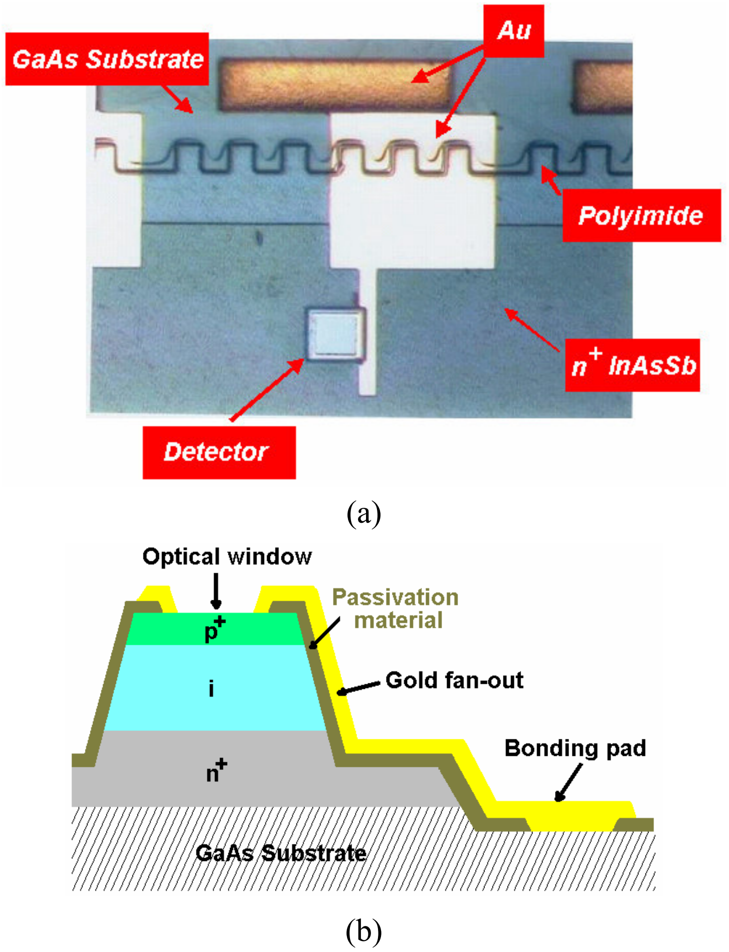

(a)

(b)

Figure 3.6: (a) Microscope picture, and (b) cross sectional illustration of a test detector fabricated with variable area test detector fabrication method.

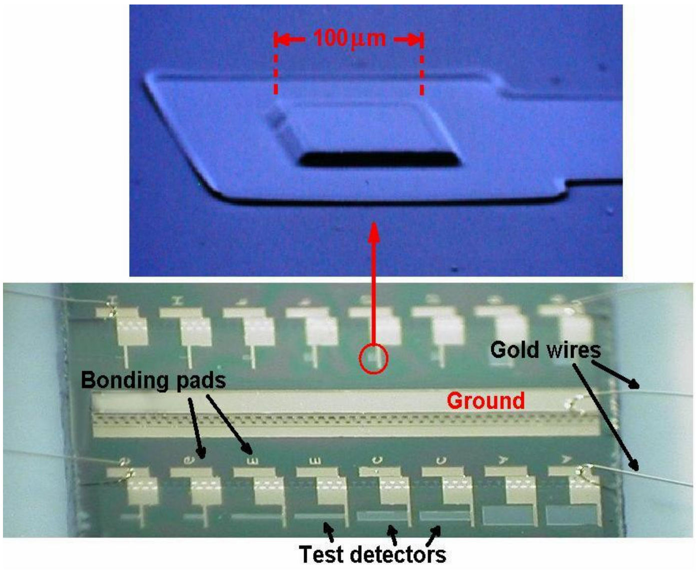

Figure 3.7: Snapshots from the sample having variable area test detectors. Top picture shows the SEM image of an individual test detector.

3.3.1.1 Dark Current Analysis of $InAs_{0.8}Sb_{0.2}$/GaAs Detector

Reverse bias differential resistance (R_D) versus bias characteristics of a 50×200 μm^2 $InAs_{0.8}Sb_{0.2}$ diode at several temperatures are given in Figure 3.8. The temperature is increased with step sizes of 10 K and 20 K between 50-100 K and 100-280 K ranges, respectively. The I-V characteristics of the diode under various temperatures are shown in the inset of Figure 3.8. The diode shows rectifying behavior up to near room temperature.

The variation of the differential resistance with temperature under zero bias and various reverse bias voltages is shown in Figure 3.9. The reverse bias differential resistance is almost temperature independent in a wide temperature range of 50-150 K. It also shows slight bias dependence under moderately large reverse bias voltages. Slight dependence of differential resistance on temperature in the 50-150 K range suggests that the dark current is not dominated by a thermal mechanism in this temperature range.

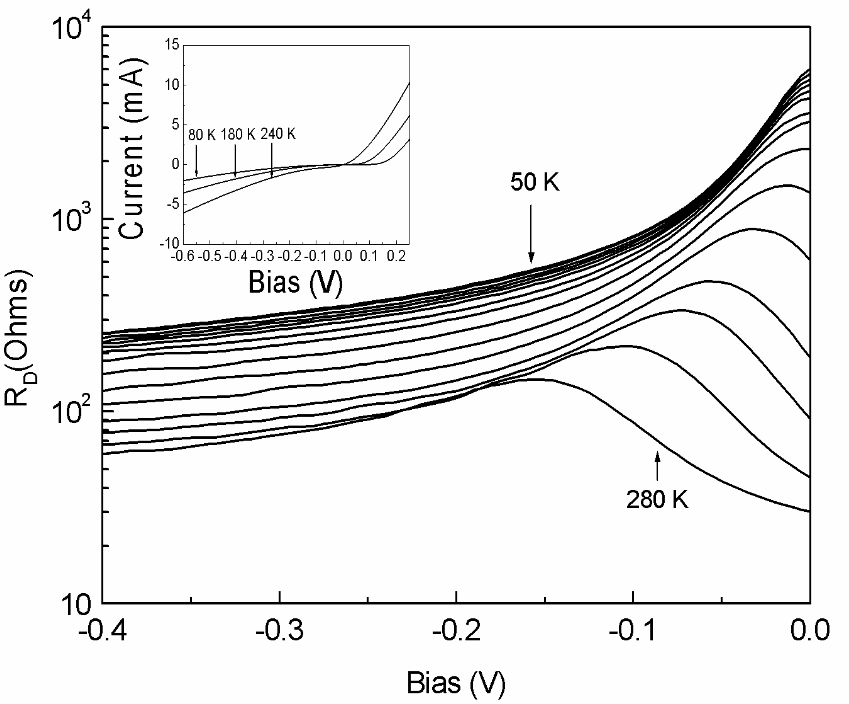

Figure 3.8: Differential resistance versus temperature characteristics of the $InAs_{0.8}Sb_{0.2}$ test diodes [47].

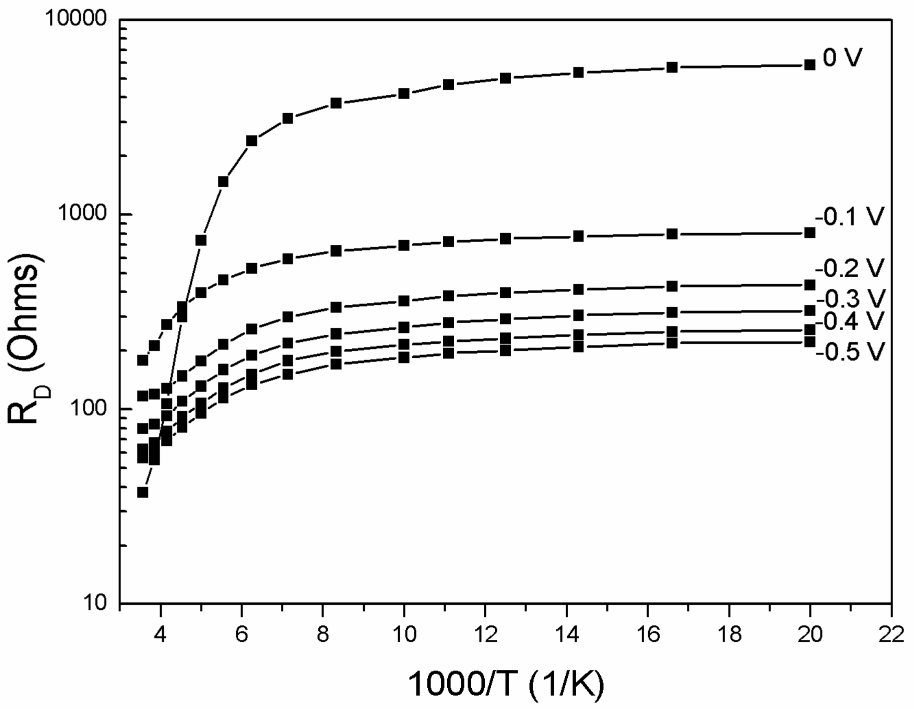

Figure 3.9: Variation of the differential resistance of $InAs_{0.8}Sb_{0.2}$ diodes with temperature under zero bias and various reverse bias voltages [47].

The significance of the various components of the dark current can be determined by a numerical fitting of the sum of the expressions for the presumably important dark current components to the measured dark current. However, in order to reveal the small changes in the current, the expression for the total resistance was fit to the measured data over a substantially large bias and temperature range. In order to find the dominant dark current components, a current model consisting of three components was used: TAT, diffusion and generation-recombination (g-r). These mechanisms are described in Appendix A. The differential resistance, which is found from the derivative of the dark current with respect to voltage, is expressed as

$$\frac{1}{R}=\frac{1}{R_{diff}}+\frac{1}{R_{tat}}+\frac{1}{R_{g-r}} \qquad (3.1)$$

If the dark current is dominated by a single component in a certain bias range, and the voltage and temperature independent constants are known, invaluable information on the related material parameters can be obtained by fitting Equation 3.1 to the measured data in this range. Figure 3.10 presents the results obtained for 80 K and 240 K in the reverse bias range of 0-0.3 V. At 80 K, the differential resistance is limited by the TAT mechanism in almost the entire reverse bias range of interest. Similar behavior was observed for temperatures up to 150 K. Above 150 K, the diffusion current becomes dominant under small reverse bias voltages. The contribution of the g-r current was found to be insignificant in the entire bias and temperature range.

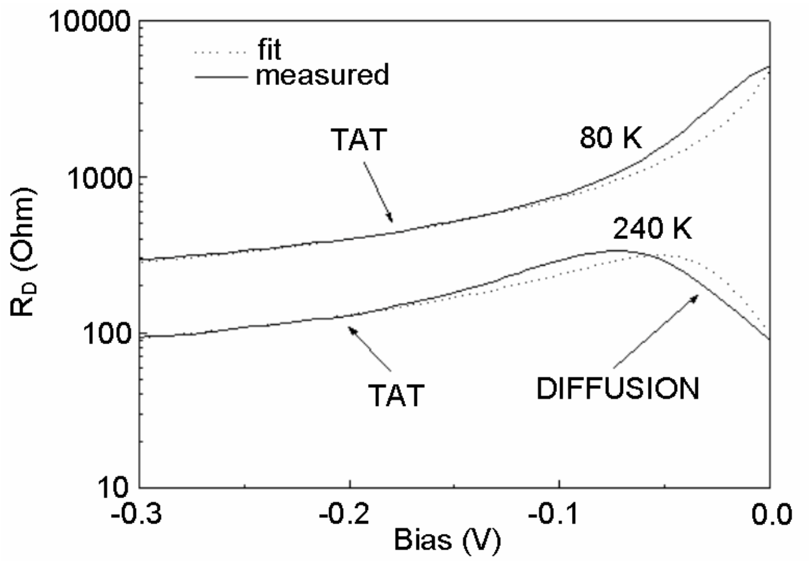

Figure 3.10: Measured and calculated differential resistance of $InAs_{0.8}Sb_{0.2}$ samples under moderately large reverse bias at 80 and 240 K [47].

In order to isolate the surface components of the dark current from the bulk components, the dark currents of detectors with different perimeter/area ratios were also analyzed. Since surface and bulk mechanisms are uncorrelated, dark current of a detector (I_D) can be expressed as

$$I_D = P \times J_P + A \times J_A \tag{3.2}$$

where P is perimeter of the detector, J_P is surface current density, A is area of the detector, and J_A is the bulk current density. Equation 3.2 can also be expressed as

$$\frac{I_D}{P} = J_P + \frac{A}{P} J_A \tag{3.3}$$

J_P and J_A can be revealed by constructing a plot of I_D/P versus A/P under different reverse bias voltages, and fitting the results to Equation 3.3. Figure 3.11 shows the fitting results.

Once $J_P(V)$ and $J_A(V)$ are obtained, dark current can be estimated for a given detector size. Figure 3.12 shows the contributions of the surface and bulk currents to the total detector dark current for detector sizes of 20×20 μm^2, 33×33 μm^2, and 100×100 μm^2. As can be seen from the figure, under small reverse bias voltages dark current is mainly generated by the bulk mechanisms. However, surface contribution increases with reverse bias, especially in the small sized detectors.

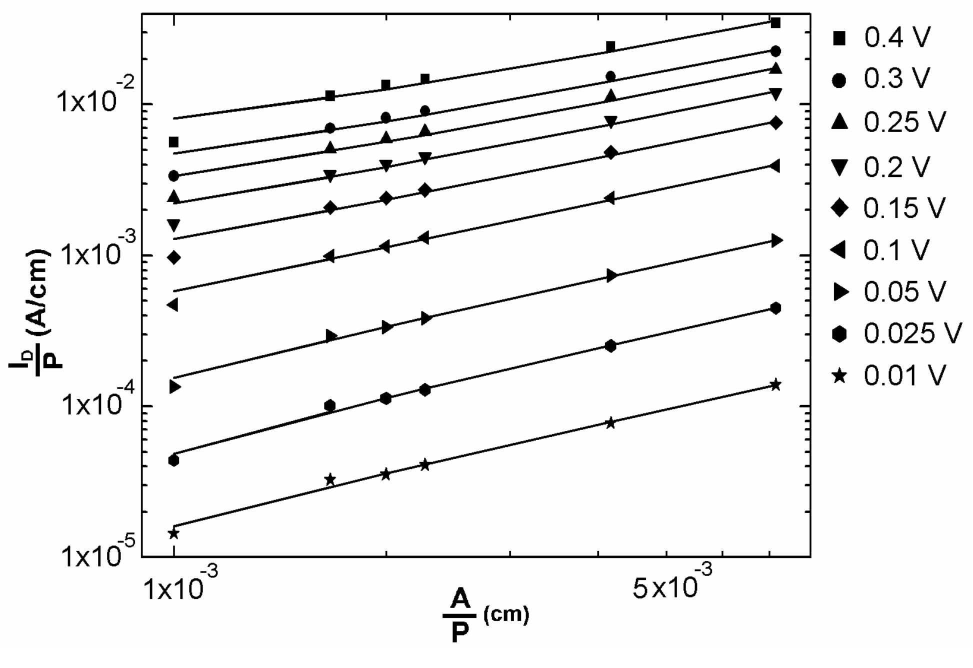

Figure 3.11: Fitting results of Equation 3.3 to experimental data. Symbols are for experimental data and solid lines show the fitting results.

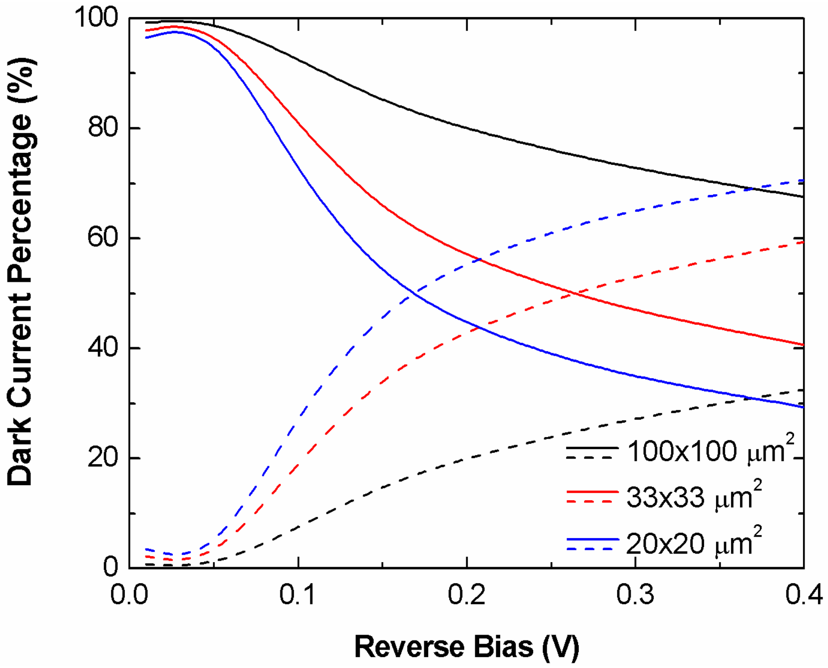

Figure 3.12: Contributions of the surface and bulk currents to the total detector dark current for 20×20 μm^2, 33×33 μm^2, and 100×100 μm^2 detectors. The dashed and solid lines indicate the surface and bulk components, respectively.

While different passivation techniques can be investigated to improve the performance (decrease the dark current) of these detectors, it should be noted that the dark current is dominated by bulk mechanisms under the typical reverse bias voltages that the FPA pixels operate. The traps participating in the TAT process may be related with the defects arising from the large lattice mismatch between the alloy and GaAs. Therefore, the material quality must be improved in order to achieve reasonably high photodetector performance, at least as high as that acceptable for a MWIR FPA. Indeed, 128×128 FPA that we fabricated using this epilayer structure was only able to detect very hot objects due to the low single to noise ratio of the pixels as a result of large dark current. The fabrication and characterization of this FPA will be presented in Section 3.4.

3.3.1.2 Noise Current Analysis of $InAs_{0.8}Sb_{0.2}$/GaAs Detector

Figure 3.13 shows the noise current spectral density at 77 K. It is observed that 1/*f* noise is significantly increased when the reverse bias exceeds 250 mV.

Figure 3.14 shows the variation of the 1/*f* noise current spectral density with the detector current. An empirical relationship between the noise current and the tunneling current can be established as [114]

$$i_n = \alpha(I)^{\beta} f^{-1/2} \tag{3.4}$$

where I is the tunneling current. When Equation 3.4 is fit to the measured data of Figure 3.14 in the region where the TAT process is dominant, α and β are found to be 1×10^{-6} and 0.5, respectively. The fitting results are also shown in Figure 3.14. The values of α and β determined for trap assisted tunneling are almost identical to those found by Nemirovsky and Unikovsky [114] for HgCdTe diodes. When the reverse bias exceeds 0.3 V, band to band tunneling becomes significant and 1/*f* noise current is increased as indicated by the change of the slope of the curve relating noise current to the diode current in Figure 3.14. The observed relation between the trap assisted tunneling current and 1/*f* noise supports the observations of Nemirovsky *et. al.* [115] on HgCdTe photodiodes.

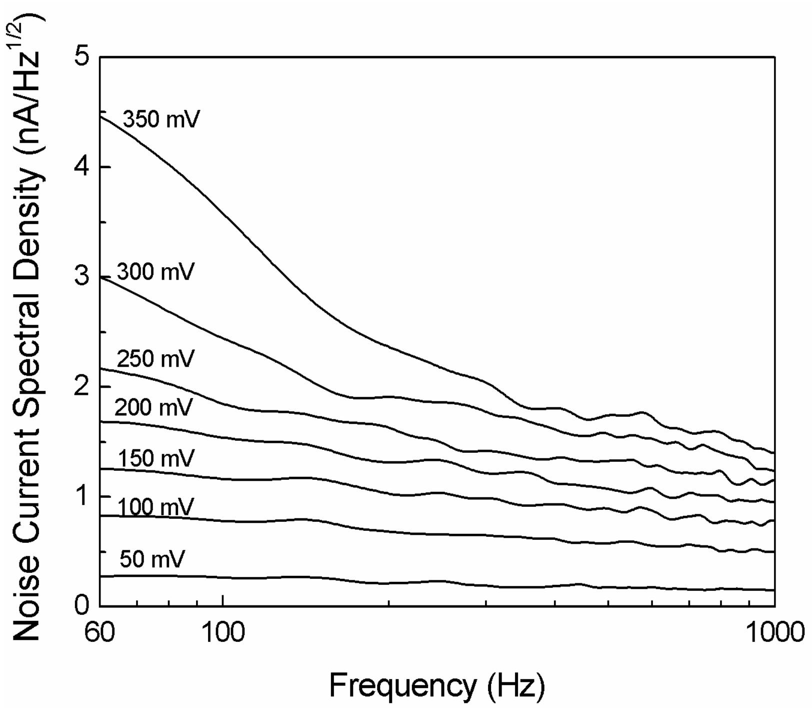

Figure 3.13: Dependence of noise current spectral density on frequency under various reverse bias voltages at 77 K [47].

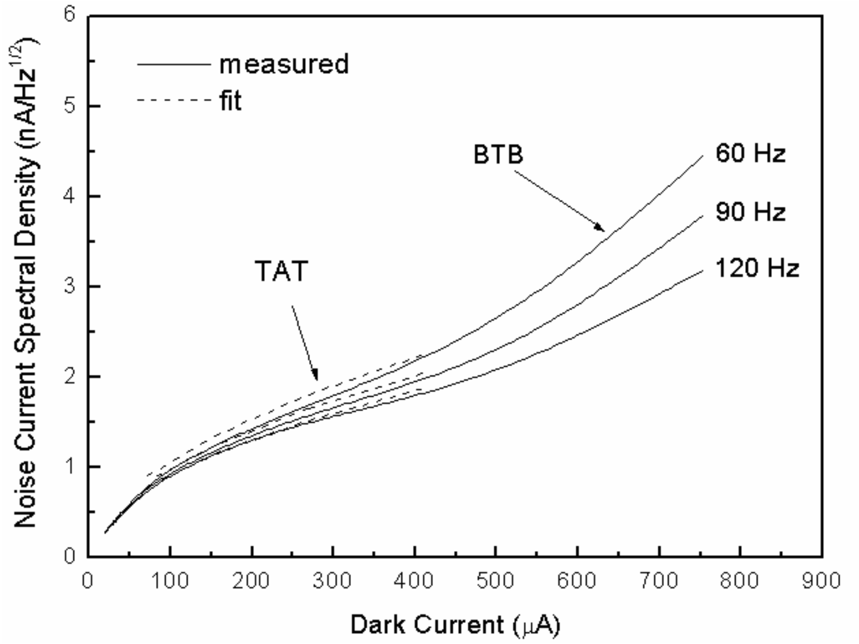

Figure 3.14: Dependence of noise current spectral density on detector current at 77 K. Fitting results for the region dominated by trap assisted tunneling are also shown in the figure [47].

3.3.1.3 Optical Characterizations of $InAs_{0.8}Sb_{0.2}/GaAs$ detector

The optical characterization of the $InAs_{0.8}Sb_{0.2}/GaAs$ photodetector was performed with the blackbody source set at 500 °C, and the chopper at 700 Hz. Figure 3.15 shows the 80 K spectral response of a 50 × 200 μm^2 detector with a peak detectivity of 1.4×10^{10} cm $Hz^{1/2}$ W^{-1} at 3.9 μm under 180° field of view (FOV). The cut-off wavelength (50% response) is 4.7 μm yielding a 80 K energy bandgap of 0.26 eV in agreement with the expectation for the Sb mole fraction of 0.2 [1].

While the measured detectivity is an order of magnitude lower than that of the state of the art MWIR photodetectors grown on lattice matched substrates, it can be improved by optimizing the detector epilayer structure, and the growth conditions.

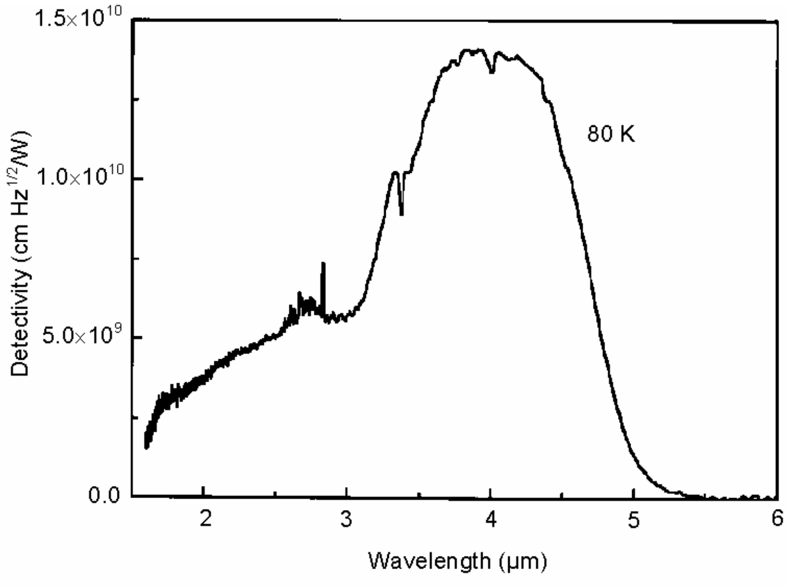

Figure 3.15: Spectral detectivity of $InAs_{0.8}Sb_{0.2}$ photodiodes at 80 K (180° FOV) [47].

Figure 3.16 shows the result of the optical measurements at 240 K. The peak detectivity is 7.5×10^8 cm $Hz^{1/2}$ W^{-1} at 4.7 μm, and the cut-off wavelength is 5.4 μm yielding an energy bandgap of 0.23 eV at this temperature. The results show that the alloy is also promising for near room temperature photon detectors.

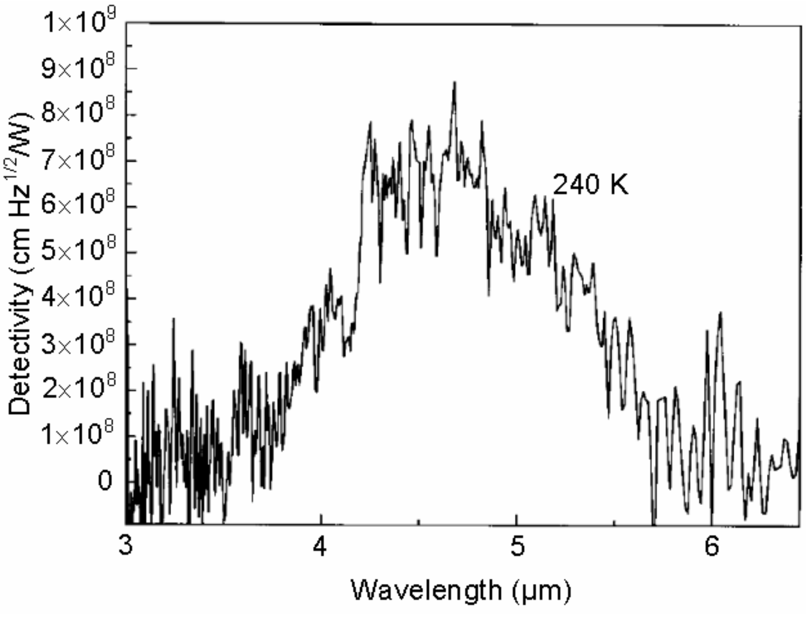

Figure 3.16: Spectral detectivity of $InAs_{0.8}Sb_{0.2}$ photodiodes at 240 K (180° FOV) [47].

3.3.2 InSb/Si Photodetector (Structure 2)

Assessment of the InSb/Si photodetectors were evaluated and studied through fabrication, testing and modeling of 33×33 μm^2 (128×128 FPA pixel size) detectors flip-chip bonded to fan-out substrates [116]. The dark current of FPA pixels is generally estimated by scaling the dark current of a large area detector. However, due to the surface effects, the dark current density may depend on the mesa perimeter/area ratio of the detector. Therefore, characterization of the test detectors having the same size and structure with the FPA pixels is necessary to estimate FPA performance accurately. This section does not discuss the fabrication process of this type of detectors, and the details are given in the FPA fabrication section (section 3.4). Each test sample contains 64×64 array of 33×33 μm^2 test detectors (4096 pixels), and is flip-chip bonded to a fan-out substrate after fabrication. Fan-out substrate shown in Figure 3.17 provides 135 electrical contacts from individual test detectors.

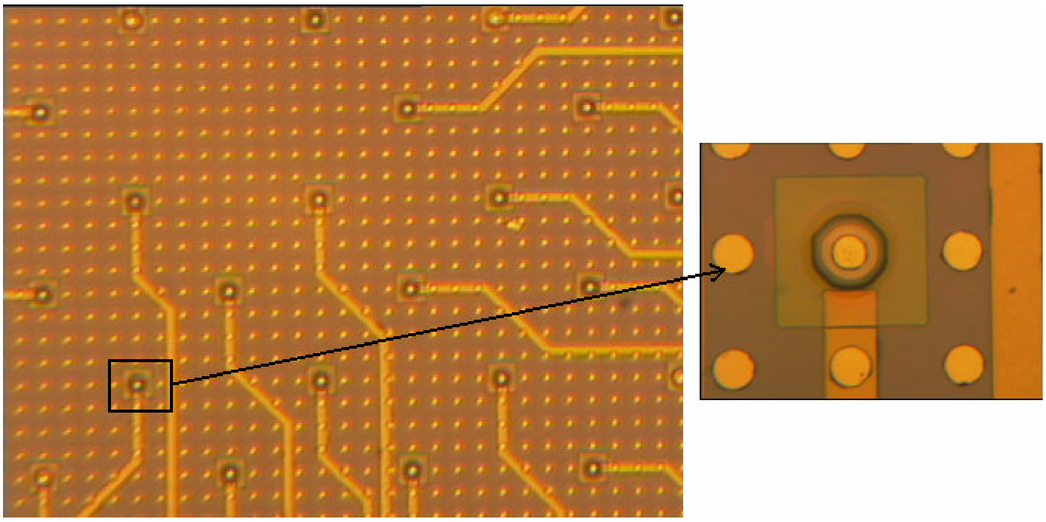

Figure 3.17: Picture of a fan-out substrate. Yellow dots are the pads corresponding to the pixels on the test sample. Yellow lines are the fan-out lines that connect the test detectors to the outside world.

After flip-chip bonding, the test hybrid was mounted on an alumina substrate with a high-vacuum thermal compound, and electrical contacts were taken between the pads by wire bonding. Figure 3.18 shows the picture of a test hybrid mounted on an alumina substrate, which is ready for characterization. Due to the thermal expansion coefficient match between the substrates of the fan-out circuit and the test detector array, good thermal cycling reliability was achieved without substrate thinning.

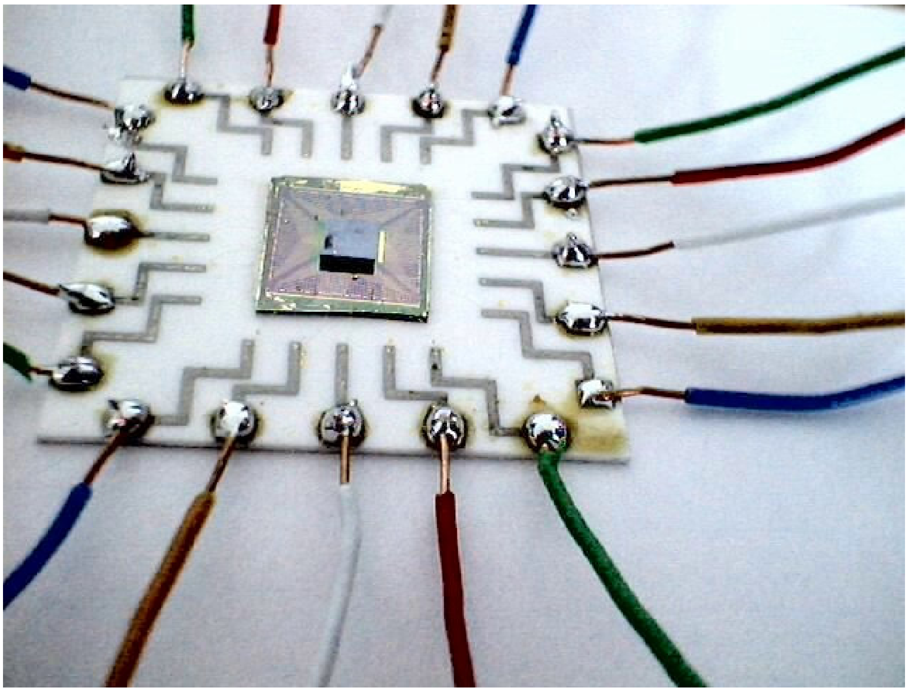

Figure 3.18: Test hybrid mounted on an alumina substrate.

3.3.2.1 Dark Current Analysis of InSb/Si Detector

Flip-chip bonded 33×33 μm^2 test detectors yielded similar characteristics, and the detailed characteristics of a typical diode will be presented for this detector structure [116]. Figure 3.19(*a*) shows the differential resistance of the diode versus bias under various temperatures. The *I–V* characteristic is also shown in the inset. Temperature dependence of the diode resistance is shown in Figure 3.19(*b*) under various reverse bias voltages. Above ~200 K, the activation energy for the zero-bias differential resistance is in agreement with the corresponding bandgap of InSb suggesting that diffusion dominates dark current in this temperature range near zero-bias. Under low temperatures, the zero-bias dynamic resistance shows a small activation energy (25 meV) which is decreased as the reverse bias is increased. Weak dependence of the differential resistance on temperature in the low temperature and large reverse bias regions suggests that the dark current is not dominated by a thermal mechanism in these regions.

In order to find the dominant dark current mechanisms in various bias and temperature regions, we used a current model including trap-assisted tunneling (TAT), diffusion, generation–recombination (g–r) and Ohmic leakage mechanisms, which are discussed in the Appendix A. The inclusion of the last component is necessary in the analysis of photodiodes hetero-epitaxially grown under large lattice mismatch, since this current component is known to be due to the leakage through the diode, which may result from dislocations intersecting the junction [112]. When the bandgap of InSb is considered, band to band tunnelling should be insignificant in the bias region used in this study. Therefore, the contribution of band to band tunnelling to the total dark current is ignored. With the inclusion of the above mechanisms, the differential resistance of the detector can be expressed as

$$\frac{1}{R}=\frac{1}{R_{diff}}+\frac{1}{R_{tat}}+\frac{1}{R_{g-r}}+\frac{1}{R_{s}} \tag{3.5}$$

where R_s represents the shunt resistance associated with the Ohmic leakage.

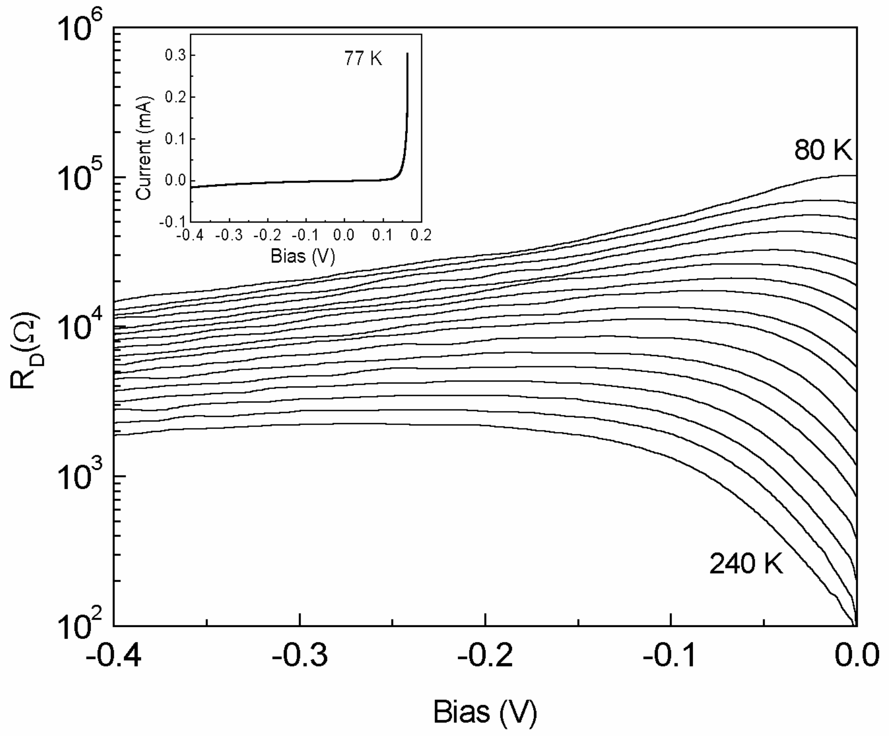

(a)

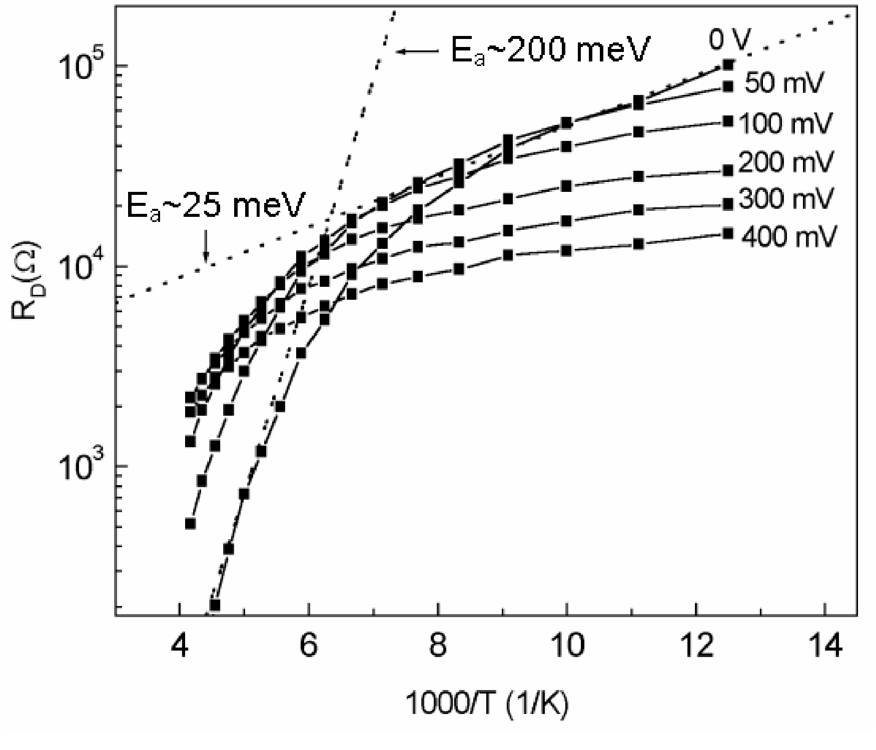

(b)

Figure 3.19: Dependence of the differential resistance of InSb/Si detectors on bias (a) and temperature (b) [116].

Equation 3.5 was fit to the measured data in a sufficiently large reverse bias range under various temperatures. Meaningful values with no ambiguity were obtained for the parameters of interest by keeping the temperature and voltage independent parameters constant during fitting. The results of the fitting process at 80 K are given in Figure 3.20(*a*). Variation of the differential resistance with bias and temperature is replotted in Figure 3.20(*b*) showing the most dominant dark current mechanisms in various regions. Zero-bias dynamic resistance at 80 K is limited by Ohmic leakage (Figure 3.20(*a*)), and trap-assisted tunnelling becomes the dominant mechanism when the reverse bias approaches 100 mV. Effective trap density at 80 K is estimated to be 1.6×10^{15} cm^{-3} and the tunnelling rate in the TAT dominated bias region is in the order of 10^7 s^{-1}. As the temperature is increased, the peak in differential resistance shifts to higher reverse bias voltages due to the increasing contributions of g–r and diffusion components (Figure 3.20(*b*)). Diffusion becomes the dominant dark current component near zero-bias for temperatures above ~200 K. Assuming that the surface recombination velocity is $\sim10^4$ cm-s^{-1} [117], the carrier lifetime was estimated to be around 0.3 ns. Fabrication of variable area diodes is necessary for more reliable evaluation of the carrier lifetime and the surface recombination velocity by isolating the surface and bulk components of the g–r current.

Figure 3.21 shows the temperature dependence of the shunt resistance in the temperature region of 80–140 K. The variation of the shunt resistance with temperature is weaker than that of the intrinsic carrier concentration, and the activation energy is 25 meV. The presence of the shunt resistance results in regions with similar activation energy in the zero-bias resistance (R_0) versus $1/T$ plot at temperatures where the resistance is determined by Ohmic leakage such as the zero-bias resistance below ~120 K in Figure 3.20(*b*). Unexpectedly small activation energy region was also reported in the zero-bias resistance–area product (R_0A) versus $1/T$ plot of long wavelength infrared HgCdTe diodes with high dislocation density [110].

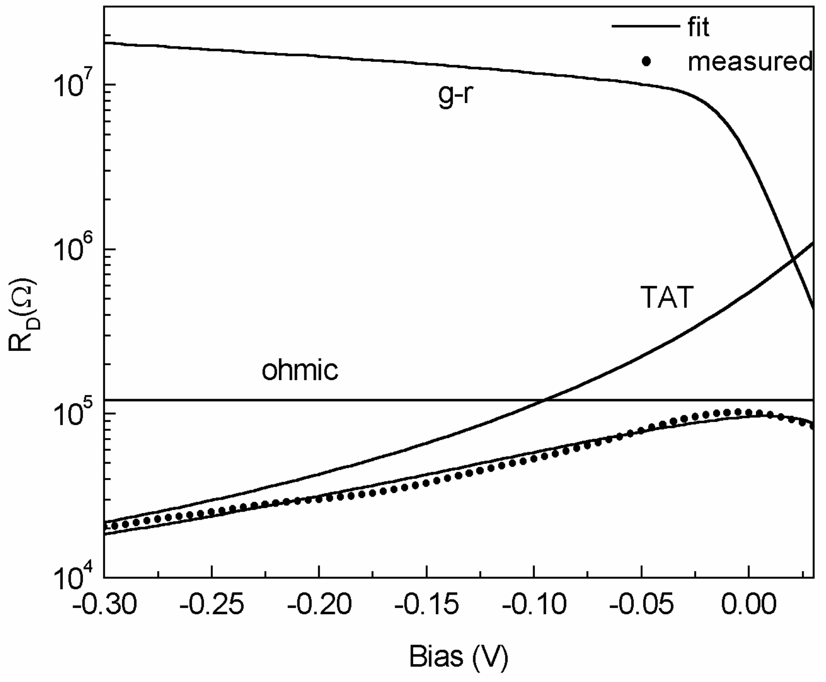

(a)

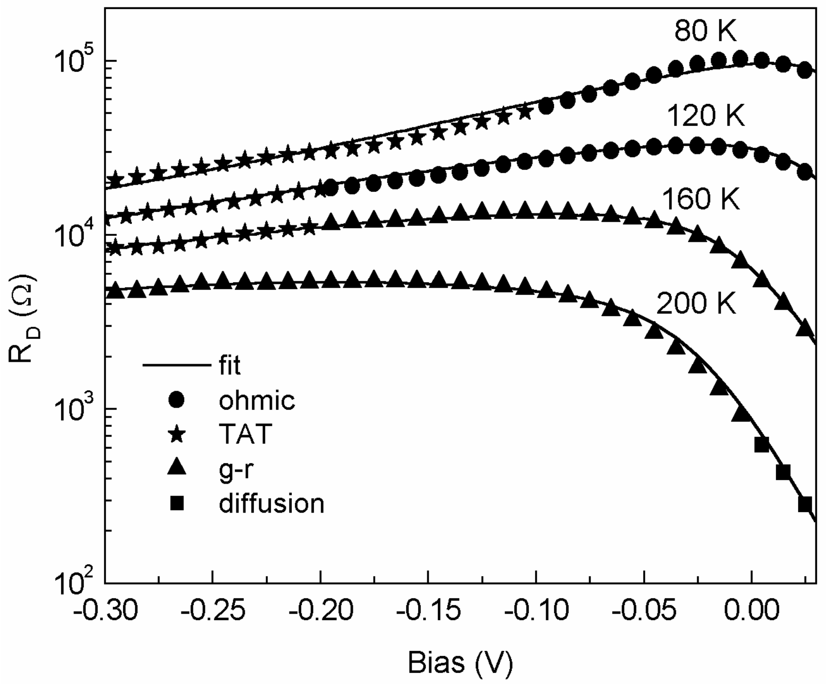

(b)

Figure 3.20: (a) 80 K fitting results, (b) theoretical fits under a range of bias voltages and at various temperatures. Symbols on curves indicate the dominant dark current mechanism at that point in (b) [116].

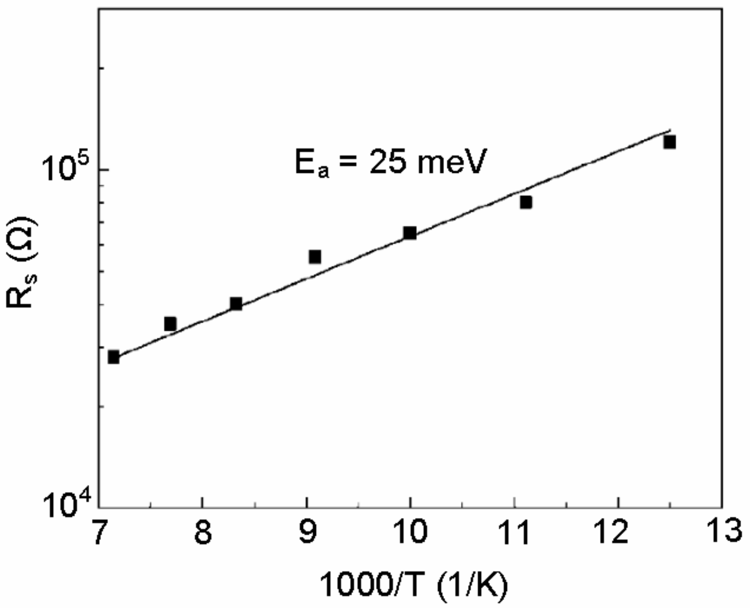

Figure 3.21: Temperature dependence of the shunt resistance in InSb/Si diodes [116].

Earlier experiments on HgCdTe showed that the dislocations degrade the dynamic resistance of the diode by increasing the g–r current in which case R_0A scales in inverse proportion to the intrinsic carrier concentration, and the dynamic resistance can considerably be improved using larger bandgap (smaller n_i) materials [118]. Photodiodes grown under highly lattice mismatched conditions may also suffer from other leakage mechanisms which are likely to be related with the threading dislocations in the epilayer structure. Based on our observations, the temperature dependence of the Ohmic leakage does not reflect a change in proportion to that of the intrinsic carrier concentration. Therefore, hetero-epitaxial growth of alternative larger bandgap materials (such as $InAs_xSb_{1-x}$ instead of InSb) may not improve detector R_0A as significantly as expected, if the detector performance is limited by the shunt resistance.

3.3.2.2 Noise Current Analysis of InSb/Si Detector

Noise measurements were performed in the frequency range of 10–4000 Hz, and $1/f$ noise at 1 Hz was found by extrapolating the data to 1 Hz. $1/f$ noise was not observed at zero-bias. Figure 3.22 shows the reverse bias dependence of the $1/f$

noise current (at 1 Hz) under various temperatures at which the contribution of diffusion to the detector noise should be negligible. At 80 K, 1/*f* noise is expected to be dominated by the TAT process. Indeed, measured 1/*f* noise current at this temperature is in good agreement with $i_{n\mathrm{TAT}} = \alpha_{\mathrm{TAT}}(I_{\mathrm{TAT}})^{\beta}$ with $\alpha_{\mathrm{TAT}} = 7.5 \times 10^{-7}$, $\beta = 0.55$ which are close to the values found by Nemirovsky and Unikovsky [114] for HgCdTe photodiodes and to those observed on $\mathrm{InAs_{0.8}Sb_{0.2}}$/GaAs diodes ($\alpha_{\mathrm{TAT}} \sim 1 \times 10^{-6}$, $\beta \sim 0.5$) [47]. In the low reverse bias region, slope of the noise current is considerably increased with rising temperature reflecting the increasing contribution of the g–r related noise to the measured noise current. The rate of increase of noise current with reverse bias is significantly decreased when the bias exceeds ~25 mV indicating that one of the noise components tends to saturate. This behaviour has also been observed at other temperatures at which the contribution of g–r current to the dark current is at a considerable level. A saturation region in the 1/*f* noise versus reverse bias characteristic was also observed in diffusion limited HgCdTe diodes beyond ~30 mV reverse bias [118], which appeared to be a disagreement with Kleinpenning's model given in [119]. For the depletion region g–r noise, Kleinpenning's model estimates the 1/*f* noise power spectral density as [120]

$$S_I(f) = \frac{2\alpha q I}{3 f \tau}\left(1 - \exp\left(-\frac{qV}{2kT}\right)\right) \tag{3.6}$$

where τ is the carrier lifetime in the junction, α is the Hooge's parameter, V is the diode bias voltage and I is the g–r current. Under high reverse bias where the carrier velocity is saturated, Equation 3.6 must be modified [121] to express the maximum noise power spectral density as [120]

$$S_I^{\max}(f) = \frac{4\alpha q I v_s}{3 f W^*} \tag{3.7}$$

where v_s is the carrier saturation velocity, and W^* the effective width of space charge region.

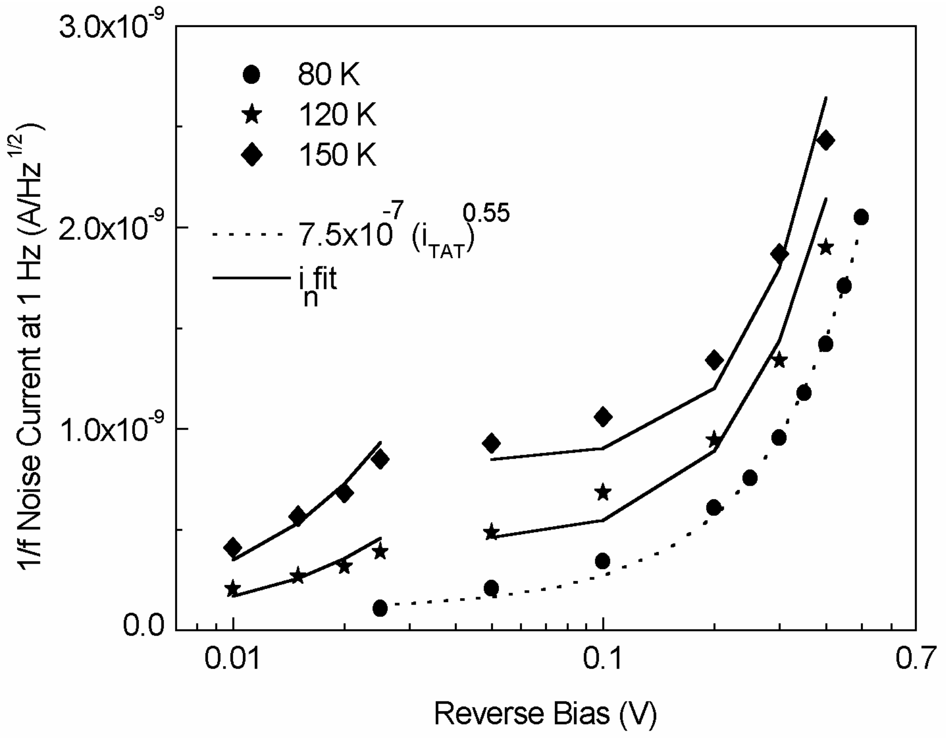

Figure 3.22: Reverse bias dependence of 1/f noise current at 1 Hz [116].

At fixed bias, Equation 3.7 predicts a change in $i_{n,\max}$ approximately in proportion to the square root of n_i. Figure 3.22 includes the total noise current (full curves) in the low and high reverse bias regions calculated using Equations 3.6 and 3.7 for the g–r noise and the empirical equation $i_n = \alpha_{TAT}(I_{TAT})^{\beta}$ for the TAT related noise. The variation of the noise current with bias and temperature is in agreement with the predictions of the Kleinpenning's model with α estimated to be in the order of 10^{-3} which is typical for the g–r related 1/*f* noise [119, 120]. The low bias 1/*f* noise is dominated by the g–r mechanism at 150 K. As the reverse bias is increased, the contribution of the TAT process is increased, and the bias dependency of the noise current is determined by the TAT component under large reverse bias. While the 1/*f* noise related with the shunt resistance was reported to be roughly dependent on R_s^{-1} [112], the voltage and temperature dependence of the 1/*f* noise current can be described considering only the g–r and TAT related noise currents in the diodes investigated in this study.

3.3.2.3 Optical Characterizations of InSb/Si Detector

Figure 3.23 shows the measured spectral response of the detectors at 80 K under backside illumination. The detector was kept near zero-bias during the measurements. In spite of the very large lattice mismatch between the detector material and substrate, the peak detectivity is ~1×10^{10} cmHz$^{1/2}$W^{-1} (near 4.8 μm) and the quantum efficiency is ~50% without anti-reflection coating. The peak detectivity is almost within an order of magnitude of the 300 K background limited detectivity at 4.8 μm, and the quantum efficiency will move closer to that of a typical InSb diode on lattice matched substrate, if anti-reflection coating is used. The results show that the dislocations do not considerably degrade the optical properties of the InSb detectors. Similar observation was reported by Johnson *et. al.* [110] for HgCdTe diodes.

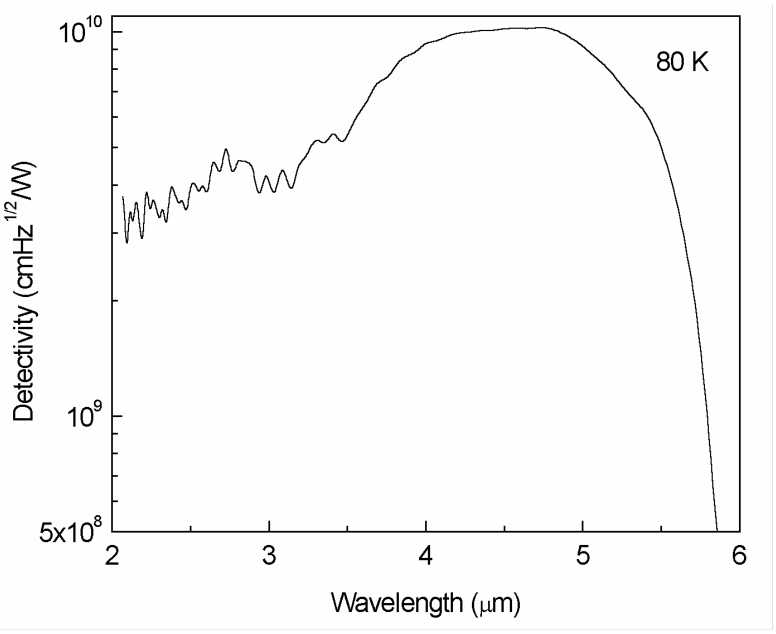

Figure 3.23: Spectral detectivity of InSb/Si photodiodes at 80 K (Structure 2) (180° FOV) [116].

3.3.3 AlInSb/InSb/Si Photodetector (Structure 3)

Assessment of the AlInSb/InSb/Si photodetectors were evaluated and studied through fabrication, testing, and modeling of 33×33 μm^2 (128×128 FPA pixel size) detectors flip-chip bonded to fan-out substrates. Fabrication process of the test detectors were discussed in Section 3.3.2. Some parts of the investigation on Structure 3 (AlInSb/InSb/Si) presented in this subsection were performed by Umid Tumkaya as a part of his M.Sc. study at the Physics Department of METU. His results will be used to compare AlInSb/InSb/Si heterojunction and InSb/Si homojunction diodes.

3.3.3.1 Dark Current Analysis of AlInSb/InSb/Si Detector

Figure 3.24 shows the I-V characteristics of a typical 33×33 μm^2 AlInSb/InSb/Si test detector. Same figure also gives the variation of the differential resistance (R_D) of the photodiode with bias. It can be seen that R_0 of AlInSb/InSb/Si detector is at least two times larger than that of InSb/Si photodiode, and the reverse bias dependence of the differential resistance of AlInSb/InSb/Si structure is stronger than that of the InSb/Si detector.

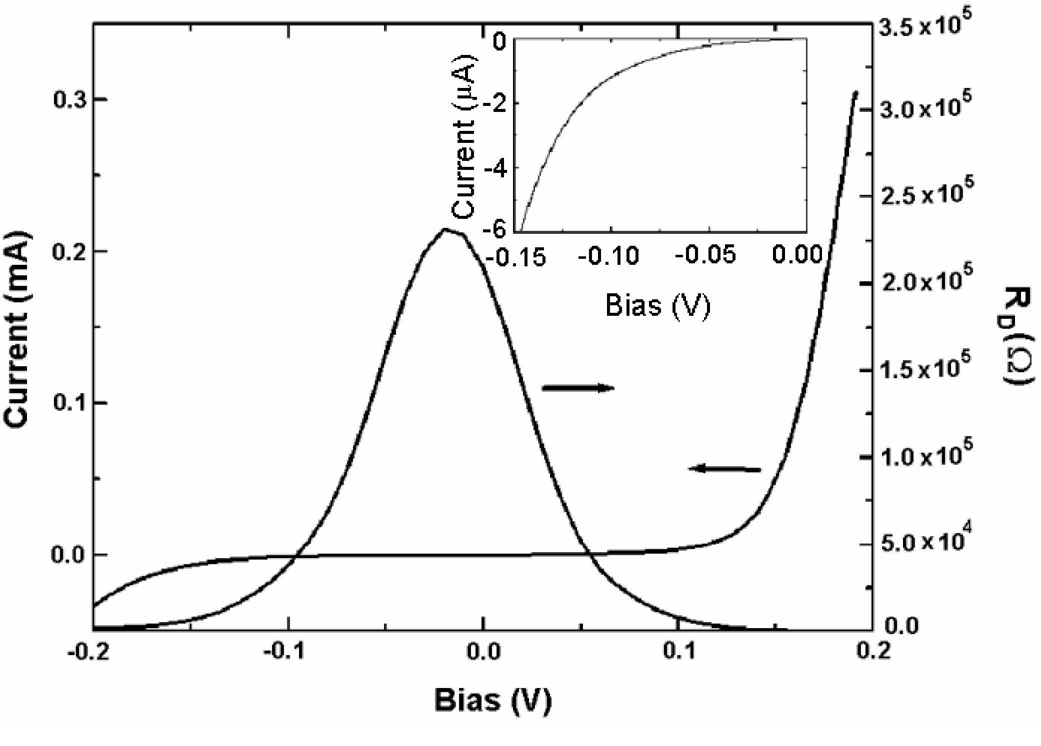

Figure 3.24: I-V characteristics and voltage dependence of R_D [122].

Figure 3.25 shows the variation of the differential resistance with bias voltage at several temperatures from 80 K to 240 K. Plots indicate that, under moderately large reverse bias voltages (~0.2V), dominant dark current mechanism determining R_D is not a thermal mechanism. In contrast, under zero bias, dominant mechanism depends on temperature strongly. Additionally, rapidly changing R_D with reverse bias at 80 K suggests that mechanisms with strong voltage dependence are dominant for reverse bias voltages larger than 0.05 V.

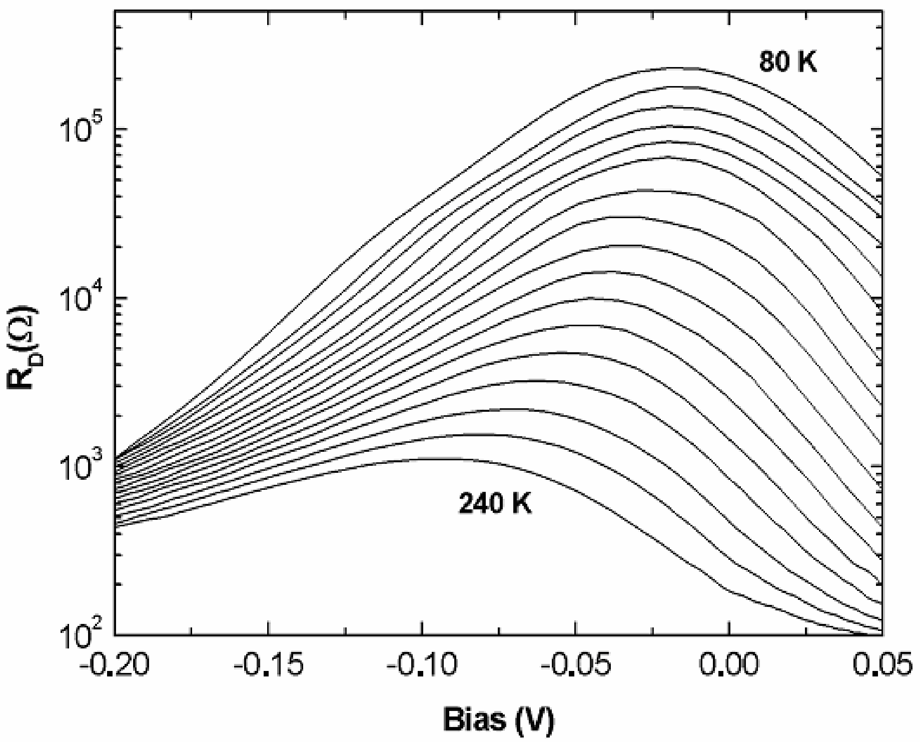

Figure 3.25: Dependence of differential resistance of AlInSb/InSb/Si heterojunction diodes on bias voltage at several temperatures from 80 K to 240 K [122].

Figure 3.26 shows the fitting results for AlInSb/InSb/Si heterojunction diode at 80 K, 120 K, 160 K, and 200 K [122]. The AlInSb/InSb/Si and InSb/Si diodes show similar dominant dark current mechanisms at low temperatures. However, due to presumably higher trap density in the AlInSb/InSb/Si photodiode (1.79×10^{17} cm^{-3}), TAT is still the dominant mechanism in the high reverse bias region at 200 K.

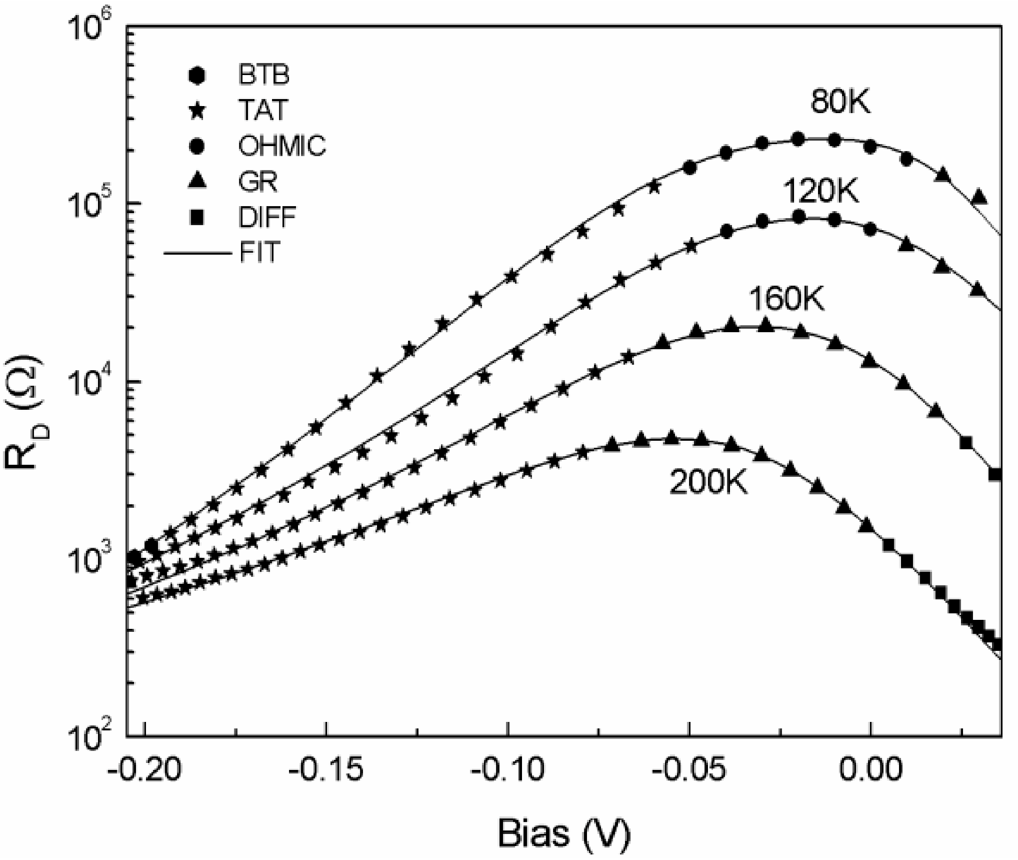

Figure 3.26: Theoretical fit to R_D versus bias voltage measurements. Symbols on curves indicate the dominant dark current mechanism at that point [122] (BTB: Band to band tunneling, TAT: trap assisted tunneling, Ohmic: shunt leakage, GR: generation-recombination, DIFF: diffusion).

3.3.3.2 Optical Characterizations of AlInSb/InSb/Si Detector

Figure 3.27 shows the spectral response of a backside illuminated 33×33 μm^2 AlInSb/InSb/Si detector without antireflection coating [122]. The measured peak detectivity of the detector is ~7×10^9 $cmHz^{1/2}/W$ and the cut-off wavelength (50% response) is 5.76 μm at 77 K. The peak detectivity of the AlInSb/InSb/Si detector is slightly lower than that of InSb/Si photodiode (~1×10^{10} $cmHz^{1/2}/W^{-1}$).

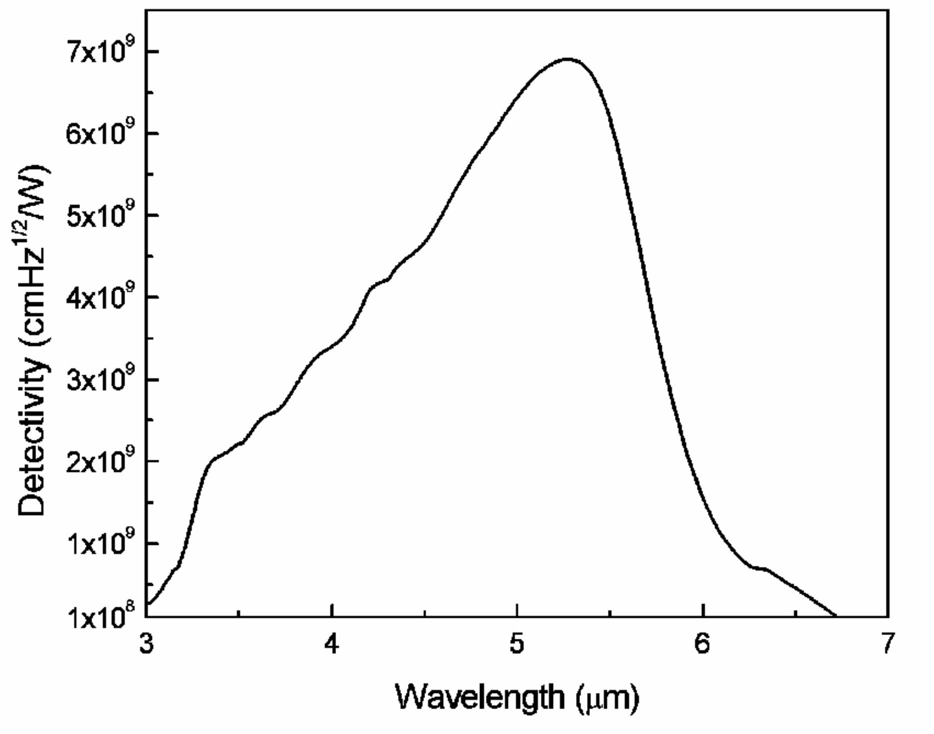

Figure 3.27: Spectral detectivity of AlInSb/InSb/Si heterojunction photodiodes on Si Substrate at 77 K (180° FOV) [122].

3.3.4 Comparison of InSb/Si and AlInSb/InSb/Si Detectors

When the dark currents of InSb/Si and AlInSb/InSb/Si detectors are compared, it is seen that the dark current of AlInSb/InSb/Si structure is almost an order of magnitude lower than that of InSb/Si structure under small reverse bias (~10 mV). As mentioned previously, lower dark current in heterostructure photodiodes is commonly attributed to the reduced thermal generation in the large bandgap contact region layer [113]. However, it is seen that the shunt resistance, which is not a thermal mechanism (activation energy is 25 meV for InSb/Si diode and ~22 meV for AlInSb/InSb/Si diode), limits the differential resistance of both structures around zero bias.

The dark current of heterostructure AlInSb/InSb/Si photodiodes is significantly better than that of the InSb/Si detectors, and 1/f noise levels of both diodes are similar [122]. Therefore, total noise (Johnson + shot + 1/f) in AlInSb/InSb/Si detectors should be lower, or at least comparable. However, optical performance of the homojunction InSb/Si photodiodes (peak detectivity ~1×10^{10} cmHz$^{1/2}$W^{-1}) is slightly better than that of the heterostructure photodiodes, which is not expected because of the lower noise in AlInSb/InSb/Si detectors. Therefore, quantum efficiency of the AlInSb/InSb/Si structure is lower than that of the InSb/Si detector. This could be possible because optical generation is suppressed in the larger bandgap material, reducing the photocurrent that is created in this layer. Moreover, when Figures 3.23 and 3.27 are compared, it can be seen that the photoresponse of AlInSb/InSb/Si structure rapidly decreases with increasing photon energy (decreasing wavelength). This can be attributed to the higher density of g-r centers close to the heterointerface between the Si substrate and InSb epilayers, which enhance the recombination of the photogenerated carriers. Since most of the higher energy photons are absorbed close to the heterointerface, spectral response rapidly decreases with decreasing wavelength. These g-r centers also destroy the carriers generated by the photons with peak absorption wavelength, resulting in a reduction in the peak quantum efficiency. Although both AlInSb/InSb/Si and InSb/Si structures are grown on similar (GaAs coated Si) substrates, the density of dislocations generated at the substrate-epilayer interface may be larger in AlInSb/InSb/Si wafer due to inferior growth conditions, as well as due to lower substrate quality.

3.4 128×128 FPA Fabrication and Characterization

While the above photodetectors, limited with the degrading effects of the lattice mismatced epitaxy, are not expected to yield high FPA performance, we fabricated 128×128 $InAs_{0.8}Sb_{0.2}$/GaAs and AlInSb/InSb/Si FPAs in order to assess the level of FPA performance achievable under the present conditions. We did not fabricate any InSb/Si FPA because of the lack of sufficient material. Following the fabrication, FPAs were tested with an evaluation camera. The subsequent subsections will present the fabrication process, and the real-time images obtained with the 128×128 AlInSb/InSb/Si and $InAs_{0.8}Sb_{0.2}$/GaAs FPAs.

3.4.1 128×128 FPA Fabrication

Fabrication process of the FPAs is more complicated than that of the test detectors because of the extra parameters that must be considered like uniformity, yield, and reproducibility. 128×128 FPA fabrication involves several lithography, etch, metallization, and coating processes, and it can be divided into seven stages, which are given by

- Alignment mark deposition
- Mesa etch
- Contact metallization
- Passivation
- Under-bump metallization (UBM)
- Indium electro-plating
- Flip-chip bonding and packaging

The following subsections will explain some of the above steps briefly.

3.4.1.1 Mesa etch

Mesa etching is performed to isolate the diode junctions from each other. Test detector mesas were wet etched down to the bottom contact layer, which provides a conduction path to common node (ground). Pixel to pixel variations in detector area must be minimized, therefore the etchant (citric acid:hydrogen peroxide solution) was stirred to keep the solution chemically uniform at this step. Temperature and stir rate were controlled to achieve uniform and reproducible etch. Pictures of the FPA pixels after mesa etching are given in Figure 3.28. Mesa etch was followed by contact metallization and passivation.

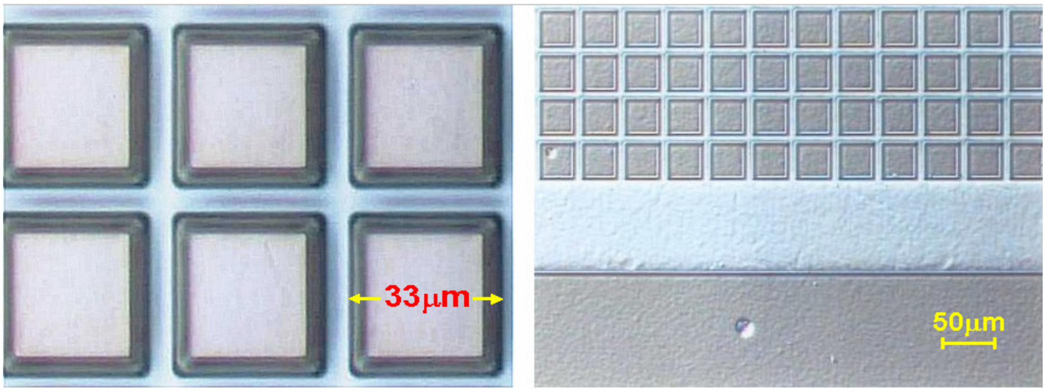

Figure 3.28: Pictures of FPA pixels after mesa etching.

3.4.1.3 Under Bump Metallization (UBM)

UBM was deposited before the indium electro-plating process. Purpose of the UBM is to prevent diffusion of the indium to the semiconductor, and to provide good adhesion between the indium bump and detector mesa. We used a three-layer metal structure as UBM. The top layer is wettable by In, the middle layer provides a barrier for In diffusion, and the bottom layer provides good adhesion to the semiconductor. Optical microscope picture of the FPA pixels after deposition of UBM are shown in Figure 3.29.

Figure 3.29: Optical microscope picture of the FPA pixels after UBM deposition.

ROIC (Indigo, ISC9806) pads were also deposited with UBM. ROIC pads are aluminium, which forms a native thin oxide layer on the surface. Before metal deposition, oxide layer was removed with a diluted HF solution. Magnified picture of a ROIC after UBM deposition is given in Figure 3.30.

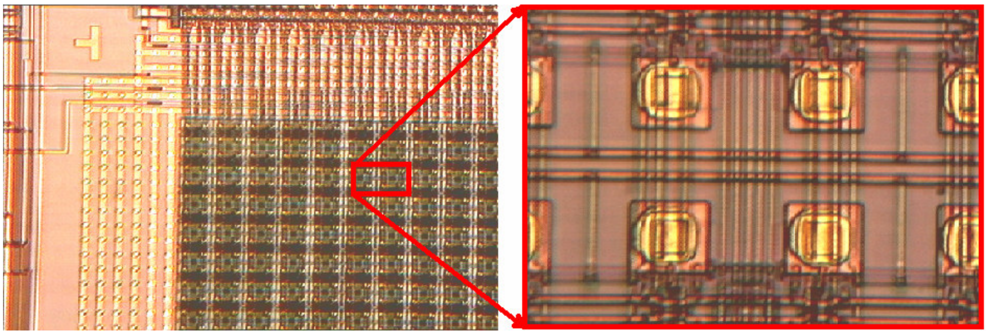

Figure 3.30: A snapshot from ROIC and magnified pictures of the pads after UBM deposition.

3.4.1.4 Indium electro-plating and reflow

ROIC and the detector FPA were coupled by flip-chip bonding technique. Indium was used as the interconnect material between FPA pixels and ROIC pads. Indium bumps were formed on detector pixels by electro-plating method. Subsequently, bumps were reflowed by heating the FPA to temperatures above the melting point of the indium in a non-oxidizing atmosphere. This process improves the adhesion between the UBM and indium. Figure 3.31 gives the optical microscope and SEM pictures of the bumps formed on detector mesas.

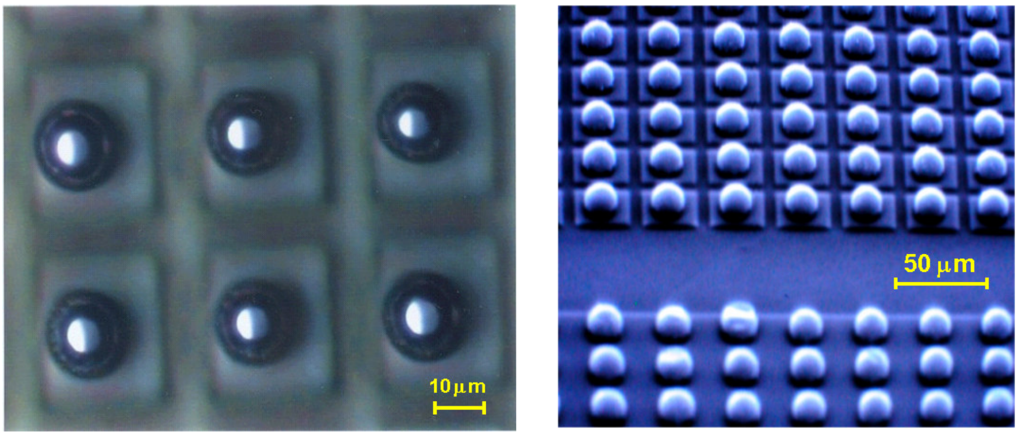

(a) (b)

Figure 3.31: (a) Optical microscope and (b) SEM pictures of indium bumps formed on mesas.

3.4.1.5 Flip-chip Bonding

The FPA was coupled to the ROIC using RD Automation M8-AN model flip-chip aligner and bonder, which has 0.5 μm X-Y direction, 5 arcsec rotational, and 0.1 mrad planarity resolutions. It uses an optical probe to display both dies on the monitor at the same time. Figure 3.32 gives a picture of the flip-chip bonder and illustration of the cross sectional view of the FPA-ROIC assembly after flip-chip bonding.

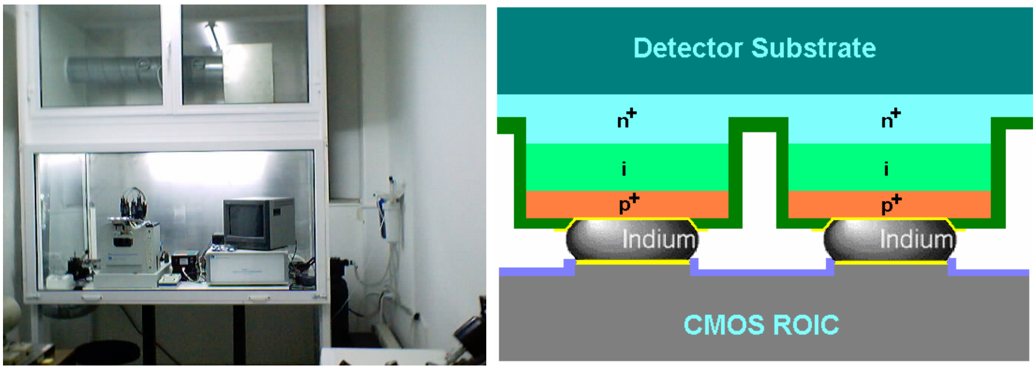

(a) (b)

Figure 3.32: (a) RD Automation M8-AN model flip-chip aligner bonder installed in the laboratory, and (b) Illustration of the cross section of FPA-ROIC assembly after flip-chip bonding.

3.4.2 Real Time Thermal Imaging

Following the flip-chip bonding step, FPA-ROIC assembly was mounted on an 84-pin LCC package with a thermally conductive epoxy, and LCC package was installed into Indigo Systems' ISC9801 Standard 128 evaluation camera. Snapshots from the FPA-ROIC assembly and a picture of the thermal imager are shown in Figure 3.33. The evaluation imager consists of electronic modules, which provide the bias voltages and clock signals to the ROIC, and generate NTSC and digital video outputs. The imager has a liquid nitrogen cooled dewar, and a 3-5 μm Ge lens with 50 mm focal length and 5.5° field of view. Additionally, it can perform 12-bit analog-to-digital conversion, 8-bit one or two point calibration, and defective pixel replacement. The storage capacity of the ROIC is 3.5×10^{7} electrons, and its readout noise is smaller than 400 electrons.

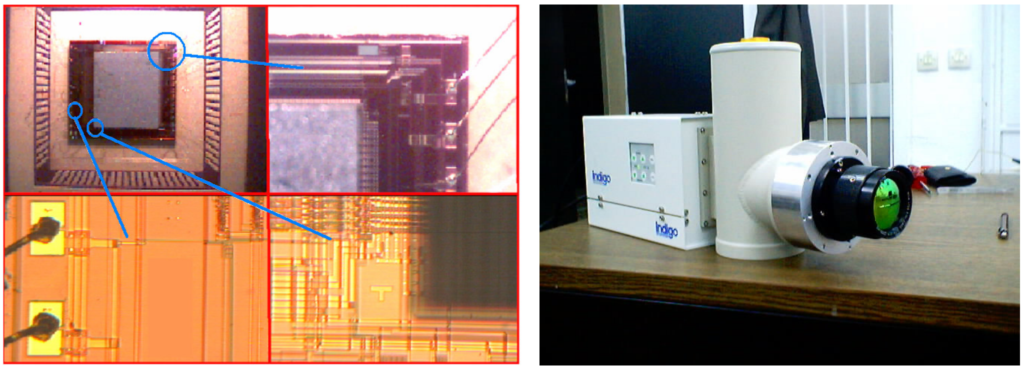

(a) (b)

Figure 3.33: (a) Snapshots from FPA-ROIC assembly after mounting on an LCC package and (b) picture of the evaluation camera used for real-time imaging.

The real-time images taken with 128×128, AlInSb/InSb/Si and $InAs_{0.8}Sb_{0.2}$/GaAs FPAs are given in Figure 3.34 and 3.35. The dark current density of the homo-epitaxially grown InSb detectors ($\sim1\times10^{-7}$ A/cm^{2}) [33] is much lower than those observed in our hetero-epitaxially grown photodetectors (1.9×10^{-3} A/cm^{2} for AlInSb/InSb/Si structure) under the same reverse bias voltages (0.01 V). Due to the large dark current of the pixels, room temperature objects cannot be recognized with these FPAs, and only hot objects can be detected. While the peak detectivities of the detectors discussed in this chapter ($\sim1\times10^{10}$ cmHz$^{1/2}$/W) are only an order of magnitude lower than the detectivity of homo-epitaxially grown InSb detectors ($\sim1\times10^{11}$ cmHz$^{1/2}$/W), significantly worse FPA performance can also be attributed to very low integration times used to prevent the ROIC capacitors from saturation. The integration time of the state of the art InSb FPAs, which were discussed in Chapter II, are around 4 ms. The sensitivity of the FPA changes with the square root of the integration time when the noise equivalent temperature difference (NETD) is limited by pixel detectivity. The real-time images shown in Figure 3.34 were taken with sub-millisecond integration times. $InAs_{0.8}Sb_{0.2}$/GaAs FPA shows lower thermal imaging performance when compared with AlInSb/InSb/Si FPA, in spite of the larger detectivity of the former. This behavior can also be explained by the excess detector dark current. R_0A product of $InAs_{0.8}Sb_{0.2}/GaAs$ structure (~0.5 $\Omega\times cm^2$) is lower than that of AlInSb/InSb/Si structure (~2.3 $\Omega\times cm^2$) at 80K.

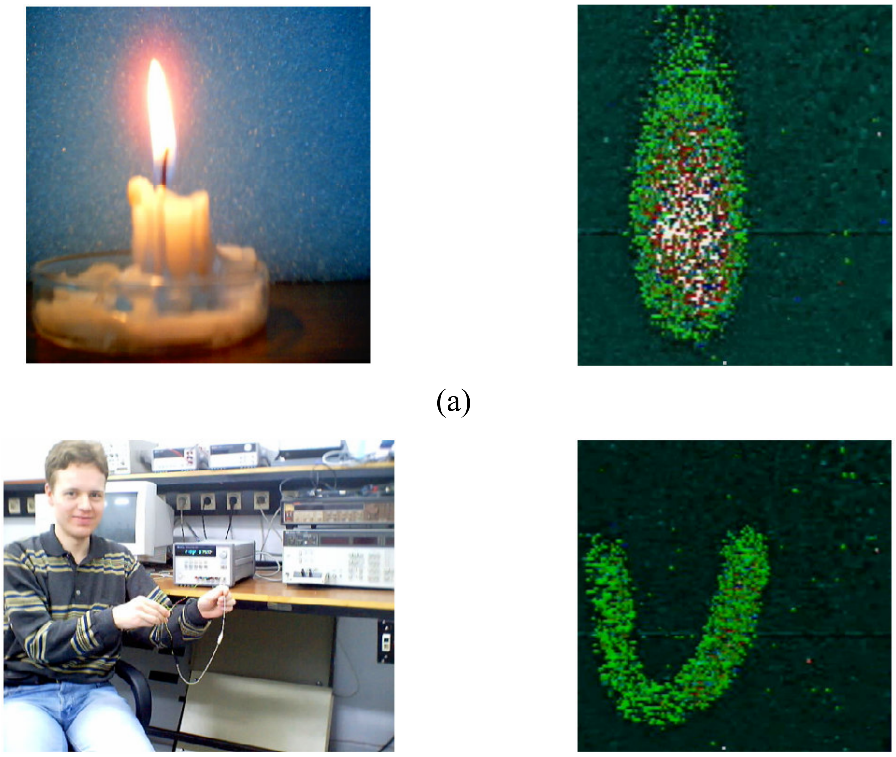

(a)

(b)

Figure 3.34: Infrared images (on the right side) obtained with 128×128 AlInSb/InSb/Si FPA: (a) candle light and (b) wire heated by electric current. Visible images are also shown on the left side.

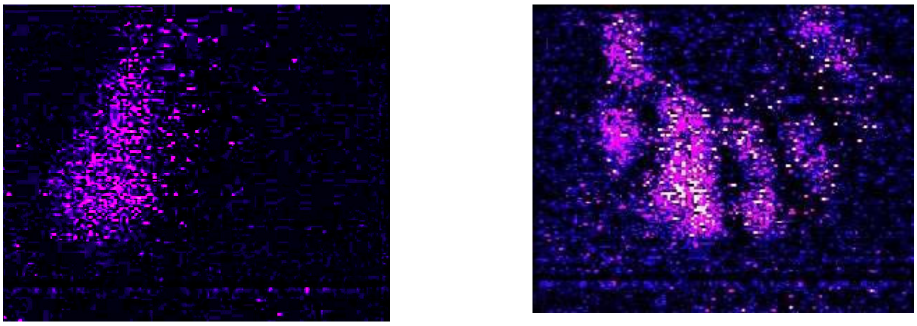

(a) (b)

Figure 3.35: Images taken with 128×128 $InAs_{0.8}Sb_{0.2}$ FPA: (a) candle light and (b) human hand in front of a hot plate.

It should be noted that the photodetectors investigated in this study were not optimized in terms of the material growth conditions, the detector layer structure and antireflection coating. If the detector dark current can significantly be decreased by optimizing the growth parameters, and making use of appropriate buffer layers, the photodetector performance can approach to a level near to that of the state of the art InSb FPAs on lattice matched substrates. The results presented in this chapter provide invaluable background information for such a further study.

3.5 Summary and Conclusions

Hetero-epitaxial growth of InSb or $InAs_xSb_{1-x}$ on Si or GaAs substrates yields many advantages like availability of large area high-quality substrates, possibility of monolithic integration with Si or GaAs ROIC, elimination of the substrate thinning process, and the problems related with thermal expansion coefficient mismatch. This chapter has reported the results of a detailed characterization study performed on $InAs_{0.8}Sb_{0.2}$/GaAs and InSb/Si homojunction, and AlInSb/InSb/Si heterojunction test photodiodes as a preliminary assessment of the feasibility of this approach. While facilitating this assessment, this study also yielded invaluable scientific information on the performance limiting dark current and noise mechanisms in lattice mismatched infrared photodetectors.

Following the fabrication of the test detectors, I-V characteristics of these detectors were investigated by fitting the sum of the expressions for the photodiode current components to experimental data over a sufficiently large voltage and temperature range in order to find the dominant dark current generation mechanisms. The detector noise was also investigated to understand the dependence of the 1/f noise on the current mechanisms by fitting the theoretical models to noise data. Development of the 128×128 FPA fabrication process was followed by FPA fabrication, and testing the FPAs in a real-time thermal imager. Table 3.1 summarizes the main characterization results of the studied structures.

Table 3.1: Main characterization results of the photodetectors.

Structure	$InAs_{0.8}Sb_{0.2}$/GaAs	InSb/Si	AlInSb/InSb/Si
Detectivity ($cmHz^{1/2}/W$)	1.4×10^{10}	1×10^{10}	7×10^{9}
Zero bias limiting mechanism at 80 K	TAT	Ohmic leakage	Ohmic leakage
Cut-off wavelength (λ_c) (μm)	4.7	5.5	5.5
R_0A product ($\Omega\times cm^2$)	0.5	1.1	2.3
Dark current density at 10 mV (A/cm^2)	2.5×10^{-2}	1.36×10^{-2}	2×10^{-3}

The following important conclusions can be drawn from this study:

- The electrical and optical characterization results of $InAs_{0.8}Sb_{0.2}$/GaAs photodiodes show that the alloy is promising for both cooled and near room temperature detectors. The detectors yield reasonably high detectivity, and surface mechanisms do not significantly contribute to the dark current of $InAs_{0.8}Sb_{0.2}$/GaAs detectors under small reverse bias voltages commonly employed in thermal imaging.

- Under low and medium reverse bias, low temperature R_0A limiting mechanism in $InAs_{0.8}Sb_{0.2}$/GaAs photodiodes is trap assisted tunneling, which introduces a considerable $1/f$ noise to the detector current. This observation is similar to that of Nemirovsky *et. al.* [115] on the HgCdTe diodes. The traps participating in the TAT process in $InAs_{0.8}Sb_{0.2}$/GaAs photodiodes may be related with the defects arising from the large lattice mismatch between the alloy and GaAs.

- 80 K zero bias differential resistance of the InSb/Si detectors is limited by Ohmic leakage, and the TAT process becomes dominant as the detector reverse bias approaches 0.1 V. The shunt resistance associated with the Ohmic leakage shows a small activation energy of 25 meV. Earlier experiments on HgCdTe showed that the dislocations degrade the dynamic resistance of the diode by increasing the g–r current, in which case R_0A scales in inverse proportion to the intrinsic carrier concentration, and the dynamic resistance can considerably be improved using larger bandgap (smaller n_i) materials [109]. Based on our observations, the temperature dependence of the Ohmic leakage does not reflect a change in proportion to that of the intrinsic carrier concentration. Therefore, hetero-epitaxial growth of alternative larger bandgap materials (such as $InAs_xSb_{1-x}$ instead of InSb) may not improve detector R_0A as significantly as expected, if the detector performance is limited by the shunt resistance.

- At 80 K, 1/*f* noise of the reverse biased InSb/Si detectors is dominated by TAT mechanism. Measured 80 K 1/*f* noise current (at 1 Hz) is in agreement with the emprical model $i_{n\mathrm{TAT}} = \alpha I^{\beta}_{TAT}$ with α and β close to those found by Nemirovsky and Unikovsky [114] for HgCdTe photodiodes, supporting their observations.

- Detailed noise characterization and modeling study on InSb/Si photodetectors showed that the bias and temperature dependence of the 1/*f* noise current is in reasonable agreement with Kleinpenning's mobility fluctuation model [120] confirming the validity of this approach.

- Near zero-bias, InSb/Si detectors yield a detectivity almost within an order of magnitude of the typical InSb photodetector detectivity achieved on lattice matched substrate. The defects do not seem to degrade the InSb/Si detector's peak quantum efficiency considerably, however they significantly increase the 1/*f* noise under moderate and large reverse bias.

- AlInSb/InSb/Si heterojunction diode displays an 80 K R_0A product of ~2.3 $\Omega\times cm^2$, which is slightly larger than that of InSb/Si homojunction photodiode (~1 $\Omega\times cm^2$) due to lower shunt leakage, whose temperature dependence was found to be weak. However, the relative decrease in R_D with reverse bias voltage in AlInSb/InSb/Si detector is much faster than that of homojunction InSb/Si detector, which can be explained by higher trap density (N_t) in the heterojunction detector. The photoresponse of the AlInSb/InSb/Si detector also degrades more rapidly with decreasing wavelength. This can be attributed to the higher density of recombination centers close to the substrate where majority of the high-energy photons is absorbed. Together with the suppressed optical generation in the larger bandgap AlInSb layer, these recombination centers must be responsible for lower peak quantum efficiency of the AlInSb/InSb/Si detectors.

- Although, the detectivity of the AlInSb/InSb/Si detectors employed in this study is almost within an order of magnitude of homo-epitaxially grown InSb detectors, their dark current is significantly larger limiting the integration time. Therefore, only hot objects were detectable with our unoptimized 128×128 AlInSb/InSb/Si FPA.

The results given in this chapter can be used as a guide for optimizing the performance of InSb or $InAs_xSb_{1-x}$ photodetectors grown on GaAs or Si substrates. Defect related non-fundamental performance degrading mechanisms should be minimized to improve the sensitivity of the FPAs. Although, high-quality epitaxial growth is the bottleneck of narrow bandgap photodetectors, it is relatively insignificant in QWIP technology because of the more stable large bandgap semiconductor materials used. However, QWIP technology has also some limitations, such as lower optical absorption efficiency. Design considerations in QWIP technology differ from those of the low bandgap photodetector technologies. We will discuss these considerations, as well as the factors affecting the QWIP FPA performance in the following chapter before presenting the results of our work on QWIPs.

CHAPTER IV

DESIGN CONSIDERATIONS for QWIP FPAs

For the production of optimal QWIP FPAs, there are several parameters that must be taken into account. These parameters must be optimized according to the desired application, operating conditions, and the components of imaging system other than the detector FPA (like read-out electronics, optics, etc.). This chapter presents the detailed design considerations for QWIP FPAs, and is divided into three parts. In the first part of the chapter, issues related to the single detector performance will be given. Although pixel performance strongly affects the overall FPA performance, spatial considerations like uniformity must also be taken into account, and this issue will be discussed in the second part of the chapter. Finally, in the third part, commonly employed readout approaches will be presented in terms of their efficiencies.

4.1 Single Pixel Considerations

In order to achieve high-quality imaging, performance of individual pixels in the FPA should be optimized. In the following subsections, factors affecting the QWIP pixel performance, and the dependence of these factors on design parameters will be discussed.

4.1.1 Dark Current in QWIPs

Understanding the dark current mechanisms in QWIPs is necessary, because dark current sets the operation temperature of the device. First of all, when the dark current is large, it determines the detector noise, which should be minimized. Additionally, it fills the read-out integration capacitors with “useless” electrons, which limits the capacity for “useful” photoelectrons. Dark current can be reduced by decreasing the operating temperature. However, this increases the cooling requirements, which increases the system cost and decreases the cooler lifetime. Therefore, dark current should be minimized at the desired operating temperature.

Electron transport in continuum states and capture-emission processes in the quantum wells determine the dark current through the device. Emission and capture processes are illustrated in Figure 4.1. Under electric field, continuum electrons drift and generate the dark current. Dark current density generated by the drift of the continuum electrons, is labeled as J_{3D} in the figure. Thermal excitation promotes 2-D electrons in the ground states to continuum states, and the excited electrons leave empty states in the quantum well. When the steady state is reached, electron density in the well is kept constant through the balance between emission and capture. Probability of a continuum electron to be captured into a quantum well is defined as capture probability (p_c).

The typical dark current versus bias voltage characteristic of an AlGaAs/GaAs QWIP is given in Figure 4.2. Although QWIP is a symmetric unipolar device, there is an asymmetry in I-V characteristic. This is attributed to the migration of dopants in the growth direction [123], which lowers the barrier height on the surface side of the quantum well. The resultant asymmetry in the conduction band discontinuities enhances the escape probability of the thermally excited electrons under positive bias.

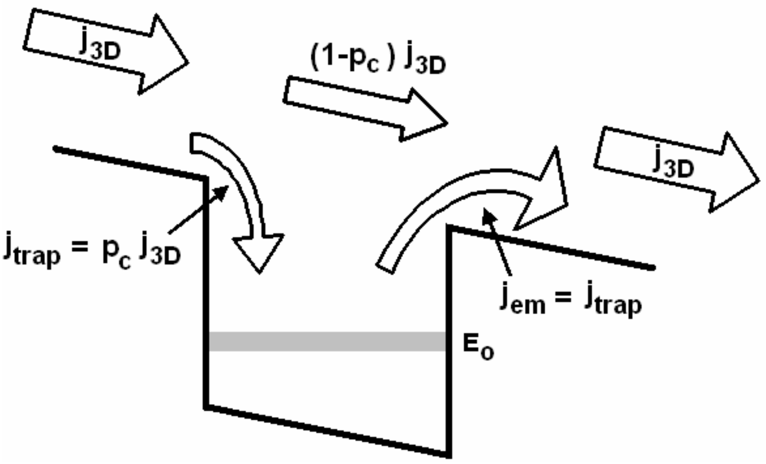

Figure 4.1: Illustration of capture and emission processes in QWIP.

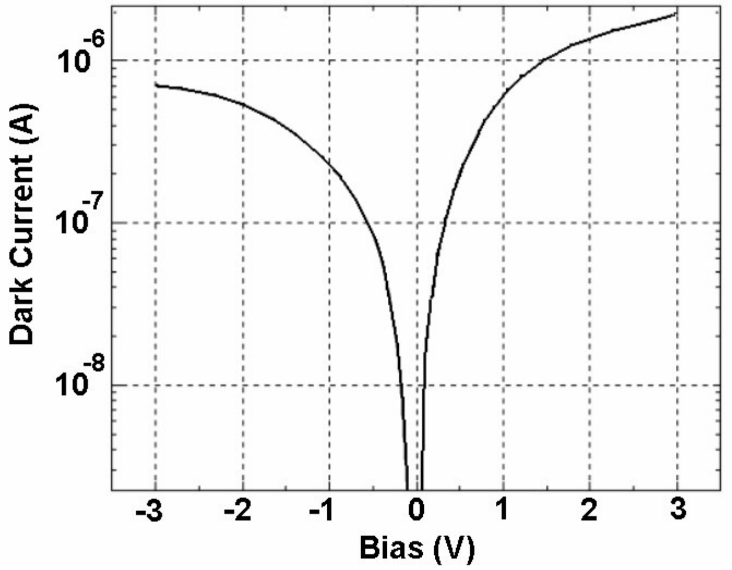

Figure 4.2: I-V characteristic of a typical AlGaAs/GaAs QWIP under dark conditions.

Dark current can be expressed as

$$I_D(V) = q \times n(V) \times v(V) \times A \tag{4.1}$$

where q is electron charge, n is density of 3-D (continuum) electrons, v is drift velocity of electrons, and A is detector area. The density of 3-D electrons, which are thermally excited from the bound state to the continuum, can be given as [18]

$$n(V) = \left(\frac{m^*}{\pi\eta^2 L_p} \right) \int_{E_0}^{\infty} f(E) T(E,V) dE \tag{4.2}$$

where m^* is electron effective mass, L_p is superlattice period, $f(E)$ is the Fermi factor, E_0 is the ground state, and $T(E,V)$ is the bias-dependent tunneling current transmission factor. Fermi factor is expressed as

$$f(E) = \frac{1}{\left[1 + e^{(E-E_0-E_f)/kT} \right]} \tag{4.3}$$

where E_f is the two dimensional Fermi level. Drift velocity of electrons is a function of electric field, and under low bias voltages, it is linearly dependent to electric field. However, under large biases electron velocity saturates. Field dependent electron velocity can be formulated as

$$v(V) = \mu F \sqrt{1 + \left(\frac{\mu F}{v_s} \right)^2} \tag{4.4}$$

where μ is the mobility, F is the average electric field, and v_s is the saturated electron velocity.

Generally three mechanisms are responsible for dark current: ground state tunneling, thermally assisted tunneling, and thermionic emission. These mechanisms are illustrated in Figure 4.3. Ground-state tunneling is not significant above 45 K [2]. Thermionic emission and thermally assisted tunneling govern the dark current when the temperature is around 70 K where QWIPs are usually operated.

Position of the second subband in a quantum well determines the difference between the energy required for thermionic emission and photoexcitation. In bound-to-continuum QWIPs, second subband energy level is slightly above the barrier energy level, hence thermionic emission requires less energy than photoexcitation. This increases the dark current without any improvements in photocurrent. However, bound-to-quasibound QWIPs maintain the balance between photoexcitation and thermionic emission, and hence reduce the dark current by an order of magnitude [2]. Thermally assisted tunneling may occur via trap levels in the barrier material. In order to minimize this component, high quality barriers should be employed. Al-free binary barriers, like InP alloy, can be used to reduce the thermally assisted tunneling. On the other hand, thermionic emission is an intrinsic mechanism and cannot be avoided.

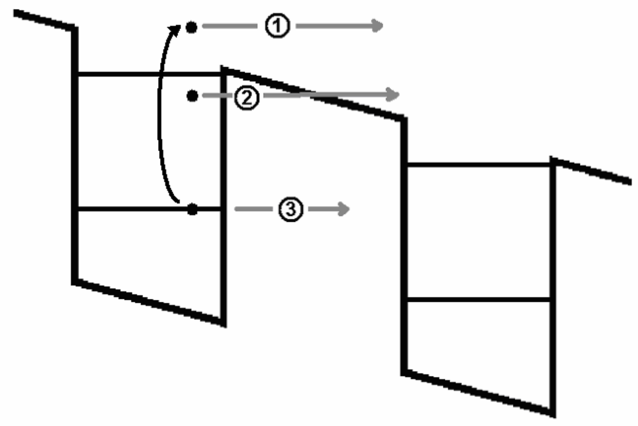

Figure 4.3: Dark current mechanisms illustrated on a quantum well energy band diagram: thermionic emission (1), thermally assisted tunneling (2), and ground state tunneling (3).

Thermionic emission must be taken into account when determining the operation temperature and cut-off wavelength, which strongly affects the dark current. Equation 4.2 can be simplified when QWIP operates under low-bias regime. In this case, when energy (E) is smaller than the barrier energy (E_b), tunneling factor (T(E)) can be assumed to be zero. Further assumptions can be made that when $E>E_b$, tunneling factor is one (T(E)=1). Under these assumptions, 3-D electron density can be reformulated as

$$n^* = (m^* kT / \pi\hbar^2 L_p) e^{-(E_c - E_f)/kT} \tag{4.5}$$

where spectral cutoff energy is defined as $E_c = E_b - E_1$. Therefore,

$$I_d / T \; \alpha \; e^{-(E_c - E_f)/kT} \tag{4.6}$$

Relation 4.6 formulates dependency of dark current on both temperature and cutoff wavelength. The expression indicates that the dark current is a strong function of temperature and cut-off wavelength.

4.1.2 Photocurrent in QWIPs

Following the absorption of infrared photons, photoexcited electrons leave empty states in the quantum wells, which must be filled by extra injection from the emitter contact. This extra injection is identified as the photocurrent. Photocurrent in a QWIP can be given as

$$i_p = qF\eta g \tag{4.7}$$

where q is charge of electron, F is the incident photon rate (1/s), and η is the quantum efficiency. Quantum efficiency is expressed as

$$\eta = N_W \eta_1 \tag{4.8}$$

where N_W is the total number of quantum wells, and η_1 is the single well quantum efficiency. In Equation 4.7, g is the photoconductive gain and can be given as

$$g \equiv \frac{p_e}{N_W p_c} \tag{4.9}$$

where p_e and p_c are emission and capture probabilities, respectively. Incident photon rate is expressed as

$$F = \Phi_B \Omega A_{\mathrm{det}} \tag{4.10}$$

where Φ_B (1/cm×sr×s) is the incident photon flux emitted by a target, Ω is the solid angle subtended by the target, and A_{det} is the QWIP area.

Photoconductive gain is due to the extra injection from the emitter contact to compensate the photoexcited electrons from the wells. Since only a fraction of injected electrons coming from the emitter contact is captured into the wells, amount of injection must be sufficient for compensation. If absorption efficiency (η) is proportional to N_W, photocurrent is independent of N_W because g is inversely proportional to N_W.

For bound-to-continuum transitions, p_e is approximately equal to one, since once an electron is excited, it is already in continuum. In this case, the photoconductive gain becomes

$$g \equiv \frac{1}{N_W p_c} \tag{4.11}$$

On the other hand, for bound-to-bound case, it takes some time for the escape of the electron after photoexcitation, which makes escape probability noticeably lower than one. This results in the reduction of photoconductive gain. On the other hand, in this case, η increases due to the increase in the oscillator strength.

Photocurrent of a QWIP must be maximized, which can be done by either maximizing the absorption quantum efficiency (η) or photoconductive gain (g). While the absorption quantum efficiency of QWIPs is much lower than the intrinsic photodetectors like InSb and HgCdTe, it can be improved by optimizing the optical coupling structure. Photoconductive gain can be improved by the reduction of capture probability, which can be done by increasing the bias. Under large electric fields, electrons gain energy, and capture probability drops. This results in increased photoconductive gain. On the other hand, dark current also increases with bias voltage, resulting in no net gain in total system performance.

Photoconductive gain can also be given by [18]

$$g = \frac{v\tau_L}{l} \tag{4.12}$$

where v is electron drift velocity, τ_L is is electron lifetime, and l is device length (multiquantum well region). The above expression indicates that the photoconductive gain depends strongly on the barrier transport. Some material systems, yield better transport properties like higher mobility and lifetime, which increase the photoconductive gain.

4.1.3 Absorption Spectrum of QWIPs

Energy difference between the ground state and excited state determines the peak absorption wavelength of the QWIP. Peak absorption wavelength (λ_p) is equal to

$$\lambda_p = \frac{2\pi\hbar c}{E_m - E_1} \tag{4.13}$$

where E_1 is the ground state energy level, and E_m is the final state energy level. In bound-to-continuum (B-C) excitation, transition energy is not determined by the available final states but by the oscillator strength of each state in continuum. The difference between the ground state energy and the final state energy (E_m) at which the absorption is maximum corresponds to λ_p. This is not the case for bound-to-bound transitions where final state is the second resonant state (E_2) below the barriers. For B-C transition case, values of E_1 and E_m for different aluminium (Al) mole fractions (x) and well widths are given in Figure 4.4 [124]. The figure also shows the dependence of the peak absorption wavelength on well width and aluminium mole fraction.

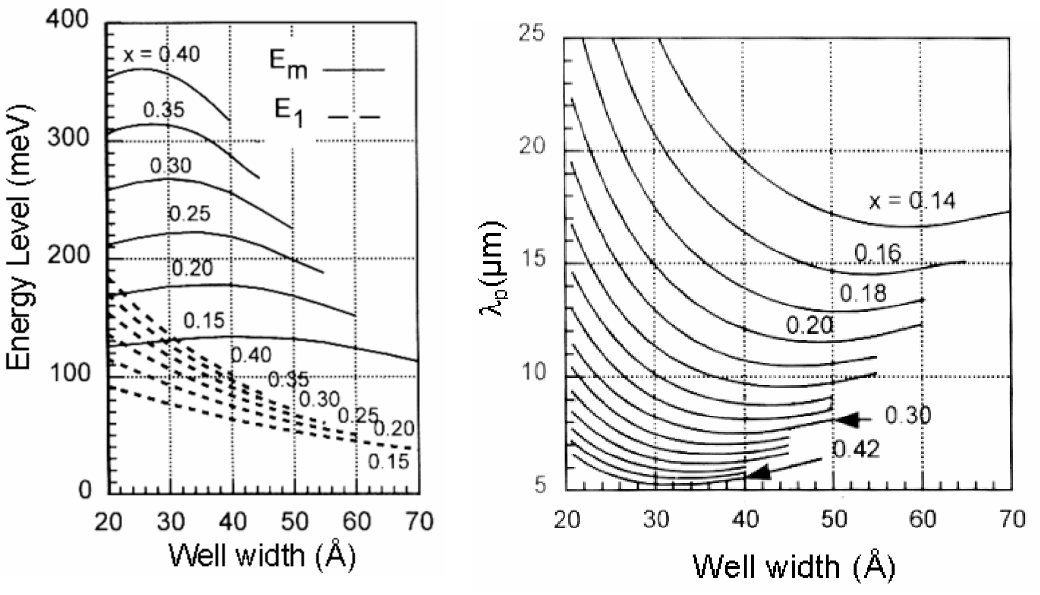

(a) (b)

Figure 4.4: Dependence of the (a) quantum well energy states, and (b) peak absorption wavelength on aluminium mole fraction and well width [124].

For bound-to-quasi bound transition case, E_2 is aligned with the barrier height. Figure 4.5 shows the dependence of peak absorption wavelength on well width. The figure also shows subband energy levels in terms of Al mole fraction and well width. For instance, for $\lambda_p = 9$ µm, well width is equal to 52 Å and Al mole fraction is 0.28.

H.C. Liu investigated the dependence of the absorption spectrum on the upper state position in QWIPs analytically [125]. He also verified his results with the experimental data published in the literature. The calculated absorption spectra of $Al_{0.33}Ga_{0.67}As$/GaAs material system with well widths varied from 35 Å to 65 Å in 3 Å steps is given in Figure 4.6. According to his theory, when the well width is increased, upper state position is pushed below the barrier level, and absorption spectrum becomes narrower in line shape. Additionally, no abrupt change in absorption spectra occurs when the transition crosses from pure B-C case (Lw < 47 A) to B-B case (Lw > 50 Å).

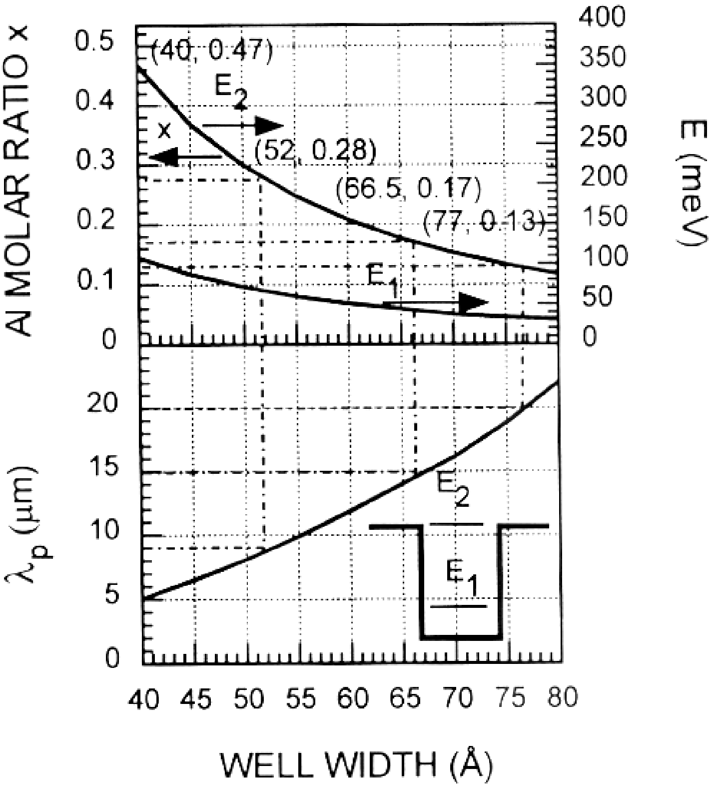

Figure 4.5: Dependence of peak absorption wavelength on well width and aluminium mole fraction for bound-to-quasi bound transition [124].

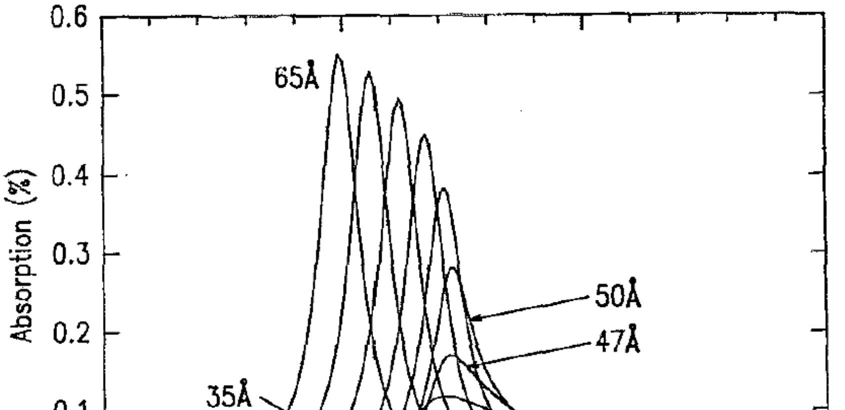

Figure 4.6: One-well absorption spectra in terms of photon energy. Well width is changed from 35 Å to 65 Å in 3 Å steps, and in calculations, $Al_{0.33}Ga_{0.67}As/GaAs$ material system parameters are used [125].

4.1.4 Responsivity of QWIPs

Absolute peak responsivity of a QWIP can be written as

$$R_p = \frac{e}{h\nu}\eta g \tag{4.14}$$

where e is electronic charge, h is the Planck's constant, ν is the frequency of photon, η is the quantum efficiency, and g is the photoconductive gain. In standard AlGaAs/GaAs QWIPs, the photoconductive gain varies from 0.2 to larger than 1. Additionally, conversion efficiency, which is defined as ηg, is typically below 10% at the maximum response. However, as discussed previously, the conversion efficiency can be improved by utilization of optimized optical coupling structures and alternative material systems.

Experimentally measured responsivity versus bias voltage curves for bound-to-bound, bound-to-quasi-bound, and bound-to-continuum QWIPs are shown in Figure 4.7 [18]. Responsivity increases linearly with bias, and saturates at high bias voltages, which is attributed to the saturation of drift velocity. For bound-to-bound sample, responsivity starts to rise at a finite bias. In this case, a sufficiently large electric field is required for the escape of photoexcited electron from the well, and finite bias is necessary to create this field.

Gunapala *et. al.* investigated the dependence of responsivity on quantum well doping and bias voltages [126]. They found that R_p is proportional to $N_D(\lambda/\Delta\lambda)$. Responsivity measurements on three samples with the quantum well doping densities of 4.7×10^{16} cm^{-3}, 1.2×10^{17} cm^{-3}, and 1.5×10^{18} cm^{-3} verified this relation. These observations suggest that doping level of the quantum wells can be increased to improve the responsivity. On the other hand, this would also increase the dark current by leading to more thermal excitation. The doping density should be optimized considering these opposing effects. More issues on the dependence of detector performance on doping density will be discussed in the following sections.

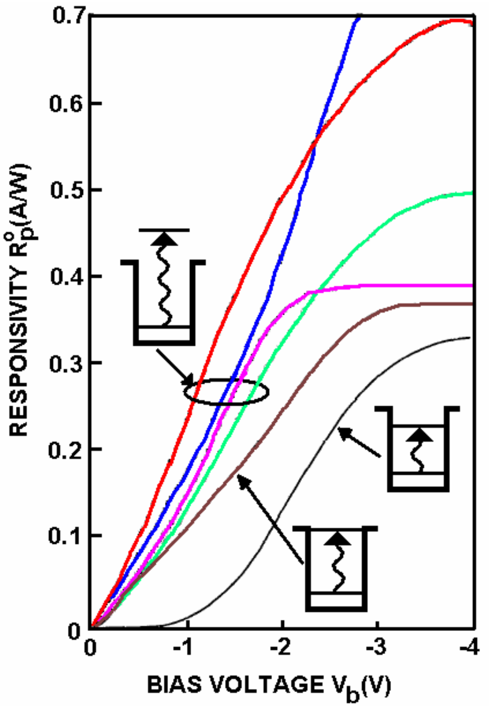

Figure 4.7: Peak responsivity versus bias curves for different QWIP types: bound-to-continuum QWIP (red, blue, violet, green), bound-to-quasi-bound (brown), bound-to-bound (black) [18].

4.1.5 Noise in QWIPs

In high performance QWIPs, signal-to-noise ratio must be as high as possible. The significant noise sources for QWIPs can be counted as Johnson noise, dark current noise, photon noise, and read-out (switch) noise. Although 1/f noise is frequently pronounced for photodiodes, for GaAs QWIPs, experimental observations show that it is not the dominant one.

Johnson noise can be given by

$$i_{n,J}^2 = \frac{4kT}{R}\Delta f \tag{4.15}$$

where Δf is the measurement bandwidth, and R is the device differential resistance. Johnson noise in a QWIP at specific bias voltage can be easily calculated from current versus bias voltage characteristics. Johnson noise is not critical when compared with dark current noise and photon noise, especially, when the bias voltage is larger than kT/qg [127, 128].

Dark current noise is due to the escape and trapping mechanisms. These mechanisms are analogous to generation-recombination (g-r) processes, and hence dark current noise is similar to g-r noise physically. Indeed, the dark current noise is often called as g-r noise in the literature, and given by

$$i_{n,dark}^2 = 4eg_n I_d \Delta f \tag{4.16}$$

where g_n is the noise gain, and I_d is the device dark current. Since g-r noise and Johnson noise are statistically independent, under dark conditions total QWIP noise current can be given by

$$i_n^2 = i_{n,J}^2 + i_{n,dark}^2 \tag{4.17}$$

At a finite applied bias and under dark conditions, g-r noise constitutes almost the entire QWIP noise. Therefore, assuming that photoconductive and noise gains are equal under moderately large bias voltages [2], photoconductive gain can be determined by the following equation:

$$g_p = \frac{i_{n,dark}^2}{4eI_d \Delta f} \tag{4.18}$$

Photon noise is associated with the photocurrent generated by background photons. Fluctuation in photon arrival rate is the source of this noise. For photoconductors, photon noise current is given by

$$i_{n,B}^2 = 4e^2 g_p^2 \Phi_B \Delta f \tag{4.19}$$

where Φ_B is the number of background photons absorbed by the detector, and g_p is photoconductive gain. When Equations 4.16 and 4.19 are compared, it is seen that g-r noise is proportional to the square root of the noise gain, while photon noise current is directly proportional to photoconductive gain.

Finally, the read-out (switch) noise is given by

$$v_{n,rms}^2 = \left(\frac{kT}{C} \right) \tag{4.20}$$

where C is the combined integration and bus capacitance. Switch noise also becomes insignificant for bias voltage larger than $v_{n,rms}$ [128].

Dark current is a strong function of temperature, and at high temperatures, dark current noise limits the performance of the QWIP. On the other hand, at low temperatures, photon noise is the limiting mechanism, in which case the detector is called to show background limited performance (BLIP). BLIP temperature (T_{BLIP}) defines the transition point where dark current noise is equal to the photon noise. Operation temperature of a detector sets the cooling requirements, and should be as high as possible. Lower BLIP temperatures of the QWIP technology is an important drawback against the HgCdTe technology. Therefore, achieving higher BLIP temperatures is necessary for the success of QWIP technology in the future. In order to increase T_{BLIP}, generation/quantum efficiency ratio must be minimized. As discussed previously, this ratio can be decreased by utilizing efficient optical coupling schemes like corrugated structures.

4.1.6 Effect of Number of Quantum Wells on the QWIP Performance

The number of quantum wells (N_w) is the design parameter that can be changed most easily. It is clear that increasing N_w increases the absorption strength. On the other hand, increasing the device width decreases the photoconductive gain (see Equation 4.12), which results in a reduction in the photocurrent. As the result, overall performance is not obvious due to these two conflicting processes. Steele *et. al.* investigated the effect of number of wells on the absorption and responsivity performance of QWIPs systematically [129]. In their experiments, they studied performances of several bound-to-quasi-bound QWIP samples with 4, 8, 16, and 32 wells. Their measurements showed that absorption varies linearly with N_w. Additionally, maximum current response is the same for samples with different well numbers, and occurs under the same electric fields. This observation coincides with the predictions explained in Section 4.1.2. They also observed that the line shapes of spectral current responsivity also do not depend on N_w. When photoconductive gain is extracted from the measured data, it was shown that photoconductive gain is inversely proportional to the number of quantum wells. It is concluded from these observations that increasing the number of wells does not affect the responsivity of the QWIPs.

4.1.7 Detectivity of Quantum Well Infrared Photodetectors

Detectivity is defined as the signal-to-noise ratio of a detector normalized to unit area and operating bandwidth of the detector, and the peak detectivity is given by

$$D^* = \frac{R_p\sqrt{A\Delta f}}{i_n} \tag{4.21}$$

where A is the detector area, and Δf is the operating bandwidth. When g-r noise limits the operation of the QWIP, detectivity can be approximated by [18]

$$D^* = \left(\frac{\eta_a p_e}{2h\nu}\right)\left(\frac{\tau_L}{n^* l}\right) \tag{4.22}$$

where τ_L is the lifetime of excited electrons, n^* is the number of excited electrons above the wells, l is the length of the active multiquantum-well region, and η_a is the absorption quantum efficiency. On the other hand, when QWIP operates in the BLIP regime, the detectivity becomes [18]

$$D^*_{BLIP} = \frac{1}{2}\left(\frac{\eta}{h\nu I_B}\right)^{1/2} \tag{4.23}$$

where I_B is the intensity of background radiation, and $\eta = \eta_a p_e$ is the net quantum efficiency. From the above expressions, the following conclusions can be drawn:

- When the detectivity is limited by g-r noise, η_a, p_e, τ_L should be large, and n^* should be low,
- When the detectivity is limited by the background radiation, net quantum efficiency $\eta = \eta_a p_e$ should be large.

Figure 4.8 illustrates the dependence of the detectivity on operation temperature. When the temperature is lower than the BLIP temperature (T_{BLIP}), detectivity is limited by the photocurrent generated by the background radiation. As the temperature is increased above T_{BLIP}, dark current increases exponentially resulting in large noise and lower detectivity. In this case, the detectivity is limited by the g-r noise. T_{BLIP} must be as high as possible to facilitate the use of smaller, low power, and long lifetime Stirling coolers.

As mentioned previously, both responsivity and thermal generation increases with quantum well doping density, therefore, the effect of doping density on detector performance is not clear due to these conflicting processes. The relation between the detectivity and doping density is given by [126]

$$D^* \alpha \; \frac{\rho}{\sqrt{e^{\rho} - 1}} \tag{4.24}$$

In the above expression, ρ is normalized doping density expressed as

$$\rho = \frac{N_D}{n_0} \tag{4.25}$$

where N_D is the doping density, and n_0 is given by

$$n_0 \equiv \left(\frac{m^* kT}{\pi\hbar^2 L_w} \right) \tag{4.26}$$

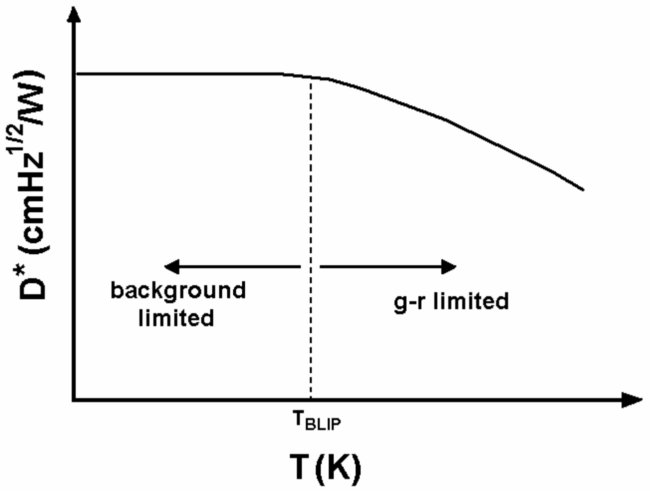

Figure 4.8: Detectivity (D^*) versus operation temperature (T) graph. Detectivity does not change with temperature when the detector operates in background limited regime.

Detectivity is plotted against the normalized doping density in Figure 4.9. The graph shows that the detectivity is maximum for ρ=1.6 (N_D=7.4×10^{17} cm^{-3}). On the other hand, peak detectivity occurs in a broad range, and when the doping density is changed by a factor of 30, from ρ=0.18 (N_D=8.35×10^{16} cm^{-3}) to ρ=5.1 (N_D=2.4×10^{18} cm^{-3}), detectivity changes by a factor of two [126]. Therefore, it can be concluded that detectivity is relatively insensitive to doping variations. This is highly desirable from the system and fabrication point of view, since detectivity will be uniform over a large format 2-D array even when the doping density is not so. As the result, doping nonuniformity should not limit the performance of large format FPAs, since MBE growth provides very uniform doping densities over the wafer (~1%).

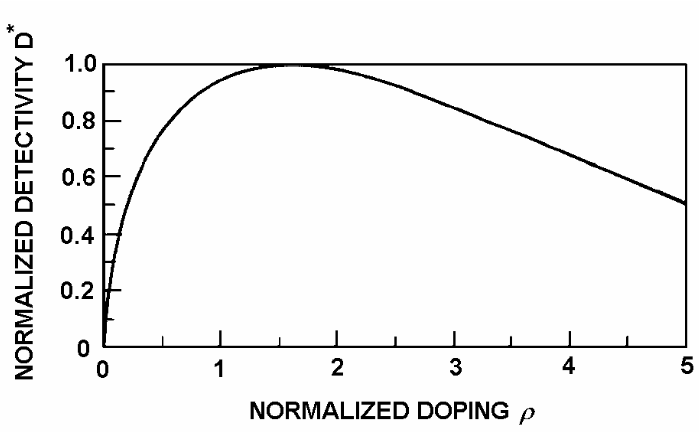

Figure 4.9: Detectivity versus normalized quantum well doping [126].

4.1.8 Optical Coupling in QWIPs

Studies on n-type QWIPs showed that incident radiation must have an electric field polarization component perpendicular to the epilayer planes for intersubband absorption [130]. Therefore, test detector performances have been commonly measured by illumination through a 45° facet. However, it is not possible to adapt this method to 2-D arrays. Consequently, optical coupling schemes, which can easily be implemented on 2-D arrays, are required.

Optical couplers can be classified according to the periodicity of its features: periodic and random gratings. Grating structure can be implemented on either front side or backside of the detector. Additionally, in some cases multi quantum well (MQW) region is also shaped to enhance the optical absorption.

The aim of the optical grating structures is to maximize the coupling efficiency. While improving the quantum efficiency, utilization of reflecting grating structures enhances the pixel-to-pixel optical crosstalk. It was observed by Kozlowski *et. al.* [131] that the amount of cross-talk can be reduced to some extent by substrate thinning.

Periodic gratings must be tuned to the natural absorption wavelength of the quantum wells to obtain the highest efficiency [132]. Otherwise, the grating structure, behaving like a filter, may make the spectral response of the QWIP narrower. In order to match the QWIP spectral response (especially that of broadband QWIP), bi-periodic grating coupler can be used to make grating response wider [132, 133]. Besides, this grating structure might be tuned to two different absorption wavelengths, which is very desirable for the implementation of dual-band QWIPs.

The efficiency of coupling can be increased by forming an optical cavity. This can be done by inserting an epilayer with smaller diffraction index than that of MQW material (for example AlAs for AlGaAs/GaAs QWIP), or by substrate thinning. Illustration of path followed by optical beams incident in normal direction on a detector with a periodic grating structure is shown in Figure 4.10(a) [134]. As shown in the figure, only two passes are possible with periodic gratings. In order to increase the efficiency of the optical cavity, random reflectors were proposed [134, 135]. Random reflectors provide more than double passes of the radiation as shown in Figure 4.10(b). θ_c shown in the figure is the critical angle between the substrate-air interface, and equal to 18° for GaAs. When the angle between the light beam and surface normal is greater than θ_c, beam is reflected back due to total reflection. Additionally, random reflectors are less wavelength selective, therefore they are suitable for broadband detection or dual band / multicolor detection.

Standard periodic and random grating structures are implemented on top of the detector mesas. On the other hand, optical structures that are implemented on the backside of the detector array have also been demonstrated. Cwik *et. al.* proposed the prism-film coupler which was developed earlier in integrated optical circuit technology [136]. They claim that a ten-fold improvement is possible over an optimized grating coupler. However, the implementation of prisms makes the fabrication process too complicated. In another approach, Vgroove gratings are etched on the backside of the wafer with an anisotropic wet etchant solution, and the device is illuminated from the front side [137].

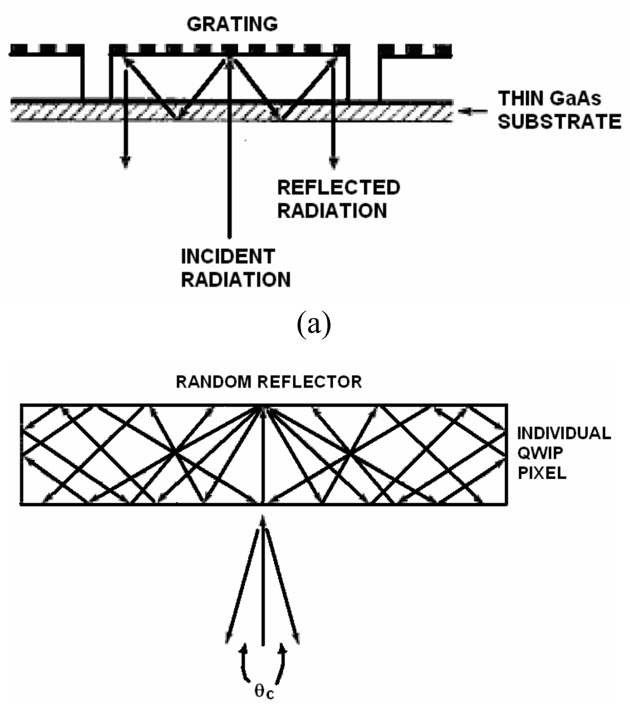

(a)

(b)

Figure 4.10: Illustration of (a) periodic and (b) random grating structures.

Optical coupling structures are also formed by shaping the MQW region. Schimert *et. al.* patterned the MQW region into two-dimensional diffraction grating [138]. The cross-sectional view of the design is shown in Figure 4.11. In this approach, some parts of the active area is removed, resulting in reduced dark current and extended integration time. Bottom side is covered with a reflective metal layer to improve the efficiency of the design.

Corrugated QWIP is also an example to optical coupling structure that is formed by patterning the MQW region [139]. V-grooves are etched through the active MQW layers, and optical coupling is achieved by total reflection of incident light beams from the etched surfaces. Cross-sectional view of a QWIP pixel with corrugated optical coupling structure is illustrated in Figure 4.12. There are several advantages offered by the corrugated pixel approach. First of all, this method eliminates the dependency of the coupling efficiency on wavelength. Besides, pixel pitch does not affect the performance of the structure much. More details on the consequence of pixel size on grating efficiency will be given in the following paragraph. This approach also decreases the dark current due to the reduced active area of the detector. Factor of two reduction in the dark current of test detectors has been reported [139]. With the corrugated structure, detectivity is boosted 2.4 times when compared with that of 45° polished facet test detectors. Choi and coworkers have adopted this structure to large format detector arrays, and they demonstrated FPAs having formats as high as 1K×1K [72]. The NETD and quantum efficiency achieved with this structure were 16 mK and 31%, respectively, after substrate thinning and without anti-reflection coating.

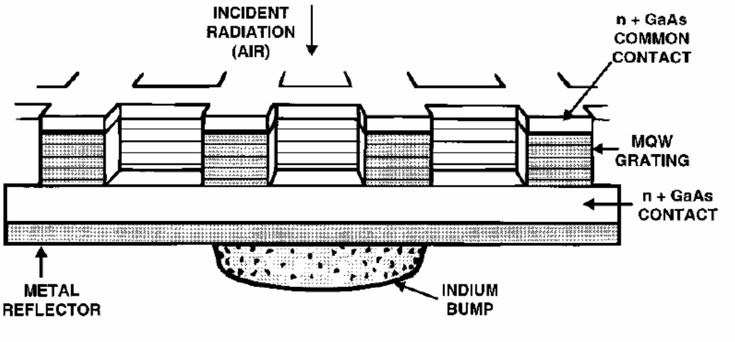

Figure 4.11: Cross-sectional view of QWIP optical coupling structure proposed by Schimert *et. al.* [138].

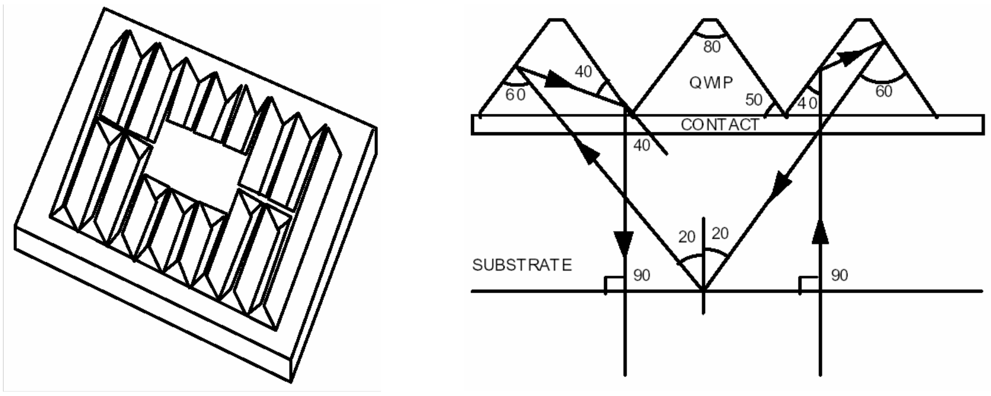

(a) (b)

Figure 4.12: Corrugated QWIP structure: (a) Top view of a mesa, and (b) illustration of path followed by infrared light in the structure [140].

In the literature, most of the grating structures are demonstrated on large area detectors. However, as the size of the pixels is reduced, the efficiency of the grating structures tends to decrease [141-143]. Figure 4.13 shows the responsivity of QWIPs with and without grating structures versus mesa size [142]. When the pixel size is reduced below 100 µm, diffraction from the mesa sidewalls starts to become effective. Additionally, below 20 µm, detectors with and without grating structures start to give similar performances. This decrease in the efficiency of the optical grating is associated with the reduction of number of grating periods, complex interaction between pixel cavity modes, grating modes that might be destructive [143], and escape of electromagnetic radiation by penetrating the mesa edge [141]. These observations prove that grating structures should be studied on small sized detectors.

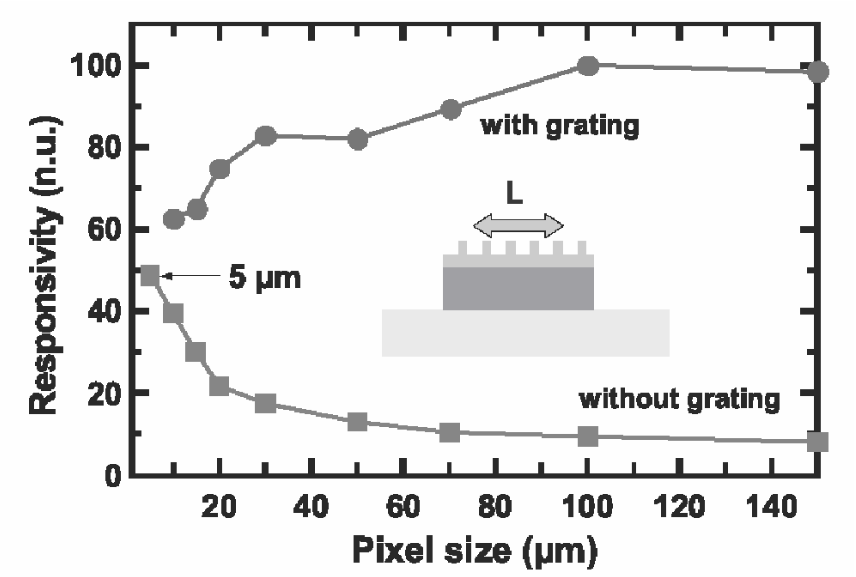

Figure 4.13: Normalized responsivity versus pixel size [142].

Although, intersubband transition is not possible when the radiation is coming in normal direction to n-type QWIPs theoretically, some experimental observations showed the absorption of normal light in detectors without coupling structures. Theoretical investigations of Fu *et. al.* support the observation of significant responsivity in QWIPs with normal incidence and without optical coupling [144]. Their theory indicates that when the surface of the detector is covered with a metal film, oscillations in the optical field at a region very close to the surface generates secondary optical waves. These optical waves have nonzero electric field component in the growth direction leading to significant absorption. They also argue that when the surface is not covered with a metal film, secondary waves are not generated and thus the polarization selection rule is observed as Liu *et. al.* reported [145].

It is claimed that the conductivity of the grating metal, when used, affects the absorption of radiation by metal layer [141]. When metals such as gold, silver, aluminium are used as the grating metal, only 1% - 2% of the incident radiation is absorbed by the metal. On the other hand, if AuGe alloy, which is used for ohmic contact formation, is used as the reflector layer, metal absorption increases by a factor of 3 or more. Additionally, rough surface texture of the AuGe layer results in poor optical coupling. Quantum efficiency of the completely AuGe covered samples is 70% of those covered with pure gold [141]. One way to avoid this reduction in quantum efficiency might be to minimize the area of the ohmic contact region.

4.2 Spatial Considerations

Unlike single pixel or line array scanning systems, pixel-to-pixel uniformity of 2-D FPAs is critical, and most of the time, uniformity is the limiting factor of FPA performance. Previously defined figure of merits for QWIPs are based on the single detectors, but FPA performance cannot be measured by single pixel characterizations. In this section, FPA figures of merit will be discussed.

4.2.1 Nonuniformity

Nonuniformity across a large format FPA affects the image quality and performance of the system significantly. This is true especially when viewing targets having low contrast detail. Due to nonuniformity, information coming from the scene will be modulated, and small temperature differences will disappear. Even when the performance of the single detectors in an FPA is low but FPA uniformity is good, it might be possible to obtain an acceptable overall performance from the FPA. Nonuniformity of an FPA is equal to the ratio of standard deviation of the pixel responses to the average pixel response [2].

Although signal-processing techniques like digital nonuniformity correction reduce the nonuniformity, residual spatial noise after the correction still degrades the FPA performance. Residual spatial noise is limited by the resolution of the analog to digital converter (ADC), for instance, when a 12-bit ADC is used, nonuniformity will be limited to 0.007% [128]. Additionally, efficient nonuniformity correction is not possible for some applications. For example, temperature of the detector in a missile seeker is not stable, and the time for calibration is very limited. Therefore, uniformity constraint across the FPA becomes more severe for missile seekers, when compared with a laboratory camera.

Nonuniformity can also be defined as the variation in the time-averaged output of the detectors across the FPA. Time-average is taken to reduce the contribution of white noise to detector response. On the other hand, spatial noise originates from the residual nonuniformity, and it is observed after correction. Although, it shows itself as a fixed pattern on the image, it changes with time and operating conditions. 1/f noise will result in a variation in the shape of fixed-pattern noise with time. The drift with time restricts the calibration precision and reduces the camera sensitivity. Additionally, noise pattern will also change with spectral distribution and illumination level of the scene.

The spatial noise cannot be estimated from nonuniformity accurately. The noise depends on the linearity of the detector responses over FPA and correction method. While two-point calibration gives good results when detector responses are linear, three-point calibration is better when detectors show parabolic dependence on radiation. On the other hand, detector response can change with radiation level in a more complicated way, which is not easy to correct.

Nonuniformity sources can originate from the detector material, fabrication process, or imager components. Nonuniformity in composition, epilayer thicknesses, and doping density across the wafer introduced during growth degrades the FPA performance. Additionally, nonuniform mesa etch, optical coupling structures, and passivation coating, and misalignments between process steps, which are introduced during fabrication, amplify the FPA nonuniformity. Optical aperture is another source for system nonuniformity. All the detectors on the array do not have the same field of view because of the optical aperture, and center of the FPA receives more radiation than the corners and edges. Moreover, readout circuits increase the system nonuniformity due to the pixel to pixel variations in MOSFET threshold voltages and the detector bias. In general, detector leakage current varies exponentially with temperature. Temperature variations across the FPA result in leakage current variations. Additionally, temperature fluctuations amplify the spatial noise.

There are several measurement methods of the FPA nonuniformity. Either a uniform source is imaged with the camera to measure the nonuniformity in camera response, or a bar pattern with cyclic bars at two different temperatures is viewed. The temperature difference between the bars required for the detection of the pattern gives a degree of the spatial noise. Field evaluations are also possible. On the other hand, they are meaningless unless two different systems are compared simultaneously because of the temporal variations in field conditions.

4.2.2 Noise Equivalent Temperature Difference (NETD) and Minimum Resolvable Temperature Difference (MRTD)

Although it is not feasible to assess the spatial performance of a system under field conditions, measurements can be standardized in the laboratory under controlled environment. Laboratory characterizations are generally performed to measure the noise equivalent temperature difference (NETD) and minimum resolvable temperature difference (MRTD) of the system. MRTD is measured by an observer which looks at a four bar pattern in front of a uniform background. Temperature of the bars is adjusted relative to the background, and half of the temperature difference between the bars and background, when the bars are observable, gives the MRTD value. NETD is measured by using two blackbody sources at different temperatures. Detector noise is measured at one temperature by taking the standard deviation of the detector signal. Subsequently, responsivity of the detectors is measured by taking the signal difference when camera looks at blackbodies at different temperatures. If the difference between blackbody temperatures is one Kelvin, noise/responsivity ratio gives the NETD value. As discussed in Chapter I, NETD can be either detectivity or uniformity limited. It was shown that NETD is directly proportional to the uniformity value. Therefore, if the detector would operate in uniformity limited regime, nonuniformity sources discussed in the previous subsection must be minimized to improve the performance. When the NETD of an imager is about 20 mK, to have a TV quality output, the corrected uniformity of the FPA must be less than 0.1% [24].

4.3 Read-out Circuit Considerations

First generation infrared imaging systems utilize single pixel or linear array scanned sensors. Detector density in these systems was relatively low, and requirements on read-out circuits were easy to achieve. However, as 2-D arrays started to appear, requirements on read-out circuits became more severe. Some of the second-generation infrared imagers make use of detector arrays, which is flip-chip bonded to read-out circuits (ROICs). Hybrid integration technology offers higher degree of design freedom by allowing the design of the detector array and ROIC independently. Moreover, with this technology, fill factors of the detector pixels can be increased up to nearly 100%.

Readout electronics must provide an efficient interface between the detectors and signal processing stage. Interface circuits should have low input impedance to increase the injection efficiency. Input referred noise level of the readout circuit must be significantly lower than the detector noise. Additionally, ROIC should exhibit large integration capacitors and high voltage swing to increase the signal dynamic range. Finally, ROIC must be able to operate at cryogenic temperatures, and its power dissipation must be small to reduce the heat load on cooler system.

4.3.1 Readout Structures

Commonly employed readout structures are self-integration readout, injection circuits, gate modulation, and capacitive transimpedance amplifier. These structures are explained briefly below.

Self-integration readout: In this approach, charges are integrated on the detector itself. Unit cell circuit of this structure is shown in Figure 4.14 [146]. This method is also referred as direct detector integration (DDI) and source follower per detector (SFD).

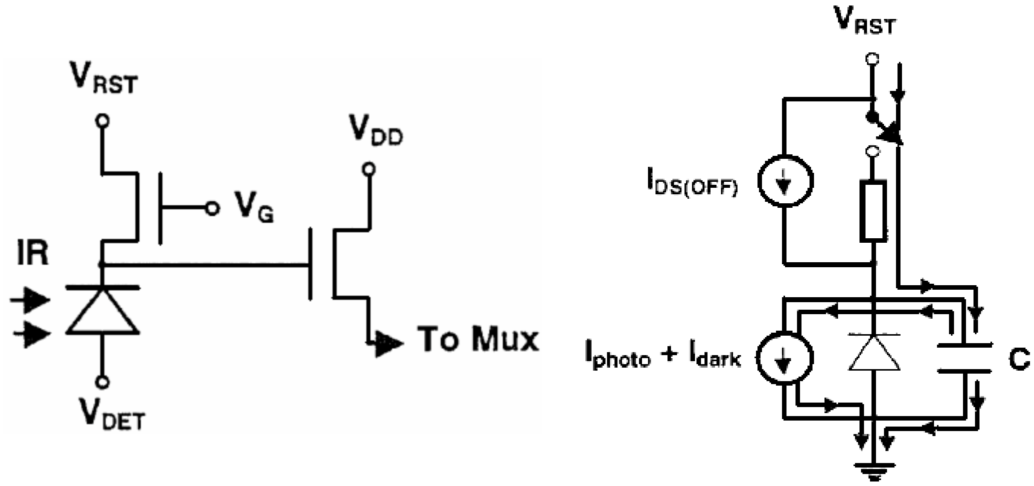

Figure 4.14: Circuit schematics of self-integration read-out interface [146].

Photodiode capacitor is charged from the reset voltage (V_{RST}) by making the reset transistor on. After switching off the reset transistor, photogenerated and dark currents in detector as well as MOSFET leakage current $I_{DS(OFF)}$ starts to discharge the stored charge. After an integration period, voltage in the sense node changes by an amount corresponding to the amount of charge discharged during integration period. Finally, sense node voltage is multiplexed to the video output amplifier through the source-follower MOSFET. Although the simplicity of the method results in small cell area and low power dissipation, the detector bias voltage changes during the integration period, which results in nonlinearity of the readout current [147].

Injection Circuits: An integration capacitor (C_{int}) is employed to integrate the detector current. The most commonly used injection circuits are direct injection (DI) and buffered direct injection (BDI). The schematics of these circuits are given in Figure 4.15.

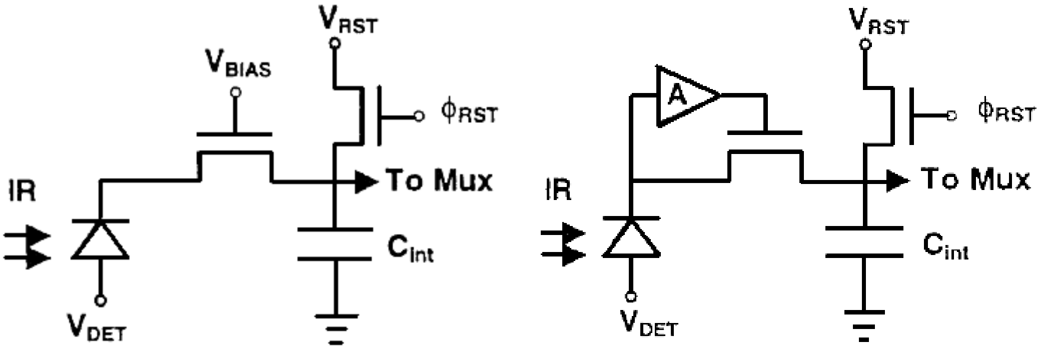

(a) (b)

Figure 4.15: (a) Direct injection and (b) buffered direct injection circuits [146].

Direct injection circuits are widely used due to its simplicity, low power consumption, and high performance, which makes this circuit suitable for high-density FPA applications. Bias control of the DI circuits is better than that of SFD circuit during the integration period. On the other hand, variations in MOSFET threshold voltage, detector bias, and detector resistance result in the injection efficiency (η_{inj}) nonuniformity across the FPA. Dark current in a photodetector can be modelled as a shunt resistor connected in parallel to detector. Some of the photocurrent is lost to the shunt resistance. Since the impedance of QWIP is high, it yields a very high injection efficiency. The injection efficiency for DI input is given by [148]

$$\eta_{inj} = \frac{g_m R_{Det}}{1 + g_m R_{Det}} [\frac{1}{1 + \frac{j\omega C_{Det} R_{Det}}{1 + g_m R_{Det}}}] \qquad (4.27)$$

where g_m is the transconductance of the input MOSFET, and it is given by $g_m = eI_{Det}/kT$. R_{Det} is the differential resistance of the detectors at applied bias, and C_{Det} is the detector capacitance. Very high injection efficiencies can be achieved with the MWIR arrays. On the other hand, injection efficiency of the LWIR detectors is slightly lower due to larger leakage currents. Charge injection efficiency increases with drain current. When the photocurrent is high, injection efficiency is better. On the other hand, injection efficiency decreases at low background flux, but in this case, dark current sets the lower limit.

BDI circuit is similar to DI circuit except the additional feedback amplifier. The input impedance of the DI configuration is decreased by a factor of A with the addition of feedback amplifier. This way injection efficiency is improved to near unity. The amplifier can be implemented by a differential pair or inverter. The virtual voltage that appears at the amplifier input provides more stable and uniform bias control over that of SFD or DI configurations. Moreover, input referred noise is improved when compared to the DI circuit. On the other hand, additional gain stage increases the power consumption. In general, injection circuits are not suitable for low background applications [146]. One drawback of direct injection circuits as compared to SFD circuit is the frame-to-frame crosstalk. Accumulated charge on detector is not reset directly, resulting in collection of photogenerated charges from the previous frame.

Gate Modulation: Two gate modulation input (GMI) structures are shown in Figure 4.16. In this approach, photogeneration induces a current through the integration capacitor by modulating the gate voltage of a MOSFET. Usually load resistance shown in Figure 4.16(a) is required to be high, therefore active loads are employed. With the help of the source voltage of the input MOSFET (V_{IN})

and V_{DET}, gain and dc levels are adjusted. Injection efficiency of GMI circuit depends on the input resistance of active load MOSFET. Current gain feature of the GMI results in superior detection sensitivity and decreased input noise, when compared to the DI. Additionally, gain level can be adjusted according to the background level leading to a higher dynamic range.

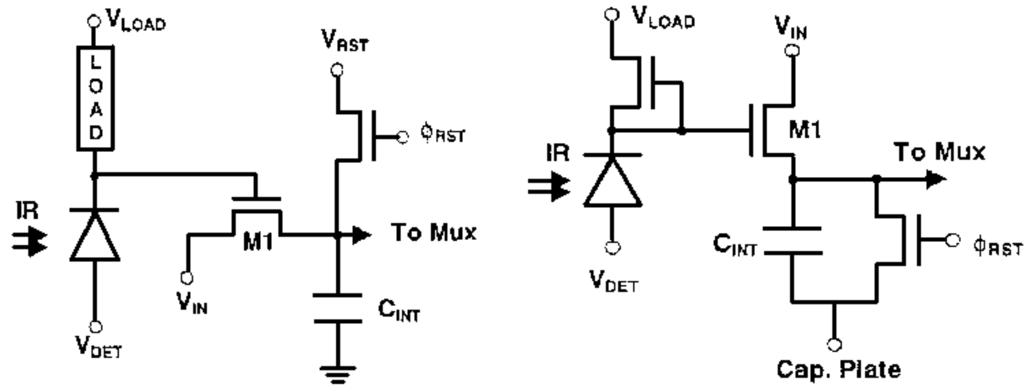

(a) (b)

Figure 4.16: Gate modulation read-out circuits with (a) passive load and (b) active load [146].

Capacitive Transimpedance Amplifier: Schematics of two different capacitive transimpedance amplifiers (CTIA) are given in Figure 4.17. The amplifier employed in the circuit can be either a simple CMOS inverter (Figure 4.17(a)) or a more complex amplifier (Figure 4.17(b)). The integration capacitor is on the feedback path of the amplifier. The applied bias to the detector is V_{REF}-V_{DET} and hence detector bias control is good. The value of C_{INT} can be chosen small to achieve low-noise and high sensitivity performance. Input impedance of the CTIA structure does not depend on the detector current. Very small detector currents can be integrated with high injection efficiency. On the other hand, reset clock can affect the stability of detector bias and amplifier operational point. Moreover, utilization of amplifier degrades the size and power consumption performance of the circuit.

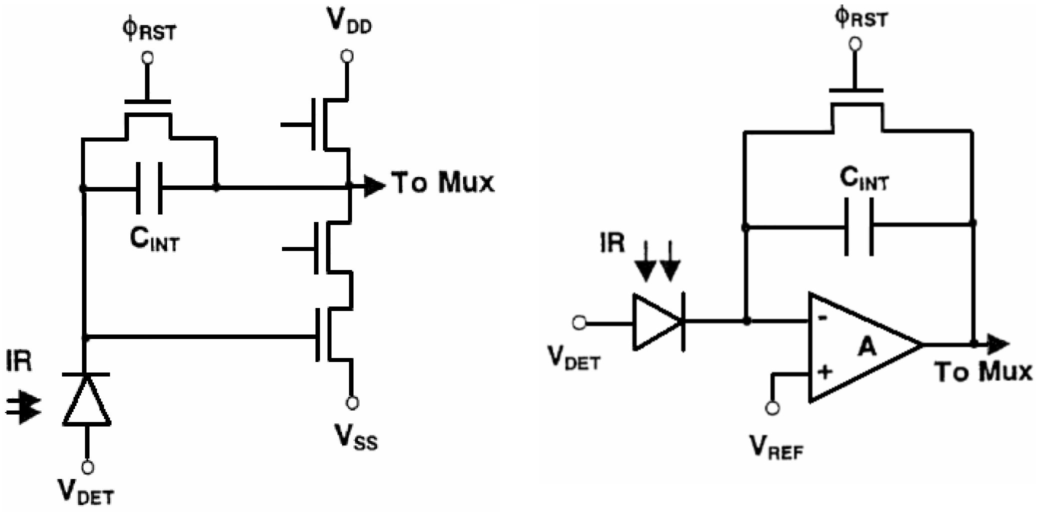

(a) (b)

Figure 4.17: Capacitive transimpedance amplifier read-out circuits with (a) a simple CMOS inverter and (b) a more complex amplifier [146].

Apart from the read-out circuits mentioned above, some other readout techniques have also been proposed in the literature. The share-buffered direct injection (SBDI) [147] circuit is an improved version of the BDI circuit. In the SBDI, the gain stage is implemented by a differential pair, some part of which is shared by all the cells in the same row. This approach yields 50% reduction in area. In the switched current integration (SCI) method, the integration capacitors are put outside of the FPA, and shared by the cells in the same column [147]. By this way, integration capacitance can be large with the expense of reduced integration time.

Current mirroring integration (CMI) technique [149-153] is another method in which integration capacitors are moved outside the FPA. This structure does not require in-pixel opamp. Overall effect is significant reduction in the size of unit cell, making very high density FPAs possible. A CMI structure, which is optimized for QWIPs, gives low input impedance, high linearity, stable detector bias, and large integration capacitors [151]. Additionally each unit cell consists of only 9 transistors yielding a very small pixel area.

Architecture of a typical direct-injection readout circuit in block form is given in Figure 4.18 [154]. At the end of each integration period, voltage accumulated on capacitors is multiplexed sequentially. A source follower transfers the voltage on capacitor to column bus, and the capacitor is reset. Shift registers generate the necessary clocks for transfer and reset. To minimize the power consumption, static CMOS registers are used.

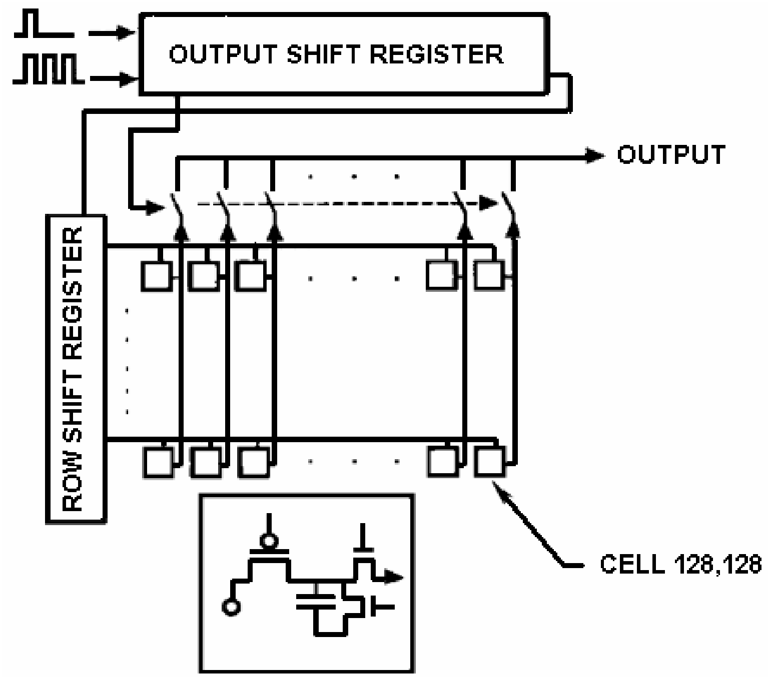

Figure 4.18: Architecture of a readout IC in block form with direct injection input [154].

4.3.2 Commercial Readout ICs

Today, megapixel readout ICs are produced by several companies. These ROICs are usually manufactured for infrared astronomy applications, and optimized for the MWIR InSb and HgCdTe detectors. Megapixel readout arrays developed at Raytheon Infrared Operations are given in Table 4.1. The table also includes the state-of-the-art microprocessors from Intel Corporation for comparison [66].

Readout circuits must be evolved in accordance with the development of the third generation 2-D detector arrays with larger physical size, smaller pixels, higher sensitivity, and faster frame rate. Utilization of on chip analog to digital converters (ADC) can reduce the susceptibility of analog signals to external noise sources, and allows much higher output data rates. In fact, Semi Conductor Devices (SCD) has already introduced such a readout integrated circuit developed for 640×512 InSb infrared detectors [155]. For tactical applications, high resolution and high-speed ADCs are necessary to achieve high frame rates with megapixel FPAs. Additionally, multispectral sensors of the third generation systems require multicontact readout schemes for simultaneous imaging in each wavelength band. In this case, each readout cell must accommodate circuitry for several pixels resulting in very dense circuits.

Table 4.1: Megapixel readout arrays at Raytheon Infrared Operations [66].

Array Format	# of Pixels	Die Size (mm)	# of Transistors	Process Technology	Application
1024×1024	1.0×10^6	22×28	$\sim2.5\times10^6$	0.5 μm 2 poly/ 3 metal	Tactical imaging
1024×1024	1.0×10^6	23×23	3.8×10^6	0.5 μm 1 poly/ 2 metal	Astronomy
1344×1344	1.8×10^6	37×39	$\sim4.0\times10^6$	0.5 μm 2 poly/ 3 metal	Tactical imaging
2048×2048	4.2×10^6	43.5×43.5	13.2×10^6	0.5 μm 1 poly/ 3 metal	Astronomy
2048×2048	4.2×10^6	54.1×54	$\sim13.2\times10^6$	2.0 μm 1 poly/ 2 metal	Astronomy
4096×4096	16.8×10^6	84.5×84.5	51×10^6	0.5μm 1 poly/ 3 metal	Astronomy
Pentium® III	N/A	9.4×11.3	9.5×10^6	0.25 μm	Microprocessor
Celeron ™	N/A	31×35	19×10^6	0.25 μm to 0.18 μm	Microprocessor
Pentium® 4	N/A	-	55×10^6	0.18 μm to 0.13 μm	Microprocessor

4.4 Summary and Conclusions

This chapter has discussed the important design considerations for FPAs based on QWIP technology. FPA performance depends on three main elements: single pixel performance, spatial issues, and readout electronics. Although some of these elements can be regarded as minor for some applications, each of them must be optimized very well for the applications requiring very high performance imaging.

When single pixel performance of the detectors are concerned, detector signal-to-noise ratios must be maximized while keeping the dark current as low as possible. Detector responsivity can be increased by utilization of material systems alternative to AlGaAs/GaAs system. Additionally, optical coupling efficiency can be increased by forming effective optical coupling structures. Dark current and noise are interrelated when the detector operates in detectivity limited regime. Therefore reduction in dark current decreases the detector noise. Dark current can be decreased to some degree by utilization of high quality barriers with lower trap densities. Moreover, some optical coupling schemes, which are formed by patterning the MQW region, reduce the active detector area, and hence decrease the dark current. Optimization of signal-to-noise ratio and dark current would also increase the BLIP temperature, which is necessary for the utilization of low cost, small, low power, and long lifetime coolers.

Uniformity becomes critical as the FPA size increases, or single pixel performance is relatively better. Nonuniformities can originate from the growth, fabrication, and imaging system components. Although field testing of the spatial performance is necessary to determine the ultimate FPA capability, it is not feasible because of the changing environmental conditions. On the other hand, FPA performance can be measured under controlled laboratory environment. NETD and MRTD are two FPA parameters that are measured and reported commonly.

Performance of the state of the art FPAs are started to be limited by readout electronics. For that reason, the readout technology should be in competition with the detector FPA technology. There are several approaches for readout interface and architectures. The widely used interfaces are self-integration readout, injection circuits, gate modulation, and capacitive transimpedance amplifier. At present, direct injection seems to be the most widely used readout interface approach in infrared detection field due to high-density layout, low power consumption, and simplicity it offers.

The considerations discussed in this chapter should be taken into account when designing the QWIP epilayer structure and FPA fabrication. In the next chapter development of the 640×512 QWIP FPA fabrication process, the FPA characterization setup and test procedure will be presented.

CHAPTER V

DEVELOPMENT of 640×512 QWIP FPA FABRICATION PROCESS and FPA CHARACTERIZATION SET UP

Infrared FPA fabrication process is a very complicated process that involves different technologies. In addition to the epitaxial growth quality, fabrication process and pixel structure have strong effects on the performance of the FPA. Detector array fabrication becomes more and more involved as the FPA size is increased. Size of LWIR AlGaAs/GaAs QWIP FPAs has been increasing rapidly since the introduction of the first QWIP FPA with a format of 128×128 in 1991 [154, 156]. This format was followed by 256×256 in 1997 [148], 640×486 in 1998 [157], and 1024×1024 in 2004 [72].

In this study, we have developed the fabrication technology for 640×512 QWIP FPAs, and this chapter is dedicated to this work. The organization of the chapter is as follows: Section 1 introduces the procedure of the standard QWIP fabrication. Section 2 gives large format QWIP FPA fabrication process developed in this study. Section 3 presents the FPA characterization setup and test procedure. Finally, Section 4 gives the characterization results of a 640×512 AlGaAs/GaAs QWIP FPA.

5.1 QWIP FPA Fabrication Process

QWIP FPA fabrication has several steps, some of which are very critical. The standard fabrication process consists of the following steps, and are illustrated in Figure 5.1:

- Alignment mark deposition
- Optical grating formation
- Mesa etch
- Ohmic contacts
- Reflector metallization
- Passivation
- Under-bump metallization
- Indium bump formation
- Hybrid coupling (flip-chip bonding) to Si ROIC
- Underfill injection
- Substrate thinning and polishing
- Packaging

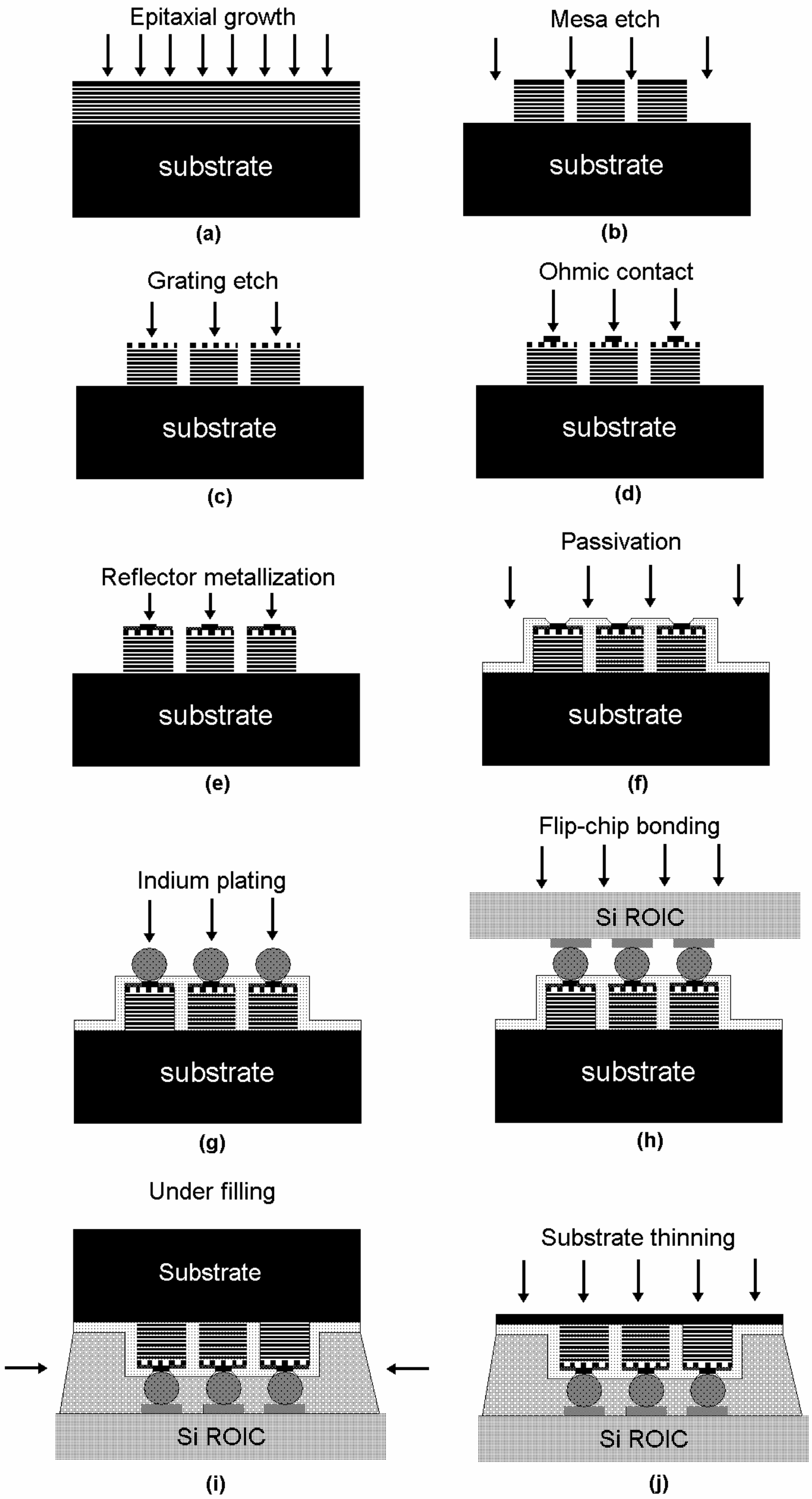

Figure 5.1: Standard QWIP fabrication process steps: (a) Epitaxial growth, (b) mesa etch, (c) grating etch, (d) ohmic contact, (e) reflector metallization, (f) passivation, (g) indium plating, (h) flip-chip bonding, (i) under filling, and (j) substrate thinning.

5.2 Development of Large Format QWIP FPA Fabrication Process

In the development study, several wafers with different epilayer structures were used to achieve the following goals:

i) Optimization of the grating structure for highest coupling efficiency,
ii) Optimization of the passivation process,
iii) Optimization of etching process,
iv) Optimization of indium electro-plating process,
v) Optimization of the hybrid integration process.

Since the details of the developed large format QWIP FPA fabrication process are forced to be confidential by the nature of this work, these details are not presented in this thesis. Instead, we concentrate on the results that are scientifically invaluable.

Each test sample used in optimization studies i-iii contains 13 different grating structures, and 2600 pixels for each grating structure. Optical gratings were formed by reactive-ion etching (RIE) on 21×21 μm^2 mesas. The samples were divided into two regions, and detector mesas on different regions were etched by RIE or wet etching methods. Additionally, several test samples were fabricated with different passivation methods to investigate the effect of surface passivation on QWIP performance. Controlled experiments were performed by changing only one parameter at each test stage to distinguish the consequence of each fabrication parameter. SEM picture of the test detectors after mesa passivation is shown in Figure 5.2. Due to the very high electrical resistance of the small size detectors, test detectors were 5×5 parallel connected in order to facilitate reliable electrical and optical measurements. After fabrication of the test samples, they were mounted on an alumina substrate which allows backside illumination. Finally, electrical contacts were taken through wire bonding. Pictures of a fabricated test sample are given in Figure 5.3.

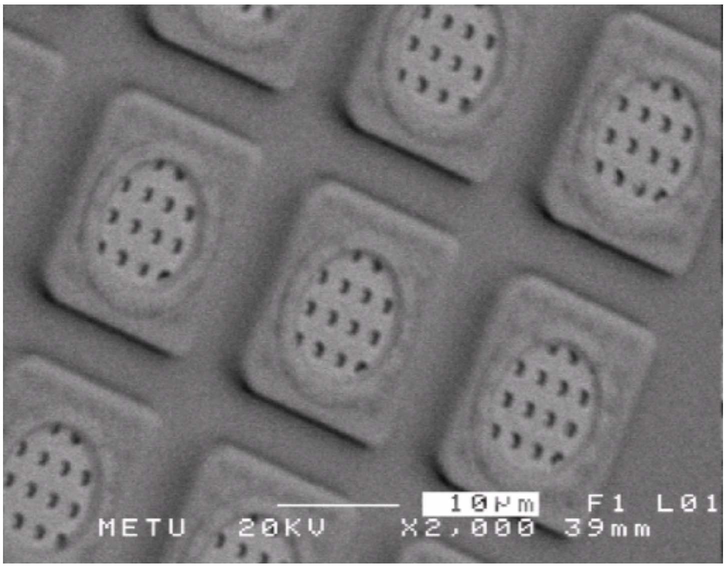

Figure 5.2: SEM picture of passivated mesas.

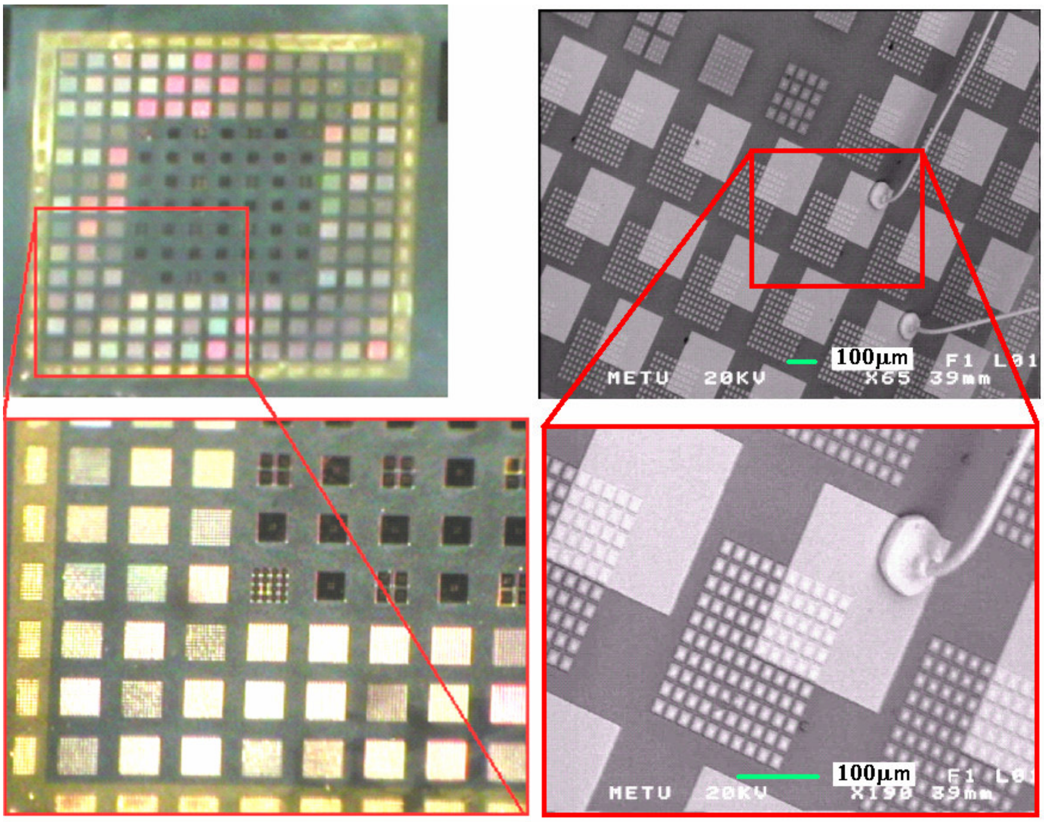

(a) (b)

Figure 5.3: Snapshots from the optimization sample: (a) optical microscope pictures, and (b) SEM pictures.

5.2.1 Optimization of Optical Grating Structures

Absorption of infrared radiation incident in normal direction to an n-type QWIP FPA requires optical diffraction gratings. Optical gratings can be classified into three groups: linear, two-dimensional, and random optical gratings. Generally, a grating structure consists of periodically repeating building cells, and the length of the repeating unit cell period is proportional to the wavelength of the radiation to be absorbed. The objective of the optical grating optimization process is to determine the grating structure that gives the highest absorption quantum efficiency. Grating structures used in this study include nearly all of the structures reported in the literature. As to our knowledge, there is no study reported on the comparison of the grating structures that incorporates such a wide range of structures. Large area detectors have usually been employed by researchers to investigate the optical coupling efficiency of the grating structures. However, the optical coupling efficiency is strongly dependent on the pixel size [142]. The fabrication process developed in this study allows the measurement of the coupling efficiency of the grating structures on detectors having the same size and structure with the FPA pixels. Therefore, grating efficiencies found in this study are expected to be similar to that of FPA pixels.

Optical gratings can be etched by either wet or dry etching methods. Underetching limits the etch-depth when the wet methods are used, since grating patterns have small feature sizes. Pictures of the optical gratings on detector mesas formed by wet and dry methods are given in Figure 5.4. As can be seen from the figure, underetch significantly reduces the masked area when structures are formed by wet method. On the other hand, dry etching method copies the mask pattern on to the detector mesa without a considerable change. This property of dry etching also provides better control over pixel-to-pixel uniformity. For these reasons, grating structures were etched by RIE in this optimization study. Figure 5.5 gives the pictures of some dry etched grating structures after ohmic contact formation.

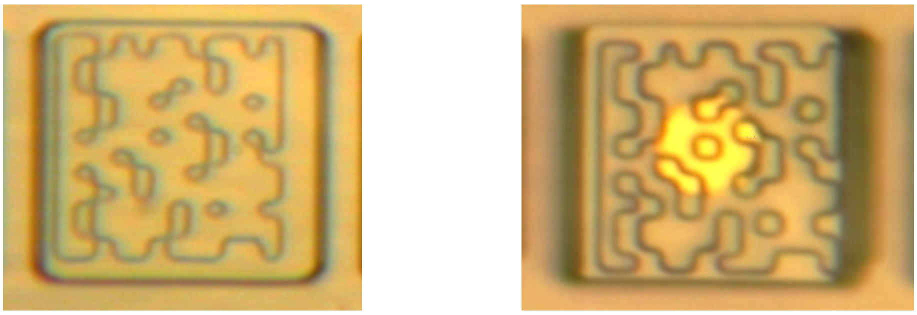

(a) (b)

Figure 5.4: Optical microscope pictures of the grating structures etched by (a) wet and (b) dry methods. Structures etched with wet chemical etchant get smaller while RIE copies the mask pattern without under etch. The light yellow region on the mesa in (b) is ohmic contact metallization.

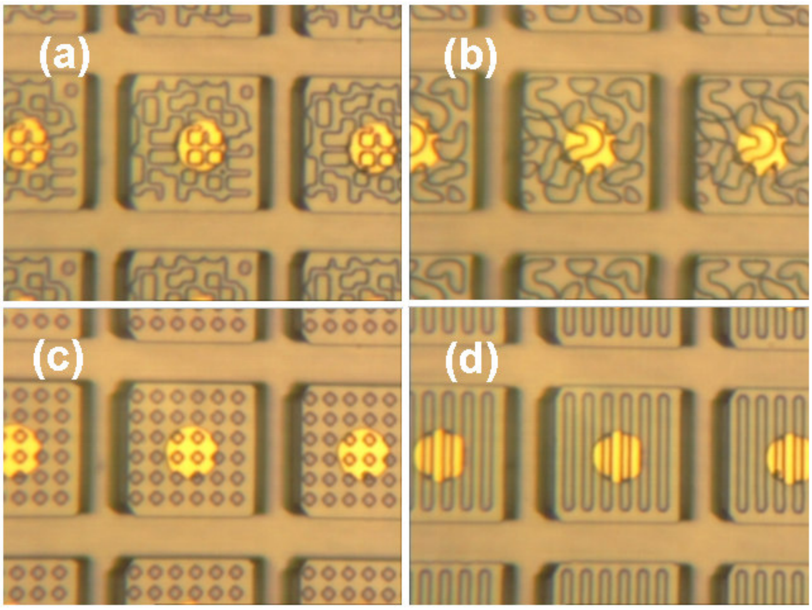

Figure 5.5: Pictures of various grating structures on optimization samples: (a) random, (b) elliptical, (c) two dimensional cross, and (d) one dimensional lamellar.

The epilayer structure of the AlGaAs/GaAs QWIP sample used in this optimization work consists of thirty periods with 45 Å thick GaAs QWs and 500 Å thick $Al_{0.275}Ga_{0.725}As$ barriers. QWs are doped at 5×10^{17} cm^{-3}, in addition to n-type top and bottom GaAs contact layers doped to 1×10^{18} cm^{-3}. After fabrication of the test samples, optical responses of the test detectors with different grating structures were measured. For each optical grating structure, five different detector groups were characterized, and the average photoresponse was calculated. While the results, being somewhat scattered, are not fully reliable, they still give an idea on the relative performance of different optical grating structures. Normalized photoresponses of the detectors with different optical gratings are given in Table 5.1. The structure with the highest response is observed to be two dimensional cross grating structure.

Table 5.1: Normalized photoresponses of the detectors with different optical gratings.

Type	Period (μm)	Peak efficiency wavelength (μm)	Normalized response
Lamellar	2.7	8.46	1.46
Lamellar	2.8	8.77	1.59
Lamellar	2.9	9.1	1.44
Lamellar	3.0	9.4	1.41
Cross	2.8	7.9	1.61
Cross	3.0	8.46	1.6
Cross	2.9	8.18	1.65
Random (33% fillfactor)	-	-	1
Random (50% fillfactor)	-	-	1.4
Elliptic	-	8.4	1.12
Rectangular Cross	$2.7\times3\ \mu m^2$	-	1.28
Rectangular Cross (tilted)	$2.7\times3\ \mu m^2$	-	1.21

5.2.2 Optimization of Passivation

Optical and electrical characterization were performed on the test detectors passivated with different methods. Spectral responses of the detectors with an unoptimized passivation and without passivation are given in Figure 5.6 (a) and (b), respectively. As clearly seen from the figure, the dips in the spectral response of the passivated detectors are due to the absorption of passivation material. Nonuniform spectral responses across an FPA significantly degrade the NETD performance of the FPA, because two or three point corrections are usually not efficient for the correction of spectral nonuniformities [62]. The multilayer passivation method (confidential) developed in this study minimizes the absorption of the passivation material, which considerably decreases the dark current of the detectors.

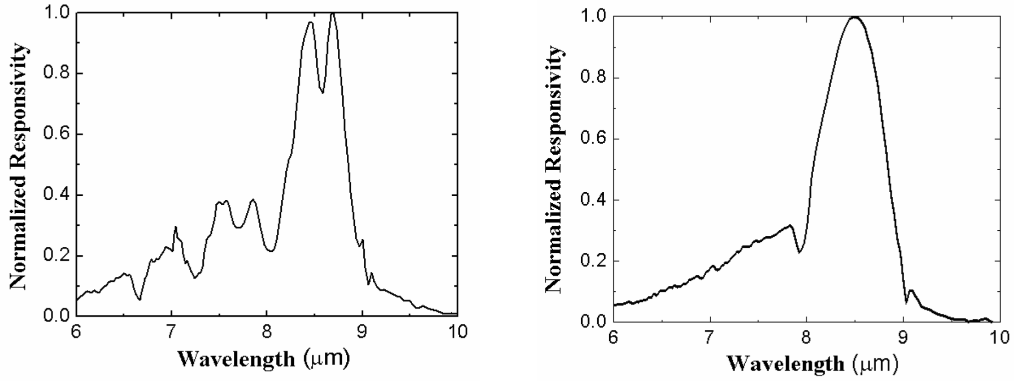

Figure 5.6: The effect of inappropriate passivation material. Several absorption lines are observed on the spectrum of passivated detector (a), while spectrum of the detector without passivation gives smoother response (b).

5.2.3 Optimization of Mesa Etch

Mesa size gets smaller as the format of an FPA becomes larger. Mesa etch turns out to be more demanding when the pixel pitch is reduced. Underetch decreases the fill factor of the detector pixel, which is not desirable. Additionally, mesa size should be uniform throughout the FPA. In the mesa etch optimization study, both wet and dry methods have been investigated. Wet etchant was optimized to give the least amount of underetch, and maximum uniformity over the 640×512 FPA. The solutions used for mesa etch optimization consist of the following mixtures with various ratios.

- $H_2O:H_2O_2:H_2SO_4$
- $H_2O:H_2O_2:HF$
- $H_2O:H_2O_2:NH_3$
- $C_6H_8O_7$ (Citric acid):H_2O_2
- $H_2O:H_2O_2:H_3PO_4$

Several AlGaAs/GaAs QWIP samples were etched by the above solutions to determine the etch rate, underetch amount, mesa sidewall profile, and reproducibility. On each sample, mesa structures were defined by photolithography. Etch rate of each solution was determined by etching QWIP samples at several time intervals and measuring the etch depth using a surface profiler. Additionally, to resolve the underetch amount, each sample was etched to a depth of 4.5 μm. For each solution, underetch amount was measured with the help of an optical microscope before removing the photoresist acting as the etch mask. A snapshot from the sample after mesa etch and before removal of the photoresist is given in Figure 5.7.

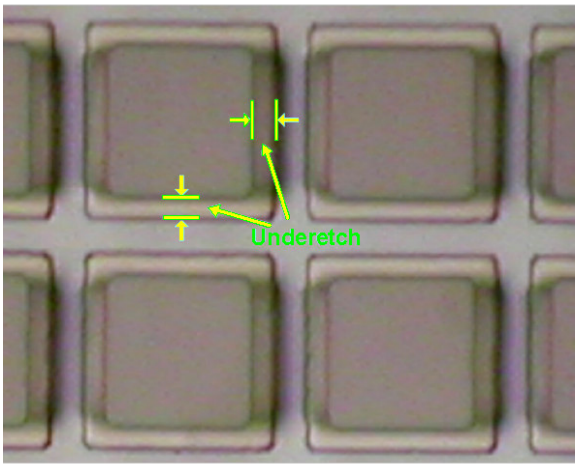

Figure 5.7: AlGaAs/GaAs QWIP mesas after wet etch. Underetch amount is indicated on the picture.

Mesa sidewalls were investigated by using scanning electron microscope (SEM). An SEM picture of the test sample, etched with an acceptable solution, is given in Figure 5.8.

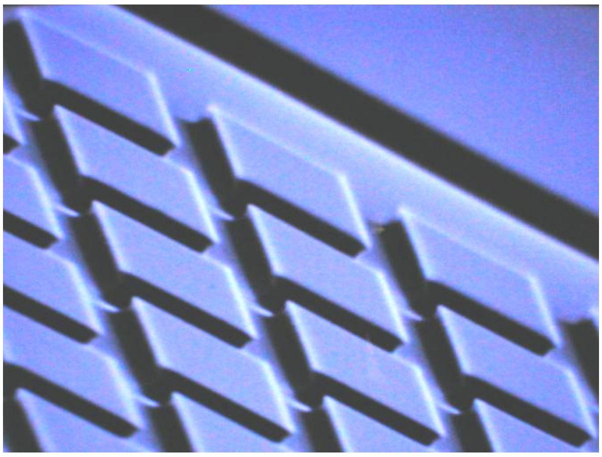

Figure 5.8: SEM picture of the mesas etched with an acceptable solution.

Wet and dry etching methods were also compared in terms of detector performance. Measurements showed that both wet etched and dry etched detectors yield similar detectivities. This shows that damage introduced by reactive ion etching (RIE) does not considerably contribute to the detector noise. On the other hand, RIE provides higher mesa fill-factors, and better pixel-to-pixel uniformity.

5.2.4 Optimization of Indium Plating

Indium bumps are used as interconnect material between the FPA pixels and ROIC pads. Indium bump technique is preferential to other techniques due to plasticity of indium element even at cryogenic temperatures and self-alignment capability. Besides, this technology provides very fine pitch bumps (less than 20 μm) and helps to the accommodation of the thermal mismatch between the detector material and silicon ROIC. There are two ways to form indium bumps on detector pixels: thermal evaporation and electro-plating. Although it is possible to form very small and uniform bumps using thermal evaporation method, it is not economical and may not be feasible for production. Therefore, electro-plating technique is utilized in this work to form the indium bumps on FPA pixels.

Uniformity control in electro-plating is not as good as that provided by the evaporation method. In order to optimize the indium plating process several test samples were prepared. Since the process depends on geometry but not on material, dummy samples cut from silicon wafers were used. In the optimization process we investigated the effect of plating current density, bump size and mask geometry on the bump height uniformity. Additionally, waveform of the plating current was also studied to improve the uniformity. DC, pulsed, and pulsed reversal current waveforms were investigated in the optimization processes. For pulsed and pulsed reversal waveforms, duty cycle was changed to obtain acceptable uniformity and bump shapes.

Preparation of the dummy samples for plating tests involves a metallization and a lithography step. After performing plating on the test samples, bump shapes were investigated by a scanning electron microscope. Initially, it was observed that the plating rates at the corners were higher than those at the center. Scanning electron microscope (SEM) pictures of the bumps at one corner and at the center of the sample are shown in Figure 5.9. The difference in the plating rate is due to the relatively high electric field formed at the regions close to the corners. This problem has been solved by modifying the indium plating mask pattern and adding some extra steps to the fabrication procedure. Eventually, almost perfectly uniform plating over the 640×512 FPA was achieved.

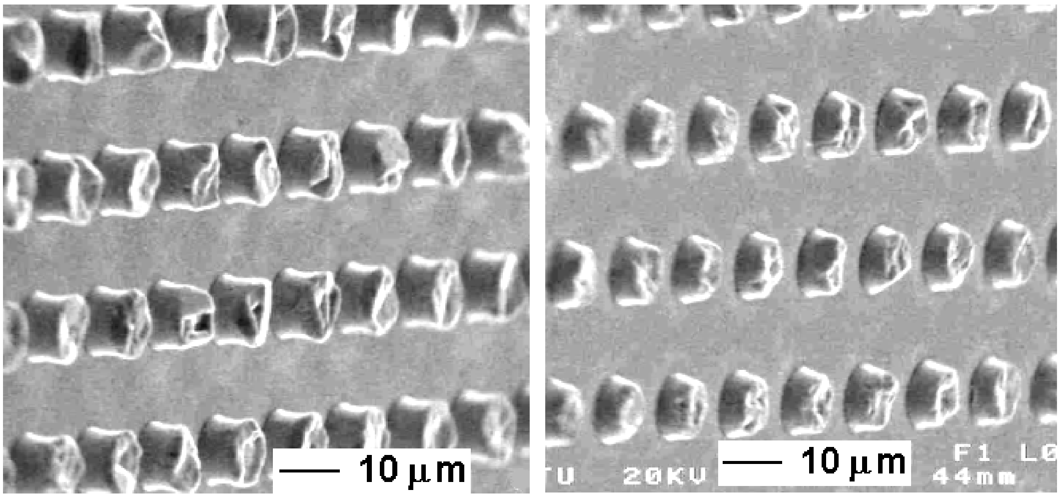

(a) (b)

Figure 5.9: SEM picture of bumps formed nonuniformly. Height of bumps at the corners (a) is significantly larger than that at the center (b).

As the result of the above optimization work, an indium plating recipe has been developed which gives 100% yield and very uniform bump heights. Optimization of the flip-chip bonding process presented in the following subsection was also required to achieve ~100% pixel yield in the FPA hybridized to ROIC.

5.2.5 Optimization of Flip-chip bonding

During the flip-chip bonding process, the FPA and ROIC must be almost perfectly parallel to each other to satisfy all electrical connections between the FPA pixels and ROIC pads. Incorrect planarity results in unconnected pixels. The requirement for planarity gets more stringent as the FPA size is increased. For example, the angle between 640×512 FPA and ROIC must be less than 0.034° to have all the pixels connected since the height of an indium bump is around 10 μm, and the length of longer side of a the FPA is 1.7 cm.

In addition to planarity, another critical flip-chip bonding parameter is the applied pressure. The compression force and temperature must be optimized to increase the reliability of the indium interconnects against thermal cycling. Application of overpressure may result in short circuited bumps as the bump diameter increases with increasing pressure. Additionally, underfill injection becomes difficult as the distance between ROIC and FPA is reduced.

When indium bumps are formed on only one side (FPA or ROIC), the dies must be heated. On the other hand, when indium bumps are formed on either side, cold compression is also possible, since indium has a unique property of cold welding to itself.

Alignment is another issue that must be considered. Fortunately, slight misalignments can be corrected by a post-reflow after flip-chip bonding. In the course of the reflow process, indium prefers to maximize its contact area with UBM metal. This way, cumulative forces applied on FPA pixels and ROIC pads by indium bumps correct the misalignments.

Flip-chip bonding optimization process involves optimization of two parameters: temperature and pressure. For optimization of the bonding parameters, dummy samples with indium bumps were fabricated and coupled to transparent glass dies. This way bumps were observable under optical microscope after flip-chip bonding. Compression amount depends on bonding temperature and pressure. Bump deformation increases by increasing temperature, pressure, or both. However, increasing the temperature too much should be avoided not to melt the indium metal. In the scope of this work, these parameters were tuned to levels that provide acceptable bump compression (3-4 µm). Figure 5.10 shows the images of indium bumps on the different regions of a test sample coupled with acceptable parameters (without reflow before bonding).

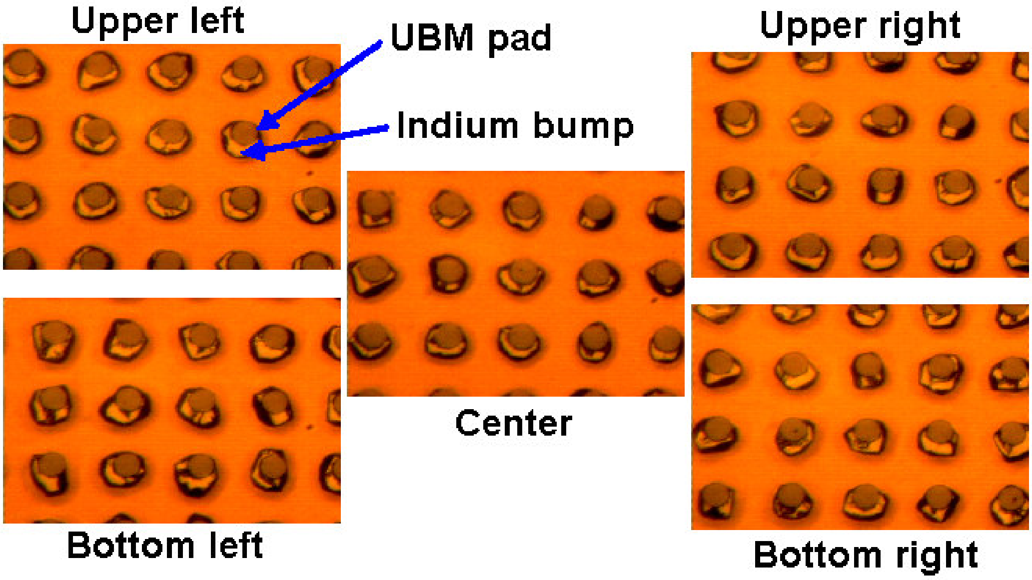

Figure 5.10: Pictures of an indium plating optimization sample flip-chip bonded with acceptable parameters (without reflow before flip-chip bonding). The amount of compression across the 640×512 array is uniform.

We fabricated a 640×512 AlGaAs/GaAs QWIP FPA with the developed fabrication process discussed in the previous subsections. Then the FPA was hybridized to a commercial ROIC (Indigo ISC9803), whose technical specifications are given in the following section.

5.3 Indigo 9803 ROIC

Indigo 9803 ROIC is built using a standard 0.6 micron CMOS process with double metal and single polysilicon layers [158]. Direct injection input circuit is used in the ROIC. Figure 5.11(a) shows the schematic of a unit cell. Detector current charges the integration capacitor through input gate transistor. After the integration period, voltage on the integration capacitor is sampled and multiplexed to the column amplifier which is shown in Figure 5.11(b). The column amplifier provides sample/hold, amplification, and skimming functions. The signal voltage from each unit cell is sampled and fed to the column amplifier. The amplifier gain can be controlled by the Gain0 and Gain1 pins. Skimming function if implemented through the Vos input.

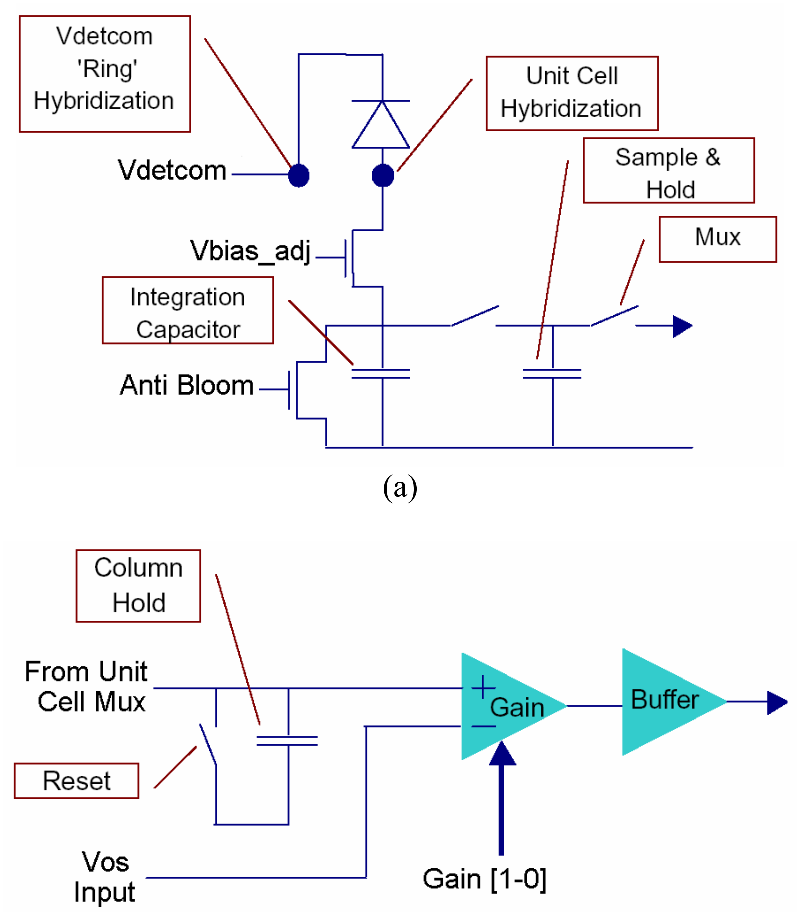

(a)

(b)

Figure 5.11: (a) Unit cell and (b) column amplifier schematics of ROIC [158].

ROIC provides up to four outputs. Outputs of column amplifiers are multiplexed to the output buffers. The maximum output data rate at 80 K operating temperature is 10 MHz per output. ROIC operates in snapshot integration mode, where all pixels are integrated simultaneously. The integration process allows both Integrate-While-Read and Integrate-Then-Read modes of operation. The technical specifications of the ROIC are summarized in Table 5.2.

Table 5.2: Technical specifications of ISC9803 ROIC [158].

Format	640×512 pixels
Pixel Pitch	25 µm
Storage Capacity	1.1×10^7 electrons (350 fF C_{int})
Operability	≥ 99.99%
Dynamic Range	> 72 dB
Readout Noise	345 electrons (at max. gain setting)
Non-Linearity	<0.5%
Cross Talk	<0.1%
Input Polarity	p on n
Integration Time	>5 µsec, adjustable
Outputs	1, 2, or 4 selectable
Output Signal Swing	2.5 V
Power Consumption	<90 mW at 30 Hz single output <180 mW at 107 Hz, 4 outputs
Max Frame Rates (640×512)	1 output, 30 Hz 2 output, 58 Hz 4 outputs, 107 Hz
Video Output	NTSC or PAL

5.4 FPA Characterization Set Up and Test Procedure

The performances of the FPAs were evaluated using a prototype thermal imager. A picture of the constructed imager for this purpose is given in Figure 5.12. The thermal imager consists of a proxy card for ISC9803 ROIC interface, DSP card, power supply card and a frame grabber card. The proxy card generates the timing and control signals and detector bias. Real-time analog data coming from the ROIC is converted to 14-bit digital data by analog-to-digital (A/D) converters. DSP card executes the necessary image processing algorithms like bad pixel replacement, and gain and offset correction on digital data. The imager provides 14-bit digital real-time video data to the frame grabber installed in a computer. FPA test software allows measurement of uniformity, signal histogram, and noise equivalent temperature difference (NETD) by processing the digital video data.

Figure 5.12: Prototype thermal imager.

NETD measurements are performed by exposing the FPA to a large area blackbody emitting uniform illumination. 64 frame average of the 14-bit digital signals read out from each pixel are recorded when they are looking at the blackbody maintained at 290 K and 300 K. Additionally, standard deviation of the signal values are measured to calculate mean rms noise. After recording the noise and pixel responses, NETD is calculated by using the following expression

$$NETD = \frac{\rho_{n,rms}}{d\rho_{avg} / dT_B} \tag{5.1}$$

where T_B is the blackbody temperature, ρ_{avg} is the average signal measured from the pixel, and $\rho_{n,rms}$ is the rms value of the pixel noise signal. In open form, Equation 5.1 can be given by

$$NETD_{i,j} = \frac{\sqrt{\frac{1}{N}\sum_{k=1}^{N}\left(\rho_{i,j,k} - \frac{1}{N}\sum_{k=1}^{N}\rho_{i,j,k}\right)^2}}{\frac{1}{10}\left\langle \left(\frac{1}{N}\sum_{k=1}^{N}\rho_{i,j,k}\right)\Big|_{T=300K} - \left(\frac{1}{N}\sum_{k=1}^{N}\rho_{i,j,k}\right)\Big|_{T=290K} \right\rangle} \tag{5.2}$$

where N is the number of averaged frames, and $\rho_{i,j,k,}$ is the 14-bit digital signal value obtained from the pixel at location (i, j) on the array at frame k. The numerator of Equation 5.2 gives the amount of rms noise for pixel (i,j) calculated at the end of 64 frames, and the denumerator gives the change in digital signal for one Kelvin degree change in blackbody temperature.

5.5 640×512 AlGaAs/GaAs QWIP FPA Fabrication and Testing

In this section, we will present the characteristics of a 640×512 AlGaAs/GaAs QWIP FPA initially fabricated with the developed process. The epilayer structure of the AlGaAs/GaAs QWIP consists of thirty periods with 40 Å thick GaAs QWs and 500Å thick $Al_{0.27}Ga_{0.73}As$ barriers. QWs are 20 Å center doped at 8×10^{17} cm^{-3}, in addition to n-type top and bottom GaAs contact layers doped to $1x10^{18}$ cm^{-3}. The epilayer structure was grown at Sheffield University with the metalorganic chemical vapor deposition technique.

Figure 5.13 shows the spectral detectivity of a typical FPA pixel at 77 K and under –2 V bias, and with 180° field of view (FOV). The detectivity peaks at ~8.4 μm with $\Delta\lambda/\lambda_p$ of 12%, which is typical for bound-to-quasi-bound QWIPs [2].

Figure 5.14 shows the dark current versus bias characteristics of the FPA pixels at various temperatures and the photocurrent obtained with f/2 aperture under 300 K background. The QWIP shows BLIP performance up to -1 V and -3.5 V at 77 K and 70 K, respectively. There is an asymmetry in the I-V characteristics and the dark current under negative bias is lower than that under positive bias. The observed asymmetry can be attributed to dopant segregation in the growth direction during the growth of AlGaAs/GaAs quantum well structures [123].

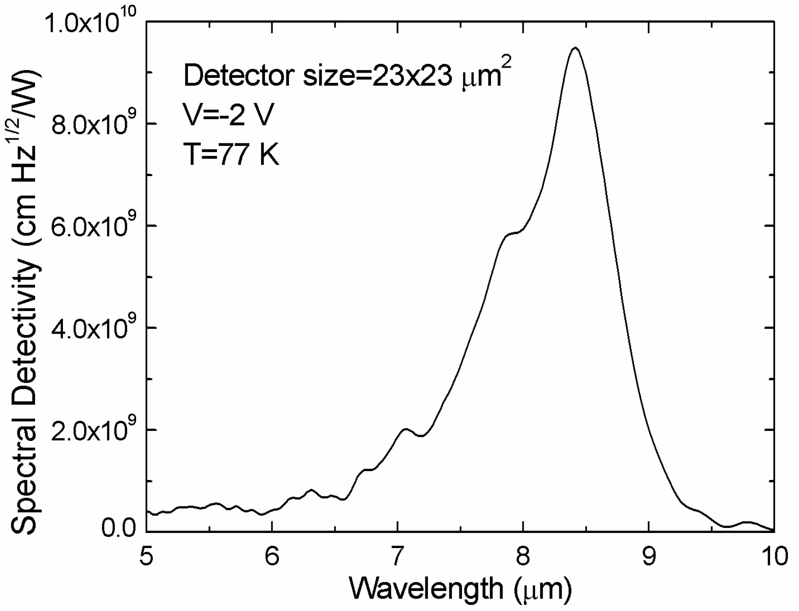

Figure 5.13: Spectral detectivity of MOCVD grown AlGaAs/GaAs QWIP (180° FOV).

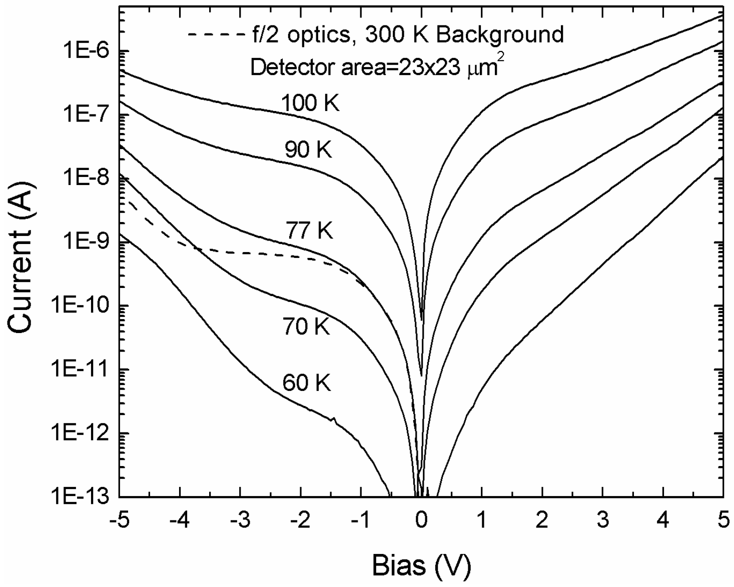

Figure 5.14: Bias dependence of the MOCVD grown AlGaAs/GaAs QWIP dark current at various temperatures and 77 K photocurrent with f/2 optics, 300 K background.

Figure 5.15 shows the dependence of 77 K peak responsivity and detectivity on reverse bias. Peak detectivity becomes maximum at 2 V reverse bias, and peak responsivity is 160 mA/W under the same bias.

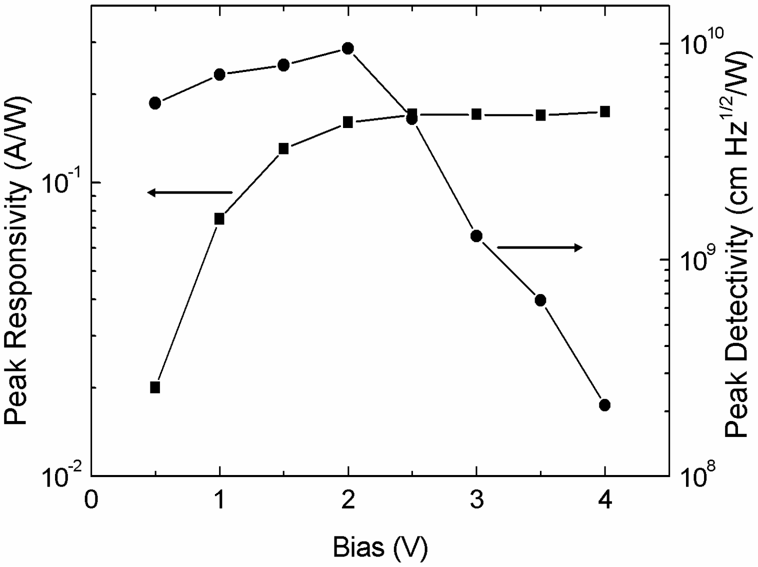

Figure 5.15: Peak responsivity and detectivity of the AlGaAs/GaAs QWIP versus reverse bias.

The FPA was installed into the prototype thermal imager for performance assessment. The AlGaAs/GaAs QWIP FPA displayed an NETD of 120 mK (half filled ROIC capacitors) at 77 K with f/1.5 optics and without multiple frame off-chip integration. The NETD histogram is given in Figure 5.16. The uncorrected DC signal nonuniformity of the FPA is 5.4% excluding bad pixels.

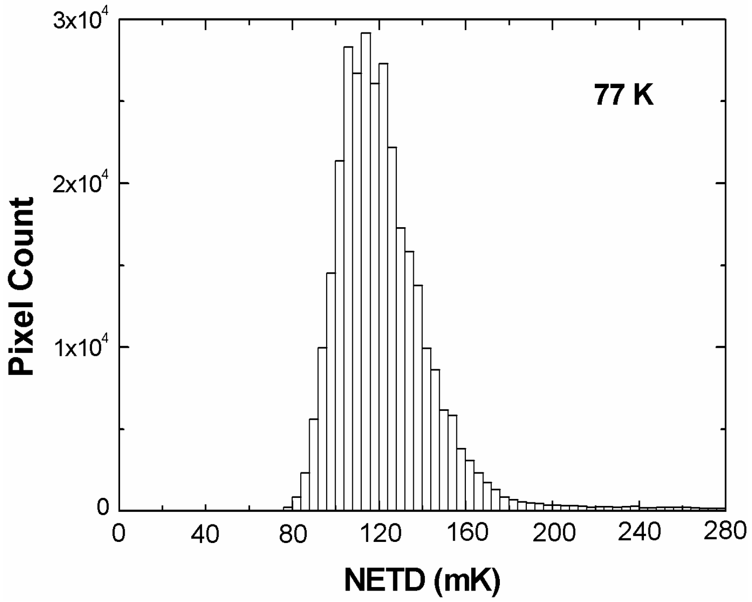

Figure 5.16: NETD histogram of the 640×512 AlGaAs/GaAs QWIP.

Integration time and reverse bias dependencies of the NETD with 2/3 filled capacitors are given in Figure 5.17. A snapshot thermal image taken with this FPA is given in Figure 5.18.

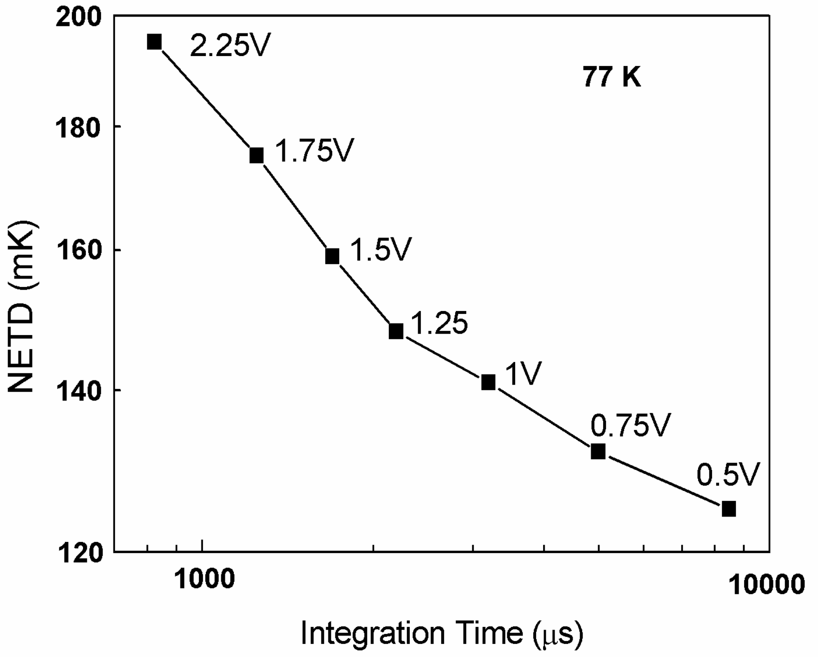

Figure 5.17: Mean NETD of the MOCVD grown 640×512 AlGaAs/GaAs QWIP FPA versus reverse bias voltage.

Figure 5.18: A snapshot from 640×512 MOCVD grown AlGaAs/GaAs QWIP FPA.

Having described our FPA fabrication and testing process in this chapter, we will present the scientifically important results of the second part of this work in the following two chapters, which are dedicated to a detailed comparative investigation on InP/InGaAs QWIPs as an alternative to the standard AlGaAs/GaAs QWIPs.

CHAPTER VI

COMPARISON of AlGaAs/GaAs and InP/InGaAs LWIR QWIP PERFORMANCES

One of the advantages that QWIP technology offers is the availability of a wide range of material systems for device implementation. AlGaAs/GaAs material system has been the most widely investigated system up to date. The first demonstrated QWIP was also based on this material system, because of the mature GaAs technology and perfect lattice match between AlGaAs and GaAs. However, the low quantum efficiency of the standard AlGaAs/GaAs QWIPs is still a bottleneck for widespread utilization of this sensor in high performance thermal imaging systems.

The researchers have started to pronounce the advantages of alternative material systems like InGaAs/GaAs and InP/InGaAs over the conventional AlGaAs/GaAs system. Al-free InP/InGaAs QWIPs offer higher responsivity, presumably lower defect density, lower growth temperatures, resistance to oxidation, and, being on InP substrate, facilitates the fabrication of lattice matched MWIR/LWIR QWIP stack with AlInAs/InGaAs MWIR QWIPs. Presumably, an important disadvantage of InP/InGaAs for QWIP applications is the lack of flexibility in adjusting the peak detection wavelength by changing the barrier/well material composition, limiting the peak responsivity wavelength to a narrow range around 8 μm. However, it has been shown by Gusakov *et. al.* [159] that it is possible to extend the operating wavelength up to 11 μm by utilizing the strain as an additional band gap engineering parameter. It is also possible to increase the peak responsivity wavelength above 8 μm by using InGaAsP, instead of InGaAs as the quantum well material [160].

Metal organic molecular beam epitaxy (MOMBE) grown LWIR InP/InGaAs QWIPs were first discussed by Gunapala *et. al.* [161] with a conclusion that the responsivity of these QWIPs is much larger than that of AlGaAs/GaAs QWIPs at high bias. A similar observation was reported by Andersson *et. al.* [162] on metal organic vapor phase epitaxy (MOVPE) grown InP/InGaAs QWIPs. Large gain and responsivity in InP/InGaAs QWIPs were also reported by other groups [163-167], and the first InP/InGaAs QWIP FPA was reported by Jiang *et. al.* [168] with a format of 256×256 using metal organic chemical vapor deposition grown material.

In spite of the above mentioned advantages, there has been limited amount of work reported on the characteristics of Al-free InP/InGaAs QWIPs. In order to reveal the detailed characteristics of InP/InGaAs QWIPs and assess the comparative performance of large format InP/InGaAs QWIP FPAs, we carried out a two-stage investigation study. In the first stage, test QWIPs based on InP/$In_{0.53}Ga_{0.47}As$ and AlGaAs/GaAs material systems were fabricated followed by detailed optical and electrical characterization with the results supported by ensemble Monte Carlo (MC) simulations [169]. In the second stage, large format (640×512) FPAs were fabricated, and subjected to characterization in a prototype thermal imager [169, 170]. This FPA, to our knowledge, is the first MBE grown InP/InGaAs LWIR QWIP FPA, and the largest format InP/InGaAs QWIP FPA ever reported. This chapter is dedicated to the results of the first stage. The characteristics of 640×512 FPAs will be presented in the following chapter.

The epilayer structures of the AlGaAs/GaAs and InP/InGaAs QWIPs, and the design considerations are given in Section 1. Section 2 presents the test detector fabrication procedure developed in this study. The results of the experimental and theoretical comparison study are presented in Section 3, and the summary and conclusions of the chapter are given in Section 4.

6.1 Epilayer structures of AlGaAs/GaAs and InP/InGaAs QWIPs

The peak detection wavelength of the designed QWIPs was calculated by solving the Schrödinger's equation. The epilayer structures, and calculated peak absorption wavelengths are discussed in the following subsections.

6.1.1 AlGaAs/GaAs QWIP Structure

AlGaAs/GaAs QWIP epilayer structure grown by MBE at IQE Inc. is shown in Figure 6.1. The difference between subband energy levels sets the peak absorption wavelength. Peak detection wavelengths for specific barrier, and quantum well parameters reported in the literature are scattered due to the deviations from the targeted values during growth, as well as to other factors such as different mesa dimensions and optical grating structures. Therefore, it may be necessary to perform several growth runs by changing the QWIP parameters to tune the peak detection wavelength to a specified value. In this study, several QWIP wafers with various structural design parameters have been investigated, and only one of them will be discussed in the following sections.

Standard QWIPs exhibit narrow spectral response, and the full width half-maximum (FWHM) of a typical bound-to-quasi bound QWIP with 8-9 μm cut-off wavelength is around 1 μm. Additionally, as discussed in Chapter IV (Equation 4.6), dark current depends on the peak detection wavelength exponentially. Setting the peak detection wavelength close to 8 μm in the LWIR window results in low dark currents, and hence higher operating temperatures, without reduction in absorbed power in LWIR window. Therefore, the barrier and well parameters utilized in this study were aimed to give peak detection wavelengths between 8 and 8.5 µm. Additionally, well doping densities were only moderately high to avoid excess leakage current, and the saturation of read-out circuit capacitors even with short integration times. The selected barrier thickness (500Å) is large enough to suppress the ground state tunneling.

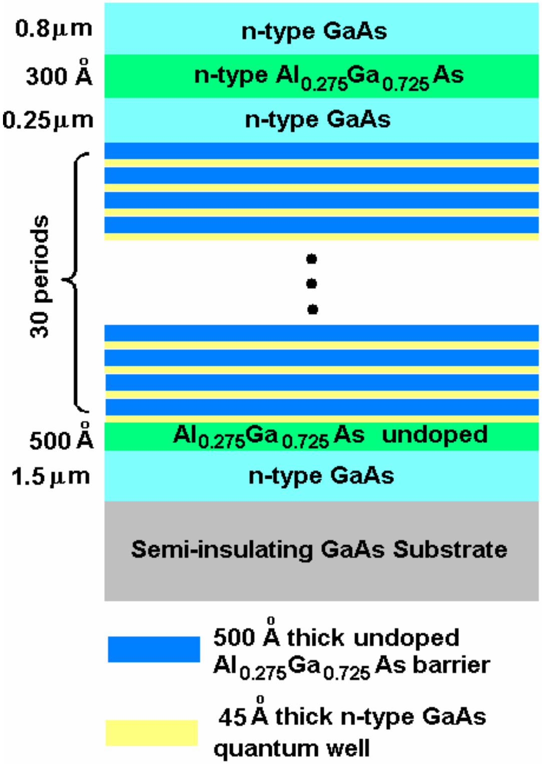

Figure 6.1: AlGaAs/GaAs QWIP epilayer structure.

Peak absorption wavelength of a QWIP structure can be determined theoretically once the barrier, and well parameters are specified. We calculated the subband energy levels in the quantum wells by solving 1-D time-independent Schrödinger equation numerically to determine the peak absorption wavelength of the $Al_xGa_{1-x}As$/GaAs QWIPs. Time-independent Schrödinger equation is given by

$$E\varphi(x) = \left[-\frac{\hbar}{2m^*}\frac{\partial^2}{\partial x^2} + V(x) \right]\varphi(x) \tag{6.1}$$

where $\hbar$ is modified Planck's constant, m^* is the effective mass of electrons, V is the electrostatic potential, E is the energy, and φ is the wavefunction of confined electrons. Numerical solution of this equation is possible after discretization, and the discrete form can be expressed as

$$-\frac{\hbar}{2m^*}\frac{\varphi_{i+1}+\varphi_{i-1}-2\varphi_i}{\Delta^2}+V_i\varphi_i=E\varphi_i \tag{6.2}$$

1-D potential profile was defined with 45 Å quantum well width, and 500 Å barrier width. Due to the large separation between quantum wells, they were considered to be isolated. While forming the potential profile, conduction band discontinuity between $Al_xGa_{1-x}As$ and GaAs was taken as 67% of the total bandgap energy difference [171]. Bandgap of $Al_xGa_{1-x}As$ and GaAs at 77 K were calculated from the following relations [172]

$$E_g(\mathrm{GaAs})=1.519-5.405\cdot10^{-4}\times T^2/(T+204)\ (\mathrm{eV}) \tag{6.3}$$

and

$$E_g(Al_xGa_{1-x}As)= 1.519+1.155x+0.37x^2-5.41\cdot10^{-4}\cdot T^2/(T+204)\ (\mathrm{eV}) \tag{6.4}$$

where T is the temperature in Kelvin, and x is the aluminium mole fraction. The potential profile was divided into cells with 1 Å width. Then discrete Schrödinger equation was converted into matrix form and solved by a FORTRAN program [173] to obtain subband energy levels. Once the energy levels were available, peak absorption wavelength was calculated by

$$\lambda_p=\frac{1.24}{E_2-E_1} \tag{6.5}$$

where E_2 and E_1 are excited and ground state subband energy levels, respectively. Peak absorption wavelengths were calculated for 45 Å well width and several aluminium mole fractions (x). The peak absorption wavelength versus Al mole fraction (x) characteristics are shown in Figure 6.2. The results are similar to those calculated by Choi [124]. As can be seen from the figure, x=0.275 gives 8.4 μm peak absorption wavelength, which is suitable for LWIR detection.

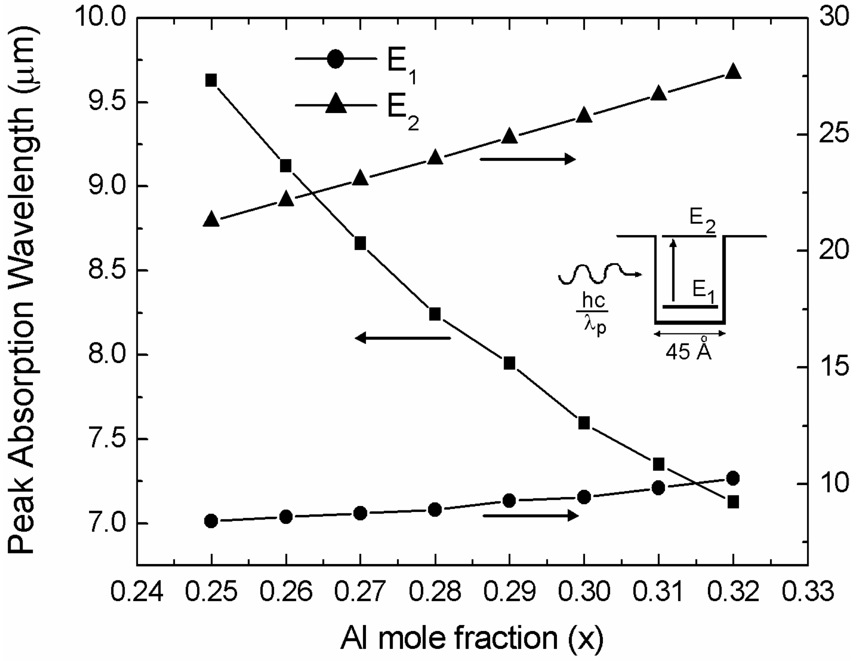

Figure 6.2: Peak absorption wavelength for various aluminium mole fractions (x) calculated by one-dimensional Schrödinger equation.

6.1.2 InP/InGaAs QWIP Structure

The InP/$In_{0.53}Ga_{0.47}As$ QWIP epilayer structure was also grown at IQE Inc. on 3-inch diameter, Fe-doped semi-insulating InP substrate using a solid source AppliedEPI modular GEN II molecular beam epitaxy (MBE) system. The epilayer structure illustrated in Figure 6.3 consists of twenty $In_{0.53}Ga_{0.47}As$ (60 Å thick) quantum wells sandwiched between 500 Å thick InP barriers, in addition to n-type top and bottom $In_{0.53}Ga_{0.47}As$ contact layers doped to 1×10^{18} cm^{-3}. Central 50 Å thick regions of the quantum wells are n-type doped at 5×10^{17} cm^{-3}. Discrete Schrödinger equation discussed in the previous subsection was used to calculate the peak absorption wavelength, which was found to be λ_P=7.9 μm when the conduction band discontinuity (ΔE_C), and InGaAs effective mass were taken as 0.242 eV and $0.041m_0$, respectively [161].

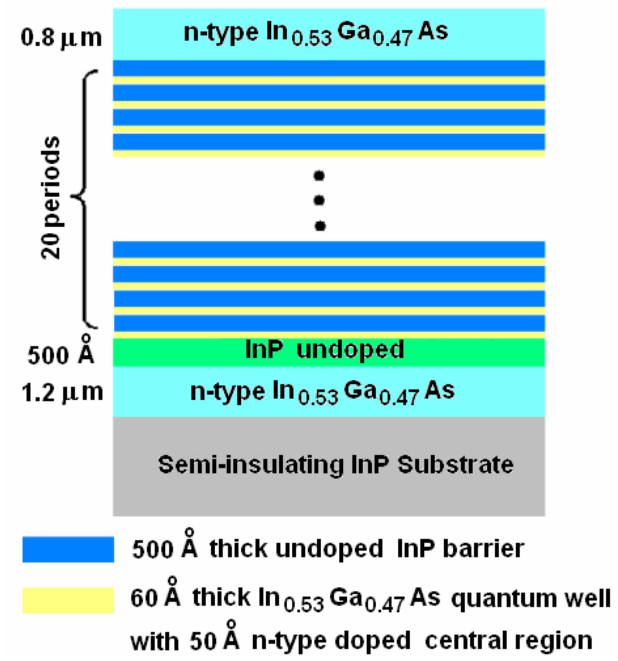

Figure 6.3: InP/$In_{0.53}Ga_{0.47}As$ QWIP epilayer structure.

6.2 Test Detector Fabrication

QWIPs to be employed in a high performance thermal imager should provide low dark current, suitable spectral response, high detectivity, and high uniformity. These quantities, except the uniformity, can be measured by single pixel characterization. Detailed electrical and optical characterization of the test detectors fabricated with the structures given in the previous section were performed to measure their performances.

It is a common approach to fabricate large area detectors and scale the results to FPA pixel size to measure the pixel performance. However, the optical coupling efficiency of the grating structures was reported to decrease with mesa size [142]. Therefore, to understand the coupling efficiency of the grating structures formed on the FPA pixels, characterization of the small size detectors is indispensable. Since QWIP is a high impedance device with very low dark current, electrical characterization of the small size detectors is not easy. Nevertheless, the problems with high QWIP impedance can be resolved by connecting several small pitch detectors in parallel. Therefore, we developed a fabrication method which yields 5×5 parallel-connected FPA pixel size test detectors. These detectors have the same size and structure (including optical grating) with the FPA pixels and were fabricated with the FPA. 21×21 μm^2 mesas (with 25 μm pitch) and lamellar optical grating were defined by standard photolithography and dry etching. Following ohmic contact and reflector formation, passivation, and under-bump metallization, indium bumps were uniformly formed through electro-plating. The test detectors with indium bumps were coupled to fan-out substrates by flip-chip bonding. After under filling, the substrate of the test detectors was thinned, and the hybrid was mounted on an LCC package. A picture of the test hybrid is shown in Figure 6.4. Fan-out substrate provides electrical connections to 25 different parallel-connected mesa groups. Therefore, any misleading data from a defected group can be eliminated by characterization of several detectors and studying those giving similar results. The following sections will discuss the results of the characterization study performed on these test hybrids.

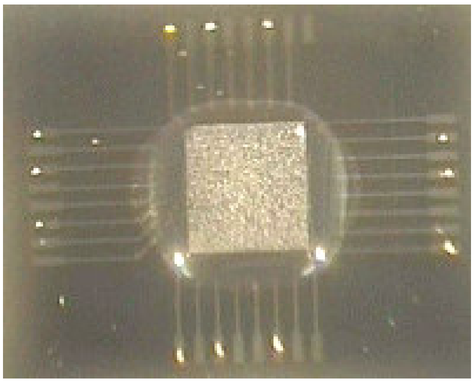

Figure 6.4: Test detector array coupled to a fan-out substrate.

6.3 Characterization, Results and Discussion

Following the test detector fabrication, detailed experimental characterization was performed to compare the performances of AlGaAs/GaAs and InP/InGaAs QWIPs [169]. The studies presented in this section were performed in collaboration with Oray Orkun Cellek who is a doctoral student in our research group.

For optical characterization, the test QWIPs were backside illuminated, and the test was performed under computer control using a blackbody source, a chopper, a transimpedance preamplifier, a lock-in amplifier and an FTIR system. Figure 6.5 displays the spectral response of the InP/InGaAs and AlGaAs/GaAs test QWIPs at 80 K. The responsivity of the InP/$In_{0.53}Ga_{0.47}As$ QWIP peaks at 7.85 μm with $\Delta\lambda/\lambda_p$ of 11%, and $Al_{0.27}Ga_{0.73}As$/GaAs QWIP responsivity peaks at 7.74 μm with $\Delta\lambda/\lambda_p$ of 15%. While the $Al_{0.27}Ga_{0.73}As$/GaAs QWIP yields slightly broader photoresponse, this difference is not expected to significantly affect the conclusions of this work. The photocurrents in the devices under 180° FOV can be calculated by

$$I_p = A \times \int_0^\infty R(\lambda) \times E(\lambda) \times d\lambda \tag{6.6}$$

where R(λ) is normalized responsivity, and E(λ) is the radiant incidence. Calculations for normalized responses and 300 K background show that the photocurrent difference should be less than 25% under similar peak responsivity.

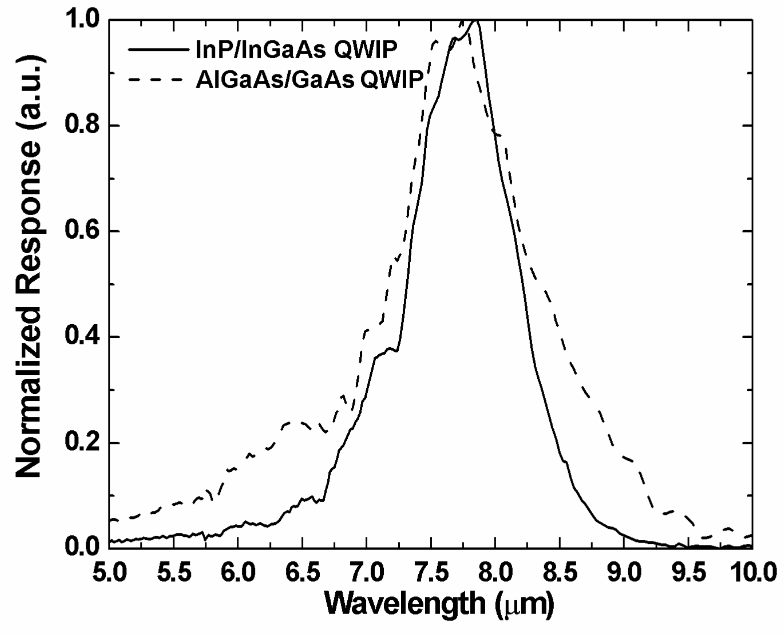

Figure 6.5: Spectral response of 21×21 μm^2 InP/InGaAs and AlGaAs/GaAs QWIPs under –1.5 V bias at 80 K [169].

Figure 6.6 shows the dark current versus bias characteristics of the InP/InGaAs QWIP at various temperatures and that of AlGaAs/GaAs QWIP at 77 K. The photocurrent obtained with f/2 aperture under 300 K background is also displayed for the InP/InGaAs QWIP showing background limited performance (BLIP) under low bias voltages at 77 K. Under reverse bias, the BLIP region extends up to 3.2 V at 70 K. At low reverse bias, 77 K dark current of the InP/InGaAs QWIP is considerably lower than that of the AlGaAs/GaAs QWIP. However, 77 K dark current of the InP/InGaAs QWIP exceeds that of AlGaAs/GaAs QWIP by nearly an order of magnitude under larger reverse bias voltages. This can be attributed to much higher rate of increase of the InP/InGaAs QWIP gain with increasing bias under moderately large bias voltages and possible onset of impact ionization under larger bias. Dark current of the AlGaAs/GaAs QWIP increases more rapidly than that of the InP/InGaAs QWIP under small reverse bias voltages. This can be attributed to the upper subband position in the quantum well. The excited subband of the AlGaAs/GaAs QWIP should be closer to the continuum than that of the InP/InGaAs QWIP, which makes the escape of the thermally excited electrons easier.

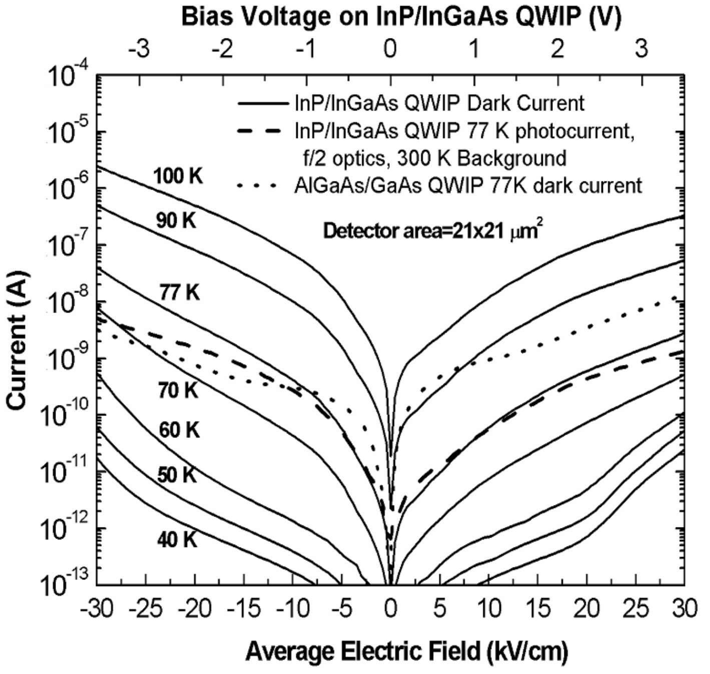

Figure 6.6: Bias dependence of the dark current at various temperatures and 77 K photocurrent with f/2 optics, 300 K background [169].

Positive bias dark current is smaller than that under negative bias for the InP/InGaAs QWIP. This is in agreement with the result repoted by Gunapala *et. al.* [161] on MOMBE grown QWIPs, and in contrast to that reported by Andersson *et. al.* [162] on MOVPE grown QWIPs. The lower dark current under forward bias (mesa top positive) suggests a lower barrier in the InGaAs on InP interface when compared with that in the InP on InGaAs interface reflecting an asymmetry. While other explanations are possible, this can be attributed to the graded nature of the InGaAs on InP interface. Positive bias spectral response is considerably narrower than that under negative bias in agreement with Ref. [161].

Figure 6.7 compares the 77 K dark current density of the InP/InGaAs test QWIPs with various mesa perimeter/area ratios indicating that the dark current is independent of surface effects in the entire bias region of interest. This shows that the large rate of increase of the dark current with bias under large bias voltages is mainly due to bulk generation mechanisms.

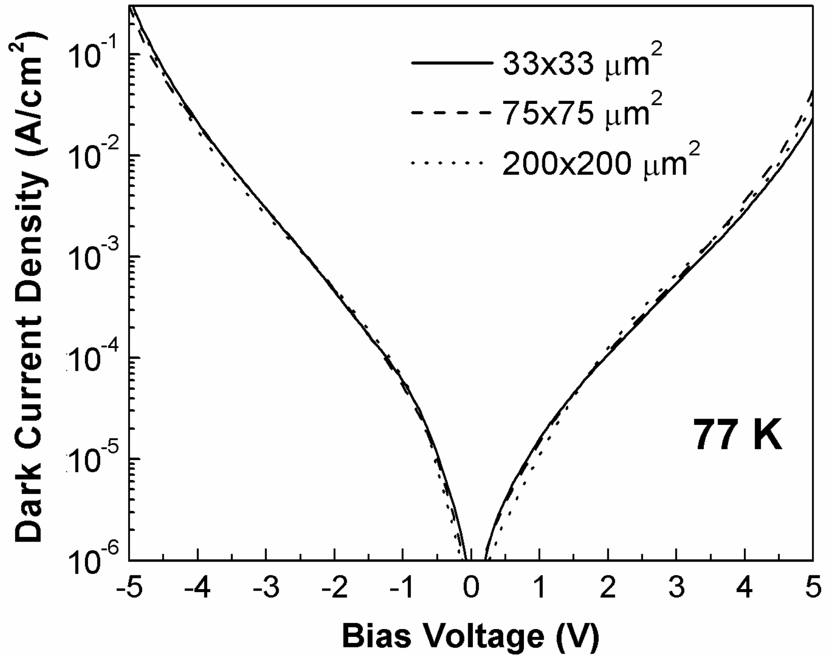

Figure 6.7: Dark current density of InP/InGaAs test QWIPs with various mesa sizes at 77 K [169].

Figure 6.8 compares the 77 K peak responsivities of the InP/InGaAs and AlGaAs/GaAs QWIPs under reverse bias. The highest responsivity obtained with the AlGaAs/GaAs QWIP is ~0.1 A/W under typical reverse bias voltages. The responsivity under positive bias is somewhat higher under large bias reaching a maximum of ~0.2 A/W in the bias region of interest. The InP/InGaAs QWIP yields an order of magnitude higher responsivities reaching 2.9 A/W at -3 V bias corresponding to 46% quantum efficiency-gain product.

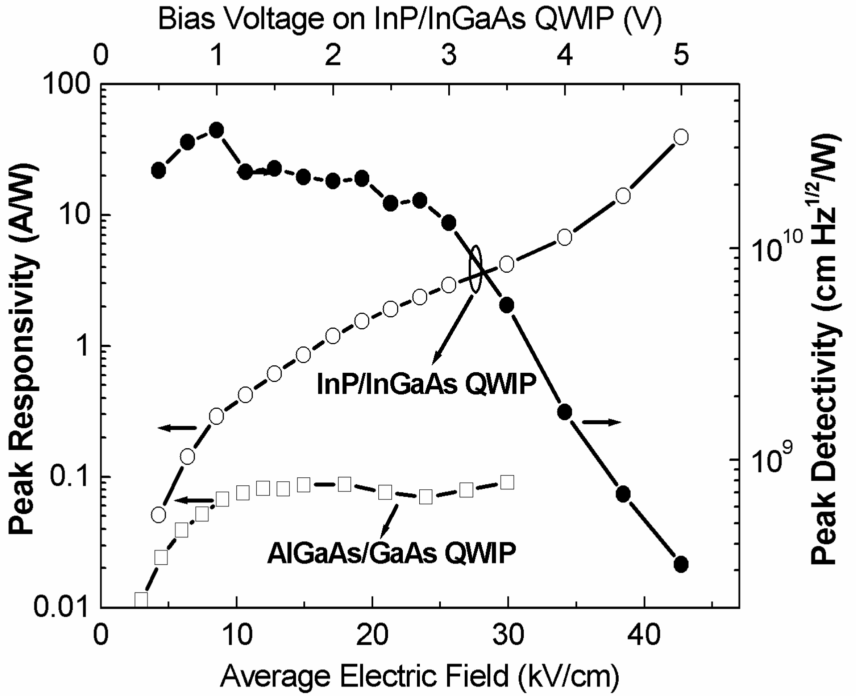

Figure 6.8: Peak responsivities of InP/InGaAs and AlGaAs/GaAs QWIPs and the peak detectivity of InP/InGaAs QWIP (without cold shield) at 77 K [169].

Under moderate bias, the detectivity of the InP/InGaAs QWIP is slightly decreased with increasing bias due to stronger increase of the noise current with bias when compared with that of responsivity. For reverse bias voltages above ~3V, detectivity is significantly decreased with increasing bias, which can be attributed to the onset of impact ionization, as we will discuss below. It should be noted that the 77 K peak detectivity (without cold shield) of the InP/InGaAs QWIP is still higher than 1×10^{10} cmHz^{½}/W at reverse bias voltages yielding peak responsivity as high as ~3 A/W. The detector can be operated under these bias levels with slightly reduced detectivity, if short integration times are needed. Higher bias levels offering even larger responsivities are not appropriate due to significantly reduced detectivity.

In spite of the lower 77 K dark current of AlGaAs/GaAs QWIPs under moderate and large reverse bias, the measured 77 K peak detectivities of these QWIPs ($\sim 1\times10^{10}$ $\mathrm{cmHz^{1/2}/W}$ at 20 kV/cm and lower under larger bias) are slightly lower than those of InP/InGaAs QWIPs under the same e-fields, due to the much lower reponsivity of the AlGaAs/GaAs QWIPs.

Figure 6.9 compares the 77 K noise gain (g_n) obtained through noise and dark current measurements with the photoconductive gain (g_p) in the InP/InGaAs QWIP. The photoconductive gain is extracted from the responsivity measurements by assuming that the noise gain is equal to the photoconductive gain under moderately large bias voltages, and determining the quantum efficiency (η) of the InP/InGaAs QWIP to be 5.8%. The bias dependence of the noise gain follows that of the responsivity until the bias reaches ~3 V (electric field ≅ 25 kV/cm). Assuming that the quantum efficiency does not significantly depend on electric field (E-field) in the bias region of interest, it can be concluded that the bias dependence of the noise gain is similar to that of the photoconductive gain in this bias region. Beyond the above E-field, the rate of increase of the noise gain with bias is apparently much higher than that of the photoconductive gain. Similar observation was reported on GaAs/InGaAs QWIPs by Rehm *et. al.* [174]. As seen in the inset of Figure 6.9, the activation energy becomes as low as ~60 meV under large E-fields, suggesting that the thermionic emission is not the dominant dark current generation mechanism under large bias. As shown in Figure 6.7, the dark current density is independent of the detector dimensions implying that the additional generation mechanism is not related with the surface effects. While, we will discuss the above observations in the framework of the impact ionization model [175, 176], we believe that this phenomenon needs further investigation.

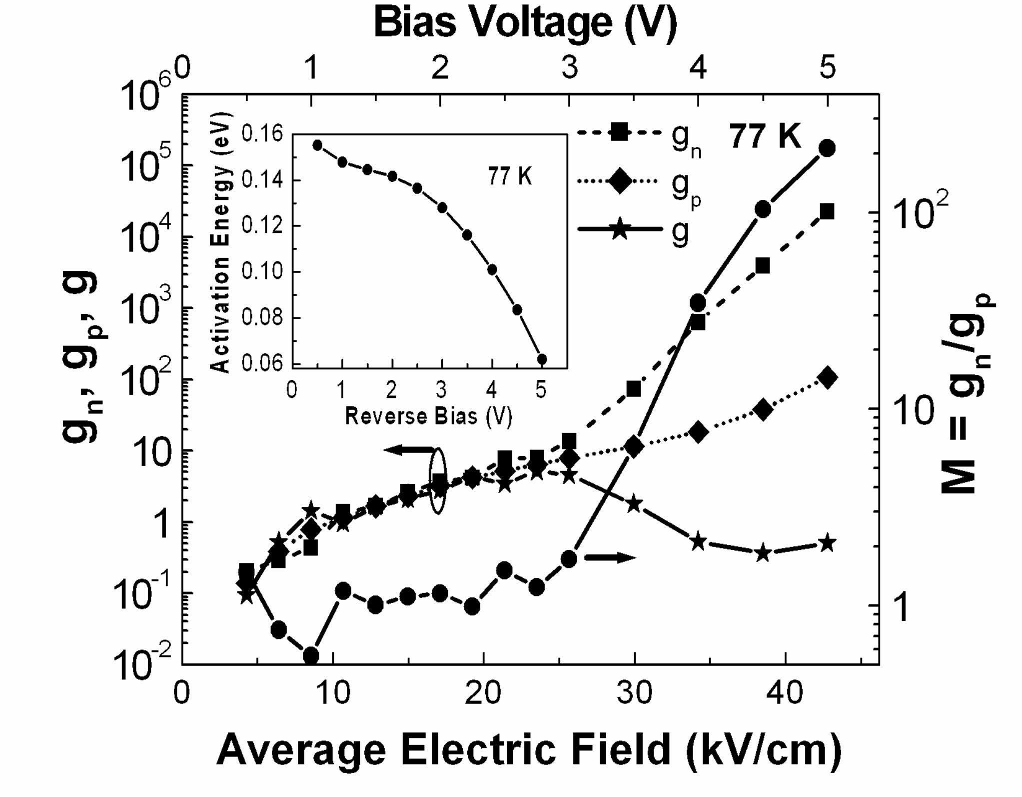

Figure 6.9: InP/InGaAs QWIP gains versus the reverse bias voltage at 77 K. The activation energy extracted from the dark current measurements at different temperatures is shown in the inset [169].

Based on the impact ionization model [175, 176], g_p=gM and g_n=gM^2 where M is the multiplication factor, if the capture probability is much smaller than 1, which is a good assumption for InP/InGaAs QWIPs as we have verified through ensemble MC simulations [177]. In the above expressions, g is the net gain, which is the gain in the absence of impact ionization. As shown in Figure 6.9, while M~1 under low and moderately large bias, it rapidly increases with bias for bias voltages exceeding 3 V, and becomes as high as 213 under 5 V. This observation is not consistent with that of Aslan *et. al.* [167] who reported the bias dependence of M in chemical beam epitaxy grown 20-well, dual band InP/InGaAs QWIPs up to 3 V, and observed the saturation of M around 2 for bias voltages exceeding 2 V. The rapid increase of M with increasing bias was also reported by Rehm *et. al.* [176] for 20-well GaAs/$In_{0.3}Ga_{0.7}As$ QWIPs for E-fields exceeding ~22 kV/cm (M=3.6 at 37 kV/cm). At similar E-fields, M, in our case, seems to be larger. However, the threshold E-field for impact ionization

(~25 kV/cm) is close to that (~22 kV/cm) observed on GaAs/$In_{0.3}Ga_{0.7}As$ QWIPs with peak responsivity wavelength of 8.5 µm [176]. The net gain, g, is also shown in Figure 6.9 suggesting a considerable decrease in the drift distance in the large bias region. The detectivity is inversely related to M. Therefore, if the detector is operated with very high responsivity in the impact ionization regime, the detectivity is significantly sacrificed [177].

An important difference between the properties of the materials utilized in InP/InGaAs and AlGaAs/GaAs QWIPs is the larger energy spacings between the central (Γ) and the satellite valleys in InP when compared with those in $Al_xGa_{1-x}As$ (x = ~0.3). The effects of this difference on the QWIP behavior were evaluated through ensemble MC simulations developed by Oray Orkun Cellek as a part of his Ph.D thesis work. Both three-dimensional (3D) and two-dimensional (2D) electrons were simulated by taking size quantization into account in Γ and L valleys of the conduction band. The rates of the presumably important 2D↔2D, and 2D↔3D scattering processes were calculated using the wavefunction solutions of the Schrödinger's equation.

The scattering mechanisms included in the simulation are polar optical phonon (POP), acoustic phonon, ionized impurity, and intervalley (equivalent and nonequivalent) scattering. The quantum mechanical reflection and transmission of the electrons by the heterointerfaces were included in the simulation. Each simulation was carried out until the steady state was reached, beyond which no significant change occured in the observed quantities.

We simulated 16-well $Al_xGa_{1-x}As$/GaAs QWIPs in the standard structure with barrier Al mole fraction (x) of 0.3. The simulated structure has 44-Å-thick GaAs wells sandwiched between 500-Å-thick $Al_{0.3}Ga_{0.7}As$ barriers. We repeated the simulations by artificially varying the energy spacings between the central and satellite valleys (to be equal to those in InP) in the conduction band.

Figure 6.10 presents a comparison of the experimentally obtained drift distances with those calculated through MC simulations [169]. Full squares represent the results of the simulations on $Al_{0.3}Ga_{0.7}As$ QWIPs, and the full circles represent the drift distance characteristic obtained when the barrier material intervalley energy spacings are artificially increased to be equal to those in InP. There is reasonable agreement between the experimental and theoretical results up to the onset of impact ionization, which was not included in the simulations. The above results suggest that the drift distance strongly depends on the energy spacing between central and satellite valleys in the conduction band of the barrier material.

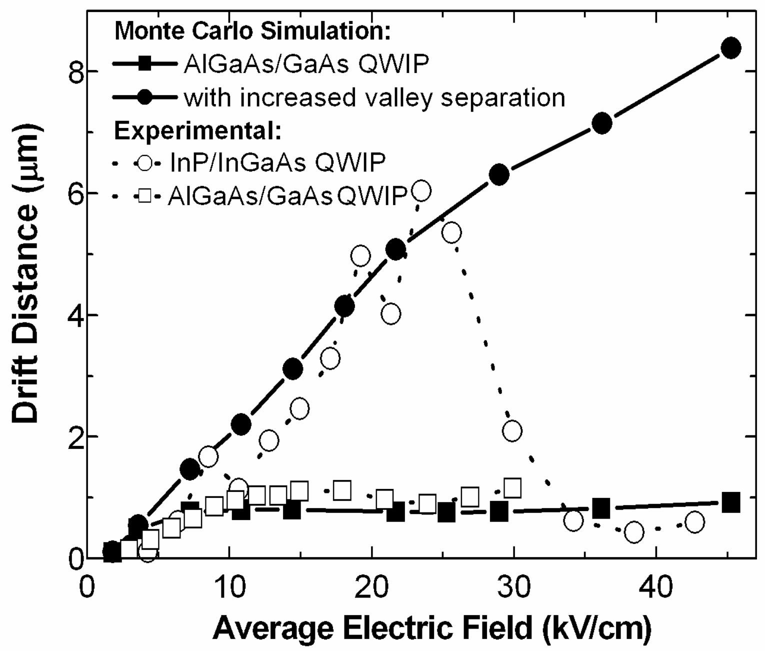

Figure 6.10: Comparison of the observed drift distances with the simulation results [169].

One of the important conclusions that can be drawn from the above observations is that the InP/InGaAs QWIPs operate with reasonably high responsivity and detectivity under moderately large bias up to an average E-field of ~25 kV/cm. While the higher responsivity in InP/InGaAs QWIPs in this bias region was attributed to better transport properties in the binary barrier material [161], our MC simulation results suggest that it mainly results from higher excited electron lifetime [177, 178]. Figure 6.11 and 6.12 show the effects of the intervalley energy spacings in the barrier material on the average electron velocity and the electron lifetime in the device.

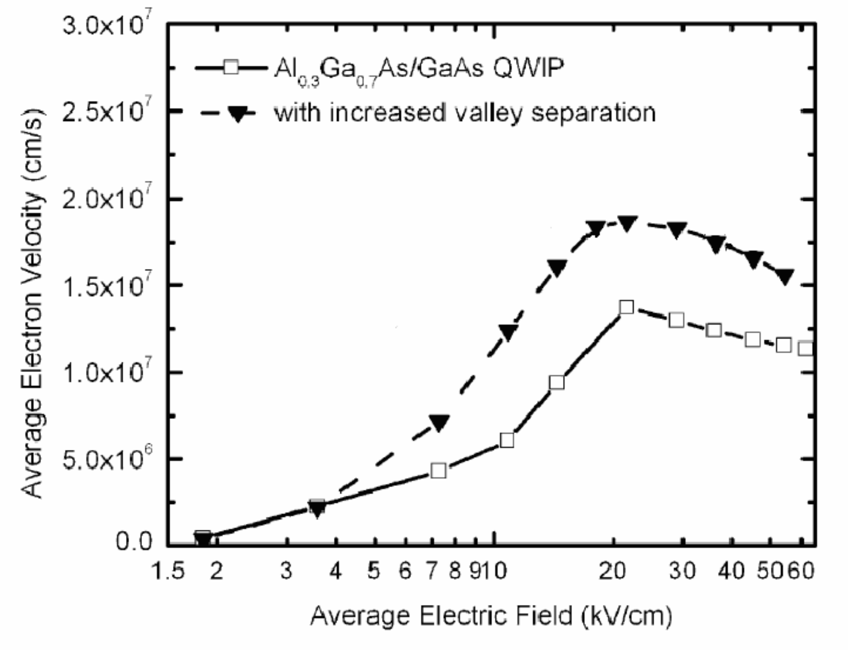

Figure 6.11: Dependence of average electron velocity on electric field [177].

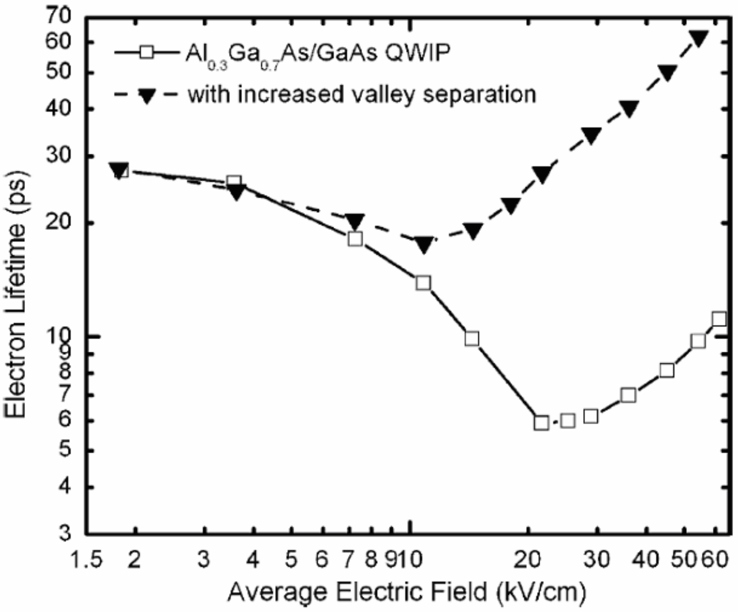

Figure 6.12: Average electron lifetime vs. the average electric field in the device [177].

Increased energy spacing between the central and satellite valleys (equal to those in InP) results in an improvement in the high bias average electron velocity by a factor of ~1.5, while the excited electron lifetime increases by a factor of ~6 resulting in an improvement in the large bias gain by a factor of ~10. These results suggest that the gain improves with increasing energy spacing between the central and satellite valleys mainly through the increase in the excited electron lifetime as a result of higher Γ valley occupancy of the continuum electrons with relatively high kinetic energy.

6.4 Summary and Conclusions

This chapter has presented the single pixel characterization results of AlGaAs/GaAs and InP/InGaAs QWIPs. After describing the fabrication process developed for the test QWIP fabrication, performance of InP/InGaAs QWIP was compared with that of AlGaAs/GaAs QWIP. The results are summarized in Table 6.1. Additionally, the reasons behind the relatively high responsivity of the InP/InGaAs QWIPs were investigated by MC simulations.

Table 6.1: Comparison of the characterization results of AlGaAs/GaAs and InP/InGaAs structures.

	AlGaAs/GaAs	InP/InGaAs
D^* (cmHz^{½}/W) (at 20 kV/cm)	1×10^{10}	1.9×10^{10}
λ_p (μm)	7.74	7.85
$\Delta\lambda/\lambda_p$	15%	11%
Number of quantum wells	30	20
Detector Area	21×21 μm^2	21×21 μm^2
Dark Current Density at 77 K (A/cm^2)	3.32×10^{-5} (at 5 kV/cm) 3.78×10^{-4} (at 25 kV/cm)	1.34×10^{-5} (at 5 kV/cm) 2.66×10^{-3} (at 25 kV/cm)
R_p (A/W)	0.029 (at 5 kV/cm) 0.075 (at 25 kV/cm)	0.073 (at 5 kV/cm) 2.75 (at 25 kV/cm)

The following important conclusions can be drawn from this part:

- InP/InGaAs material system yields significantly larger photoconductive gain, and hence larger quantum efficiency-gain products.

- InP/InGaAs QWIP with the given parameters shows BLIP under low bias voltages at 77 K, and the BLIP region extends up to large reverse bias voltages (3.2 V) at 70 K.

- 77 K dark current of the InP/InGaAs QWIP is lower than that of AlGaAs/GaAs QWIP under small reverse bias voltages, but becomes larger under moderately large reverse bias voltages. I-V characteristics of InP/InGaAs QWIPs with various mesa perimeter/area ratios show that the effect of the surface mechanisms on the detector dark current is negligible, and the higher dark current of the InP/InGaAs QWIPs under large reverse bias is generated by bulk mechanisms.

- The InP/InGaAs QWIP yields an order of magnitude higher responsivity than that of the AlGaAs/GaAs QWIP reaching 2.9 A/W at –3 V bias corresponding to a quantum efficiency-gain product of 0.46. The detectivity is still above 1×10^{10} cmHz$^{1/2}$/W at this bias voltage.

- Beyond the electric field of 25 kV/cm, noise gain starts to increase more rapidly than the photoconductive gain in InP/InGaAs QWIP as also observed previously by other groups. The difference in the rates of increase can be attributed to impact ionization. While photoconductive and noise gains increase in the avalanche region, the net gain decreases due to a considerable decrease in the drift distance in the large bias region.

- The experimental and MC simulation results regarding the drift distance in the InP/InGaAs and AlGaAs/GaAs QWIPs are compatible showing that the drift distance strongly depends on the energy spacings between the central and satellite valleys in the conduction band of the barrier material. The results suggest that the higher responsivity in InP/InGaAs QWIPs under large bias results from higher excited electron lifetime rather than better transport properties in the binary barrier material, which was suggested previously [161].

The single pixel characterizations discussed in this chapter shows that InP/InGaAs QWIP has better responsivity while its detectivity is comparable to that of AlGaAs/GaAs QWIPs. Large format FPA characteristics of the InP/InGaAs QWIPs will be assessed in the next chapter.

CHAPTER VII

InP/InGaAs QWIPs: FPA PERFORMANCE

The characteristics of MBE grown LWIR InP/InGaAs QWIPs were discussed in the previous chapter with a conclusion that the responsivity of these QWIPs is much larger than that of AlGaAs/GaAs QWIPs at moderate and high bias. The first InP/InGaAs QWIP FPA was reported recently by Jiang *et. al.* [168] with a format of 256×256 using metal organic chemical vapor deposition grown material. With the main objective of assessing the FPA level performance of InP/InGaAs QWIPs, we present in this chapter the characteristics of 640×512 InP/InGaAs QWIP FPA, which, to our knowledge, is the largest format InP/InGaAs QWIP FPA reported [169, 170].

We fabricated the 640×512 InP/InGaAs QWIP FPA with the optimized fabrication process presented in Chapter V. Some fabrication steps were modified due to the different material system employed in this part. The FPA was hybridized to an Indigo ISC9803 ROIC. Following under filling, FPA substrate was thinned, and the hybrid was mounted on an 84-pin LCC package. Figure 7.1 shows the picture of the FPA after packaging.

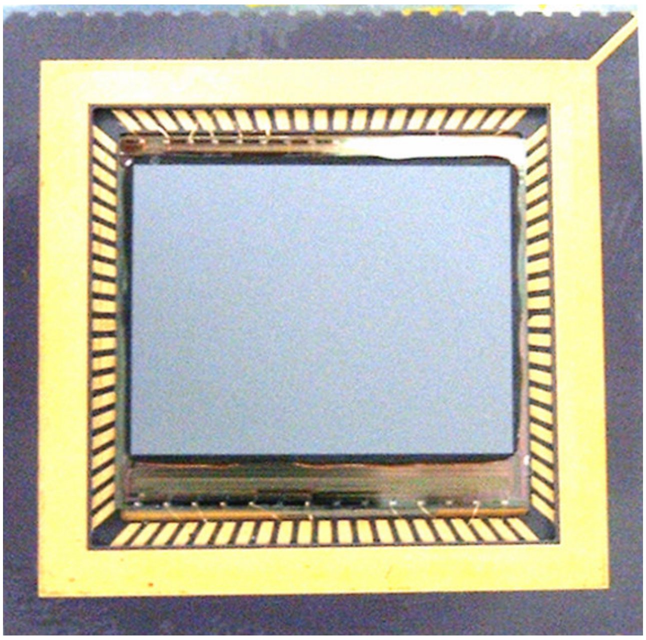

Figure 7.1: 640×512 InP/InGaAs QWIP FPA after packaging.

Figure 7.2 shows the mean NETD of the 640×512 InP/InGaAs QWIP FPA versus the detector bias at 70 and 77 K with half and 2/3 filled ROIC capacitors, and f/1.5 optical aperture. Due to a misalignment during flip-chip bonding, a small percentage of the pixels (gathered at one corner) had no electrical connection with the corresponding ROIC pixels. The total number of the bad pixels was smaller than 3%. These pixels and those with NETD values above 500 mK were excluded in the determination of the mean NETD. It should be noted that the FPA yields reasonably low NETD (83 mK with half filled capacitors) at 70 K even under 2.5 V bias which offers very high responsivity (2 A/W, see Figure 6.8) allowing short integration times.

Figure 7.3 shows the variation of the NETD with the integration time for the InP/InGaAs QWIP FPA at 70 K (half filled ROIC capacitors). The FPA yields reasonably low NETDs with sub-millisecond integration times, and the NETD is nearly proportional to the inverse of the square root of the integration time up to ~1 ms. For larger integration times, the decrease in NETD with increasing integration time is slower.

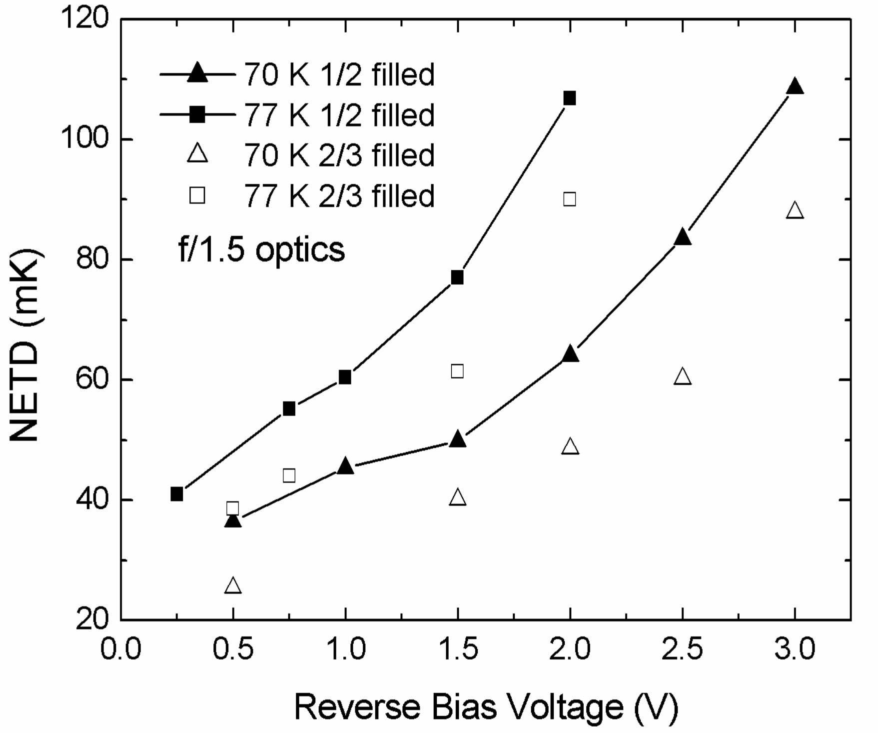

Figure 7.2: Mean NETD of the 640×512 InP/InGaAs QWIP FPA versus reverse bias voltage.

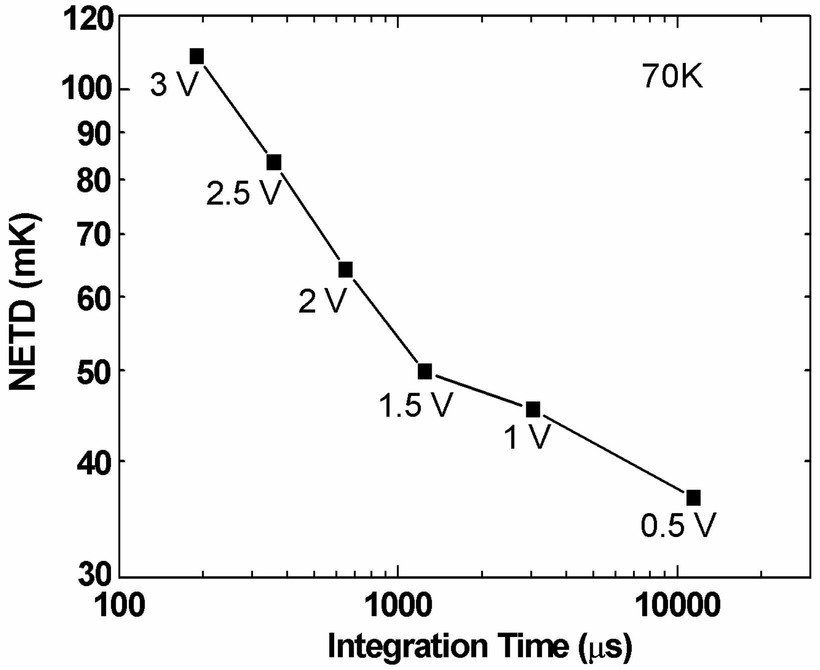

Figure 7.3: Mean NETD of the 640×512 InP/InGaAs QWIP FPA versus integration time at 70 K with half filled ROIC capacitors [169].

Figure 7.4 shows the portions of the integration capacitors filled by dark current and photocurrent at 77 K under various reverse bias voltages when the detectors were looking at 290 K background with f/2 aperture. As shown in the figure, as the reverse bias is increased, dark current fills a larger portion of the capacitor at the above FPA temperature. For an FPA under BLIP conditions, half of the integration capacitors must be filled to maximize the dynamic range. However, as can be seen from Figure 7.4, more than half of the capacitors can be filled without considerably sacrificing the dynamic range under moderately large bias voltages, if the detector is not ~100% BLIP. The signal-to-noise ratio can thus be improved without considerable reduction in the dynamic range, since NETD improves with integrated charge.

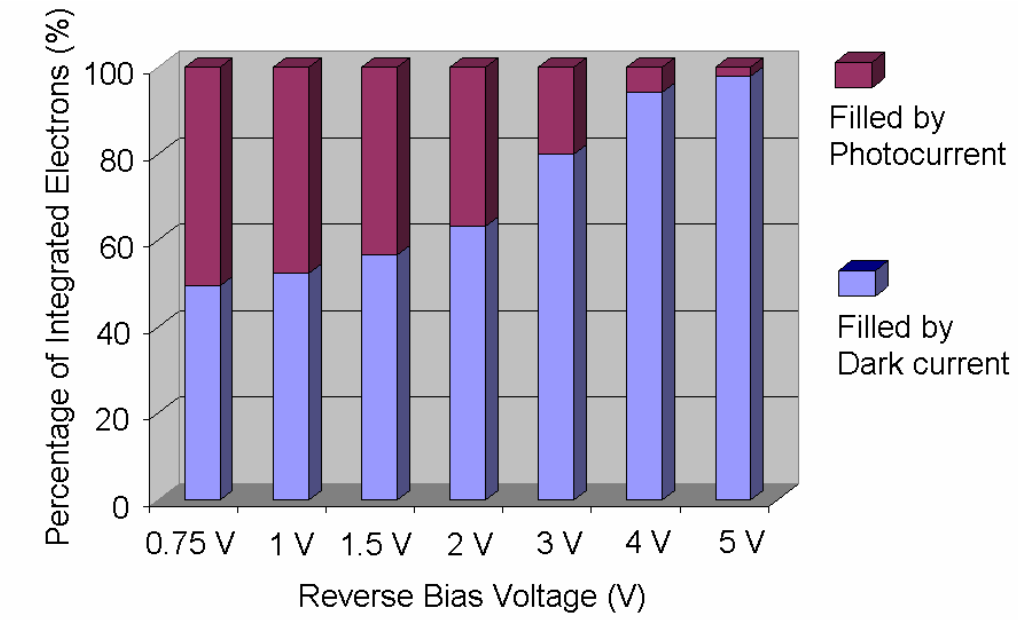

Figure 7.4: Percentage of integrated electrons constituting photocurrent and dark current at 77 K.

Figure 7.5 shows the uncorrected NETD histogram of the FPA. The NETD nonuniformity (σ/mean) is 17%, which is comparable to that of LWIR AlGaAs/GaAs QWIP FPAs with the same format [179]. The uncorrected DC signal nonuniformity of the FPA is 5.9% excluding bad pixels. This nonuniformity level is comparable to that of LWIR AlGaAs/GaAs QWIP FPAs (5.5% for 256×256 FPA) [179].

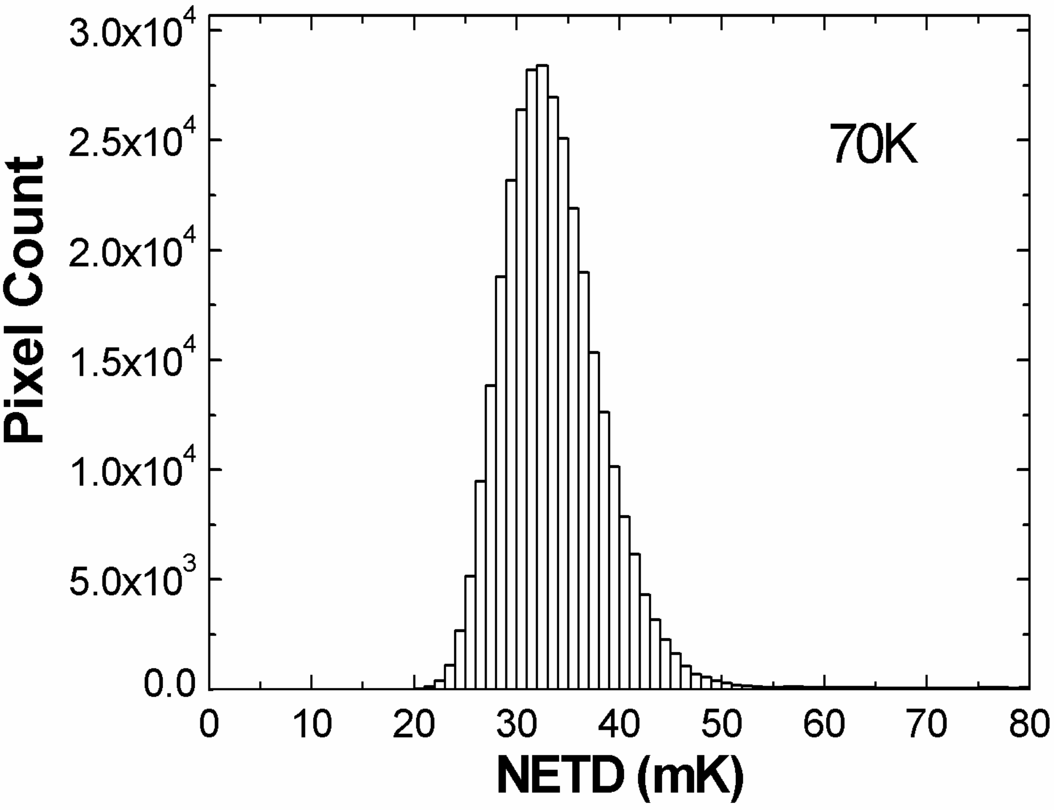

Figure 7.5: Uncorrected NETD histogram of the 640×512 InP/InGaAs QWIP FPA at 70 K with 0.5 V bias [169].

Figure 7.6 shows the corrected DC signal histogram of the FPA with 77 K operation temperature and background temperature of 307 K. After two-point calibration at 27 and 37 ˚C, the nonuniformity level drops to ~0.1%. Figure 7.7 shows the 14-bit digital signal distribution over 2-D array when the FPA looks at 307 K background through f/1.5 field of view. In this figure, the corner with bad pixels is excluded. In order to make the distribution more clear the FPA is divided into 8×8 sub-matrices. The effect of $\cos^4\theta$ shading can be easily seen over the signal distribution in the FPA. Cold stop limits the field of view of FPA pixels in a nonuniform manner. Due to the larger solid angle of the central pixels, they receive higher flux density relative to those at the corners and edges. $\mathrm{Cos}^4\theta$ shading effect is radially symmetrical where θ is the angle from the optical axis to a detector when measured from lens' plane [180].

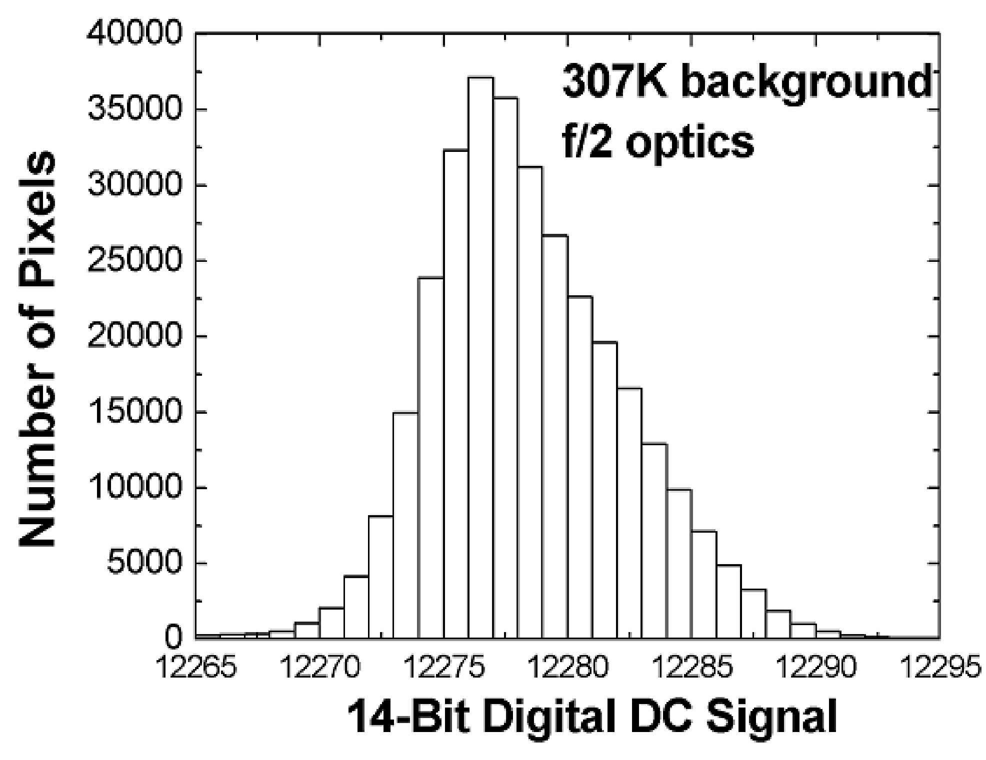

Figure 7.6: Corrected DC signal histogram of the fabricated FPA with background temperature of 307K and cold finger temperature of 77 K [170].

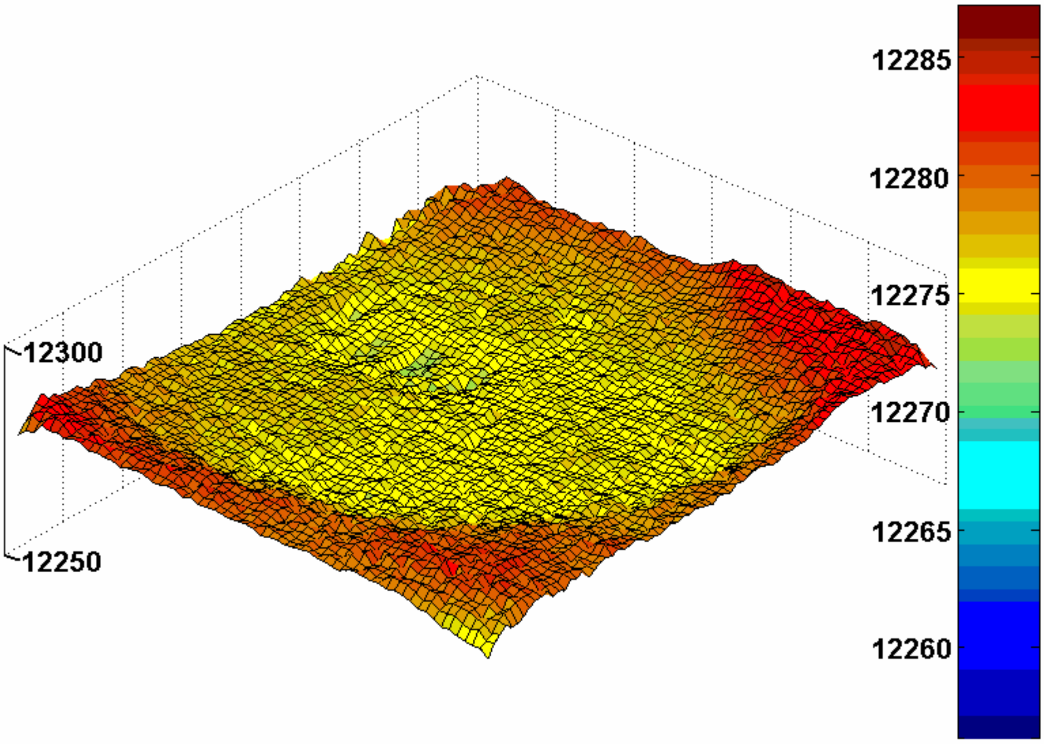

Figure 7.7: Digital signal distribution over 2-D array.

Figure 7.8 shows two thermal images (indoor and outdoor) taken with the 640×512 InP/InGaAs QWIP FPA at a sensor temperature of 78 K. The bad pixels due to misalignment during hybridization can be seen on the top right corner in Figure 7.8(a). Figure 7.8(b) shows a thermal image windowed with the format of 640×448, which was taken on a summer day after midnight. The regions where the cars parked during daytime can easily be detected.

(a)

(b)

Figure 7.8: Thermal images (a) indoor [170], and (b) outdoor taken with the 640×512 InP/InGaAs QWIP FPA at a sensor temperature of 78 K. The regions where the cars parked during daytime can easily be detected in (b).

Figures 7.9 and 7.10 show indoor and outdoor thermal images taken with the 640×512 InP/InGaAs QWIP FPA at a sensor temperature of 70 K. The images are windowed with the format of 640×448. The integration times for indoor and outdoor images were 4 and 7.5 msec, respectively. The outdoor image was taken at a winter night when the outside temperature was -6 °C. These thermal images confirm the high sensitivity of the InP/InGaAs QWIP FPA.

Figure 7.9: Indoor thermal image taken with the InP/InGaAs QWIP FPA at 70 K sensor temperature [169].

Figure 7.10: Outdoor thermal image taken with the InP/InGaAs QWIP FPA at 70 K sensor temperature.

The sensitivity of the FPA can be improved by at least 30% if anti-reflection coating is used, the fill factor (71%) is increased, and the optical grating is optimized, in which case the NETD performance of the FPA becomes comparable to the state of the art LWIR AlGaAs/GaAs QWIP FPAs [179]. In this case, the InP/InGaAs QWIP FPA, being able to tolerate higher ROIC noise floors, would be superior to AlGaAs/GaAs FPAs for applications requiring short integration times.

NETD can be either detectivity or uniformity limited. In the uniformity limited NETD case, pixel to pixel signal variation must be smaller than the signal difference generated by the temperature difference to be detected. Thermal contrast is defined as the percent change in photon flux for one Kelvin change in the background temperature at a specific wavelength. When the thermal contrast is large, uniformity limited NETD improves. Nonuniformity determines the minimum amount of detectable DC signal produced by temperature difference equal to uniformity limited NETD. Under ~100% BLIP conditions, where the dark current is negligible when compared with the photocurrent, DC signal produced for 1 K difference when the FPA looks at 290 K background can be given by

$$\Delta Signal = Mean \quad Signal \times \int_{\lambda_1}^{\lambda_2} ThermalContrast(\lambda) \times \eta_a(\lambda) \times g_p \times d\lambda \qquad (7.1)$$

where *Mean Signal* is the average DC signal corresponding to 290 K background, $\eta_a(\lambda)$ is absorption quantum efficiency as a function of wavelength, and g_p is photoconductive gain. Then uniformity limited NETD is given by

$$NETD = \frac{u \times Mean \quad Signal}{\Delta Signal} = \frac{u}{\int_{\lambda_1}^{\lambda_2} ThermalContrast(\lambda) \times \eta_a(\lambda) \times g_p \times d\lambda} \qquad (7.2)$$

On the other hand, when the NETD is limited by detectivity rather than nonuniformity, NETD is given by [5]

$$NETD = \frac{T_B}{2} \sqrt{\frac{g}{Q}} \qquad (7.3)$$

where T_B is the background temperature, g is the photoconductive gain, and Q is number of the accumulated electrons in the integration capacitor.

Figure 7.11 shows the calculated NETD values for the InP/InGaAs QWIP FPA operating at 77 K under uniformity and detectivity limited cases. As the bias voltage is reduced, dark current decreases resulting in improved NETD performance. On the other hand, for small reverse bias voltages nonuniformity becomes dominant and limits the NETD. Reverse bias voltage should be set according to the application that the imager is intended to be used for. When high frame rates are desired, moderately large bias voltages should be applied. On the other hand, small reverse bias voltages with longer integration times can be chosen for more sensitive imaging. Smallest NETD is achieved under uniformity limited regime. As can be seen from Equation 7.2, uniformity limited NETD is directly proportional to *u*. A tenfold improvement in uniformity would result in NETD value of 5 mK. Uniformity of the FPA should be improved, if it is to be used in uniformity limited regime, otherwise detectivity of the pixels must be optimized.

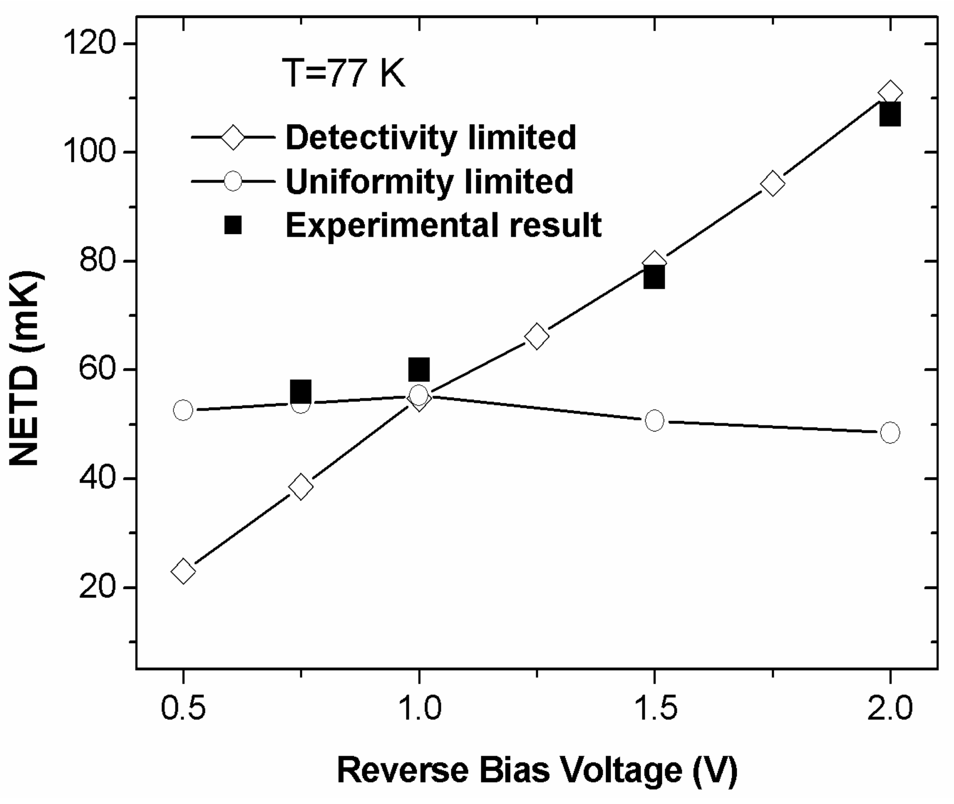

Figure 7.11: 77 K Detectivity and uniformity limited NETD values versus reverse bias voltage.

In the last two chapters, we reported the detailed electrical and optical characteristics of small size (21×21 μm^2), MBE grown InP/InGaAs QWIPs, and the performance of 640×512 InP/InGaAs QWIP FPA, as well as a comparison of the detector characteristics with that of LWIR AlGaAs/GaAs QWIPs displaying similar spectral response. At 70 K, the InP/InGaAs QWIPs show background limited performance (f/2 aperture) with a detectivity above 1×10^{10} $cmHz^{1/2}/W$ up to ~3 V bias where the responsivity (2.9 A/W) is an order of magnitude higher than that of AlGaAs/GaAs QWIPs. The results suggest that the impact ionization does not start until the average E-field in the device reaches ~25 kV/cm in InP/InGaAs QWIPs, and the relatively high responsivity for lower E-fields is due to the large photoconductive gain. In addition to the other advantages of the InP/InGaAs material system over AlGaAs/GaAs, this property of InP/InGaAs QWIPs can be utilized for thermal imaging applications requiring high responsivity and short integration times. Large format InP/InGaAs QWIP FPA offers reasonably low NETD even at short integration times with spatial nonuniformity comparable to that of LWIR AlGaAs/GaAs QWIP FPAs. The results clearly show the potential of InP/InGaAs as an alternative to the most widely employed AlGaAs/GaAs system for LWIR QWIP applications.

CHAPTER VIII

CONCLUSIONS

This thesis reports the results of a detailed study on the investigation of MBE grown midwavelength infrared $InAs_xSb_{1-x}$ photodiodes on GaAs and Si substrates, and LWIR InP/InGaAs QWIPs. In the first part of the study, InSb and $InAs_{0.8}Sb_{0.2}$ photodiodes grown on Si and GaAs substrates were fabricated, characterized and modeled in detail in order to reveal the dominant dark current mechanisms arising from large lattice mismatch. With the main objective of assessing the feasibility of InP/InGaAs material system as an alternative to AlGaAs/GaAs for QWIP applications, the second part of the study investigates the characteristics of LWIR $InP/In_{0.53}Ga_{0.47}As$ QWIPs, and 640×512 FPA.

Detector quality growth of InSb or $InAs_xSb_{1-x}$ on Si or GaAs substrates is indispensable due to the availability of large area high-quality GaAs and Si substrates, possibility of monolithic integration with Si or GaAs ROIC, elimination of the substrate thinning process, and the problems related with thermal expansion coefficient mismatch. In the first part of this study, a detailed characterization study was carried out on $InAs_{0.8}Sb_{0.2}$/GaAs and InSb/Si homojunction, and AlInSb/InSb/Si heterojunction test photodiodes as an assessment of the feasibility of this approach. This study yielded important scientific information on the performance limiting dark current and noise mechanisms in infrared photodetectors grown on lattice mismatched substrates. Following the fabrication of the test detectors, they were subjected to detailed electrical and optical characterization, and to a dark current modeling study. The detector noise was also investigated by fitting the theoretical models to noise data. 128×128 FPAs were also fabricated with the AlInSb/InSb/Si and $InAs_{0.8}Sb_{0.2}$/GaAs detector epilayer structures to assess the FPA level performance. The following important conclusions can be drawn from this part of the work.

- The electrical and optical characterization results on $InAs_{0.8}Sb_{0.2}$/GaAs photodiodes display potential for both cooled and near room temperature detectors. The photodiodes yield peak detectivities of 1.4×10^{10} and 7.5×10^{8} cmHz^{½}/W at 77 K and 240 K, respectively, and surface mechanisms do not significantly contribute to the dark current of the detectors under small reverse bias voltages commonly employed in thermal imaging.

- Under low and medium reverse bias, low temperature R_oA limiting mechanism in $InAs_{0.8}Sb_{0.2}$/GaAs photodiodes is trap assisted tunneling, which also introduces considerable 1/*f* noise. This observation is similar to that of Nemirovsky *et. al.* [115] on the HgCdTe diodes.

- 80 K zero bias differential resistance of the InSb/Si detectors is limited by Ohmic leakage, and the TAT process becomes dominant as the detector reverse bias approaches 0.1 V. The shunt resistance associated with the Ohmic leakage shows a small activation energy of 25 meV showing that hetero-epitaxial growth of alternative larger bandgap materials (such as $InAs_xSb_{1-x}$ instead of InSb) may not improve detector R_0A as significantly as expected, if the detector performance is limited by the shunt resistance.

- At 80 K, 1/*f* noise of the InSb/Si detectors is dominated by TAT mechanism. Measured 1/*f* noise current (at 1 Hz) is in agreement with the emprical model

$i_{nTAT} = \alpha I_{TAT}^{\beta}$ with α and β close to those found by Nemirovsky and Unikovsky [114] for HgCdTe photodiodes, supporting their observations.

- The bias and temperature dependence of the $1/f$ noise current in InSb/Si detectors is in agreement with Kleinpenning's mobility fluctuation model [120] confirming the validity of this approach.

- Near zero-bias, InSb/Si photodiodes yield peak 77 K detectivity as high as $\sim 1\text{x}10^{10}$ cmHz $^{1/2}$/W in spite of the large lattice mismatch. This detectivity is almost within an order of magnitude of the typical InSb photodetector detectivity achieved on lattice matched substrate. The defects do not seem to degrade the InSb/Si detector's peak quantum efficiency considerably, however they significantly increase the $1/f$ noise under moderate and large reverse bias.

- AlInSb/Si heterojunction diode yields an 80 K R_0A product slightly larger than that of InSb/Si homojunction photodiode due to lower shunt leakage, whose temperature dependence was found to be weak. However, the decrease in R_D with reverse bias voltage in AlInSb/Si detector is much faster than that of homojunction InSb/Si detector, which can be explained by higher trap density (N_t) in the heterojunction detector. The photoresponse of the AlInSb/Si detector also degrades more rapidly with decreasing wavelength, which can be attributed to the higher density of recombination centers close to substrate.

The above information can be used as reference for optimizing the performance of InSb or $InAs_xSb_{1-x}$ photodetectors grown on GaAs or Si substrates in the scope of further studies.

The second part of the study investigates the characteristics of LWIR $InP/In_{0.53}Ga_{0.47}As$ QWIPs, and 640×512 focal plane array (FPA), which to our knowledge, is the largest format InP/InGaAs QWIP FPA, and the first MBE grown LWIR InP/InGaAs QWIP FPA reported. $Al_{0.27}Ga_{0.73}As/GaAs$ QWIPs with similar spectral response were also fabricated and characterized for comparison. Following conclusions can be drawn from the second part of the work.

- 77 K dark current of the InP/InGaAs QWIP is lower than that of AlGaAs/GaAs QWIP under small reverse bias voltages, but becomes larger under moderately large reverse bias voltages. The effect of the surface mechanisms on the detector dark current is negligible, and the higher dark current of the InP/InGaAs QWIPs under large reverse bias is generated by bulk mechanisms.

- Impact ionization in InP/InGaAs QWIPs does not start until the average electric-field reaches ~25 kV/cm, and detectivity remains high under moderate bias (~2×10^{10} cmHz$^{1/2}$/W at 77 K). Beyond the electric field of 25 kV/cm, noise gain starts to increase much more rapidly than the photoconductive gain in InP/InGaAs QWIP as also observed by other groups. While photoconductive and noise gains increase in the avalanche region, the net gain decreases due to a considerable decrease in the drift distance in the large bias region.

- InP/InGaAs QWIPs yield quantum efficiency-gain product as high as 0.46 under –3 V bias. At 70 K, detector performance is background limited with f/2 aperture up to ~3 V bias where the peak responsivity (2.9 A/W) is an order of magnitude higher than that of the AlGaAs/GaAs QWIP.

- The experimental and theoretical (MC simulation) results show that the drift distance strongly depends on the energy spacings between the central and satellite valleys in the conduction band of the barrier material. The results suggest that the higher responsivity in InP/InGaAs QWIPs under large bias results from higher excited electron lifetime rather than better transport properties in the binary barrier material.

- The 640×512 InP/InGaAs QWIP FPA yields noise equivalent temperature difference of ~ 40 mK at an FPA temperature as high as 77 K. The FPA offers low NETD even with short integration times (τ). 70 K NETD values of the FPA with f/1.5 optics are 36 and 64 mK under –0.5 V (τ=11 ms) and –2 V (τ=650 μs) bias, respectively.

- The NETD nonuniformity (σ/mean) of the 640×512 InP/InGaAs QWIP FPA is 17%, which is comparable to that of LWIR AlGaAs/GaAs QWIP FPAs with the same format [179]. The uncorrected DC signal nonuniformity of the FPA is 5.9% excluding bad pixels. This nonuniformity level is comparable to that of LWIR AlGaAs/GaAs QWIP FPAs (5.5% for 256×256 FPA) [179].

- When the above findings are considered with the other advantages of the InP/InGaAs material system over AlGaAs/GaAs, it can be concluded that the InP/InGaAs material system is a very promising alternative to AlGaAs/GaAs for QWIPs in thermal imaging applications requiring high responsivity and short integration times.

In conclusion, the study reported in thesis has made considerable contribution to the field of infrared sensors and thermal imaging in both midwavelength and long wavelength infrared bands. The presented information is invaluable for the optimization of the sensors designed to operate in these bands toward lower cost and higher sensitivity thermal imaging with the infrared photon detectors.

APPENDIX A

DARK CURRENT GENERATION MECHANISMS

When 1/f noise is neglected, detectivity of a photodiode can be given as [1]

$$D^* = \frac{\eta q}{h\nu}\left[\frac{4kT}{R_0} + 2q^2\eta\phi_B\right]^{-1/2} \tag{A.1}$$

where η is the quantum efficiency, ϕ_B is background photon flux, and R_0 is the zero bias differential resistance of the photodiode. The second term in the parenthesis is due to the background noise, and the first term is due to Johnson and shot noise. The equation shows that high R_0 (and low dark current) is necessary for background limited operation of the detector. The reasons behind the detector dark current must be understood to minimize it.

Dark current generation mechanisms originate in the surface, bulk, or depletion region of a photodiode. Each of these mechanisms has its own individual relationship to voltage and temperature. By fitting the sum of the current components to experimental data over a range of both applied voltage and temperature, one can find the dominant mechanism at a specific temperature and bias. Once the performance limiting mechanisms are found, they may be eliminated by improving the growth conditions, fabrication process, and structural design. In this study, in order to reveal the dominant mechanisms, dark current versus bias characteristics at several temperatures have been measured, and theoretical models were fit to experimental results. Dark current generation mechanisms commonly encountered in MWIR photodiodes are diffusion, generation-recombination, tunneling, and ohmic leakage. The following sections discuss the dependence of these mechanisms on bias, temperature, and detector parameters.

A.1 Diffusion current

Diffusion current results from the flow of thermally generated minority carriers in p- and n-type regions to the other side of the junction. Diffusion is a fundamental mechanism and cannot be eliminated or lowered by optimizing the growth and detector parameters. This mechanism occurs in the bulk region and is not related to the surface. Diffusion current density can be given as [1]

$$J_D = J_s\left[\exp\left(\frac{qV}{kT}\right)-1\right] \tag{A.2}$$

where q is electron charge, V is the applied bias, k is the Boltzmann constant, T is diode temperature, and J_s is the saturation current density, which is given by

$$J_s = n_i^2\left(qkT\right)^{1/2}\left[\frac{1}{p_p}\left(\frac{\mu_n}{\tau_n}\right)^{1/2}+\frac{1}{n_n}\left(\frac{\mu_p}{\tau_p}\right)^{1/2}\right]^{-1} \tag{A.3}$$

where n_i is intrinsic carrier concentration, μ_n, μ_p are electron and hole mobilities respectively, and τ_n, τ_p are electron and hole life-times in the p and n type regions, respectively. Diffusion current is a function of n_i^2 which strongly depends on the temperature. Therefore, diffusion becomes the dominant dark current mechanism at elevated temperatures and under small biases.

A.2 Generation-Recombination Current

Generation-recombination (g-r) current can be either surface or depletion region related. There are several g-r mechanisms encountered in narrow bandgap semiconductors. Shockley-Read-Hall (SRH) centers within the depletion region act as intermediate states for thermal generation and recombination of carriers. Radiative recombination occurs via photon emission. Auger recombination takes place when a carrier gives its energy to another carrier. Localized surface states are also g-r centers, which increases the leakage current and detector noise. Additionally, photogenerated carriers close to the detector surface are destroyed by recombination, which results in lower quantum efficiency. Radiative and Auger g-r mechanisms are fundamental mechanisms resulting from the intrinsic properties of semiconductor. Although these intrinsic mechanisms cannot be eliminated, SRH centers in the depletion region can be reduced with optimization of the material growth or processing conditions. Similarly, surface generation can be lowered by passivating the surface with an optimized coating. Generation-recombination current density is defined as [1]

$$J_{g-r} = \left(\frac{n_i W_o kT}{V_{bi} (\tau_e \tau_h)^{1/2}} + \frac{P s_o n_i W_o kt}{A V_{bi}} \right) \left(\frac{2 \sinh\left(\frac{qV}{2kT} \right)}{\left(\frac{V_{bi} - V}{V_{bi}} \right)^{1/2}} \right) f(b) \qquad \text{(A.4)}$$

where τ_e and τ_h are the carrier lifetimes of electrons and holes respectively, V is the applied bias, W_o is the zero bias depletion region width, s_o is the surface recombination velocity, V_{bi} is the built-in potential, P and A are the perimeter and the area of the diode, respectively. $f(b)$ is given by

$$f(b) = \int_0^\infty \frac{du}{u^2 + 2bu + 1} \qquad \text{(A.5)}$$

where

$$b = \exp\left(-\frac{qV}{2kT}\right)\cosh\left(\frac{E_t + E_i}{kT} + \frac{1}{2}\ln\left(\frac{\tau_h}{\tau_e}\right)\right) \tag{A.6}$$

with E_i and E_t intrinsic and trapping energy levels, respectively.

A.3 Tunneling Current

Tunneling mechanisms in a photodiode can be grouped into two: band-to-band tunneling (BTB) and trap assisted tunneling (TAT). BTB tunneling can be defined as the tunneling of electrons from the valance band of the p-type region to the conduction band of the n-type region across the junction. This phenomenon occurs especially in narrow bandgap semiconductors and under high reverse bias voltages. In general, BTB tunneling current is not pronounced for MWIR photodiodes at operating temperatures and under bias voltages employed commonly. On the other hand, this mechanism becomes dominant for LWIR photodiodes especially when they are operated at low temperatures or under moderately large bias voltages. Similar to the diffusion mechanism, BTB tunneling is also a fundamental mechanism. A simplified version of BTB tunneling current expression can be given as [181]

$$J_{BTB} = \frac{q}{4\hbar\pi^2}\left[\frac{E_g kT}{P^2}\right]^{1/2} \int_{-E_{\max}}^{0} T_p\left(\frac{E}{2}\right) dE \tag{A.7}$$

where, $E_{\max} = -qV + E_F$, P is the momentum matrix, E_F is the Fermi energy, and T_P is the tunneling probability which can be expressed as

$$T_P = \exp\left[-\left(\frac{2m_e}{\hbar^2}\right)^{1/2}\left(\frac{2\varepsilon_0\varepsilon_s}{q^2 N_d}\right)^{1/2} E_g\left\{\left(1-\frac{E}{E_g}\right)\left[\frac{\pi}{2}-\sin^{-1}\left(\frac{-E}{E_g - E}\right)^{1/2}\right]-\left(-\frac{E}{E_g}\right)^{1/2}\right\}\right] \tag{A.8}$$

TAT current is created by occupied traps located either in the depletion region or in the quasi-neutral region very close to the depletion edge. Electrons are excited to the trap states thermally and then tunnel to the empty band states on the other side of the junction. Association of trap levels enhances the tunneling rate and this mechanism is more pronounced than BTB tunneling at moderate temperatures. TAT current density is given by [115]

$$J_{TAT} = qN_t \left[\frac{c_p p_1 wN_c}{c_p p_1 + wN_c} \right] x_d \tag{A.9}$$

where N_t is the trap density, x_d is the depletion layer width, c_p is the capture coefficient of holes, $p_1 = N_v \exp[-E_t/kT]$, N_v is the density of states in the valence band, E_t is the trap energy level, and wN_c is the tunneling rate. TAT current is composed of the combination of a thermal mechanism (band state to trap state thermal excitation) and a tunneling mechanism (occupied trap state to empty band state tunneling). When the dark current is limited by tunneling from the trap level, the trap-assisted tunneling current density can be approximated as [114]

$$J_{TAT} = qN_t (wN_c) x_d \tag{A.10}$$

and the tunneling rate is

$$wN_c = \frac{\pi^2 q m_e^* E M^2}{h^3 (E_g - E_t)} \exp\left[-\frac{4(2m_e^*)^{1/2} (E_g - E_t)^{3/2}}{3\hbar q E} \right] \tag{A.11}$$

where M is the matrix element of the trap potential, m_e^* is the effective mass of electrons, and E is the electric field associated with the tunneling barrier.

A.4 Ohmic Leakage Current

Ohmic leakage current owes its origin to surface leakage current and dislocations intersecting the junction. Ohmic leakage current can be expressed as [181]

$$I_{sh} = \frac{V}{R_{sh}} \tag{A.12}$$

where V is the applied voltage across the junction and R_{sh} is the diode shunt resistance.

REFERENCES

[1] A. Rogalski, *Infrared Photon Detectors*, SPIE press, 1995.

[2] H. C. Liu, *Intersubband Transitions in Quantum Wells: Physics and Device Applications I*, Semiconductors and Semimetals vol. 62, Academic Press, 2000.

[3] M. A. Fauci, R. Breiter, W. Cabanski, W. Fick, R. Koch, J. Ziegler, and S. D. Gunapala, "Medical infrared imaging – differentiating facts from fiction, and the impact of high precision quantum well infrared photodetector camera systems, and other factors, in its reemergence," *Infrared Physics & Technology*, vol. 42, pp. 337-344, 2001.

[4] W. A. Goddard, D. W. Brenner, S. E. Lyshevski, and G. J. Iafrate, *Handbook of Nanoscience Engineering and Technology*, CRC Press LLC, 2003.

[5] A. Goldberg, K. K. Choi, "Recent progress in the application of large format and multispectral QWIP IR FPAs," *Proceedings of SPIE*, vol. 5406, pp. 624-638, 2004.

[6] J. D. Vincent, *Fundamentals of Infrared Detector Operation and Testing*, Wiley Press, 1990.

[7] A. Rogalski and K. Chrzanowski, "Infrared devices and techniques," *Opto-electronics Review*, vol. 10, pp. 111–136, 2002.

[8] M. Marquis, *Handouts on Thermal imaging systems theory*, Texas Instruments Incorporated Defense Systems and Electronics, May 1996.

[9] H. Schneider, T. Maier, J. Fleissner, M. Walther, P. Koidl, G. Weimann, "Dual-Band QWIP Focal Plane Array for the Second and Third Atmospheric Windows," presented at the International Workshop on Quantum Well Infrared Photodetectors (QWIP2004), Kananaskis, Canada, August 9-13, 2004.

[10] H. M. Runciman, *Thermal Imaging*, CRC Press LLC, 2000.

[11] A. Manissadjian, P. Fillon, P. Ribolet, “Sofradir IR detectors for LW applications,” *Proceedings of SPIE*, vol. 5251, pp. 45-55, 2004.

[12] M. P. Alatman, B. Backer, M. Kohin, R. Blackwell, N. R. Butler, J. H. Cullen, “Lockheed Martin’s 640×480 uncooled microboometer camera,” *Proceedings of SPIE*, vol. 3698, pp. 137-143, 2003.

[13] T. Ishikawa, M. Ueno, K. Endo, Y. Nakaki, H. Hata, T. Sone, M. Kimata, T. Ozeki, “Low-cost 320×240 uncooled IRFPA using a conventional silicon IC process,” *Proceedings of SPIE*, vol. 3698, pp. 556-564, 2003.

[14] T. Kanno, M. Saga, S. Matsumoto, M. Uchida, N. Trukamato, A. Tanaka, S. Itoh, A. Nakazato, T. Endoh, S. Tohyama, Y. Yamamoto, S. Murashima, N. Fujimoto, N. Teranishi, “Uncooled infrared focal plane array having 128×128 thermopile detector elements,” *Proceedings of SPIE*, vol. 2269, pp. 450-459, 1994.

[15] L. Esaki and H. Sakaki, “New photoconductor,” *IBM Tech. Disc. Bull.*, vol. 20, pp. 2456-2457, 1977.

[16] B. F. Levine, K. K. Choi, C. G. Bethea, J. Walker, and R. J. Malik, “New 10-micron infrared detector using intersubband absorption in resonant tunneling GaAlAs superlattices,” *Appl. Phys. Lett.*, vol. 50, pp. 1092-1094, 1987.

[17] S. D. Gunapala, S. V. Bandara, J. K. Liu, C. J. Hill, S. B. Rafol, J. M. Mumolo, J. T. Trinh, M. Z. Tidrow, and P. D. LeVan, “1024 × 1024 pixel mid-wavelength and long-wavelength infrared QWIP focal plane arrays for imaging applications,” *Semicond. Sci. Technol.*, vol. 20, pp. 473–480, 2005.

[18] B. F. Levine, “Quantum-well infrared photodetectors,” *J. Appl. Phys.*, vol. 74, pp. R1-R81, 1993.

[19] A. Zussman, B. F. Levine, J. M. Kuo, and J. Jong, “Extended long-wavelength λ = 11-15 μm GaAs/$AI_xGa_{1-x}As$ quantum-well infrared photodetectors,” *J. Appl. Phys.*, vol. 70, pp. 5101-5107, 1991.

[20] A. Goldberg, T. Fischer, S. Kennerly, W. Beck, V. Ramirez, and K. Garner, “Laboratory and field imaging test results on single-color and dual-band QWIP focal plane arrays,” *Infrared Physics & Technology*, vol. 42, pp. 309-321, 2001.

[21] S. D. Gunapala, S. V. Bandara, A. Singh, J. K. Liu, S. B. Rafol, E. M. Luong, J. M. Mumolo, N. Q. Tran, D. Z.-Y. Ting , J. D. Vincent, C. A. Shott, J. Long, and P. D. LeVan, “640×486 Long-Wavelength Two-Color GaAs/AlGaAs Quantum Well Infrared Photodetector (QWIP) Focal Plane Array Camera,” *IEEE Trans. Electron Devices*, vol. 47, pp. 963-971, 2000.

[22] S. D. Gunapala, S. V. Bandara, J. K. Liu, S. B. Rafol, and J. M. Mumolo, "640×512 Pixel Long-Wavelength Infrared Narrowband, Multiband, and Broadband QWIP Focal Plane Arrays," *IEEE Trans. Electron Devices*, vol. 50, pp. 2353-2360, 2003.

[23] S. V. Bandara, S. D. Gunapala, J. K. Liu, S. B. Rafol, D. Z. Ting, J. M. Mumolo, R. W. Chuang, T. Q. Trinh, J. H. Liu, K. K. Choi, M. Jhabvala, J. M. Fastenau, W. K. Liu, "Four-band quantum well infrared photodetector array," *Infrared Physics & Technology*, vol. 44, pp. 369-375, 2003.

[24] S. D. Gunapala, S. V. Bandara, J. K. Liu, S. B. Rafol, J. M. Mumolo, C. A. Shott, R. Jones, J. Woolaway II, J. M. Fastenau, A. K. Liu, M. Jhabvala, K. K. Choi, "640×512 pixel narrow-band, four-band, and broad-band quantum well infrared photodetector focal plane arrays," *Infrared Physics & Technology*, vol. 44, pp. 411-425, 2003.

[25] M. Sundaram, S. C. Wang, M. F. Taylor, A. Reisinger, G. L. Milne, K. B. Reiff, R. Roger, E. Rose, R. R. Martin, "Two-color quantum well infrared photodetector focal plane arrays," *Infrared Physics & Technology*, vol. 42, pp. 301-308, 2001.

[26] J. C. Chiang and S. S. Li, "A two-stack indirect-barrier/triple-coupled quantum well infrared detector for mid-wavelength and long-wavelength infrared dual band detection," *Appl. Phys. Lett.*, vol. 71, pp. 3546-3548,1997.

[27] A. Guzman, J. L. Sanchez-Rojas, J. M. G. Tijero, J. Hernando, E. Calleja, E. Munoz, G. Vergara, R. Almazan, F. J. Sanchez, M. Verdu, and M. T. Montojo, "Voltage-tunable two-colour quantum well infrared detector with Al-graded triangular confinement barriers," *Semicond. Sci. Technol.*, vol. 16, pp. 285–288, 2001.

[28] A. Majumdar, K. K. Choi, L. P. Rokhinson, and D. C. Tsui, "Towards a voltage tunable two-color quantum-well infrared photodetector," *Appl. Phys. Lett.*, vol. 80, pp. 538-540, 2002.

[29] A. Majumdar, K. K. Choi, J. L. Reno, L. P. Rokhinson, and D. C. Tsui, "Two-color quantum-well infrared photodetector with voltage tunable peaks," *Appl. Phys. Lett.*, vol. 80, pp. 707-709, 2002.

[30] M. Z. Tidrow, K. K. Choi, C. Y. Lee, W. H. Chang, F. J. Towner, and J. S. Ahearn, "Voltage tunable three-color quantum well infrared photodetector," *Appl. Phys. Lett.*, vol. 64, pp. 1268-1270, 1994.

[31] X. Jiang, S. S. Li, and M. Z. Tidrow, "Investigation of a Multistack Voltage-Tunable Four-Color Quantum-Well Infrared Photodetector for

Mid- and Long-Wavelength Infrared Detection," *IEEE J. of Quantum Electronics*, vol. 35, 1999.

[32] Y. Zhang, D. S. Jiang, J. B. Xia, L. Q. Cui, C. Y. Song, Z. Q. Zhou, and W. K. Gem "A voltage-controlled tunable two-color infrared photodetector using GaAs/AlAs/GaAlAs and GaAs/GaAlAs stacked multiquantum wells," *Appl. Phys. Lett.*, vol. 68, pp. 2114-2116, 1996.

[33] A. Rogalski, K. Adamiec, J. Rutkowski, *Narrow-Gap Semiconductor Photodiodes*, SPIE Press, 2000.

[34] C. Besikci, "III-V Infrared Detectors on Si Substrates," *Proceedings of SPIE*, vol. 3948, pp. 31-39, 2000.

[35] B. F. Levine, A. Y. Cho, J. Walker, R. J. Malik, D. A. Kleinman, and D. L. Sivco, "InGaAs/InAlAs multiquantum well intersubband ansorption at a wavelength of λ=4.4 μm," *Appl. Phys. Lett.*, vol. 52, pp. 1481-1483, 1988.

[36] G. Hasnain, B. F. Levine, D. L. Sivco, and A. Y. Cho, "Mid-infrared detectors in the 3-5 μm band using bound to continuum state absorption in InGaAs/InAlAs multiquantum well structures," *Appl. Phys. Lett.*, vol. 56, pp. 770-772, 1988.

[37] M. O. Watanabe, Y. Ohba, "Interface properties for GaAs/InGaAlP heterojunctions by the capacitance voltage profiling technique," *Appl. Phys. Lett.*, vol. 50, pp. 906-908, 1987.

[38] S. D. Gunapala, B. F. Levine, R. A. Logan, T. Tanbun-Ek, and D. A. Humprey, "GaAs/GaInP multiquantum well long-wavelength infrared detector using bound-to-continuum state absorption," *Appl. Phys. Lett.*, vol. 57, pp. 1802-1804, 1990.

[39] M. Henini and M. Razeghi, *Handbook of Infrared Detection Technologies*, Elsevier Science Ltd., 2002.

[40] R. Rawe, A. Timlin, M. Davis, J. Devitt, M Greiner, "Advanced large format InSb IR FPA maturation at CMC Electronics," *Proceedings of SPIE*, vol. 5406, pp. 152-162, 2004.

[41] P. Castelein, F. Marion, J.-L. Martin, J. Baylet, N. Moussy, O. Gravrand, A. Durand, J.-P. Chamonal, and G. Destefanis, "A Megapixel HgCdTe MWIR Focal plane array with a 15 μm pitch," *Proceedings of SPIE*, vol. 5251, pp. 65-72, 2004.

[42] J. D. Kim, S. Kim, D. Wu, J. Wojkowski, J. Xu, J. Piotrowski, E. Bigan, and M. Razeghi, "8–13 μm InAsSb heterojunction photodiode operating at near room temperature," *Appl. Phys. Lett.*, vol. 67, pp. 2645-2647, 1995.

[43] J. D. Kim, D. Wu, J. Wojkowski, J. Piotrowski, J. Xu, and M. Razeghi "Long-wavelength InAsSb photoconductors operated at near room temperatures (200–300 K)," *Appl. Phys. Lett.*, vol. 68, pp. 99-101, 1996.

[44] A. Rakovska, V. Berger, X. Marcadet, B. Vinter, G. Glastre, T. Oksenhendler, and D. Kaplan, "Room temperature InAsSb photovoltaic midinfrared detector," *Appl. Phys. Lett.*, vol. 77, pp. 397-399, 2000.

[45] X. Marcadet, A. Rakovska, I. Prevot, G. Glastre, B. Vinter, V. Berger, "MBE growth of room-temperature InAsSb mid-infrared detectors," *Journal of Crystal Growth*, vol. 227–228, pp. 609–613, 2001.

[46] W. Dobbelaere, J. De Boeck, P. Heremans, R. Mertens, and G. Borghs, W. Luyten, and J. Van Landuyt, "$InAs_{0.85}Sb_{0.15}$ infrared photodiodes grown on GaAs and GaAs-coated Si by molecular beam epitaxy," *Appl. Phys. Lett.*, vol. 60, pp. 3256-3258, 1992.

[47] C. Besikci, S. Ozer, C. V. Hoof, L. Zimmermann, J. John, and P. Merken, "Characteristics of $InAs_{0.8}Sb_{0.2}$ photodetectors on GaAs substrates," *Semicond. Sci. Technol.*, vol. 16, pp. 992–996, 2001.

[48] C. G. Bethea, M. Y. Yen, B. F. Levine, K. K. Choi, and A. Y. Cho, "Long wavelength $InAs_{1-x}Sb_x$/GaAs detectors prepared by molecular beam epitaxy," *Appl. Phys. Lett.*, vol. 51, pp. 1431-1432, 1987.

[49] M. Kudo and T. Mishima, "Improved Electron Mobility of AlInSb/InAsSb/AlInSb Heterostructures Grown Lattice-Mismatched on GaAs Substrates," *Jpn. J. Appl. Phys.*, vol. 37, pp. L1132-L1134, 1998.

[50] J. J. Lee, J. D. Kim, and M. Razeghi, "Growth and characterization of InSbBi for long wavelength infrared Photodetectors," *Appl. Phys. Lett.*, vol. 70, pp. 3266-3268, 1997.

[51] J. J. Lee, J. D. Kim, and M. Razeghi, "Long-wavelength infrared photodetectors based on InSbBi grown on GaAs substrates," *Appl. Phys. Lett.*, vol. 71, pp. 2298-2300, 1997.

[52] K. Y. Ma, Z. M. Fang, D. H. Jaw, R. M. Cohen, G. B. Stringfellow, W. P. Kosar, and D. W. Brown, "Organometallic vapor phase epitaxial growth and characterization of InAsBi and InAsSbBi," *Appl. Phys. Lett.*, vol. 55, pp. 2420-2422, 1989.

[53] K. T. Huang, C. T. Chiu, R. M. Cohen, and G. B. Stringfellow, "InAsSbBi alloys grown by organometallic vapor-phase epitaxy," *J. Appl. Phys.*, vol. 75, pp. 2857-2863, 1994.

[54] Q. Du, J. Alperin, W. I. Wang, "Molecular beam epitaxial growth of GalnSbBi for infrared detector applications," *Journal of Crystal Growth*, vol. 175/176, pp. 849-852, 1997.

[55] Y. H. Choi, C. Besikci, F. L. Sudharsanan, and M. Razeghi, “Growth of $In_{1-x}Tl_xSb$, a new infrared material, by low-pressure metalorganic chemical vapor deposition,” *Appl. Phys. Lett.*, vol. 63, pp. 361-363, 1993.

[56] Y. H. Choi, P. T. Staveteig, E. Bigan, and M. Razeghi, “Characterization of InTISb/lnSb grown by low-pressure metal-organic chemical vapor deposition on a GaAs substrate,” *J. Appl. Phys.,* vol. 75, pp. 3196-3198, 1994.

[57] J. J. Lee and M. Razeghi, “Tl incorporation in InSb and lattice contraction of $In_{1-x}Tl_xSb$,” *Appl. Phys. Lett.*, vol. 76, pp. 297-299, 2000.

[58] P. T. Staveteig, Y. H. Choi, G. Labeyrie, E. Bigan, and M. Razeghi, “Photoconductance measurements on InTISb/lnSb/GaAs grown by low-pressure metalorganic chemical vapor deposition,” *Appl. Phys. Lett.*, vol. 64, pp. 460-462, 1994.

[59] J. D. Kim, E. Michel, S. Park, J. Xu, S. Javadpour, and M. Razeghi, “Room-temperature operation of InTlSb infrared photodetectors on GaAs,” *Appl. Phys. Lett.*, vol. 69, pp. 343-344, 1996.

[60] M. V. Schilfgaarde, A. Chen, S. Krishnamurthy, and A. Sher, “InTlP—a proposed infrared detector material,” *Appl. Phys. Lett.*, vol. 65, pp. 2714-2716, 1994.

[61] D. Sengupta, V. Jandhyala, S. Kim, W. Fang, J. Malin, P. Apostolakis, K. C. Hseih, Y. C. Chang, S. L. Chuang, S. Bandara, S. Gunapala, M. Feng, E. Michielssen, and G. Stillman, “Redshifting and Broadening of Quantum-Well Infrared Photodetector’s Response via Impurity-Free Vacancy Disordering,” *IEEE J. of Selected Topics in Quantum Electronics*, vol. 4, pp. 746-757, 1998.

[62] A. Rogalski, “Assessment of HgCdTe photodiodes and quantum well infrared photoconductors for long wavelength focal plane arrays,” *Infrared Physics & Technology,* vol. 40, pp. 325-330, 1999.

[63] A. Rogalski, “Toward third generation HgCdTe infrared detectors,” *Journal of Alloys and Compounds*, vol. 371, pp. 53–57, 2004.

[64] J. Ziegler, M. Bruder, M. Finck, R. Kruger, P. Menger, T. Simon, R. Wollrab, “Advanced sensor technologies for high performance infrared detectors,” *Infrared Physics & Technology*, vol. 43, pp. 239–243, 2002.

[65] W. Cabanski, R. Breiter, R. Koch, W. Gross, K.-H. Mauk, W. Rode, J. Ziegler, H. Schneider, M. Walther, R. Oelmaier, “Third gen focal plane array IR detection modules at AIM,” *Infrared Physics & Technology*, vol. 43, pp. 257-263, 2002.

[66] D. J. Gulbransen, P. J. Love, M. P. Murray, N. A. Lum, C. L. Fletcher, E. Corrales, R. E. Mills, A. W. Hoffman, and K. J. Ando, "Megapixel and Larger Readouts and FPAs for Visible and Infrared Astronomy," *Proceedings of SPIE*, vol. 4841, pp. 770-781, 2003.

[67] T. Ashley, R. A. Ballingall, J. E. Beale, I. D. Blenkinsop, T. M. Burke, J. H. Firkins, D. J. Hall, L. Hipwood, C. Hollier, P. Knowles, D. J. Lees, J. C. Little, and C. Shaw, "Large Format MWIR Focal Plane Arrays," *Proceedings of SPIE*, vol. 4820, pp. 400-405, 2003.

[68] G. Destefanis. (2004, June). Leti 6th Annual Review. Leti Corp., France.

[69] S. D. Gunapala, S. V. Bandara, J. K. Liu, S. B. Rafol, C. Hill, J. Mumolo, J. Thang, M. Tidrow, and P. D. LeVan, "Mid-wavelength infrared 1024×1024 pixel QWIP focal plane array," *Proceedings of SPIE*, vol. 5406, pp. 600-604, 2004.

[70] E. Brochier, P. Tribolet, P. Chorier, P. Costa, P. Fillon, "Cooled large IR staring arrays : towards third generation," *Proceedings of SPIE*, vol. 5251, pp. 26-36, 2004.

[71] C. M. Bacon, C. W. McMurtry, J. L. Pipher, W. J. Forrest, J. D. Garnett, D. Lee, and D. D. Edwallm "Characterization of Rockwell Scientific LWIR HgCdTe Detector Arrays," *Proceedings of SPIE*, vol. 5167, pp. 313-319, 2004.

[72] M. Jhabvala, K. Choi, A. Goldberg, A. La, S. Gunapala, "Development of a 1K × 1K GaAs QWIP Far IR Imaging Array," *Proceedings of SPIE*, vol. 5167, pp. 175-185, 2004.

[73] www.qwip.com

[74] S. D. Gunapala, S. V. Bandara, J. K. Liu, E. M. Luong, S. B. Rafol, J. M. Mumolo, D. Z. Ting, J. J. Bock, M. E. Ressler, M. W. Werner, P. D. LeVan, R. Chehayeb, C. A. Kukkonen, M. Levy, P. LeVan, M. A. Fauci, "Quantum well infrared photodetector research and development at Jet Propulsion Laboratory," *Infrared Physics & Technology*, vol. 42, pp. 267-282, 2001.

[75] J. L. Tissot, "Advanced IR detector technology development at CEA/LETI," *Infrared Physics & Technology*, vol. 43, pp. 223–228, 2002.

[76] D. Scribner, J. Schuler, P. Warren, M. Satyshur, and M. Kruer, "Infrared color fusion: separating objects from backgrounds", *Proceedings of SPIE*, vol. 3379, 1998.

[77] W. Cabanski, K. Eberhardt, W. Rode, J. Wendler, J. Ziegler, J.Fleiner, F. Fuchs, R. Rehm, J. Schmitz, H. Schneider, M. Walther, "3rd Gen Focal

Plane Array IR Detection Modules and Applications," *Proceedings of SPIE*, vol. 5406, pp. 184-192, 2004.

[78] H. Schneider, T. Maier, J. Fleissner, M. Walther, P. Koidl, G. Weimann, W. Cabanski, M. Finck, P. Menger, W. Rode, J. Ziegler, "Dual-band QWIP focal plane array for the second and third atmospheric windows," *Infrared Physics & Technology*, to be published.

[79] T. Ashley, A. B. Dean, C. T. Elliott, C. F. McConville, and C. R. Whitehouse, "Molecular-beam growth of homoepitaxial InSb photovoltaic detectors," *Electron. Lett.*, vol. 24, pp. 1270–1272, 1988.

[80] S. R. Kurtz, L. R. Dawson, T. E. Zipperian, O. Whaley "High-detectivity (> 1 × 10^{10} cmHz$^{1/2}$/W), InAsSb strained-layer superlattice, photovoltaic infrared detector," *IEEE Electron Device Letters.*, vol. 11, pp. 54-56, 1990.

[81] T. Ashley, A. B. Dean, C. T. Elliott, C. F. McConville, H. Whitehouse, "Molecular-beam growth of homoepitaxial InSb photovoltaic detectors," *Electronics Letters*, pp. 1270-1272, 1988.

[82] I. Bloom and Y. Nemirovsky "Surface Passivation of Backside-Illuminated Indium Antimonide Focal Plane Array," *IEEE Trans. on Electron Dev.*, vol. 40, pp. 309-314, 1991.

[83] D. T. Cheung, A. M. Andrews, E. R. Gertner, G. M. Williams, J. E. Clarke, J. G. Pasko, and J. T. Longo, "Backside-illuminated $InAs_{1-x}Sb_x$-InAs narrow-band photodetectors," *Appl. Phys. Lett.,* vol. 30, pp. 587-589, 1977.

[84] L. O. Bubulac, A. M. Andrews, E. R. Gertner, and D. T. Cheung, "Backside illuminated InAsSb/GaSb broadband detectors," *Appl. Phys. Lett.,* vol. 36, pp. 734-736,1980.

[85] K. Mohammed, F. Capasso, R. A. Logan, J. P. van der Ziel, and A. L. Hutchinson, "High dedectivity $InAs_{0.85}Sb_{0.15}$/InAs infrared (1.8-4.8 μm) detectors," *Electron. Lett.,* vol. 22, pp. 215-216, 1986.

[86] J. L. Zyskind, A. K. Srivastava, J. C. DeWinter, M. A. Pollack, and J. W. Sulhoff, "Liquid phase epitaxial $InAs_ySb_{1-y}$ on GaSb substrates using GaInAsSb buffer layers: growth, characterization, and application to mid-IR photodiodes," *J. Appl. Phys.*, vol. 61, pp. 2898-2903, 1987.

[87] J.-I. Chyi, S. Kalem, N. S. Kumar, C. W. Litton, and H. Morkoç, "Growth of InSb and $InAs_{1-x}Sb_x$ on GaAs by molecular beam epitaxy," *Appl. Phys. Lett.*, vol. 53, pp. 1092-1094, 1988.

[88] C. Besikci, Y. H. Choi, R. Sudharsanan, and M. Razeghi, "Anomalous Hall effect in InSb layers grown by metalorganic chemical vapor

deposition on GaAs substrates," *J. Appl. Phys.*, vol. 73, pp. 5009-5013, 1993.

[89] J. R. Söderström, M. M. Cumming, J-Y Yao, and T. G. Andersson, "Molecular beam epitaxy growth and characterization of InSb layers on GaAs substrates," *Semicond. Sci. Technol.*, vol. 7, pp. 337-343, 1992.

[90] G. M. Williams, C. R. Whitehouse, C. F. McConville, A. G. Cullis, T. Ashley, S. J. Courtney, and C. T. Elliott, "Heteroepitaxial growth of InSb on (100) GaAs using molecular beam epitaxy," *Appl. Phys. Lett.*, vol. 53, pp. 1189-1191, 1988.

[91] J. E. Oh, P. K. Bhattacharya, Y. C. Chen, and S. Tsukamato, "Molecular-beam epitaxial growth of high-quality InSb on InP and GaAs substrates," *J. Appl. Phys.*, vol. 66, pp. 3618-3621, 1989.

[92] C. Besikci, Y. H. Choi, G. Labeyrie, E. Bigan, M. Razeghi, J. B. Cohen, J. Carsello, and V. P. Dravid, "Detailed analysis of carrier transort in $InAs_{0.3}Sb_{0.7}$ layers grown on GaAs substrates by metalorganic chemical-vapor deposition," *J. Appl. Phys.*, vol. 76, pp. 5820-5828, 1994.

[93] M. Y. Yen, "Molecular-beam epitaxial growth and electrical properties of lattice mismatched $InAs_{1-x}Sb_x$ on (100) GaAs," *J. Appl. Phys.*, vol. 64, pp. 3306-3309, 1988.

[94] L. K. Li, Y. Hsu, and W. I. Wang, "Molecular-beam epitaxial growth of InSb on GaAs and Si for infrared detector applications," *J. Vac. Sci. Technol. B*, vol. 11, pp. 872-874, 1993.

[95] P. E. Thompson, J. L. Davis, J. Waterman, R. J. Wagner, D. Gammon, D. K. Gaskill, and R. Stahlbush, "Use of atomic layer epitaxy buffer for the growth of InSb on GaAs by molecular beam epitaxy," *J. Appl. Phys.*, vol. 69, pp. 7166-7172, 1991.

[96] E. Michel, G. Singh, S. Slivken, C. Besikci, P. Bove, I. Ferguson, and M. Razeghi, "Molecular beam epitaxial growth of high quality InSb," *Appl. Phys. Lett.*, vol. 65, pp. 3338-3340, 1994.

[97] E. Michel, J. Xu, J. D. Kim, I. Ferguson, M. Razeghi, "InSb Infrared Photodetectors on Si Substrates Grown by Molecular Beam Epitaxy," *IEEE Photonics Technology Letters*, vol. 8, pp. 673-675, 1996.

[98] J.-I. Chyi, D. Biswas, S. V. Iyer, N. S. Kumar, and H. Morkoç, "Molecular-beam epitaxial growth and characterization of InSb on Si," *J. Vac. Sci. Technol. B*, vol. 7, pp. 345-347, 1989.

[99] G. E. Franklin, D. H. Rich, H. Hong, T. Miller, and T.-C. Chiang, "Interface formation and growth of InSb on Si(100)," *Physical Review B*, vol. 45, pp. 3426-3434, 1992.

[100] S. V. Ivanov, A. A. Boudza, R. N. Kutt, N. N. Ledentsov, B. Y. Meltser, S. S. Ruvimov, S. V. Shaposhnikov, P. S. Kop'ev, "Molecular beam epitaxial growth of InSb/GaAs(100) and InSb/Si(100) heteroepitaxial layers (thermodynamic analysis and characterization)," *Journal of Crystal Growth*, vol. 156, pp. 191-205, 1995.

[101] M. Kitabatake, T. Kawasaki, and T. Korechika, "Heteroepitaxial growth of InSb(111) on Si(111)," *Thin Solid Films*, vol. 281-282, pp 17-19, 1996.

[102] M. Mori, Y. Tsubosaki, T. Tambo, H. Ueba, C. Tatsuyama, "Growth of InSb films on a Si(001) substrate with Ge buffer layer," *Applied Surface Science*, vol. 117/118, pp. 512-517, 1997.

[103] W. K. Liu, J. Winesett, W. Ma, X. Zhang, M. B. Santos, X. M. Fang, and P. J. McCann, "Molecular beam epitaxy of InSb on Si substrates using fluoride buffer layers," *J. Appl. Phys.*, vol. 81, pp. 1708-1714, 1997.

[104] B.V. Rao, D. Gruznev, T. Tambo, C. Tatsuyama, "Growth of high-quality InSb films on Si(111) substrates without buffer layers," *Journal of Crystal Growth*, vol. 224, pp. 316–322, 2001.

[105] I. Kimukin, N. Biyikli, T. Kartaloglu, O. Aytür, and E. Ozbay, "High-Speed InSb Photodetectors on GaAs for Mid-IR Applications," *IEEE J. of Selected Topics in Quantum Electronics*, vol. 10, pp. 766-770, 2004.

[106] I. Kimukin, N. Biyikli, and E. Ozbay, "InSb high-speed photodetectors grown on GaAs substrate," *J. of Appl. Phys.*, vol. 94, pp. 5414-5416, 2003.

[107] R. Ashokan, N. K. Dhar, B. Yang, A. Akhiyat, T. S. Lee, S. Rujirawat, S. Yousuf, and Sivananthan, "Variable Area MWIR Diodes on HgCdTe/Si Grown by Molecular Beam Epitaxy" *J. Electron. Mater.*, vol. 29, pp. 636-640, 2000.

[108] J. B. Varesi, R. E. Bornfreund, A. C. Childs, W. A. Radford, K. D. Maranowski, J. M. Peterson, S. M. Johnson, L. M. Giegerich, T. J. Lyon, and J. E. Jensen, "Fabrication of High-Performance Large-Format MWIR Focal Plane Arrays from MBE-Grown HgCdTe on 4" Silicon Substrates," *J. Electron. Mater.,* vol. 30**,** pp. 566-573, 2001.

[109] S. M. Johnson, M. H. Kalisher, W. L. Ahlgren, J. B. James, and C. A. Cockrum, "HgCdTe 128×128 infrared focal plane arrays on alternative substrates of CdZnTe/GaAs/Si," *Appl. Phys. Lett.,* vol. 56, pp. 946-948, 1990.

[110] S. M. Johnson, D. R. Rhiger, J. P. Rosbeck, J. M. Peterson, S. M. Taylor, and M. E. Boyd, "Effect of dislocations on the electrical and optical properties of long-wavelength infrared HgCdTe photovoltaic detectors," *J. Vac. Sci. Technol. B*, vol. 10, pp. 1499-1506, 1992.

[111] P. W. Norton and A. P. Erwin, “Etch pit study of dislocation formation in $Hg_{1-x}Cd_xTe$ during array hybridization and its effect on device performance,” *J. Vac. Sci. Technol. A*, vol. 7, pp. 503-508, 1989.

[112] I. M. Baker and C. D. Maxey, “Summary of HgCdTe 2D Array Technology in the U.K.,” *J. Electron. Mater.,* vol. 30, pp. 682-689, 2001.

[113] A. Rogalski, “Heterostructure infrared photodiodes,” *Semicond. Phys., Quantum Elect. & Optoelect.*, vol. 3, pp. 111-120, 2000.

[114] Y. Nemirovsky and A. Unikovsky, “Tunneling and 1/f noise currents in HgCdTe photodiodes,” *J. Vac. Sci. Technol. B*, vol. 10, pp. 1602-1610, 1992.

[115] Y. Nemirovsky, R. Fastow, M. Meyassed, and A. Unikovsky, “Trapping effects in HgCdTe,” *J. Vac. Sci. Technol. B*, vol. 9, pp. 1829-1839, 1991.

[116] S. Ozer and C. Besikci, “Assessment of InSb photodetectors on Si substrates,” *J. Phys. D: Appl. Phys.*, vol. 36, pp. 559–563, 2003.

[117] P. A. Skountzos and P. C. Euthymiou, “Dependence of surface recombination velocity of InSb on temperature and alpha bombardment dose,” *J. Appl. Phys.,* vol. 47, pp. 4693-4696, 1976.

[118] J. Bajaj, E. R. Blazejewski, G. M. Williams, R. E. Dewames, M. Brown, “Noise (1/f) and dark currents in midwavelength infrared PACE-I HgCdTe photodiodes,” *J. Vac. Sci. Tecnol. B*, vol. 10, pp. 1617-1625, 1992.

[119] T. G. M. Kleinpenning, “1/f noise in pn junction diodes,” *J. Vac. Sci. Technol. A*, vol. 3, pp. 176-182, 1985.

[120] T. G. M. Kleinpenning, “1/f Mobility fluctuations in p-i-n and pn diodes,” *Physica B*, vol. 154, pp. 27-34, 1988.

[121] L. K. J. Vandamme and B. Orsal, “1/f Noise in Short n^-p^+ diffisuon current dominated (HgCd)Te Avalanche Photodiodes,” *IEEE Tran. Electron Dev.*, vol. 35, pp. 502-506, 1988.

[122] U. Tumkaya, “Performance Assessment of Indium Antimonide Photodetectors Photodetectors in Silicon Substrates,” *M.Sc. Thesis*, Middle East Technical University, Phys. Dept., June 2003.

[123] H. C. Liu, Z. R. Wasilewski, and M. Buchanan, “Segregation of Si δ doping in GaAs-AlGaAs quantum wells and the cause of the asymmetry in the current-voltage characteristics of intersubband infrared detectors,” *Appl. Phys. Lett.*, vol. 63, pp. 761-763, 1993.

[124] K. K. Choi, *The Physics of Quantum Well Infrared Photodetectors*, World Scientific, 2000.

[125] H. C. Liu, "Dependence of absorption spectrum and responsivity on the upper state position in quantum well intersubband photodetectors," *J. Appl. Phys.*, vol. 73, pp. 3062-3067, 1993.

[126] S. D. Gunapala, B. F. Levine, L. Pfeiffer, and K. West, "Dependence of the performance of GaAs/AlGaAs quantum well infrared photodetectors on doping and bias," *J. Appl. Phys.*, vol. 69, pp. 6517-6520, 1991.

[127] B. Xing, H. C. Liu, P. H. Wilson, M. Buchanan, Z. R. Wasilewski, and J. G. Simmons, "Noise and photoconductive gain in AlGaAs/GaAs quantum well intersubband infrared photodetectors," *J. Appl. Phys.*, vol. 76, pp. 1889-1894, 1994.

[128] J. L. Pan and C. G. Fonstad, "Theory, fabrication and characterization of quantum well infrared photodetectors," *Materials Science and Engineering*, vol. 28, pp. 65-147, 2000.

[129] A. G. Steele, H. C. Liu, M. Buchanan, and Z. R. Wasilewski, "Influence of the number of wells in the performance of multiple quantum well intersubband infrared detectors," *J. Appl. Phys.*, vol. 72, pp. 1062-1064, 1992.

[130] L. C. West, S. J. Eglash, "First observation of an extremely large-dipole infrared transition within the conduction band of a GaAs quantum well," *Appl. Phys. Lett.*, vol. 46, pp. 1156-1158, 1985.

[131] L. J. Kozlowski, J. M. Arias, G. M. Williams, K. Vural, D. E. Cooper, S. A. Cabelli, and C. Bruce, "Recent Advances in Staring Hybrid Focal Plane Arrays: Comparison of HgCdTe, InGaAs, and GaAs/AlGaAs Detector Technologies," *Proceedings of SPIE*, vol. 2274, pp. 93-116, 1994.

[132] C. P. Lee, K. H. Chang, and K. L. Tsai, "Quantum well infrared photodetectors with bi-periodic grating couplers," *Appl. Phys. Lett.*, vol. 61, pp. 2437-2439, 1992.

[133] K. L. Tsai, C. P. Lee, J. S. Tsang, H. R. Chen, and K. H. Chang, "Two-Dimensional Bi-Periodic Grating Coupled One- and Two-Color Quantum Well Infrared Photodetectors," *IEEE Electron Device Letters*, vol. 16, pp. 49-51, 1995.

[134] G. Sarusi, B. F. Levine, S. J. Peat-ton, K. M. S. Bandara, and R. E. Leibenguth, "Improved performance of quantum well infrared photodetectors using random scattering optical coupling," *Appl. Phys. Lett.*, vol. 64, pp. 960-962, 1994.

[135] V. Jandhyala, D. Sengupta, E. Michielssen, B. Shanker, and G. Stillman, "Two-dimensional rough surface couplers for broadband quantum-well infrared photodetectors," *Appl. Phys. Lett.*, vol. 73, pp. 3495-3497, 1998.

[136] T. Cwik and C. Yeh, "Highly sensitive quantum well infrared photodetectors," *J. Appl. Phys.*, vol. 86, pp. 2779-2784, 1999.

[137] S.-Y. Deng, J. Y.-M. Lee, J.-T. Lai, Y.-D. Chih, T.-P. Sun, and H.-M. Hong, "Front-illuminated long wavelength multiple quantum-well infrared photodetectors with backside gratings," *J. Appl. Phys.,* vol. 78, pp. 6822-6825, 1995.

[138] T. R. Schimert, S. L. Barnes, A. J. Brouns, F. C. Case, P. Mitra, and L. T. Claiborne, "Enhanced quantum well infrared photodetector with novel multiple quantum well grating structure," *Appl. Phys. Lett.,* vol. 68, pp. 2846-2848, 1996.

[139] C.-J. Chen, K.-K. Choi, W. H. Chang, and D. C. Tsui, "Corrugated Quantum Well Infrared Photodetectors with Polyimide Planarization for Detector Array Applications," *IEEE Trans. on Elect. Dev.*, vol. 45, pp. 1431-1437, 1998.

[140] K. K. Choi, C. J. Chen, A. C. Goldberg, W. H. Chang, and D. C. Tsui, "Performance of corrugated quantum well infrared photodetectors," *Proceedings of SPIE*, vol. 3379, 441-452, 1998.

[141] J. Y. Andersson and L. Lundqvist, "Grating-coupled quantum-well infrared detectors: Theory and performance," *J. Appl. Phys.*, vol. 71, pp. 3600-3610, 1992.

[142] A. D. Rossi, E. Costard, N. Guerineau, S. Rommeluere, "Effect of finite pixel size on optical coupling in QWIPs," *Infrared Physics & Technology*, vol. 44, pp. 325-330, 2003.

[143] W. A. Beck and M. S. Mirotznik, "Microstrip antenna coupling for quantum-well infrared photodetectors," *Infrared Physics & Technology*, vol. 42, pp. 189-198, 2001.

[144] Y. Y. Fu, M. Willander, W. Lu, W. L. Xu, N. Li, X. Q. Liu, Y. D. Chen, and S. C. Shen, "Near-field coupling effect in normal-incidence absorption of quantum-well infrared photodetectors," *J. of Appl. Phys.*, vol. 85, pp. 1237-1239, 1999.

[145] H. C. Liu, M. Buchanan, and Z. R. Wasilewski, "How good is the polarization selection rule for intersubband transitions," *Appl. Phys. Lett.*, vol. 72, pp. 1682-1684, 1998.

[146] C. Qiu, "A Novel Readout Method for Focal Plane Array Imaging in the Presence of Large Dark Current," *Dissertation for the Degree of Doctor of Philosophy*, New Jersey Institute of Technology, Dept. of Electrical and Computer Eng., January 1999.

[147] C.-C. Hsieh, C.-Y. Wu, F.-W. Jih, and T.-P. Sun, "Focal-Plane-Arrays and CMOS Readout Techniques of Infrared Imaging Systems," IEEE *Transactions on Circuits and Systems for Video Technology*, vol. 7, pp. 594-605, 1997.

[148] S. D. Gunapala, J. K. Liu, J. S. Park, M. Sundaram, C. A. Shott, T. Hoelter, T.-L. Lin, S. T. Massie, P. D. Maker, R. E. Muller, and G. Sarusi, "9 μm Cutoff GaAs/AlGaAs Quantum Well Infrared Photodetector Hand-Held Camera," *IEEE Trans. on Elect. Dev.*, vol. 44, pp. 51-57, 1997.

[149] H. Kulah and T. Akin, "A Current Mirroring Integration Based Readout Circuit for High Performance Infrared FPA Applications," *IEEE Transactions on Circuits and Systems-II: Analog and Digital Signal Processing*, vol. 50, pp. 181-186, 2003.

[150] H. Kulah and T. Akin, "A CMOS Current Mirroring Integration Readout Structure for Infrared Focal Plane Arrays," *Proceedings Europian Solid-State Circuits Conference*, pp. 468-471, September 1998.

[151] M. Tepegoz and T. Akin, "A Readout Circuit for QWIP Infrared Detector Arrays Using Current Mirroring Integration," *European Solid-State Circuits Conference*, 2003.

[152] H. Kulah, "A CMOS Integrated PtSi Schottky-Barrier Infrared Detector for Night Vision Applications," *M.Sc. Thesis*, Middle East Technical University, Electrical and Electronics Dept., July 1998.

[153] M. Tepegoz, "A CMOS 64×64 Integrated Readout Circuit for Infrared Photodetector Focal Plane Arrays," *M.Sc. Thesis*, Middle East Technical University, Electrical and Electronics Dept., August 2003.

[154] L. J. Kozlowski, G. M. Williams, G. J. Sullivan, C. W. Farley, R. J. Anderson, J. Chen, D. T. Cheung, W. E. Tennant, and R. E. DeWames, "LWIR 128×128 GaAs/AlGaAs Multiple Quantum Well Hybrid Focal Plane Array," *IEEE Trans. on Electron Devices*, vol. 38, pp. 1124-1130, 1991.

[155] O. Nesher, S. Elkind, A. Adin, I. Nevo, A. B. Yaakov, S. Raichshtain, A. B. Marhasev, A. Magner, M. Katz, T. Markovitz, D. Chen, M. Kenan, A. Ganany, J. O. Schlesinger, and Z. Calahorra, "A Digital Cooled InSb Detector for IR Detection," *Proceedings of SPIE*, vol. 5074, pp. 120-129, 2003.

[156] B. F. Levine, C. G. Bethea, K. G. Glogovsky, J. W. Stayt, and R. E. Leibenguth, "Long-wavelength 128×128 GaAs Quantum Well Infrared Photodetector Arrays," *Semicond. Sci. Technol.*, vol. 6, pp. C114-C119, 1991.

[157] S. D. Gunapala, S. V. Bandara, J. K. Liu, W. Hong, M. Sundaram, P. D. Maker, R. E. Muller, C. A. Shott, and R. Carralejo, "Long-Wavelength 640×486 GaAs/AlGaAs Quantum Well Infrared Photodetector Snap-Shot Camera," *IEEE Trans. on Elect. Dev.*, vol. 45, pp. 1890-1895, 1998.

[158] www.indigosystems.com

[159] Y. Gusakov, E. Finkman, G. Bahir, and D. Ritter, "The effect of strain in InP/InGaAs quantum-well infrared photodetectors on the operating wavelength," *Appl. Phys. Lett.*, vol. 79, pp. 2508-2510, 2001.

[160] S. D. Gunapala, B. F. Levine, D. Ritter, R. A. Hamm, and M. B. Panish, "Lattice-matched InGaAsP/InP long-wavelength quantum well infrared photodetectors," *Appl. Phys. Lett.*, vol. 60, pp. 636-638, 1992.

[161] S. D. Gunapala, B. F. Levine, D. Ritier, R. Hamm, and M. B. Panish, "InGaAs/lnP long wavelength quantum well infrared photodetectors," *Appl. Phys. Lett.*, vol. 58, pp. 2024-2026, 1991.

[162] J. Y. Andersson, L. Lundqvist, Z. F. Paska, K. Streubel, and J. Wallin, "Long-wavelength quantum-well infrared detectors based on intersubband transitions in InGaAs/InP quantum wells," *Proceedings of SPIE*, vol. 1762, pp. 216-226, 1992.

[163] D. K. Sengupta, S. L. Jackson, A. P. Curtis, W. Fang, J. I. Malin, T. U. Horton, Q. Hartman, H. C. Kuo, S. Thomas, J. Miller, K. C. Hsieh, I. Adesida, S. L. Chuang, M. Feng, G. E. Stillman, Y. C. Chang, W. Wu, J. Tucker, H. Chen, J. M. Gibson, J. Mazumder, L. Li, and H.C. Liu, "Growth and characterization of n-type InP/InGaAs quantum well infrared photodetectors for response at 8.93 μm," *J. Electron. Mater.*, vol. 26, pp. 1376-1381, 1997.

[164] C. Jelen, S. Slivken, T. David, M. Razeghi, and G. J. Brown, "Noise Performance of InGaAs–InP Quantum-Well Infrared Photodetectors," *IEEE Journal of Quantum Electronics*, vol. 34, pp. 1124-1128, 1998.

[165] H. C. Liu, C. Song, E. Dupont, P. Poole, P. H. Wilson, B. J. Robinson, and D. A. Thompson, "Near and middle infrared dual band operation of InGaAs/InP quantum well infrared photodetector," *Electronics Letters*, vol. 35, pp. 2055-2056, 1999.

[166] J. Jiang, C. Jelen, M. Razeghi, and G. J. Brown, "High Detectivity GaInAs–InP Quantum-Well Infrared Photodetectors Grown on Si Substrates," *IEEE Photonics Technology Letters*, vol. 14, pp. 372-374, 2002.

[167] B. Aslan, H. C. Liu, A. Bezinger, P. J. Poole, M. Buchanan, R. Rehm and H. Schneider, "High responsivity, dual-band response and intraband

avalanche multiplication in InGaAs/InP quantum well photodetectors," *Semicond. Sci. Technol.,* vol. 19, 442–445, 2004.

[168] J. Jiang, K. Mi, R. McClintock, M. Razeghi, G. J. Brown, and C. Jelen, "Demonstration of 256×256 Focal Plane Array Based on Al-Free GaInAs–InP QWIP," *IEEE Photonics Technology Letters*, vol. 15, pp. 1273-1275, 2003.

[169] O. O. Cellek, S. Ozer, and C. Besikci, "High Responsivity InP/InGaAs Quantum well Infrared Photodetectors: Characteristics and Focal Plane Array performance," *IEEE Journal of Quantum Electronics*, to be published.

[170] S. Ozer, O. O. Cellek, and C. Besikci, "Assessment of large format InP/InGaAs quantum well infrared photodetector focal plane array," *Infrared Physics & Technology*, to be published.

[171] H. Okumura, S. Misawa, S. Yoshida, and S. Gonda, "Determination of the conduction-band discontinuities of GaAs/Al$_x$Ga$_{1-x}$As interfaces by capacitance-voltage measurements," *Appl. Phys. Lett.*, vol. 46, pp. 377-379, 1985.

[172] http://www.ioffe.rssi.ru

[173] O. O. Cellek, "Modeling, Fabrication, and Characterization of Quantum Well Infrared Photodetectors and Focal Plane Arrays," *Ph. D. Prestudy Report*, Middle East Technical University, Dept. of Electrical and Electronics Eng., December 2003.

[174] R. Rehm, H. Schneider, K. Schwarz, M. Walther, P. Koidl, and G. Weimann, "Responsivity and gain of InGaAs/GaAs-QWIPs and GaAs/AlGaAs QWIPs: a comparative study," *Proceedings of SPIE*, vol. 4288, pp. 379-385, 2001.

[175] H. Schneider, "Theory of avalanche multiplication and excess noise in quantum-well infrared photodetectors," *Appl. Phys. Lett.*, vol. 82, pp. 4376-4378, 2003.

[176] R. Rehm, H. Schneider, M. Walther, P. Koidl, and G. Weimann, "Avalanche multiplication due to impact ionization in quantum-well infrared photodetectors: A quantitative approach," *Appl. Phys. Lett.*, vol. 82, pp. 2907-2909, 2003.

[177] O. O. Cellek, S. Memis, U. Bostanci, S. Ozer, and C. Besikci, "Gain and transient photoresponse of quantum well infrared photodetectors: a detailed ensemble Monte Carlo study," *Physica E*, vol. 24, pp. 318–327, 2004.

[178] O. O. Cellek and C. Besikci, “Detailed investigation of electron transport, capture and gain in $Al_{0.3}Ga_{0.7}As$/GaAs quantum-well infrared photodetectors,” *Semicond. Sci. Technol.*, vol. 19, pp. 183-190, 2004.

[179] E. Costard, P. Bois, A. D. Rossi, A. Nedelcu, O. Cocle, F. H. Gauthier, and F. Audier, “QWIP detectors and thermal imagers,” *C. R. Physique*, vol. 4, pp. 1089–1102, 2003.

[180] G. C. Holst, *Testing and Evaluation of Infrared Imaging Systems*, SPIE Optical Engineering Press, 1998.

[181] V. Gopal, S. K. Singh, R. M. Mehra, “Analysis of dark current contributions in mercury cadmium telluride junction diodes,” *Infrared Physics & Technology*, vol. 43, pp. 317-326, 2002.

CURRICULUM VITAE

PERSONAL INFORMATION

Surname, Name: Özer, Selçuk
Nationality: Turkish (TC)
Date and Place of Birth: 1 March 1976, Bursa
Marital Status: Single
Phone: +90 312 210 45 79
Fax: +90 312 210 12 61
e-mail: selcukozer@hotmail.com

EDUCATION

Degree	Institution	Year of Graduation
MS	METU Electrical and Electronics Engineering	2000
BS	METU Electrical and Electronics Engineering	1997
High School	Eskişehir Fatih Fen Lisesi, Eskişehir	1992

WORK EXPERIENCE

Year	Place	Enrollment
2000-Present	METU Department of Electrical and Electronics Engineering	Teaching Assistant
1997-2000	KAREL Elektronik A.Ş.	Design Engineer
1995 August	Nergis Textile Industries Corp.	Intern Engineering Student

FOREIGN LANGUAGES

Advanced English

PUBLICATIONS

1. C. Besikci, S. Ozer, C. V. Hoof, L. Zimmermann, J. John and P. Merken, "Characteristics of $InAs_{0.8}Sb_{0.2}$ photodetectors on GaAs substrates," *Semicond. Sci. Technol.*, vol. 16, pp. 992-996, 2001.

2. S. Ozer and C. Besikci, "Assessment of InSb photodetectors on Si substrates," *J. Phys. D: Appl. Phys.*, vol. 36, pp. 559–563, 2003.

3. O.O. Cellek, S. Memis, U. Bostanci, S. Ozer, C. Besikci, "Gain and transient photoresponse of quantum well infrared photodetectors: a detailed ensemble Monte Carlo study," *Physica E*, vol. 24, pp. 318–327, 2004.

4. S. Ozer, O. O. Cellek, C. Besikci, "Assessment of large format InP/InGaAs quantum well infrared photodetector focal plane array," *Infrared Physics & Technology*, to be published.

5. O. O. Cellek, S. Ozer, C. Besikci, "High Responsivity InP/InGaAs Quantum well Infrared Photodetectors: Characteristics and Focal Plane Array performance," *IEEE Journal of Quantum Electronics*, to be published.

HOBBIES

Movies, Football, Reading, Sightseeing